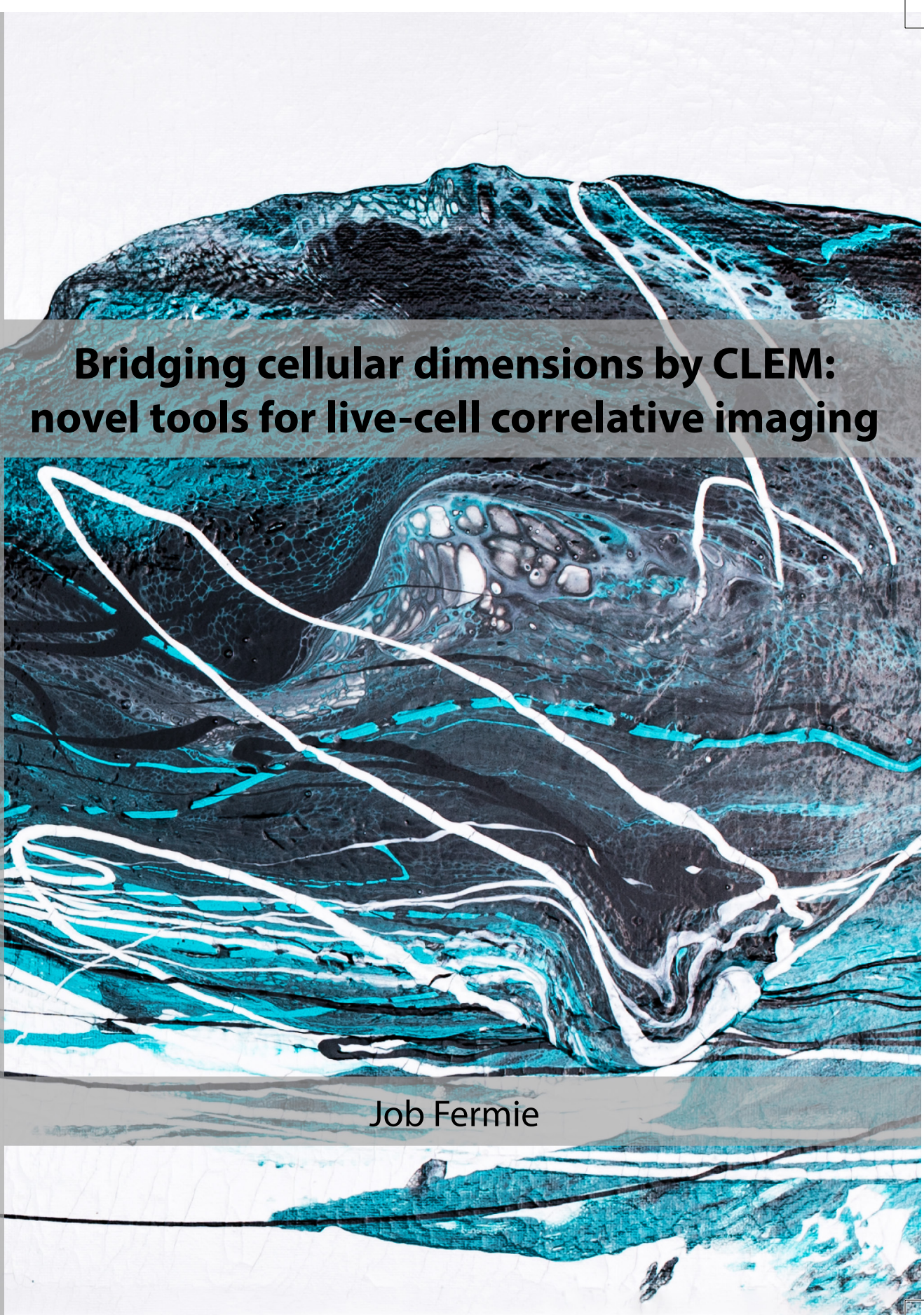




Bridging cellular dimensions by CLEM: novel tools for live-cell correlative imaging

Job Fermie

2019



# Bridging cellular dimensions by CLEM: novel tools for live-cell correlative imaging

Job Fermie

**Bridging cellular dimensions by CLEM:  
novel tools for live-cell correlative imaging**

Job Fermie

**Bridging cellular dimensions by CLEM: novel tools for live-cell correlative imaging**  
Job Fermie, 2019

**Paranimfen**

Jan A. van der Beek  
Reini E.N. van der Welle

The work described in thesis was performed in the section **Cell Biology** of the Center for Molecular Medicine, University Medical Center Utrecht, Utrecht University, as well as in the section **Molecular Biophysics** of the Debye Institute for Nanomaterials Science, Utrecht University. This work was financially supported by NWO-TTW as part of the project 'Microscopy Valley' (12715).

**ISBN**

978-94-6375-660-0

**Printed by**

Ridderprint | [www.ridderprint.nl](http://www.ridderprint.nl)

Printing of this thesis was financially supported by the Stichting tot Bevordering van de Electronenmicroscopie in Nederland (SEN).

**Cover artwork**

Marloes Kok

# **Bridging cellular dimensions by CLEM: novel tools for live-cell correlative imaging**

**Overbrugging van cellulaire dimensies door nieuwe correlatieve licht- en elektronenmicroscopie technieken**

(met een samenvatting in het Nederlands)

## **Proefschrift**

ter verkrijging van de graad van doctor aan de  
Universiteit Utrecht  
op gezag van de  
rector magnificus, prof. dr. H.R.B.M. Kummeling,  
ingevolge het besluit van het college voor promoties  
in het openbaar te verdedigen op

woensdag 4 december 2019 des ochtends te 10.30 uur

door

**Job Fermie**

geboren op 18 augustus 1990  
te Naarden

**Promotoren:**

Prof. dr. H.C. Gerritsen  
Prof. dr. J. Klumperman

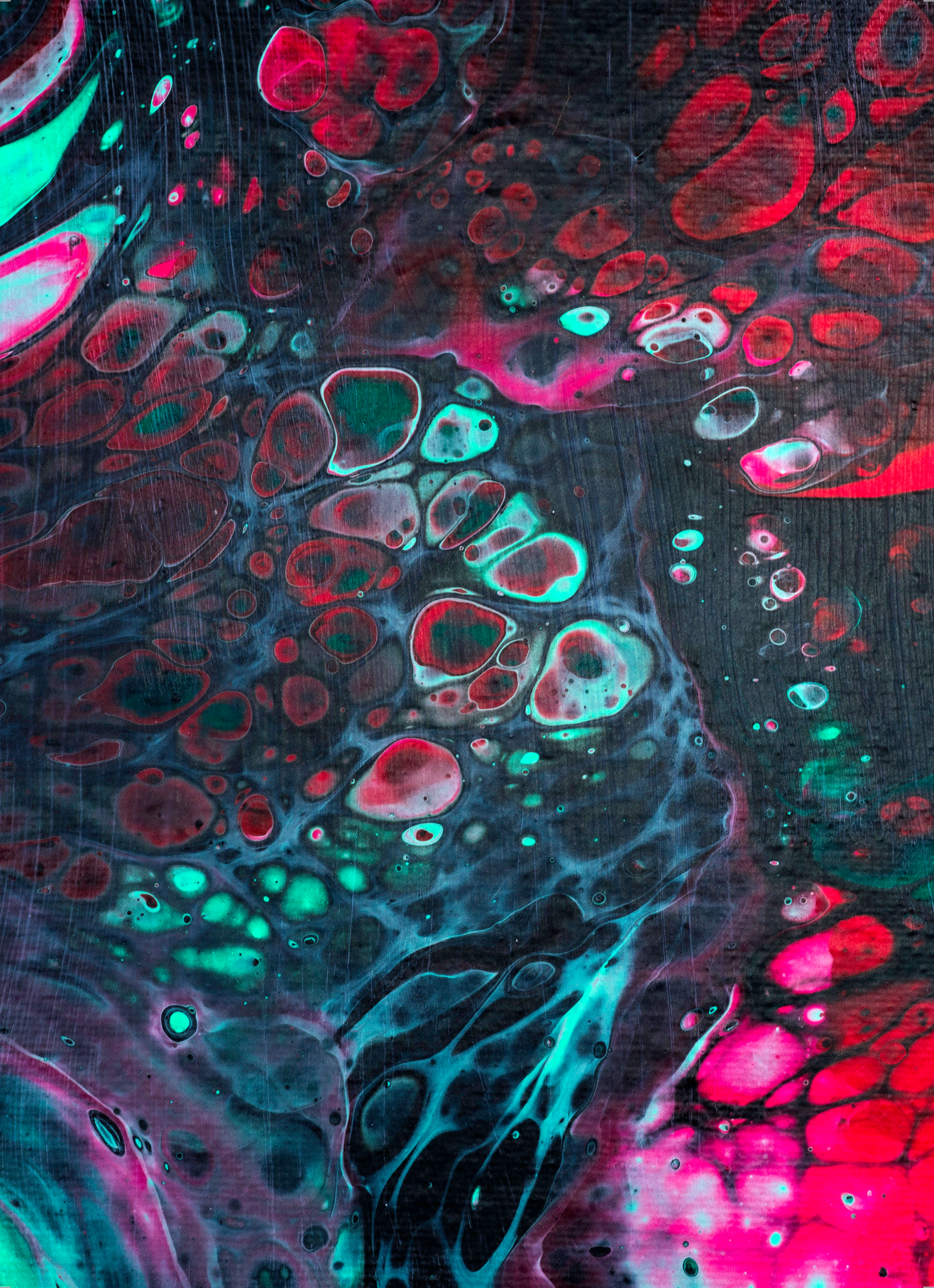
**Copromotoren:**

Dr. N. Liv  
Dr. W.H. Müller

Dit proefschrift werd mogelijk gemaakt met financiële steun van NWO-TTW als onderdeel van het project 'Microscopy Valley' (12715).

## Table of contents

<b>Chapter 1</b>	General introduction	7
<b>Chapter 2</b>	Single organelle dynamics linked to 3D structure by correlative live-cell – 3D electron microscopy	31
<b>Chapter 3</b>	Functional characterization of endo-lysosomal compartments by correlative light electron microscopy	61
<b>Chapter 4</b>	A bimodal endocytic probe for three-dimensional correlative light and electron microscopy	93
<b>Chapter 5</b>	Fluorescently labelled silica coated gold nanoparticles as fiducial markers for correlative light and electron microscopy	115
<b>Chapter 6</b>	Summarizing discussion	137
	<b>Nederlandse samenvatting</b>	148
	<b>Dankwoord/acknowledgements</b>	151
	<b>About the author</b>	154



---

# Chapter 1

---

## General introduction

Job Fermie<sup>1,2</sup>, Nalan Liv<sup>1</sup>, Wally Müller<sup>3</sup>, Hans Gerritsen<sup>2</sup>, Judith Klumperman<sup>1</sup>

1. Section Cell Biology, Center for Molecular Medicine, University Medical Center Utrecht, Utrecht University, Utrecht, The Netherlands
2. Section Molecular Biophysics, Debye Institute for Nanomaterials Science, Utrecht University, Utrecht, The Netherlands
3. Section Cell Biology & Mycology, Department of Biology, Utrecht University, Utrecht, The Netherlands

## Microscopy in Biology

Light microscopy (LM) and electron microscopy (EM) have been essential tools in life sciences since the inception of cell biology. Microscopy has contributed to novel insights in the compositional, dynamic and structural bases underlying biological processes. Both LM and EM have gone through significant evolutions in terms of performance and sensitivity at a variety of length scales. State of the art LM is now able to resolve details far beyond the diffraction limit (approximately 200 nm)[1,2], and track fluorescently tagged proteins over extended periods of time without specimen damage, even in large samples[3–6]. For EM, several developments have completely changed the potential of the system, including enhancements to electron image formation, automation of image collection, direct electron detection and advanced processing software. The combination of these developments have resulted in angstrom resolution imaging at a sensitivity of single electrons [7–10]. The insights obtained through this ‘resolution revolution’ in microscopy have contributed to multiple Nobel Prizes in the last five years: first for the development of super-resolution fluorescence microscopy FM by William E. Moerner, Eric Betzig and Stefan Hell in 2014 [11], and later followed by one for cryo-EM for Joachim Frank, Richard Henderson and Jacques Dubochet in 2017 [12].

In biological research, investigation of intra and intercellular processes requires a multi-parametric approach addressing both the structure and spatio-temporal organization of molecules and organelles, as well as the transduction of chemical signals and forces involved in molecular interactions. For a holistic view of a process, information from multiple microscopic techniques should be collected and correlated from a single specimen. However, the sample preparation techniques required to obtain this information often have a limited compatibility in between distinct techniques. This means that our understanding of organelles and processes is often based on averages of dynamic, compositional and ultrastructural data each derived from different imaging techniques.

To overcome this lack of direct integration of multiple parameters, strategies have been devised to integrate different types of data from a single sample. These approaches have collectively become known as correlative light and electron microscopy (CLEM). By combining LM and EM, CLEM has the potential to record the compositional, dynamic and ultrastructural aspects of cells, in a single sample. This thesis aims to further expand the capabilities of CLEM, by providing means to study organelle dynamics, functional properties and ultrastructural detail in an integrated fashion, and by developing tools designed to improve the registration of fluorescence and electron imaging data.

### Light and Fluorescence Microscopy

LM has been a crucial tool for biological research, thanks to its ability to image live specimens and directly visualize biological processes. Of the LM techniques, FM is the most employed approach in life sciences, since it provides a means to label and study specific molecules in a sample. FM exploits the property of fluorescence, the phenomenon where long-wavelength photons are emitted from a sample after excitation with shorter-wavelength photons. Emitted photons can be detected directly by eye, or by sensitive cameras or photomultipliers to form a digital image.

Fluorescent labeling of a specimen can be used to localize specific molecules or structures in cells and tissues. Labeled molecules can also be followed in live cells over time, thanks to microscopes equipped with climate-controlled housings. Since

FM depends on the presence of a label to form images, many different probes have been developed to detect specific proteins or protein complexes, genetic material or small molecules.

A commonly used strategy for fluorescent marking is immunolabeling, which exploits the epitope recognition specificity of antibodies. Antibodies are generated against specific proteins or molecules in laboratory animals. Desired antibody clones are purified and conjugated to a specific fluorescent dye. Alternatively, fluorescent dyes can be conjugated to naturally occurring compounds or drugs, for example the actin-binding compound phalloidin. Antibodies and other probes are generally membrane-impermeable, meaning that cells need to be permeabilized to label intracellular targets. Permeabilizing reagents are highly damaging to cells however, limiting the application of antibodies for live-cell imaging.

The capabilities to image a specimen live improved drastically with the cloning of green fluorescent protein (GFP), found in the jellyfish *Aequorea victoria*[13]. The genetic sequence of GFP could be inserted before or after the genetic sequence of proteins of interest[14], so that once transcribed and translated, cells expressed a fluorescent fusion protein of interest. This revolutionized cellular imaging, as tagged proteins could be followed in live cells and model animals. In this fashion, the spatio-temporal organization of molecules and organelles can be examined. In addition, live imaging of GFP-tagged proteins reveals information about the dynamics of proteins and organelles, such as trafficking, turnover, fusion, and fission. Following the initial validation of GFP, development of genetically encoded fluorescent probes (FPs) rapidly resulted in a variety of new FPs. Early improvements resulted in more photostable and better folding versions of GFP, but more importantly in different color variants[15,16], enabling simultaneous labeling of multiple proteins in a single organism. Later FP improvements were mostly catered towards emerging microscopic techniques. Photoactivatable and photoswitchable versions of FPs have proven instrumental in superresolution microscopy, and genetically encoded FRET (Förster resonance energy transfer) donor/acceptor pairs are common tools the study of protein interactions[17–21].

The spectral and photoactivation properties of FPs were not the only properties to receive attention. Fluorescence characteristics (*e.g.* intensity, lifetime, emission spectrum) of FPs and many other fluorophores are dependent on environmental properties, a factor that can be exploited: once characterized, the variation of fluorescence can be used as a biosensor, a readout for functional parameters in live cells. Modified versions of FPs are now employed as biosensors for a variety of cellular properties, including metal ions, GTPase activity, specific lipids and pH[22–27].

Biosensors are not necessarily genetically encoded, but can also be specifically designed chemical compounds. A prime example are biosensors for catabolic enzyme activity, as FPs are vulnerable to degradation and extreme pH environments. Organic dye molecules provide an alternative here, as these can be designed with less constraints than genetically encoded tags. In addition to their increased stability, organic dyes can be modified for membrane permeability and targeting towards specific organelles. More importantly, organic dyes do not require the genetic manipulation needed for fluorescent protein production, enabling specific imaging in vulnerable or hard to manipulate specimens, like primary cell cultures. Organic biosensors are widely available and provide a range of readouts for parameters like enzyme activity, pH, metal ions, with more probes being actively developed [24–34].

## Localizing molecules in time and space in live specimens

Even though the earliest observations of microorganisms in pond water by Antonie van Leeuwenhoek could be considered live imaging [35,36], the use of time-lapse and video microscopy for prolonged observation of microorganisms only emerged several hundred years later, at the turn of the 20<sup>th</sup> century[37–39]. These first devices used photographic film, which was prone to damage and required lengthy processing steps. Still, they were crucial in understanding (relatively) long-term processes like embryological development and bacterial infections. Hardware developments in FM later transformed these early time-lapse systems into the live-cell imaging systems we know today, where automated microscopes can image multiple fluorophores simultaneously at multiple frames per second, and allow gentle, prolonged imaging up to several days[4,40,41]. The ability to track fluorescently labeled molecules in both space and time has proven essential to examine biological processes on a broad scale, in cell biology, immunology and other fields.

### FM has limited resolution

One of the limitations of LM is its limited resolution due to the diffraction of light, which is described as the diffraction limit by Ernst Abbe. In practical terms, this limits the resolution attainable in a microscope to roughly half the length of the wavelength used for imaging. For visible light, the achievable resolution is around 200-300 nm in the lateral direction. While this resolution is high in the context of tissues and cells (10-1000  $\mu\text{m}$ ), it is not enough to resolve subcellular structures like organelles or proteins (1-100 nm) in detail. In the last decades however, several strategies have been developed to ‘break’ the diffraction limit, enabling resolving power beyond the diffraction limit, which are coined as superresolution microscopy. Superresolution approaches can be roughly divided into two different categories, one based on patterning of illumination, and another based on single molecule localization. In patterned illumination approaches, resolution is improved by introducing sub-diffraction limited features into the excitation pattern[1,2]. In the most common example of this strategy, stimulated emission depletion (STED) microscopy, this patterning is employed to add a circular depletion ‘donut’ around the excitation spot. Excited fluorophores illuminated by the depletion beam are suppressed before fluorescence can occur, drastically limiting the volume from which fluorescence is recorded. State of the art STED systems can achieve resolutions down to 40-50 nm[42].

In single molecule localization microscopy (SMLM) the diffraction limit is circumvented by using the on/off switching properties of some fluorescent labels. This on-off switching can be achieved through different strategies, but all of them are aimed at detecting the switching events of single molecules. By fine-tuning the excitation light intensity, individual switching events can be registered using high-speed detection. The resulting image data is then computationally reconstructed to allow high-precision localization of individual fluorophores. The two most common SMLM approaches, photoactivation localization microscopy (PALM) and stochastic optical reconstruction microscopy (STORM) are capable of achieving 20 nm resolution on high-end setups if enough photons are detected from the individual fluorophores[43,44]. With novel developments, this number may improve even further, down to nanometer resolution[45,46].

Superresolution microscopy has enabled FM to resolve fine subcellular details, and is becoming increasingly implemented in commercial solutions. Still, both diffraction-limited and superresolution FM only image the labeled portion of molecules in a

cell, which is only a small fraction of its total content. FM therefore only provides information on localization or dynamics, but not in which structural context they take place. Techniques that provide this ultrastructural information are essential to complement the images collected by FM.

## Electron Microscopy

### Electron microscopy reveals the entire ultrastructure of a specimen

Unlike FM, EM does not depend on the presence of specifically labeled molecules. Instead, EM visualizes a sample by recording the interactions of electrons with the sample. Since electrons have a considerably shorter wavelength than photons of visible light, EM achieves a significantly resolving power, with state-of-the-art EMs achieving sub-angstrom resolution. In biology, EM is the technique of choice to record ultrastructural detail in samples, visualizing subcellular details and providing structural context. Two different electron imaging strategies are routinely used in biological research.

As the name implies, image formation in transmission EM depends on electrons transmitted through a specimen. Electron-dense materials will scatter or absorb electrons from the coherent beam, resulting in a projection image through the specimen. Using a series of electrostatic lenses, this projection is magnified and projected onto a camera or direct electron detector, or a phosphorescent screen for easy viewing. To achieve high-quality images, samples are typically cut into thin (50-100 nm) sections. Greater sample thickness introduces excessive scattering of the electron beam, which reduces image quality and makes image interpretation more difficult.

In scanning EM (SEM), the electron beam is scanned over the surface of a sample in a line-by-line fashion to form an image. These (primary) electrons interact with the sample, and generate a variety of interaction products, including secondary and backscattered electrons, X-rays and visible light. These are collected using detectors mounted in the vacuum chamber, above the specimen. Scanning EM is primarily employed to acquire topographical data (surface structures) or compositional data. In addition, both SEMs and TEMs can be equipped with specialized detectors to characterize the presence of specific elements through energy-dispersive X-ray analysis (EDX), or electron-material interactions through cathodoluminescence imaging (CL). Depending on the energy of the primary electrons (the acceleration voltage), this data can originate from directly beneath the surface (< 100 nm) to relatively deep in the specimen (> 5  $\mu\text{m}$ ).

### EM can be combined with protein localization methods

Both SEM and TEM are essential in biology, thanks to their ability to record (ultra) structural detail in samples. However, their methods of image formation are not conducive to identify individual molecules within this ultrastructural data. EM therefore greatly benefits from methods that aim to incorporate molecular data. Several approaches are commonly used to detect proteins in EM, with immunolabeling as the most prevalent technique. Like in FM, antibodies are used to detect specific molecules, but these are coupled to an electron-dense probe like colloidal gold or quantum dots instead of a fluorescent moiety [47,48]. Colloidal gold and quantum dots can both be synthesized at predefined sizes, meaning several markers can be discerned by using differently sized colloids. Alternatively, samples can be labeled by artificially generating osmiophilic precipitates around a labeled or genetically tagged sample, usually by polymerizing the compound

diaminobenzidine (DAB) using peroxidase activity. Peroxidase labeling strategies were initially performed using biomolecules conjugated to horseradish peroxidase (HRP)[49,50], but have evolved to include genetically encoded peroxidase tags such as APEX, FIAsH, ReAsH and other derivatives[51–53]. Peroxidase labeling is well suited for large samples due to the high penetrating power of DAB, allowing staining of large model systems. Compared to immunogold labeling, DAB labeling can only be used to label one target at a time, and may obscure morphological details caused by the electron-dense precipitates.

### **Volume EM has revolutionized imaging by providing large-scale 3D ultrastructure information**

As described before, EM imaging typically collects data from ultrathin sections, or the surface of a sample. Biological specimens are rarely this thin, and biological processes occur in three dimensions, meaning a single EM sample only contains a fraction of a cell or the structure of interest. Thus, to fully understand interactions between different cells or organelles, 3D visualization is essential.

Initially this information was collected through serial sectioning, where long ribbons of consecutive sections are collected onto specimen holders and imaged sequentially. 3D information can then be derived from the resulting stack of images [54,55]. Further capabilities for 3D imaging arose with the introduction of electron tomography (ET). Here, a series of projection images from a thick samples is collected at multiple tilt angles, which can be reconstructed into a 3D representation of a sample [56,57]. ET provides good lateral and axial resolution, and is able to image thicker samples (250–350 nm). Depending on the size of the volume and the resolution required, serial sectioning can be combined with ET, to further increase the imaging volume.

3D EM imaging on a large scale was made possible with the development of high-resolution SEMs and automation software. State of the art SEMs achieve TEM-like resolutions, making them capable of visualizing subcellular structures in detail. Compared to TEMs however, SEMs scan far larger surfaces of a specimen, allowing large-scale imaging of serial sections and volume (3D) imaging. Three different approaches are used with modern SEMs. In array tomography (AT), long ribbons of serial sections are deposited on a conductive substrate and sequentially imaged by SEM to be integrated into 3D images [58]. In serial block-face SEM (SBF-SEM), a miniaturized ultramicrotome is integrated in the SEM chamber[59]. The sample surface is imaged using the electron beam of the SEM, after which the top layer of the sample is removed using the microtome knife, revealing a new imaging surface. The third approach, focused ion beam SEM (FIB-SEM), collects volume data by repeatedly exposing a new imaging surface for the SEM[60] using the focused ion beam for material removal. FIB-SEM is capable of achieving section thicknesses of <5 nm, while routine sections thicknesses in AT and SBF-SEM are 30–50 nm [59,61]. SBF-SEM imaging can be further improved by using a strategy known as multi energy deconvolution, allowing reconstruction of 10 nm isotropic voxels from thicker sections [62]. Automated volume imaging techniques have transformed the field of EM, and have been instrumental for the advances seen in large-scale projects like connectomics, where volume EM data is used to construct highly detailed synaptic connection maps of the brain [63,64].

## Cryo-electron microscopy directly images native structures at nanoscale resolution

Cryo-EM is the method which likely is the best in reflecting native state of cells and molecules [65]. For cryo-EM, samples are vitrified and preserved at cryogenic temperatures in a frozen-hydrated state, introducing minimal structural alterations in the sample. In this frozen-hydrated state, samples are stable enough for electron imaging, whilst avoiding harsh crosslinking and contrasting regimes. Two specific applications of cryo-EM have revolutionized the way structural biologists and cell biologists visualize (sub)cellular structures and proteins in recent years.

The first approach, single particle analysis (SPA), is mainly used as a structural biology tool. Isolated proteins or protein complexes are applied to EM grids in a small volume of solution and rapidly frozen in a thin ice layer. Proteins will be oriented randomly in this layer, producing different 2D projections on the detector based on their orientation[66,67]. These projections can be grouped in orientation classes and combined to form a 3D model of the specimen. Developments in detector sensitivity and the sophisticated computational image reconstruction have resulted in an imaging platform capable of achieving <3 angstrom resolution, rivaling the image resolution of X-ray crystallography [68–72]. Compared to X-ray crystallography however, specimen preparation for SPA is significantly more permissive for a broad range of specimens, which previously would have been impossible to resolve in crystallography. The SPA workflow is also relatively fast, opening up interesting novel avenues for fields like drug discovery, where the high resolution structures can be used to identify binding sites for novel therapeutics[73,74].

Another application domain of cryo-EM is cryo-ET. Like in room-temperature ET, the frozen sample is rotated around its axis to collect a series of 2D projection images, which is reconstructed into a 3D volume. Cryo-ET is generally performed on lamellae, which are thin slices of a sample acquired by thinning frozen material mostly in a cryo-FIB-SEM [75–78]. Since the ultrastructure of frozen hydrated material in these lamellae is well preserved, cryo-ET provides high-quality 3D morphological data of a specimen. Protein complexes and other cellular components are preserved in their native hydrated environment, which provides an interesting opportunity for structural biologists: for the first time, protein structure can be studied *in situ*, allowing 3D reconstruction and modeling of proteins and complexes not amenable to approaches like crystallography or SPA, which require purification of the protein of interest[65,76,79,80]. Interestingly, this approach can now be used to relate conformational information of protein complexes to their location in the cellular landscape[81–83].

## Restrictions of electron microscopy

Throughout the evolution of EM techniques, high quality specimen preparation has remained crucial. First of all, samples should retain their form in the vacuum required for EM operation. Without preparation, most biological specimens are incompatible with EM, since vacuum exposure would cause them to lose their hydrated state. Biological material therefore needs to undergo preparation steps to retain a morphology similar to their hydrated state.

For cryo-EM applications, samples must be observed in vitrified conditions, a state where water is in an amorphous solid form. This state is achieved by rapid cooling of the sample, either through plunge-freezing or high pressure freezing [84,85]. Vitrified samples are then imaged directly in the EM, but should be kept below

-150°C to prevent devitrification of the ice [79,85]. Once this occurs, the water in the sample may become crystalline, which severely perturbs the ultrastructure of the samples. Exposure to the electron beam introduces local heating in a specimen, which may drive it over the threshold for devitrification. Care must therefore be taken to limit the electron dose, at the cost of producing images of lower contrast.

For room-temperature applications, several steps are required before samples can be imaged in the EM. A common route for room-temperature EM is fixing the material with crosslinking chemicals, dehydrating with acetone or ethanol and embedding in a support material, usually an epoxy or acrylic resin. In addition to acting as support material to retain the original form of the specimen, these resins enable consistent sectioning of the specimen, which is crucial for transmission EM. Alternatively, samples can also be rapidly frozen through high-pressure freezing, after which water in the frozen sample is gradually replaced by an organic solvent containing heavy metals for contrasting [85–90]. Once contrasted, the samples are brought back to room temperature and embedded in a resin of choice. This approach yields improved morphology compared to chemical fixation, and can be used to preserve the morphology of samples that are difficult to fix with chemical fixation [86,91].

In addition to the requirement of stabilization, biological material requires electron-dense contrasting agents. Electron imaging depends on local differences of electron scattering in the sample to achieve image contrast. Most biological material is comprised of light elements, such as carbon, oxygen and nitrogen, which produce very little contrast on their own. Contrast can instead be generated by treating samples with contrasting agents like osmium tetroxide, uranyl acetate and lead citrate. These react with a variety of biomolecules in a specimen, enhancing the visibility of organelles, protein complexes and biomembranes in EM. These steps however do preclude imaging of live specimens: most of the reagents used for fixation and contrasting are highly toxic to cells, killing the specimen. As a result, electron micrographs represent a snapshot in time, making EM unsuited to study cellular dynamics.

Another challenge in EM is that the structural details to be investigated necessitate imaging at high magnification, which limits the field of view compared to FM, especially in cryo-EM. Analysis of large areas or identification of rare events therefore takes a considerable amount of time, especially if 3D data are required. This problem is further complicated in volume imaging: the described SBF-SEM and FIB-SEM imaging techniques are destructive, since the material that is physically removed from the sample cannot be retrieved for further imaging. Missing a region of interest (ROI) or wrong imaging settings can therefore mean that a sample is lost before the required data is collected. These considerations force users to make trade-offs between resolution, image acquisition time and volume size.

## **Correlative light and electron microscopy**

### **CLEM combines the strengths of different modalities**

Correlative light-electron microscopy (CLEM) aims to integrate data from LM and EM on the same sample. Combining the strengths of the different modalities creates a novel imaging tool that provides integrated compositional, functional and ultrastructural information. The wide overview of FM is used to find rare events and record molecular composition and dynamics, which subsequently are imaged by EM to reveal the corresponding ultrastructure and surrounding context.

With the development of digital imaging techniques that ease the overlay of LM and EM images, and introduction of new techniques like microCT to navigate through complex samples, the field of CLEM has become genuinely booming over the past several years [92,93]. Novel tools and software solutions have made CLEM more amenable to daily practice, yet, the basic concept of CLEM remains largely the same: samples are imaged sequentially on different modalities, after which data from one mode is overlaid over data from the other.

While the methods and microscopy approaches can vary greatly, CLEM is primarily used for two sets of applications. The first is primarily directed towards ‘needle in the haystack’ type of questions. Without prior knowledge, structures of interest can be difficult to find or recognize by EM because of the limited field of view. The large field of view and high sensitivity of LM (usually FM) can be used to screen for rare or novel phenotypes that then are recorded for further analysis by EM. FM imaging can combine multiple fluorescent labels to target a structure of interest, or provide detailed information on its molecular composition or functional characteristics. Applications of this type of CLEM are for example to find a single tumor cell or newly forming blood vessels within a complex tissue, or detect viral particles within a cell[94–96].

A second, highly challenging, CLEM approach is the integration of live-cell imaging and EM. Live-cell CLEM is especially valuable because live imaging in EM is unfeasible. A common application is to screen for transient cellular processes by live-cell imaging, after which the sample is fixed to be imaged in the EM for structural details [97,98]. Live-cell imaging can also be used to image the dynamics and kinetics of (sub)cellular processes, after which these are registered to structures revealed by EM.

Both approaches have successfully been used in a variety of topics, ranging from subcellular trafficking of vesicles, to models for bacterial infection, to blood vessel formation in zebrafish [95,96,98–102]. Thanks to improvements in the correlation efficiency and accuracy of registration procedures, any fluorescent probe can now in principle be used to integrate localization or compositional data to ultrastructure, without the need for an electron-dense readout. Fluorescent probes for CLEM include (genetic) fluorescent tags, as well as biosensors that monitor biological processes, or the presence of ions, signaling molecules, and mRNA[24,27,103–105]. The data from all these read-outs can be inferred to ultrastructural data. CLEM is therefore the technique of choice to integratively study dynamic, functional and ultrastructural parameters in a single sample.

## Challenges in CLEM

### **CLEM depends on the accuracy to retrace structures in different modalities**

The accurate registration of light and electron datasets remains one of the main challenges in CLEM. Current methods mostly rely on identifying a structure in the EM that was previously imaged in FM. Generally, some form of fiducial marking is used to identify the same ROI in both light and electron microscopy. This can be as simple as using the unique shape of a cell, or a pattern on the sample substrate (commercially available from Ibidi, Mattek and EMS) or sample holder (Zeiss’ Shuttle and Find, Thermo Fisher’s Corrsight and Maps), which usually provides registration accuracy in the order of micrometers. More complex approaches are essential when higher accuracy towards nanoscale is required, or when

the cell of interest is present in a complex tissue. For complex tissues, naturally occurring features such as branching blood vessels are sufficient as fiducial[96], although exogenous marking strategies such as near-infrared branding can also be employed[106]. To retrace small subcellular features higher precision correlation is crucial, ideally below 50-100 nm. The use of fiducials is vital here, as this is the only method currently available to achieve such high precision. A variety of particles has been demonstrated as effective fiducials, including polystyrene beads, gold nanorods and labeled silica[107–110]. When combined with appropriate software, correlative approaches can achieve retracing accuracies of below 100 nm in 2D approaches[107,111]. With the advent of volume EM, novel registration strategies are required, since fiducials are currently mostly applied to a section or underlying substrate. As a result, systems that allow distribution of fiducials in three dimensions are highly sought after.

Another major challenge is registration in time. Processes in cells are highly dynamic, and an event of interest may only last (less than) seconds. To prevent a time gap between the last live image and the fixed state of cells, rapid fixation methods are essential to retrace dynamic organelles. Chemical fixation procedures allow fixation *in situ*, preserving the orientation and position of the cell used for live cell imaging. When the fixation process is documented during imaging, it usually takes a few seconds until all movement has ceased[112]. For high-pressure freezing fixation, different strategies are required. Although cryofixation is a rapid process in itself, it takes time to transfer a sample from the FM to a freezing system. To counteract this, special holders and rapid transfer systems have been devised, that reduce the time between imaging and freezing[113–115]. Regardless, these transfer systems still have a 10-15 second gap between the last frame of imaging and the frozen state, making them less suitable for the correlative imaging of highly dynamic events.

### **CLEM sample preparation**

Compared to either of the separate techniques, sample preparation for CLEM brings its own challenges since the material has to be prepared for, and imaged in different microscopes. Also, samples are oftentimes subjected to processing and transfer steps between different microscopes, which can introduce distortions and poor sample handling can cause damage or loss of a specimen. These factors can hamper an accurate correlation from FM to EM.

Specimen preparation is crucial for any microscopic experiment and can be opposite for different modalities. For instance, labeling for FM often uses permeabilizing agents that would perturb ultrastructure in EM. Preparation for EM often quenches most organic fluorophores and fluorescent proteins. Therefore, specimen preparation for CLEM is generally a compromise between sufficient fluorescent signal and acceptable morphological preservation, although optimized protocols and specialized fluorescent probes have been developed to ameliorate some of these issues [116–118].

Another challenge with CLEM lies in the limited availability of bimodal probes. Compared to the wealth of probes for dedicated fluorescence or electron microscopy, bimodal probes (*i.e.* visible in both FM and EM) are scarce. Immunolabeling can be performed by combining immunofluorescence and immunogold labeling, using a fluorescent secondary antibody tagged with protein-A-gold, or conjugates such as fluoronanogold. Also streptavidin-conjugated quantum dots can be used as bimodal labels. For genetically encoded tags, bimodal visibility can be achieved by linking to enzymes that are able to polymerize DAB [119–123]. Use of these probes

has the drawback that the electron-dense precipitates can obscure morphological detail [124]. Overall, bimodal labeling can be tedious and not always possible. This highlights the need for accurate registration of data between modalities, and improved data processing tools.

## Microscopy in cell biology

In the past, both LM and EM have proven essential in cell biology. Van Leeuwenhoek's single-lens microscopic studies on living micro-organisms like bacteria marked the beginning of the field of microbiology[35,36]. These first observations were made using transmitted light, which provides little detail on the composition of biological specimens. With the introduction of FM, the properties of fluorophores or materials could be used to provide compositional information of a sample. These initial observations were primarily made through autofluorescence of the sample, which provides limited opportunity to identify specific structures or molecules[125,126]. This limitation was overcome with the advent of vital dyes, which provided contrast to specific cell types, or even individual organelles [127,128]. From that time on, detection of specific molecules was made possible by the work of Coon and Kaplan [129], who for the first time introduced immunolabeling as a strategy to label and detect individual proteins in cells through fluorescence. Together with the discovery of GFP and the toolbox for genetic manipulation to obtain fluorescent fusion proteins [51,130], these discoveries have made FM a well-established tool in cell biology, enabling the study of cellular processes and dynamics under live conditions.

For EM, it was Keith Porter who made the first electron microscopic image of an intact eukaryotic cell[131]. Later, Palade termed this first electron microscopic image as the birth certificate of the field of Cell Biology[132]. By the use of EM and biochemistry of cell fractions, Palade was able to integrate structural and functional information on a number of cellular components and discovered that the microsomes were part of the endoplasmic reticulum and contained large amounts of ribosomes[133]. The procedural and technical developments of EM have made it a firmly established cell-biological tool to integrate structure and function[134].

## The endo-lysosomal system

### Composition of the endo-lysosomal system

The endo-lysosomal system is one of the cellular systems where the combination of dynamics, molecular composition and structure is essential to fully understand all aspects of function and regulation. The system consists of a series of membrane-enclosed compartments that are highly dynamic and interact with each other and other organelles in the cell [135,136]. It is mainly known as the primary means of eukaryotic cells to sort and degrade materials from the extracellular space. Extracellular cargo is internalized into endocytic vesicles which bud from the plasma membrane, and fuse with **early endosomes**. Here, the decision is made whether cargo is recycled or sorted for degradation. Recycling to the cell surface occurs either via a direct pathway or via an additional sorting step in **recycling endosomes**. Alternatively, cargo can be transported to the trans-Golgi network (TGN). Material destined for degradation is retained in early endosomes, which undergo a maturation process towards **late endosomes**, characterized by formation of many intraluminal vesicles (ILVs). During this maturation drastic changes occur in the lipid and protein composition of the endo-lysosomal limiting membrane. Finally, the now-mature endosomes fuse with **lysosomes**, which maintain a low pH

1 that activates hydrolases required for degradation of the contained material. Upon fusion, a hybrid **endolysosome** compartment is formed which releases membranes to form new lysosomes in a continuous fusion – fission – regeneration cycle. Late endosomes can also fuse with **autophagosomes**, which bring the cells' own material to lysosomes for degradation and recycling. These processes are schematically shown in figure 1.

The mechanisms required for endo-lysosomal transport, maturation and fusion are tightly controlled. Only when the right position, and all required molecular switches, tethers and parts of the fusion machinery have assembled is an endosome capable of fusion, which is crucial to retain the identity of individual compartments [137,138].

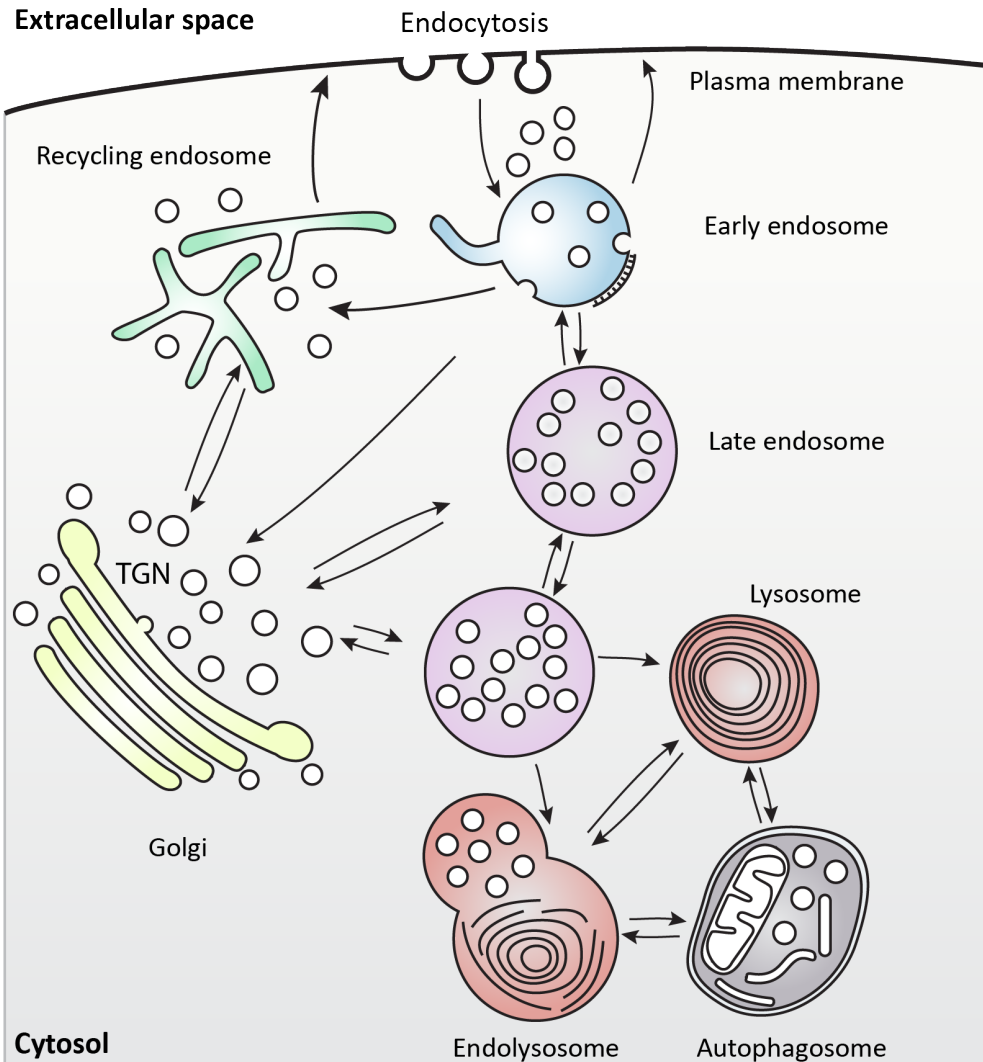
### Functions and diseases of the endo-lysosomal system

Gradually, more and more functions are discovered and ascribed to endosomes and lysosomes. In recent years, endosomes have become known as a signaling hub in a variety of processes, including immunity, metabolic regulation, membrane repair and more (reviewed in [139]). One of the most important of these functions is metabolic regulation. Lysosomes, as the degradative endpoint for endocytosed and autophagic material, are the location where catabolic products are exported into the cytosol. By docking nutrient sensing complexes such as mTORC on lysosomes, cells are able to sense the changing availability of cellular building blocks like amino acids, allowing efficient responses to changing nutrient conditions through processes such as autophagy [140–143].

The diversity and complexity of the endo-lysosomal system is further expanded by membrane-bound compartments required for specialized functions in higher organisms. Known as lysosome-related organelles (LRO), these compartments are crucial for processes like pigmentation (melanosomes), immunity (lytic granules, phagolysosomes, MHCII containing compartments), bone remodeling (osteoclasts) and hemostasis (alpha granules, Weibel-Palade bodies)[144–146]. These organelles share many characteristics with lysosomes in their content, and membrane-integrated and membrane-associated proteins. However, they contain specialized cargo and their membrane is further decorated with the signaling and fusion machinery required for proper positioning, membrane docking[147–149].

Tight regulation of the endo-lysosomal system is crucial for cellular homeostasis. Disruption of their function, for example by reduced functionality of lysosomal hydrolases or impaired fusion and trafficking can result in severe neurological disorders like Alzheimer's, Parkinson's and ALS and lysosomal storage disorders[150–154]. Deregulation of lysosome function, especially dynamics and positioning, is also seen in cancer. Although the full impact of this change is not yet clear, lysosomal hydrolases are known to break down part of the extracellular matrix around these cells, facilitating invasion and metastasis [155,156].

Endo-lysosomal perturbation is also seen under other pathological conditions, such as bacterial and viral infections. For viruses, the endo-lysosomal system provides the main route of entry into cells while shielding them from the body's immune system. By exploiting the trafficking systems of host cells, virions are efficiently transported throughout the cell, while also providing the correct conditions for their escape into the cytosol and release of genetic material, or their replication [157–161]. Similar exploits are also found in many bacteria, such as *Shigella*, *Salmonella*, and *Mycobacterium tuberculosis* [162–164]. Depending on the bacterial species, the



1

Figure 1: Schematic representation of the endo-lysosomal system. Arrows indicate interactions between different endo-lysosomal organelles. Cargo is endocytosed from the plasma membrane in endocytic vesicles that are collected in early endosomes. From here, cargo can be recycle back to through a direct recycling pathway, or indirectly via recycling endosomes. Cargo destined for degradation is trafficked through late endosomes into lysosomes, where it is degraded through catabolic enzymes. Autophagosomes contain cytoplasmic components destined for degradation and recycling in lysosomes.

endo-lysosomal system can either serve as a means of access to the cell's cytosol after endo-lysosomal escape, or as a replicative niche, where the bacteria reside in modified endo-lysosomal compartments.

### **Electron microscopy reveals fine structural details of the endo-lysosomal system.**

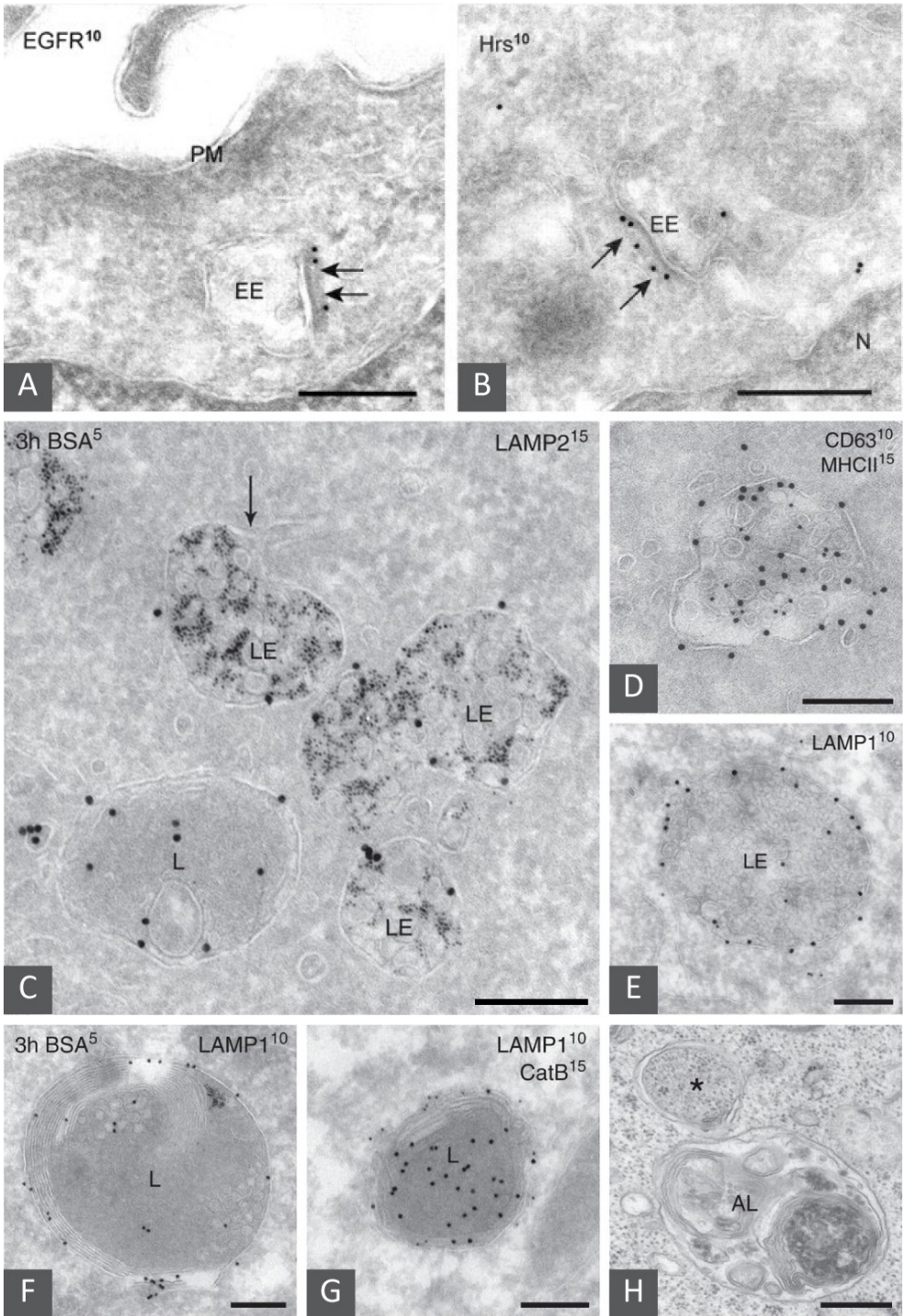
Since endo-lysosomal proteins often show overlapping distributions between different endo-lysosomal compartments, FM alone is unable to reveal the precise identity of a given endo-lysosomal organelle. By EM all membrane and structural details are properly resolved and this morphological information is generally used to classify endo-lysosomal compartments into subgroups like early or late endosomes and lysosomes [165–168]. A collection of EM images showing the typical ultrastructural details of different endo-lysosomal intermediates is shown in figure 2.

Early endosomes are irregularly shaped vacuoles which can exhibit a clathrin coat and tubular extensions and an electron lucent lumen with loosely packed ILVs. Late endosomes are more globularly shaped and can be tightly or loosely packed with ILVs. Late endosomes can also form tubular extensions, but these have greater electron density than those emanating from early endosomes. Lysosomes are mostly spherical in shape with an electron-dense content, often containing membrane whorls. Autolysosomes are formed by fusion of autophagic compartments with lysosomes and are usually large, irregularly shaped vacuoles with a mixed content. Sometimes cytoplasmic constituents and organelles can be found, like ribosomes, but under control conditions these are rapidly degraded.

### **CLEM captures all functional and morphological parameters of endo-lysosomal compartments**

These morphological criteria shown in figure 2 are commonly used to identify endo-lysosomal compartments by EM, and will be used as a reference for morphological features of endo-lysosomal organelles in this thesis. However, since EM only

Figure 2: Electron micrographs of organelles labeled for characteristic markers in the endosomal system in various cell types. (A,B) HeLa cells incubated for 10 min with EGF. (A) EGFR (10-nm gold) and (B) Hrs (10-nm gold) are localized to the coated areas (arrows) of early endosomes (EEs). PM, plasma membrane. (C) HepG2 cells pre-incubated for 3h with BSA5 and immunogold-labeled for LAMP2 (15-nm gold). Late endosomes (LE) contain multiple ILVs but differ in size and shape. Note the recycling tubule emerging from the LE (arrow). The lysosome (L) has not been reached by BSA5. (D) MVB/MHC class II compartment of a dendritic cell immunogold-labeled for MHC class II (15-nm gold) and CD63 (10-nm gold). (E) Typical example of a late endosome (LE). Immunogold labeling for LAMP-1 (10-nm gold) is mainly restricted to the limiting membrane. Note the different morphological features of the ILVs present in the distinct LEs (C-E). (F) HepG2 cells pre-incubated for 3 h with BSA5 and immunogold-labeled for LAMP1 (10-nm gold). Example of a typical lysosome with lamellar membranes, some ILVs, and an overall electron-dense content. LAMP1 is mainly restricted to the limiting membrane. (G) Another typical lysosome from a HepG2 cell, showing the presence of lysosomal enzyme cathepsin B (CatB) (15-nm gold) in the electron-dense lumen and LAMP1 (10-nm gold) at the limiting membrane. (H) Autophagic compartments in a stimulated B cell. The asterisk points to a double-membrane vesicle; the autophagosome. The autolysosome (AL) contains a more heterogeneous content than a regular lysosome. Scale bars: 200 nm. Images adapted from Sachse M, Urbé S, Oorschot V, Strous GJ, Klumperman J. Bilayered clathrin coats on endosomal vacuoles are involved in protein sorting toward lysosomes. *Mol Biol Cell*. 2002 Apr;13(4):1313-28 (A,B) and Klumperman J, Raposo G. The Complex Ultrastructure of the Endolysosomal System. *Cold Spring Harb Perspect Biol* 2014;6 (C-H).



shows snapshots of the dynamic and interacting continuum of endo-lysosomal intermediates, morphology alone cannot capture the complete nature of a given endo-lysosomal compartment. To understand the different facets of the endo-lysosomal system, researchers need to employ a broad range of techniques available in the bioimaging toolbox. Proteins need to be localized in real time, structural detail needs to be captured, and compositional information is crucial to elucidate the identity of endo-lysosomes. Ideally, these parameters are examined in the same sample. This is why combining EM and LM in CLEM methods is crucial to study the functional organization of the endo-lysosomal system in its full complexity. In this thesis, we examine a variety of different dynamic and ultrastructural characteristics of the endo-lysosomal system in an integrated fashion using CLEM.

## **Scope of this thesis: development of live cell - 3D CLEM pipelines and their application**

The aim of this thesis is to develop novel tools that facilitate correlation of dynamic and functional parameters from live-cell imaging to an ultrastructural context in 3 dimensions. The chapters in this thesis describe novel workflows for live-cell CLEM, and introduce novel fiducials that enable accurate registration of light and electron data.

In **chapter 2**, the focus is on the development and validation of a workflow suitable to link data obtained in live-cell FM of highly dynamic events to 3D ultrastructure. We demonstrate the methods necessary to retrace cells from live-cell imaging to FIB-SEM imaging, to accurately select regions of interest suitable for automated serial imaging, and ensure efficient registration of fluorescent organelles to 3D ultrastructure. By real time tracking of single endolysosomal compartments over several minutes and retracing these same compartments in EM, we show that live-cell imaging combined with FIB-SEM provides a powerful way to integrate dynamic, structural and morphological parameters into one single organelle.

**Chapter 3** further expands on this newly developed correlative approach by integrating fluorescent functional probes into the workflow, to examine endo-lysosomal parameters such as acidity, calcium content and enzyme activity. This expansion enables the use of a broad pallet of fluorescent reporters and biosensors in CLEM. We traced back hundreds of fluorescent spots within a single dataset, enabling quantitative analysis of CLEM data, which revealed a steep functional difference between late endosomes and lysosomes.

**Chapter 4** describes the synthesis and use of fBSA-Au<sup>5</sup> as a bimodal endocytic probe, which we use to examine endo-lysosomal trafficking and as correlative fiducial. fBSA-Au<sup>5</sup> is efficiently endocytosed and highly visible in both FM and EM.

In **chapter 5** the synthesis and optimization of nanoparticles consisting of a gold core and rhodamine B-labeled silica shell is presented. The optimized synthesis yields nanoparticles with high visibility in both FM and EM. We demonstrate the use of these particles as fiducials, to accurately register FM and EM data. The particles are efficiently endocytosed by HeLa cells, and are easily recognized in FIB-SEM data. This makes these nanoparticles highly suitable for correlative light-volume electron microscopy, as they provide highly visible landmarks in both modalities.

## References

1. Huang B, Bates M, Zhuang X. Super resolution fluorescence microscopy. *Annu Rev Biochem* 2010;78:993–1016.
2. Schermelleh L, Ferrand A, Huser T, Eggeling C, Sauer M, Biehlmair O, Drummen GPC. Super-resolution microscopy demystified. *Nat Cell Biol* 2019;21:72–84.
3. Huisken J, Swoger J, Del Bene F, Wittbrodt J, Stelzer EHK. Optical sectioning deep inside live embryos by selective plane illumination microscopy. *Science* 2004;305:1007–9.
4. Chen BC, Legant WR, Wang K, Shao L, Milkie DE, Davidson MW, Janetopoulos C, Wu XS, Hammer JA, Liu Z, English BP, Mimori-Kiyosue Y, Romero DP, Ritter AT, Lippincott-Schwartz J, Fritz-Laylin L, Mullins RD, Mitchell DM, Bembenek JN, Reymann AC, Böhme R, Grill SW, Wang JT, Seydoux G, Tulu US, Kiehart DP, Betzig E. Lattice light-sheet microscopy: Imaging molecules to embryos at high spatiotemporal resolution. *Science* (80- ) 2014;346.
5. Liu Z, Lavis LD, Betzig E. Imaging Live-Cell Dynamics and Structure at the Single-Molecule Level. *Mol Cell* 2015;58:644–659.
6. Liu TL, Upadhyayula S, Milkie DE, Singh V, Wang K, Swinburne IA, Mosaliganti KR, Collins ZM, Hiscock TW, Shea J, Kohrman AQ, Medwig TN, Dambournet D, Forster R, Cunniff B, Ruan Y, Yashiro H, Scholpp S, Meyerowitz EM, Hockemeyer D, Drubin DG, Martin BL, Matus DQ, Koyama M, Megason SG, Kirchhausen T, Betzig E. Observing the cell in its native state: Imaging subcellular dynamics in multicellular organisms. *Science* (80- ) 2018;360.
7. Mastronarde DN. Automated electron microscope tomography using robust prediction of specimen movements. *J Struct Biol* 2005;152:36–51.
8. Kuhlbrandt W. The Resolution Revolution. *Science* (80- ) 2014;343:1443–1444.
9. Hanske J, Sadian Y, Müller CW. The cryo-EM resolution revolution and transcription complexes. *Curr Opin Struct Biol* 2018;52:8–15.
10. Schorb M, Haberbosch I, Hagen WJH, Schwab Y, Mastronarde DN. Software tools for automated transmission electron microscopy. *Nat Methods* 2019;
11. Orrit M. Celebrating optical nanoscopy. *Nat Photonics* 2014;8:887–888.
12. Cressley D, Callaway E. Cryo-electron microscopy wins chemistry Nobel. *Nature* 2017;550:167–167.
13. Shimomura O, Johnson FH, Saiga Y. Extraction, Purification and Properties of Aequorin, a Bioluminescent Protein from the Luminous Hydromedusa, *Aequorea*. *J Cell Comp Physiol* 1962;59:223–239.
14. Chalfie M, Tu Y, Euskirchen G, Ward WW, Prasher DC. Green fluorescent protein as a marker for gene expression. *Science* 1994;263:802–5.
15. Heim R, Prasher DC, Tsien RY. Wavelength mutations and posttranslational autoxidation of green fluorescent protein. *Proc Natl Acad Sci U S A* 1994;91:12501–4.
16. Heim R, Tsien RY. Engineering green fluorescent protein for improved brightness, longer wavelengths and fluorescence resonance energy transfer. *Curr Biol* 1996;6:178–182.
17. Ando R, Hama H, Yamamoto-Hino M, Mizuno H, Miyawaki A. An optical marker based on the UV-induced green-to-red photoconversion of a fluorescent protein. *Proc Natl Acad Sci U S A* 2002;99:12651–6.
18. Sekar RB, Periasamy A. Fluorescence resonance energy transfer (FRET) microscopy imaging of live cell protein localizations. *J Cell Biol* 2003;160:629–33.
19. Habuchi S, Ando R, Dedecker P, Verheijen W, Mizuno H, Miyawaki A, Hofkens J. Reversible single-molecule photoswitching in the GFP-like fluorescent protein Dronpa. *Proc Natl Acad Sci* 2005;102:9511–9516.
20. Day RN, Davidson MW. The fluorescent protein palette: Tools for cellular imaging. *Chem Soc Rev* 2009;38:2887–2921.
21. Day RN, Davidson MW. Fluorescent proteins for FRET microscopy: Monitoring protein interactions in living cells. *BioEssays* 2012;34:341–350.
22. Kimura S, Noda T, Yoshimori T. Dissection of the autophagosome maturation process by a novel reporter protein, tandem fluorescent-tagged LC3. *Autophagy* 2007;3:452–460.
23. Baird GS, Zacharias DA, Tsien RY. Circular permutation and receptor insertion within green fluorescent proteins. *Proc Natl Acad Sci U S A* 1999;96:11241–6.
24. Yu D, Baird GS, Tsien RY, Davis RL. Detection of Calcium Transients in *Drosophila* Mushroom Body Neurons with Camgaroo Reporters. *J Neurosci* 2003;23:64–72.
25. VanEngelenburg SB, Palmer AE. Fluorescent biosensors of protein function. *Curr. Opin. Chem. Biol.* 2008;12:60–65.
26. Hodgson L, Shen F, Hahn K. Biosensors for characterizing the dynamics of rho family GTPases in living cells. *Curr Protoc cell Biol* 2010;Chapter 14:Unit 14.11.1-26.
27. Qin Y, Sammond DW, Braselmann E, Carpenter MC, Palmer AE. Development of an Optical Zn<sup>2+</sup> Probe Based

- on a Single Fluorescent Protein. *ACS Chem Biol* 2016;11:2744–2751.
28. Morgan AJ, Davis LC, Galione A. Imaging approaches to measuring lysosomal calcium. Elsevier Ltd; 2015.
  29. Christensen K, Myers JT, Swanson J. pH-dependent regulation of lysosomal calcium in macrophages. *J Cell Sci* 2002;115:599–607.
  30. Leung K, Chakraborty K, Saminathan A, Krishnan Y. A DNA nanomachine chemically resolves lysosomes in live cells. *Nat Nanotechnol* 2018;
  31. Thekkan S, Jani MS, Cui C, Dan K, Zhou G, Becker L, Krishnan Y. A DNA-based fluorescent reporter maps HOCl production in the maturing phagosome. *Nat Chem Biol* 2018;1.
  32. Modi S, Swetha MG, Goswami D, Gupta GD, Mayor S, Krishnan Y. A DNA nanomachine that maps spatial and temporal pH changes inside living cells. *Nat Nanotechnol* 2009;4:325–330.
  33. Chakraborty K, Veetil AT, Jaffrey SR, Krishnan Y. Nucleic Acid–Based Nanodevices in Biological Imaging. *Annu Rev Biochem* 2016;85:349–373.
  34. Surana S, Bhat JM, Koushika SP, Krishnan Y. An autonomous DNA nanomachine maps spatiotemporal pH changes in a multicellular living organism. *Nat Commun* 2011;2:340–347.
  35. van Leeuwenhoek A. Observations, communicated to the publisher by Mr. Antony van Leeuwenhoek, in a dutch letter of the 9th Octob. 1676. here English'd: concerning little animals by him observed in rain-well-sea- and snow water; as also in water wherein pepper had lain infus. *Philos Trans R Soc London* 1677;12:821–831.
  36. van Leeuwenhoek A. An abstract of a letter from Mr. Anthony Leevvenhoek at Delft, dated Sep. 17. 1683. Containing some microscopical observations, about animals in the scurf of the teeth, the substance call'd worms in the nose, the cuticula consisting of scales. *Philos Trans R Soc London* 1683;14:568–574.
  37. Ries J. Kinematographie der Befruchtung und Zellteilung. *Arch für mikroskopische Anat* 1909;
  38. Chevroton L, Vlès MF. La cinématique de la segmentation de l'oeuf et la chronophotographie du développement de l'Oursin. *CR Seances Acad Sci* 1909;149:806–809.
  39. Whitman C. The embryology of Clepsine. 1878;
  40. Nixon-Abell J, Obara CJ, Weigel A V, Li D, Legant WR, Xu CS, Pasolli HA, Harvey K, Hess HF, Betzig E, Blackstone C, Lippincott-Schwartz J. Increased spatiotemporal resolution reveals highly dynamic dense tubular matrices in the peripheral ER. *Science (80- )* 2016;354:aaf3928–aaf3928.
  41. Valm AM, Cohen S, Legant WR, Melunsi J, Hershberg U, Wait E, Cohen AR, Davidson MW, Betzig E, Lippincott-Schwartz J. Applying systems-level spectral imaging and analysis to reveal the organelle interactome. *Nature* 2017;546:162–167.
  42. Hell SW, Wichmann J. Breaking the diffraction resolution limit by stimulated emission: stimulated-emission-depletion fluorescence microscopy. *Opt Lett* 1994;19:780–2.
  43. Rust MJ, Bates M, Zhuang X. Sub-diffraction-limit imaging by stochastic optical reconstruction microscopy (STORM). *Nat Methods* 2006;3:793–5.
  44. Betzig E, Patterson GH, Sougrat R, Lindwasser OW, Olenych S, Bonifacino JS, Davidson MW, Lippincott-Schwartz J, Hess HF. Imaging intracellular fluorescent proteins at nanometer resolution. *Science* 2006;313:1642–5.
  45. Balzarotti F, Eilers Y, Gwosch KC, Gynnå AH, Westphal V, Stefani FD, Elf J, Hell SW. Nanometer resolution imaging and tracking of fluorescent molecules with minimal photon fluxes. *Science* 2017;355:606–612.
  46. Hulleman CN, Li W, Gregor I, Rieger B, Enderlein J. Photon Yield Enhancement of Red Fluorophores at Cryogenic Temperatures. *ChemPhysChem* 2018;19:1774–1780.
  47. Slot JW, Geuze HJ. Sizing of protein A-colloidal gold probes for immunoelectron microscopy. *J Cell Biol* 1981;90:533–536.
  48. Giepmans BNG, Deerinck TJ, Smarr BL, Jones YZ, Ellisman MH. Correlated light and electron microscopic imaging of multiple endogenous proteins using Quantum dots. *Nat Methods* 2005;2:743–749.
  49. Graham RC, Karnovsky MJ. The early stages of absorption of injected horseradish peroxidase in the proximal tubules of mouse kidney: ultrastructural cytochemistry by a new technique. *J Histochem Cytochem* 1966;14:291–302.
  50. Nakane PK. Simultaneous localization of multiple tissue antigens using the peroxidase-labeled antibody method: a study on pituitary glands of the rat. *J Histochem Cytochem* 1968;16:557–560.
  51. Griffin BA, Adams SR, Tsien RY. Specific covalent labeling of recombinant protein molecules inside live cells. *Science (80- )* 1998;281:269–272.
  52. Adams SR, Campbell RE, Gross LA, Martin BR, Walkup GK, Yao Y, Llopis J, Tsien RY. New biarsenical ligands and tetracysteine motifs for protein labeling in vitro and in vivo: Synthesis and biological applications. *J Am Chem Soc* 2002;124:6063–6076.
  53. Martell JD, Deerinck TJ, Sancak Y, Poulos TL, Mootha VK, Sosinsky GE, Ellisman MH, Ting AY. Engineered ascorbate peroxidase as a genetically encoded reporter for electron microscopy. *Nat Biotechnol*

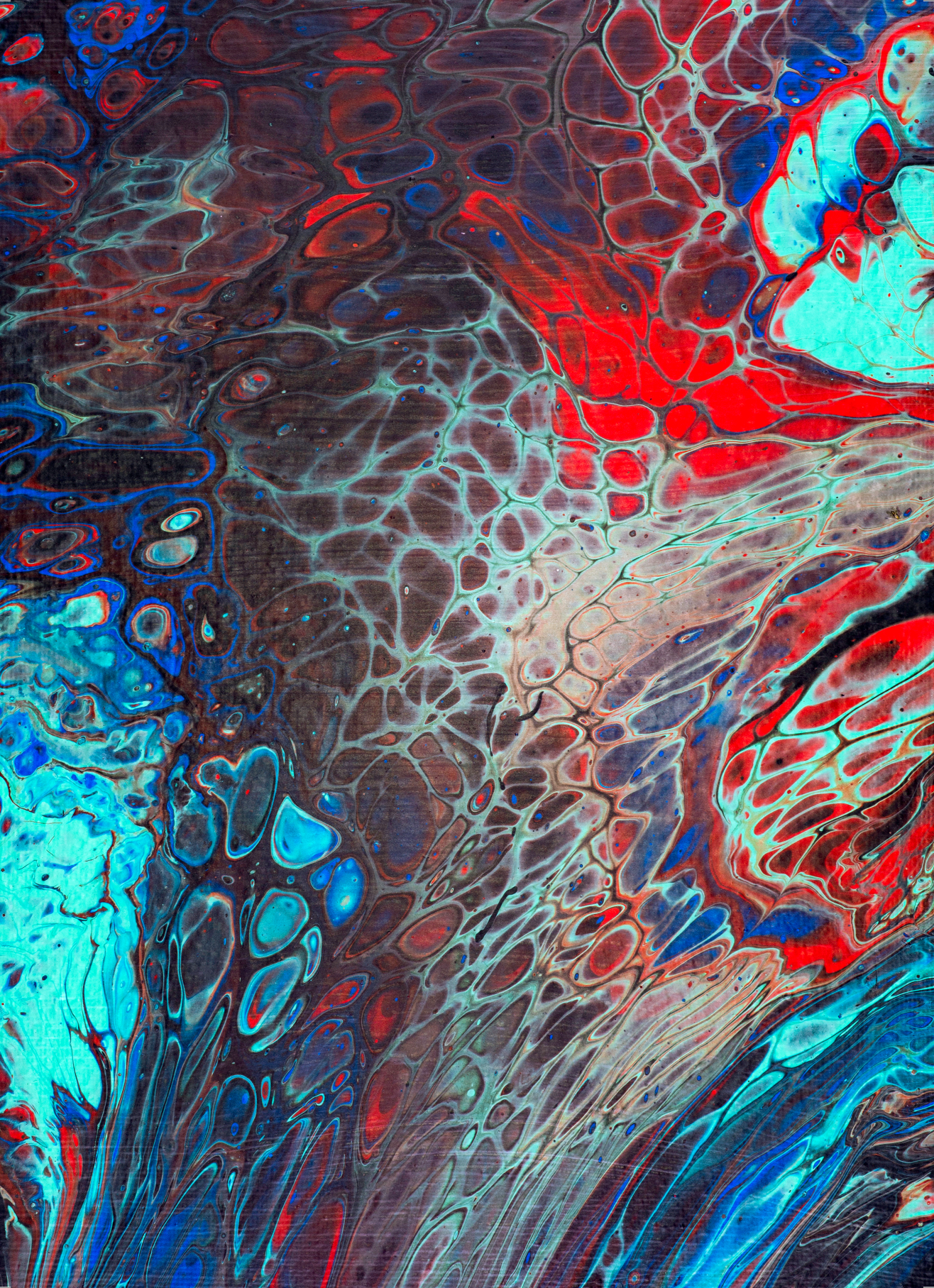
- 2012;30:1143–1148.
54. Birch-Andersen A. Reconstruction of the Nuclear Sites of *Salmonella typhimurium* from Electron Micrographs of Serial Sections. *J Gen Microbiol* 1955;13:327–329.
  55. Bang BG, Bang FB. Graphic reconstruction of the third dimension from serial electron microphotographs. *J Ultrastructure Res* 1957;1:138–146.
  56. Crowther RA, DeRosier DJ, Klug A. The Reconstruction of a Three-Dimensional Structure from Projections and its Application to Electron Microscopy. *Proc R Soc A Math Phys Eng Sci* 1970;317:319–340.
  57. Kremer JR, Mastronarde DN, McIntosh JR. Computer visualization of three-dimensional image data using IMOD. *J Struct Biol* 1996;116:71–6.
  58. Mischeva KD, Smith SJ. Array Tomography: A New Tool for Imaging the Molecular Architecture and Ultrastructure of Neural Circuits. *Neuron* 2007;55:25–36.
  59. Denk W, Horstmann H. Serial block-face scanning electron microscopy to reconstruct three-dimensional tissue nanostructure. *PLoS Biol* 2004;2.
  60. Heymann JAW, Hayles M, Gestmann I, Giannuzzi LA, Lich B, Subramaniam S. Site-specific 3D imaging of cells and tissues with a dual beam microscope. *J Struct Biol* 2006;155:63–73.
  61. Narayan K, Subramaniam S. Focused ion beams in biology. *Nat Methods* 2015;12:1021–1031.
  62. Lich B, Zhuge X, Potocek P, Journal FB-B, 2013 U. Bringing deconvolution algorithmic techniques to the electron microscope. *Biophys J* 2013;104:500a.
  63. Xu CS, Hayworth KJ, Lu Z, Grob P, Hassan AM, García-Cerdán JG, Niyogi KK, Nogales E, Weinberg RJ, Hess HF. Enhanced FIB-SEM systems for large-volume 3D imaging. *Elife* 2017;6:1–36.
  64. Zheng Z, Lauritzen JS, Perlman E, Robinson CG, Nichols M, Milkie D, Torrens O, Price J, Fisher CB, Sharifi N, Calle-Schuler SA, Kmecova L, Ali IJ, Karsh B, Trautman ET, Bogovic JA, Hanslovsky P, Jefferis GSXE, Kazhdan M, Khairy K, Saalfeld S, Fetter RD, Bock DD. A Complete Electron Microscopy Volume of the Brain of Adult *Drosophila melanogaster*. *Cell* 2018;174:730–743.e22.
  65. Wagner J, Schaffer M, Fernández-Busnadiego R. Cryo-electron tomography-the cell biology that came in from the cold. *FEBS Lett* 2017;591:2520–2533.
  66. Boekema EJ, Folea M, Kouřil R. Single particle electron microscopy. *Photosynth Res* 2009;102:189–96.
  67. Elmlund D, Elmlund H. Cryogenic Electron Microscopy and Single-Particle Analysis. *Annu Rev Biochem* 2015;84:499–517.
  68. Kimanius D, Forsberg BO, Scheres SH, Lindahl E. Accelerated cryo-EM structure determination with parallelisation using GPUs in RELION-2. *Elife* 2016;5.
  69. Lander GC, Stagg SM, Voss NR, Cheng A, Fellmann D, Pulokas J, Yoshioka C, Irving C, Mulder A, Lau P-W, Lyumkis D, Potter CS, Carragher B. Appion: an integrated, database-driven pipeline to facilitate EM image processing. *J Struct Biol* 2009;166:95–102.
  70. Khoshouei M, Radjainia M, Baumeister W, Danev R. Cryo-EM structure of haemoglobin at 3.2 Å determined with the Volta phase plate. *Nat Commun* 2017;8:16099.
  71. Campbell MG, Veelsler D, Cheng A, Potter CS, Carragher B. 2.8 Å resolution reconstruction of the *Thermoplasma acidophilum* 20S proteasome using cryo-electron microscopy. *Elife* 2015;4.
  72. Zheng SQ, Palovcak E, Armache J-P, Verba KA, Cheng Y, Agard DA. MotionCor2: anisotropic correction of beam-induced motion for improved cryo-electron microscopy. *Nat Methods* 2017;14:331–332.
  73. Subramaniam S, Earl LA, Falconieri V, Milne JL, Egelman EH. Resolution advances in cryo-EM enable application to drug discovery. *Curr Opin Struct Biol* 2016;41:194–202.
  74. Renaud J-P, Chari A, Ciferri C, Liu W, Rémygy H-W, Stark H, Wiesmann C. Cryo-EM in drug discovery: achievements, limitations and prospects. *Nat Rev Drug Discov* 2018;17:471–492.
  75. Plitzko JM, Rigort A, Leis A. Correlative cryo-light microscopy and cryo-electron tomography: from cellular territories to molecular landscapes. *Curr Opin Biotechnol* 2009;20:83–9.
  76. Villa E, Schaffer M, Plitzko JM, Baumeister W. Opening windows into the cell: focused-ion-beam milling for cryo-electron tomography. *Curr Opin Struct Biol* 2013;23:771–7.
  77. Rigort A, Bäuerlein FJB, Villa E, Eibauer M, Laugks T, Baumeister W, Plitzko JM. Focused ion beam micromachining of eukaryotic cells for cryoelectron tomography. *Proc Natl Acad Sci U S A* 2012;109:4449–54.
  78. Hsieh C, Schmelzer T, Kishchenko G, Wagenknecht T, Marko M. Practical workflow for cryo focused-ion-beam milling of tissues and cells for cryo-TEM tomography. *J Struct Biol* 2014;185:32–41.
  79. Lučić V, Rigort A, Baumeister W. Cryo-electron tomography: The challenge of doing structural biology in situ. *J Cell Biol* 2013;202:407–419.
  80. Dunstone MA, de Marco A. Cryo-electron tomography: An ideal method to study membrane-associated proteins. *Philos Trans R Soc B Biol Sci* 2017;372.
  81. Albert S, Schaffer M, Beck F, Mosalaganti S, Asano S, Thomas HF, Plitzko JM, Beck M, Baumeister W,

- Engel BD. Proteasomes tether to two distinct sites at the nuclear pore complex. *Proc Natl Acad Sci U S A* 2017;114:13726–13731.
82. Kovtun O, Leneva N, Bykov YS, Ariotti N, Teasdale RD, Schaffer M, Engel BD, Owen DJ, Briggs JAG, Collins BM. Structure of the membrane-assembled retromer coat determined by cryo-electron tomography. *Nature* 2018;561:561–564.
  83. Bharat TAM, Hoffmann PC, Kukulski W. Correlative Microscopy of Vitreous Sections Provides Insights into BAR-Domain Organization In Situ. *Structure* 2018;26:879-886.e3.
  84. Dubochet J, Adrian M, Chang J-J, Homo J-C, Lepault J, McDowell AW, Schultz P. Cryo-electron microscopy of vitrified specimens. *Q Rev Biophys* 1988;21:129–228.
  85. Studer D, Michel M, Müller M. High pressure freezing comes of age. *Scanning Microsc Suppl* 1989;3:253–68; discussion 268-9.
  86. McDonald K, Morpew MK. Improved preservation of ultrastructure in difficult-to-fix organisms by high pressure freezing and freeze substitution: I. *Drosophila melanogaster* and *Strongylocentrotus purpuratus* embryos. *Microsc Res Tech* 1993;24:465–473.
  87. Hohenberg H, Mannweiler K, Müller M. High-pressure freezing of cell suspensions in cellulose capillary tubes. *J Microsc* 1994;175:34–43.
  88. Dahl R, Staehelin LA. High-pressure freezing for the preservation of biological structure: Theory and practice. *J Electron Microsc Tech* 1989;13:165–174.
  89. Hawes P, Netherton CL, Mueller M, Wileman T, Monaghan P. Rapid freeze-substitution preserves membranes in high-pressure frozen tissue culture cells. *J Microsc* 2007;226:182–9.
  90. McDonald KL. Out with the old and in with the new: rapid specimen preparation procedures for electron microscopy of sectioned biological material. *Protoplasma* 2014;251:429–48.
  91. Murk JLAN, Posthuma G, Koster AJ, Geuze HJ, Verkleij AJ, Kleijmeer MJ, Humbel BM. Influence of aldehyde fixation on the morphology of endosomes and lysosomes: quantitative analysis and electron tomography. *J Microsc* 2003;212:81–90.
  92. de Boer P, Hoogenboom JP, Giepmans BNG. Correlated light and electron microscopy: ultrastructure lights up! *Nat Methods* 2015;12:503–13.
  93. Karreman MA, Mercier L, Schieber NL, Solecki G, Allio G, Winkler F, Ruthensteiner B, Goetz JG, Schwab Y. Fast and precise targeting of single tumor cells in vivo by multimodal correlative microscopy. *J Cell Sci* 2016;129:444–56.
  94. Murphy GE, Narayan K, Lowekamp BC, Hartnell LM, Heymann J a W, Fu J, Subramaniam S. Correlative 3D imaging of whole mammalian cells with light and electron microscopy. *J Struct Biol* 2011;176:268–78.
  95. Bushby AJ, Mariggi G, Armer HEJ, Collinson LM. Correlative light and volume electron microscopy: using focused ion beam scanning electron microscopy to image transient events in model organisms. *Methods Cell Biol* 2012;111:357–82.
  96. Karreman MA, Mercier L, Schieber NL, Solecki G, Allio G, Winkler F, Ruthensteiner B, Goetz JG, Schwab Y. Fast and precise targeting of single tumor cells in vivo by multimodal correlative microscopy. *J Cell Sci* 2016;129:444–56.
  97. Olmos Y, Hodgson L, Mantell J, Verkade P, Carlton JG. ESCRT-III controls nuclear envelope reformation. *Nature* 2015;522:236–9.
  98. Russell MRG, Lerner TR, Burden JJ, Nkwe DO, Pelchen-Matthews A, Domart M-C, Durgan J, Weston A, Jones ML, Peddie CJ, Carzaniga R, Florey O, Marsh M, Gutierrez MG, Collinson LM. 3D correlative light and electron microscopy of cultured cells using serial blockface scanning electron microscopy. *J Cell Sci* 2017;130:278–291.
  99. Polishchuk RS, Polishchuk E V., Marra P, Alberti S, Buccione R, Luini A, Mironov AA. Correlative light-electron microscopy reveals the tubular-saccular ultrastructure of carriers operating between Golgi apparatus and plasma membrane. *J Cell Biol* 2000;148:45–58.
  100. Polishchuk RS, San Pietro E, Di Pentima A, Teté S, Bonifacino JS. Ultrastructure of long-range transport carriers moving from the trans-Golgi network to peripheral endosomes. *Traffic* 2006;7:1092–1103.
  101. Rijnsoever C Van, Oorschot V, Klumperman J. Correlative light-electron microscopy (CLEM) combining live-cell imaging and immunolabeling of ultrathin cryosections. *Nat Methods* 2008;5:973–980.
  102. Kühn S, Lopez-Montero N, Chang YY, Sartori-Rupp A, Enninga J. Imaging macropinosomes during Shigella infections. *Methods* 2017;
  103. Hölttä-Vuori M, Sezgin E, Eggeling C, Ikonen E. Use of BODIPY-Cholesterol (TF-Chol) for Visualizing Lysosomal Cholesterol Accumulation. *Traffic* 2016;17:1054–1057.
  104. Bolbat A, Schultz C. Recent developments of genetically encoded optical sensors for cell biology. *Biol Cell* 2017;109:1–23.
  105. Kallemeijn WW, Li KY, Witte MD, Marques ARA, Aten J, Scheij S, Jiang J, Willems LI, Voorn-Brouwer TM,

- Van Roomen CPAA, Ottenhoff R, Boot RG, Van Den Elst H, Walvoort MTC, Florea BI, Codée JDC, Van Der Marel GA, Aerts JMFG, Overkleef HS. Novel activity-based probes for broad-spectrum profiling of retaining  $\beta$ -exoglucosidases in situ and in vivo. *Angew Chemie - Int Ed* 2012;51:12529–12533.
106. Bishop D, Nikić I, Brinkoetter M, Knecht S, Potz S, Kerschensteiner M, Misgeld T. Near-infrared branding efficiently correlates light and electron microscopy. *Nat Methods* 2011;8:568–70.
  107. Kukulski W, Schorb M, Welsch S, Picco A, Kaksonen M, Briggs JAG. Correlated fluorescence and 3D electron microscopy with high sensitivity and spatial precision. *J Cell Biol* 2011;192:111–119.
  108. Watanabe S, Punge A, Holloper G, Willig KI, Hobson RJ, Davis MW, Hell SW, Jorgensen EM. Protein localization in electron micrographs using fluorescence nanoscopy. *Nat Methods* 2011;8:80–4.
  109. Kopek BG, Shtengel G, Xu CS, Clayton D a, Hess HF. Correlative 3D superresolution fluorescence and electron microscopy reveal the relationship of mitochondrial nucleoids to membranes. *Proc Natl Acad Sci U S A* 2012;109:6136–41.
  110. Fokkema J, Fermie J, Liv N, van den Heuvel DJ, Konings TOM, Blab GA, Meijerink A, Klumperman J, Gerritsen HC. Fluorescently Labelled Silica Coated Gold Nanoparticles as Fiducial Markers for Correlative Light and Electron Microscopy. *Sci Rep* 2018;8:13625.
  111. Paul-Gilloteaux P, Heiligenstein X, Belle M, Domart MC, Larijani B, Collinson L, Raposo G, Salamero J. EC-CLEM: Flexible multidimensional registration software for correlative microscopies. *Nat. Methods* 2017;14:102–103.
  112. Stepanek L, Pigino G. Microtubule doublets are double-track railways for intraflagellar transport trains. *Science (80- )* 2016;352:721–724.
  113. Verkade P. Moving EM: The Rapid Transfer System as a new tool for correlative light and electron microscopy and high throughput for high-pressure freezing. *J Microsc* 2008;230:317–328.
  114. Heiligenstein X, Heiligenstein J, Delevoye C, Hurbain I, Bardin S, Paul-Gilloteaux P, Sengmanivong L, Régnier G, Salamero J, Antony C, Raposo G. The CryoCapsule: Simplifying Correlative Light to Electron Microscopy. *Traffic* 2014;15:700–716.
  115. Fuest M, Nocera GM, Modena MM, Riedel D, Mejia YX, Burg TP. Cryofixation during live-imaging enables millisecond time-correlated light and electron microscopy. *J Microsc* 2018;00:1–9.
  116. Karreman M a, Agronskaia A V, van Donselaar EG, Vocking K, Fereidouni F, Humbel BM, Verrips CT, Verkleij AJ, Gerritsen HC. Optimizing immuno-labeling for correlative fluorescence and electron microscopy on a single specimen. *J Struct Biol* 2012;180:382–6.
  117. Karreman M a, Van Donselaar EG, Agronskaia A V, Verrips CT, Gerritsen HC. Novel contrasting and labeling procedures for correlative microscopy of thawed cryosections. *J Histochem Cytochem* 2013;61:236–47.
  118. Paez-Segala MG, Sun MG, Shtengel G, Viswanathan S, Baird M a, Macklin JJ, Patel R, Allen JR, Howe ES, Piszczek G, Hess HF, Davidson MW, Wang Y, Looger LL. Fixation-resistant photoactivatable fluorescent proteins for CLEM. *Nat Methods* 2015;
  119. Lev-ram V, Green DPL, Tsien RY, Spector DL, Resource I, Diego S, Jolla L, Harbor CS. Fluorescence Photooxidation with Eosin : A Method for High Resolution Immunolocalization and In Situ Hybridization Detection for Light and Electron Microscopy. *J Cell Biol* 1994;126:901–910.
  120. Grabenbauer M, Geerts WJC, Fernandez-Rodriguez J, Hoenger A, Koster A, Nilsson T. Correlative microscopy and electron tomography of GFP through photooxidation. *Nat Methods* 2005;2:857–862.
  121. Shu X, Lev-Ram V, Deerinck TJ, Qi Y, Ramko EB, Davidson MW, Jin Y, Ellisman MH, Tsien RY. A genetically encoded tag for correlated light and electron microscopy of intact cells, tissues, and organisms. *PLoS Biol* 2011;9:e1001041.
  122. Kuipers J, van Ham TJ, Kalicharan RD, Veenstra-Algra A, Sjollem KA, Dijk F, Schnell U, Giepmans BNG. FLIPPER, a combinatorial probe for correlated live imaging and electron microscopy, allows identification and quantitative analysis of various cells and organelles. *Cell Tissue Res* 2015;360:61–70.
  123. de Beer MA, Kuipers J, van Bergen en Henegouwen PMP, Giepmans BNG. A small protein probe for correlated microscopy of endogenous proteins. *Histochem Cell Biol* 2018;149:261–268.
  124. Miles BT, Greenwood AB, Benito-Alifonso D, Tanner H, Galan MC, Verkade P, Gersen H. Direct Evidence of Lack of Colocalisation of Fluorescently Labelled Gold Labels Used in Correlative Light Electron Microscopy. *Sci Rep* 2017;7:44666.
  125. Pawley J, Masters B. Handbook of biological confocal microscopy. *Opt. Eng.* 1996;35:11–17.
  126. Masters BR. The Development of Fluorescence Microscopy. In: *Encyclopedia of Life Sciences*. Chichester, UK: John Wiley & Sons, Ltd; 2010.
  127. Kasten FH. The development of fluorescence microscopy up through World War II. In: *History of Staining*. 1983. p. 147–185.
  128. Kasten FH. The Origins of Modern Fluorescence Microscopy and Fluorescent Probes. In: *Cell Structure and Function by Microspectrofluorometry*. Academic Press; 1989. p. 3–50.

129. Coons AH, Kaplan MH. Localization of antigen in tissue cells: II. Improvements in a method for the detection of antigen by means of fluorescent antibody. *J Exp Med* 1949;91:1–13.
130. Tsien RY. The Green Fluorescent Protein. *Annu Rev Biochem* 1998;67:509–544.
131. Porter KR. A Study of Tissue Culture Cells By Electron Microscopy: Methods and Preliminary Observations. *J Exp Med* 1945;81:233–246.
132. Moberg CL. Entering an unseen world : a founding laboratory and origins of modern cell biology, 1910-1974.
133. Palade GE, Siekevitz P. Liver microsomes; an integrated morphological and biochemical study. *J Biophys Biochem Cytol* 1956;2:171–200.
134. Koster AJ, Klumperman J. Electron microscopy in cell biology: integrating structure and function. *Nat Rev Mol Cell Biol* 2003;4:SS6--SS9.
135. Huotari J, Helenius A. Endosome maturation. *EMBO J* 2011;30:3481–500.
136. Raposo G, Klumperman J. The Complex Ultrastructure of the Endolysosomal System. *Cold Spring Harb Perspect Biol* 2014;6:1–22.
137. Pu J, Guardia CM, Keren-Kaplan T, Bonifacino JS. Mechanisms and functions of lysosome positioning. *J Cell Sci* 2016;129:4329–4339.
138. van Bergeijk P, Hoogenraad CC, Kapitein LC. Right Time, Right Place: Probing the Functions of Organelle Positioning. *Trends Cell Biol* 2016;26:121–134.
139. Settembre C, Fraldi A, Medina DL, Ballabio A. Signals from the lysosome: a control centre for cellular clearance and energy metabolism. *Nat Rev Mol Cell Biol* 2013;14:283–96.
140. Sardiello M, Palmieri M, Ronza A Di, Medina DL, Valenza M, Gennarino VA, Di Malta C, Donaudo F, Embrione V, Polishchuk RS, Banfi S, Parenti G, Cattaneo E, Ballabio A. A gene network regulating lysosomal biogenesis and function. *Science* (80-) 2009;325:473–477.
141. Palmieri M, Impey S, Kang H, di Ronza A, Pelz C, Sardiello M, Ballabio A. Characterization of the CLEAR network reveals an integrated control of cellular clearance pathways. *Hum Mol Genet* 2011;20:3852–3866.
142. Korolchuk VI, Saiki S, Lichtenberg M, Siddiqi FH, Roberts EA, Imarisio S, Jahreis L, Sarkar S, Futter M, Menzies FM, O’Kane CJ, Deretic V, Rubinsztein DC. Lysosomal positioning coordinates cellular nutrient responses. *Nat Cell Biol* 2011;13:453–60.
143. Korolchuk VI, Rubinsztein DC. Regulation of autophagy by lysosomal positioning. *Autophagy* 2011;1–2.
144. Dell’Angelica EC, Mullins C, Caplan S, Bonifacino JS. Lysosome-related organelles. *FASEB J* 2000;14:1265–1278.
145. Marks MS, Heijnen HFG, Raposo G. Lysosome-related organelles: Unusual compartments become mainstream. *Curr Opin Cell Biol* 2013;25:495–505.
146. Luzio JP, Hackmann Y, Dieckmann NMG, Griffiths GM. The biogenesis of lysosomes and lysosome-related organelles. *Cold Spring Harb Perspect Biol* 2014;6:a016840.
147. Hume AN, Collinson LM, Rapak A, Gomes AQ, Hopkins CR, Seabra MC. Rab27a regulates the peripheral distribution of melanosomes in melanocytes. *J Cell Biol* 2001;152:795–808.
148. Ostrowski M, Carmo NB, Krumeich S, Fanget I, Raposo G, Savina A, Moita CF, Schauer K, Hume AN, Freitas RP, Goud B, Benaroch P, Hacohen N, Fukuda M, Desnos C, Seabra MC, Darchen F, Amigorena S, Moita LF, Thery C. Rab27a and Rab27b control different steps of the exosome secretion pathway. *Nat Cell Biol* 2010;12:19–30.
149. Novick P, Zerial M. The diversity of Rab proteins in vesicle transport. *Curr Opin Cell Biol* 1997;9:496–504.
150. Verhoeven K, De Jonghe P, Coen K, Verpoorten N, Auer-Grumbach M, Kwon JM, FitzPatrick D, Schmedding E, De Vriendt E, Jacobs A, Van Gerwen V, Wagner K, Hartung HP, Timmerman V. Mutations in the small GTP-ase late endosomal protein RAB7 cause Charcot-Marie-Tooth type 2B neuropathy. *Am J Hum Genet* 2003;72:722–727.
151. Pal A, Severin F, Hoepfner S, Zerial M. Regulation of Endosome Dynamics by Rab5 and Huntingtin-HAP40 Effector Complex in Physiological versus Pathological Conditions. *Methods Enzymol* 2008;438:239–257.
152. Fraldi A, Klein AD, Medina DL, Settembre C. Brain Disorders Due to Lysosomal Dysfunction. *Annu Rev Neurosci* 2016;39:277–295.
153. Gowrishankar S, Yuan P, Wu Y, Schrag M, Paradise S, Grutzendler J, De Camilli P, Ferguson SM. Massive accumulation of luminal protease-deficient axonal lysosomes at Alzheimer’s disease amyloid plaques. *Proc Natl Acad Sci* 2015;112:E3699–E3708.
154. Samie MA, Xu H. Lysosomal exocytosis and lipid storage disorders. *J Lipid Res* 2014;55:995–1009.
155. Hämälistö S, Jäättelä M. Lysosomes in cancer - living on the edge (of the cell). *Curr Opin Cell Biol* 2016;39:69–76.
156. Grimm C, Bartel K, Vollmar AM, Biel M. Endolysosomal cation channels and cancer—a link with great potential. *Pharmaceuticals* 2018;11:1–8.
157. Mercer J, Helenius A. Virus entry by macropinocytosis. *Nat Cell Biol* 2009;11:510–20.

158. Mercer J, Schelhaas M, Helenius A. Virus entry by endocytosis. *Annu Rev Biochem* 2010;79:803–33.
159. Yamauchi Y, Helenius A. Virus entry at a glance. *J Cell Sci* 2013;126:1289–95.
160. Stoeck IK, Lee J-Y, Tabata K, Romero-Brey I, Paul D, Schult P, Lohmann V, Kaderali L, Bartenschlager R. Hepatitis C virus replication depends on endosomal cholesterol homeostasis. *J Virol* 2017;92:JV1.01196-17.
161. Staring J, Raaben M, Brummelkamp TR. Viral escape from endosomes and host detection at a glance. *J Cell Sci* 2018;131:jcs216259.
162. Cossart P, Helenius A. Endocytosis of viruses and bacteria. *Cold Spring Harb Perspect Biol* 2014;6.
163. Cossart P, Sansonetti PJ. Bacterial Invasion: The Paradigms of Enteroinvasive Pathogens. *Science* (80- ) 2004;304:242–248.
164. Pizarro-Cerdá J, Cossart P. Bacterial Adhesion and Entry into Host Cells. *Cell* 2006;124:715–727.
165. van Meel E, Klumperman J. Imaging and imagination: understanding the endo-lysosomal system. *Histochem Cell Biol* 2008;129:253–66.
166. Saftig P, Klumperman J. Lysosome biogenesis and lysosomal membrane proteins: trafficking meets function. *Nat Rev Mol Cell Biol* 2009;10:623–35.
167. Eskelinen EL, Reggiori F, Baba M, Kovács AL, Seglen PO. Seeing is believing: The impact of electron microscopy on autophagy research. *Autophagy*. 2011;7:935–956.
168. Klumperman J, Raposo G. The complex ultrastructure of the endolysosomal system. *Cold Spring Harb Perspect Biol* 2014;6.



---

# Chapter 2

---

## Single organelle dynamics linked to 3D structure by correlative live-cell – 3D electron microscopy

Job Fermie<sup>1,2</sup>, Nalan Liv<sup>1</sup>, Corlinda ten Brink<sup>1</sup>, Elly G. van Donselaar<sup>1</sup>, Wally H. Müller<sup>3</sup>, Nicole L. Schieber<sup>4</sup>, Yannick Schwab<sup>4</sup>, Hans C. Gerritsen<sup>2</sup>, Judith Klumperman<sup>1</sup>

1. Section Cell Biology, Center for Molecular Medicine, University Medical Center Utrecht, Utrecht University, Heidelberglaan 100, 3584CX Utrecht, The Netherlands
2. Section Molecular Biophysics, Debye Institute for Nanomaterials Science, Utrecht University, 3508 TA Utrecht, Netherlands.
3. Section Cryo-EM, Department of Chemistry, Utrecht University, Padualaan 8, 3584 CH Utrecht, The Netherlands
4. Electron Microscopy Core Facility, EMBL Heidelberg, Meyerhofstrasse 1, 69117 Heidelberg, Germany

This chapter is published as:

**Fermie J**, Liv N, ten Brink C, van Donselaar EG, Müller WH, Schieber NL, Schwab Y, Gerritsen HC, Klumperman J. Single organelle dynamics linked to 3D structure by correlative live-cell imaging and 3D electron microscopy. *Traffic*. 2018 May;19(5):354-69.

## Abstract

Live-cell correlative light-electron microscopy (live-cell-CLEM) integrates live movies with the corresponding EM image, but a major challenge is to relate the dynamic characteristics of single organelles to their 3D ultrastructure. Here we introduce focused ion beam scanning electron microscopy (FIB-SEM) in a modular live-cell CLEM pipeline for single organelle CLEM. We transfected cells with LAMP-1-GFP, analyzed the dynamics of individual GFP-positive spots, and correlated these to their corresponding fine-architecture and immediate cellular environment. By FIB-SEM we quantitatively assessed morphological characteristics, like number of intraluminal vesicles and contact sites with endoplasmic reticulum and mitochondria. Hence, we present a novel way to integrate multiple parameters of subcellular dynamics and architecture onto a single organelle, which is relevant to address biological questions related to membrane trafficking, organelle biogenesis and positioning. Furthermore, by using CLEM to select regions of interest, our method allows for targeted FIB-SEM, which significantly reduces time required for image acquisition and data processing.

## Introduction

Correlative light-electron microscopy (CLEM) comprises a collection of techniques that integrate light and electron microscopic data from a single sample, thereby combining the strengths of the two techniques. CLEM uses the large field of view of the light microscope (LM) to search for regions of interest (ROI), i.e. rare or transient phenotypes or specific subpopulations of cells within a complex tissue, and combines this with electron microscopy (EM) for subsequent ultrastructural context investigation. Using fluorescence microscopy (FM) as LM approach, CLEM can in addition be used to infer molecular information to EM images. EM on the other hand is the only method to directly visualize membranes at high resolution, allowing the visualization of the compartment of interest as well as its ultrastructural context. A powerful but also highly challenging CLEM approach is the combined use of live-cell FM and EM. Live-cell CLEM links subcellular dynamics to ultrastructural information, two parameters that are conventionally studied in separate samples. Consequently, our understanding of organelles is based on an average of dynamic data and an average of ultrastructural data. The live-cell CLEM method presented here has the potential to unequivocally resolve transient interactions between molecularly identified organelles, by combining dynamic recordings of subcellular compartments with ultrastructural snapshots of the exact same compartments.

For live-cell CLEM, live-cell data can be obtained using various FM techniques such as widefield, confocal or super-resolution, depending on the research question and kinetics and size of objects of interest. After imaging, the material is generally chemically fixed, and embedded in resin or prepared for cryosectioning[1–4]. Alternatively, samples are cryo-immobilized by either plunge freezing or high pressure freezing. Samples can then be observed by cryo-fluorescence microscopy and cryo-ET[5], or freeze-substituted and resin embedded, after which the samples are observed at room temperature[6–8]. Most strategies then rely on serial sectioning to find back the ROI in EM[3,4,9–11]. Despite its frequent use, serial sectioning is labor intensive, and suffers from several problems, including material loss, deformation of sections, and difficulty with registration of consecutive sections.

Recently, scanning EM (SEM)-based approaches have emerged as alternative tools to serial sectioning TEM[12]. By improvements in resolution and detector sensitivity, state of the art SEM systems can be used to study intracellular structures,

at a slightly lower resolution than TEM. This has led to rapid developments in array tomography (AT)[13], serial block face SEM (SBF-SEM)[14] and focused ion beam SEM (FIB-SEM)[15,16], techniques that are often referred to as volume EM since they yield information in 3D. In AT manually or automatically cut serial sections are collected on conductive supports, and automatically imaged in a SEM to reconstruct 3D structures. In SBF-SEM sectioning occurs in the SEM vacuum chamber, by use of a miniaturized ultramicrotome and diamond knife. In FIB-SEM a highly focused gallium ion beam ablates a thin layer of the sample after which the newly exposed surface is imaged with the scanning electron beam. The system repeats this cycle for hundreds or thousands of slices until the volume of interest is imaged, generating imaged volumes that can upwards of  $10^6 \mu\text{m}^3$  in state of the art systems[17,18]. Of these volume EM techniques FIB-SEM provides the highest resolution in z (4 nm), making it the technique of choice for imaging subcellular structures where visualization of morphological details is essential to establish their identity[18,19]. Moreover, since the gallium ion beam is precisely controlled, it can be used to target specific ROIs for imaging, which reduces the time for imaging and data processing. This is important since FIB-SEM imaging is time-consuming (on average 2-5 days of image acquisition per cell) and destructive (individual slices are destroyed during imaging). It is therefore highly advantageous to precisely select the ROI before starting image acquisition. This can be achieved through CLEM.

In previous studies demonstrating the ability to combine live-cell FM with either FIB-SEM or SBF-SEM[2,20,21], live-cell FM was primarily used as a method to identify a sporadic event within a prolonged time period. Here, we present a correlative live-cell FM to volume EM approach that for the first time links characteristic dynamic behavior of a single organelle to a complete analysis of its ultrastructural characteristics and does so in the context of its cellular surroundings. To reach this goal, we integrated known protocols for live-cell imaging, CLEM and FIB-SEM in such a way that we obtained an optimal pipeline for viewing single organelles from live FM to 3D FIB-SEM. We apply our method to the endo-lysosomal system, a complex and dynamic system of interacting membranes. By real time tracking of single endo-lysosomal compartments over several minutes and retracing these same compartments in EM, we show that live-cell imaging combined with FIB-SEM provides a powerful way to integrate dynamic, structural and morphological parameters onto one, single organelle. Moreover, the use of CLEM enables the selection of small, well-defined ROIs for examination by FIB-SEM, thereby greatly reducing imaging time and volume of an ROI (from 2-5 days per cell to 24-36 hours per ROI).

## Results

### Optimized correlation of live-cell fluorescence and FIB-SEM of single organelles

The endo-lysosomal system coordinates multiple processes in the cell: degradation of biomaterials obtained by endocytosis or autophagy, nutrient sensing, signaling and exocytosis[22]. Endocytosed cargo destined for degradation is brought by vesicular transport to early endosomes, which mature into late endosomes and then fuse with lysosomes. During endo-lysosomal maturation the compartments change in morphology, cargo composition, position and intraluminal acidity in a tightly controlled manner[23–29]. The most widely used manner to indicate distinct endo-lysosomal intermediates is their classification into ‘early endosomes’, ‘late endosomes’ and lysosomes (or variations hereon using other names)[30]. However, these 3 categories are too limited in discriminating power when it comes to describing the dynamic continuum of interacting endo-lysosomal compartments or to indicate sub-populations of endo-lysosomes that differ by content, function, lysosomal activity, positioning or dynamics[31,32]. Additional criteria are therefore required to be able to address fundamental yet still standing questions like: do all lysosomes carry out similar functions? How are lysosomal positioning and dynamics linked to endo-lysosomal maturation and functioning?

In our studies we label endo-lysosomes by both genetically expressed LAMP-1-GFP[33] and endocytosed fluorescent dextran. LAMP-1 is a well characterized integral membrane protein that in steady state is mostly confined to the limiting membrane of late endosomes and lysosomes[24]. However, since newly synthesized LAMP-1 can travel to the plasma membrane for subsequent endocytosis, low levels can be found in early endosomes, as was shown in previous immuno-EM studies[34,35]. Moreover, since late endosomes and lysosomes fuse with autophagosomes, LAMP-1 is also present in autolysosomes. An overview of compartments that can contain LAMP-1 is given in figure 1. Fluorescent dextran is a fluid phase endocytic tracer, which predominantly labels the degradative pathway[36]. Thus, constitutively endocytosed dextran will mark early and late endosomes, lysosomes and autolysosomes. Consequently, the identity of the LAMP-1-GFP and/or dextran positive compartments cannot be deduced from fluorescent images alone, but requires ultrastructural characterization. The main distinguishing morphological characteristics of endo-lysosomal compartments are described in numerous papers (reviewed in references[25,26]; summarized in supplementary table 1 of reference [24]) and described in table 1.

A schematic overview of our live cell to 3D FIB-SEM CLEM procedure is given in figure 2. We start our approach by culturing cells on gridded glass coverslips[4], which are etched with marks that are visible by both light microscopy and FIB-SEM (by imprinting the pattern in the Epon), allowing a first, coarse correlation between the two microscopes. The coverslips were coated with a circa 20 nm layer of carbon for easy removal of the coverslip once the cells were embedded in resin. HeLa cells were grown overnight on the carbon layer and transfected for LAMP-1-GFP for 5 hours. Then, the transfection medium was replaced with medium containing fluorescent dextran for 30 minutes at 37°C, followed by 2 hours at 20°C to block Golgi exit of newly synthesized GFP-tagged LAMP-1[35,37]. Since under these conditions the newly synthesized LAMP-1-GFP only starts exiting the ER, and has not yet reached the endo-lysosomal compartments, the 20°C block induces an accumulation of LAMP-1-GFP in the Golgi against an overall dark background of the

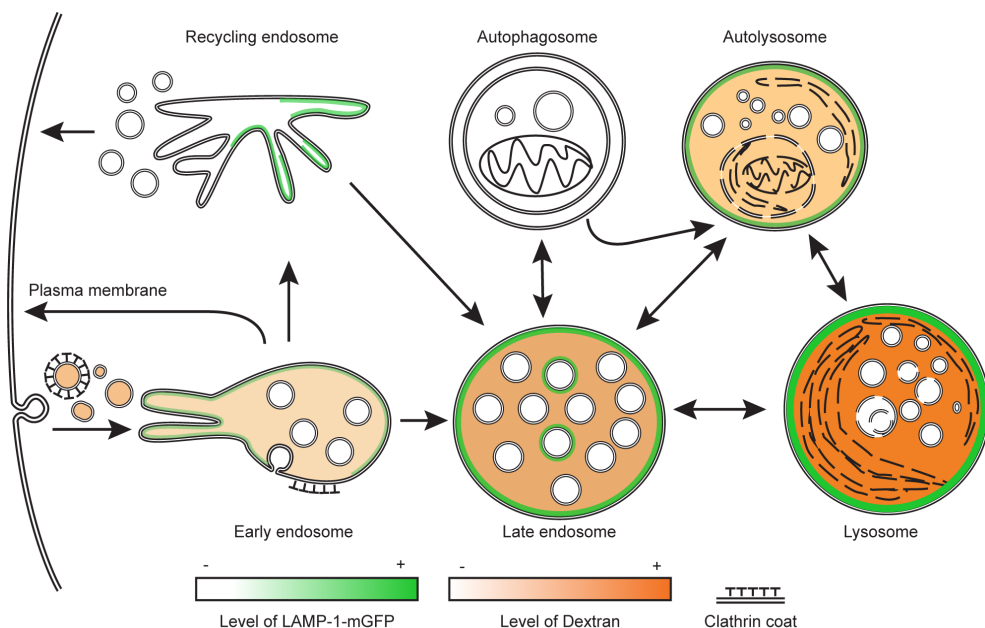


Figure 1: (A) Schematic representation of the endo-lysosomal system showing the location of internalized fluorescent dextran (orange) and LAMP-1-GFP (green) and the morphological characteristics of different types of endo-lysosomal compartments. Arrows indicate sites of interactions between compartments, either via compartment fusion or vesicular transport.

Organelle type	Defining characteristics	References
Early endosome	Irregular shaped vacuole (100-500 nm) with electron-lucent lumen, often one or multiple tubular extensions. Loosely packed ILVs. Patches of bi-layered clathrin lattices on limiting membrane.	27,40,79–82
Recycling endosome	Tubulo-vesicular membranes (60-100 nm diameter), with no discernable interior material. Clathrin coated membrane buds can occur on tubules.	34,83–85
Late endosome	Irregularly shaped to globular shaped vacuole (250-1000 nm), sometimes with short tubular extensions. Densely packed with ILVs.	25,29,43,86–88
Lysosome	Highly variable, heterogeneous shaped vacuole (200 - >1000 nm). Electron-dense lumen or irregular or amorphous content. Characteristic membrane whorls.	25,89–91
Autolysosome	Large, irregularly shaped vacuole (300nm - >2000 nm), with highly heterogeneous content, electron-lucent and electron-dense regions, sometimes with remnants of degraded organelles and cytosolic material	92–95

Table 1: Ultrastructural characteristics of endo-lysosomal compartments

cell. This facilitates the tracking of individual LAMP-1-GFP spots after releasing the block by placing cells at 37°C. We placed cells at 37°C 15 minutes prior to the start of live imaging, since this was the optimal period for warming up and create maximal visibility of post-Golgi LAMP-1-GFP-positive compartments.

During live-cell imaging (figure 2A), we only recorded the GFP channel, in a single focal plane, to reach the temporal resolution required to visualize transient trafficking events on a scale of seconds to tens-of-seconds (less than 500 ms between frames). We fixed cells *in situ* by adding double concentrated fixative directly to the medium in the live-cell holder, while the camera was still acquiring images. This prevented an imaging gap between the last live-cell frame and the fixed material. Movies were analyzed for regions of interest (ROIs) showing LAMP-1-GFP structures with distinct dynamic behaviors, such as travelling, fusion or interaction with other compartments. In the fixed material, Z-stacks of the ROI were recorded to visualize LAMP-1-GFP and in addition fluorescent dextran (figure 2B). The area surrounding the ROI was imaged with both fluorescence and polarized light to map the location of cells in relation to the grid pattern (figure 2C).

After completion of the steps described above, samples were postfixed in half-strength Karnovsky's fixative and stored in 1% formaldehyde in PHEM buffer or immediately taken for further processing. We applied two different post-fixation strategies, either osmium tetroxide ( $\text{OsO}_4$ ) followed by tannic acid and uranyl acetate (staining applied in figure 3), or a heavier staining strategy using reduced osmium tetroxide – thiocarbohydrazide – osmium tetroxide (R-OTO) followed by uranyl acetate and Walton's lead aspartate (staining applied in figures 4-6)[38,39]. Both protocols are described in-depth in the methods section. The latter strategy yielded more pronounced membranes and an overall better visualization of morphological details.

After resin embedding and polymerization of the resin, the Epon block containing the imaged cell was separated from the coverslip by repeatedly dipping in liquid nitrogen and separating the glass from the resin surface with a clean razor blade. The pattern of the gridded coverslip on the resin surface (figure 2D) greatly facilitated retracing of the ROI in the FIB-SEM.

The resin blocks were mounted on standard specimen stubs for SEM with the basal side of the cells facing up, rendered conductive by carbon paint and platinum sputter coating, and transferred to the FIB-SEM. We found that the contours of the cells on the resin surface can be visualized by the backscattered electron (BSE) detector and that these contours closely match the cell shape imaged by brightfield microscopy (figure 2D). By comparing the contours seen in SEM with the original live-cell imaging data, we could locate the ROI containing the previously live imaged GFP-positive compartments. This allowed us to target relatively small regions for volume imaging (figure 2D, 2E), reducing the time required to image the ROI, while insuring that the volume EM data contained all live imaged organelles (figure 2F). We performed automated serial imaging either using a FEI Scios (figures 2-4) or a FEI Helios G3 UC (figure 5), which provides higher electron beam resolution. This is primarily advantageous to resolve small morphological characteristics and structures where distinct membranes are in close proximity, such as membrane contact sites (figure 6). The imaging settings of all datasets are summarized in supplementary table 1.

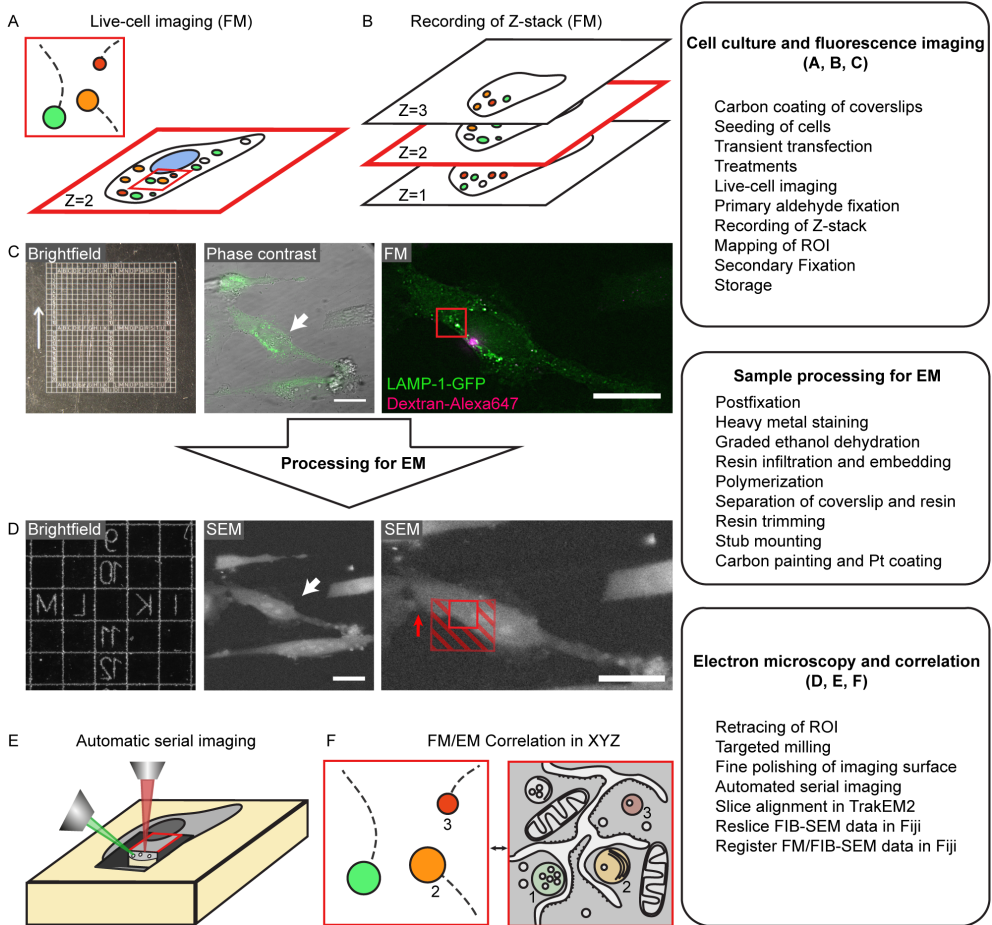


Figure 2: Schematic of the live-cell fluorescence to FIB-SEM workflow. (A) LAMP-1-GFP transfected cells were incubated with dextran and after a 20°C block imaged live for several minutes, followed by in-situ fixation. (B) Z-stacks are recorded to define the focal plane of live imaging. (C) Coordinates etched on gridded coverslips enable the retracing of cells after resin embedding. Coordinates of live imaged cells (middle panel, white arrow) are registered using phase contrast after fixation, and ROIs for FIB-SEM imaging are determined based on live-cell data (right panel, red square). (D) Retracing of live-imaged cells and targeting of ROIs is achieved through the imprinted coordinates of the gridded coverslips. Live imaged cells are retraced in SEM using the imprinted coordinates after the glass coverslip is removed (middle panel, white arrow), followed by targeted milling of excess material around the ROI (right panel, ROI indicated in red, excess material indicated in striped red). Milling and imaging direction are indicated by red arrow. The middle and right panels are horizontally flipped to show the matching orientation with the FM images. (E) Automated serial imaging is performed by repeatedly milling and imaging the ROI. (F) Acquired FIB-SEM datasets are aligned and correlated to live-cell data and Z-stack.

After automated imaging, we reconstructed the dataset in the same orientation as our live-cell movies to compare the volume EM data to the fluorescence Z-stack. We retraced the focal plane of live-cell imaging by selecting at least three fluorescent spots from the live cell imaging plane and measured the distances between the centers of these spots using Fiji. The pattern formed by these spots was then retraced in the volume EM data to identify the slice containing the previously live-imaged organelles (supplementary figure 1). Thus, we used individual compartments as landmarks for correlation between FM and FIB-SEM. When the Z-plane of live imaging was retraced in the FIB-SEM dataset, we correlated all live imaged compartments for ultrastructural analysis.

### Live-cell CLEM of a LAMP-1-GFP positive early endosome

After establishing the optimized CLEM protocol for live-cell 3D CLEM (figure 2), we performed a series of experiments on ROIs containing distinct LAMP-1-GFP positive compartments that were visible for the duration of the movie and showed distinctive dynamic behaviors. In figure 3A we identify a dense LAMP-1-GFP spot with a dark core (further indicated as spot 1 in figure 3A and supplementary movie 2). This staining pattern is typical for LAMP-1, which is mostly present in the limiting membrane of endo-lysosomal compartments (figure 1). The dense fluorescence represents LAMP-1-GFP in the limiting membrane, while the dark core represents the lumen that is devoid of LAMP-1-GFP. During live imaging, spot 1 was motile but within a restricted area, it remained within 2  $\mu\text{m}$  from the plasma membrane (figure 3B, table 3).

The Z-stack after fixation revealed that the central compartment of spot 1 contained dextran, indicating that it was reached by internalized cargo (figure 3C, 3D). After resin embedding, we retraced the cell and position of the ROI in the FIB-SEM (figure 3E, supplementary movie 3) and identified spot 1 as an irregularly shaped compartment measuring 1.28  $\mu\text{m}$  in X, 0.8  $\mu\text{m}$  in Y, and 1.28  $\mu\text{m}$  in Z, with an electron-lucent lumen containing intraluminal vesicles (ILVs) (figure 3F). Using segmentation, we identified 45 ILVs. Moreover, part of the limiting membrane of the compartment was decorated with a clathrin coat, which covered a typical indentation of the vacuolar membrane[40] (figure 3G, arrowheads, supplementary movie 3). Clathrin coats on the limiting membrane of early, and to a lesser extent late endosomes contain concentrated cargo for ESCRT dependent sorting into ILVs[41–43]. The irregular shape of the central vacuole, the electron lucent lumen with loosely packaged ILVs and the presence of a clathrin coat define spot 1 as early endosome (figure 1).

Combined, these live cell and EM data show a LAMP-1-GFP positive early endosome, which displays diffusive movement in a restricted area near the plasma membrane. The presence of LAMP-1 in early endosomes may seem atypical since LAMPs are established markers of late endosomes and lysosomes. However, LAMPs can exit the TGN via the secretory pathway and travel via the plasma membrane and early endosomes to lysosomes[44], thus temporarily residing in early endosomes. Our data are also in line with previous immuno-EM studies showing the presence of endogenous LAMP-1 in early endosomes[34].

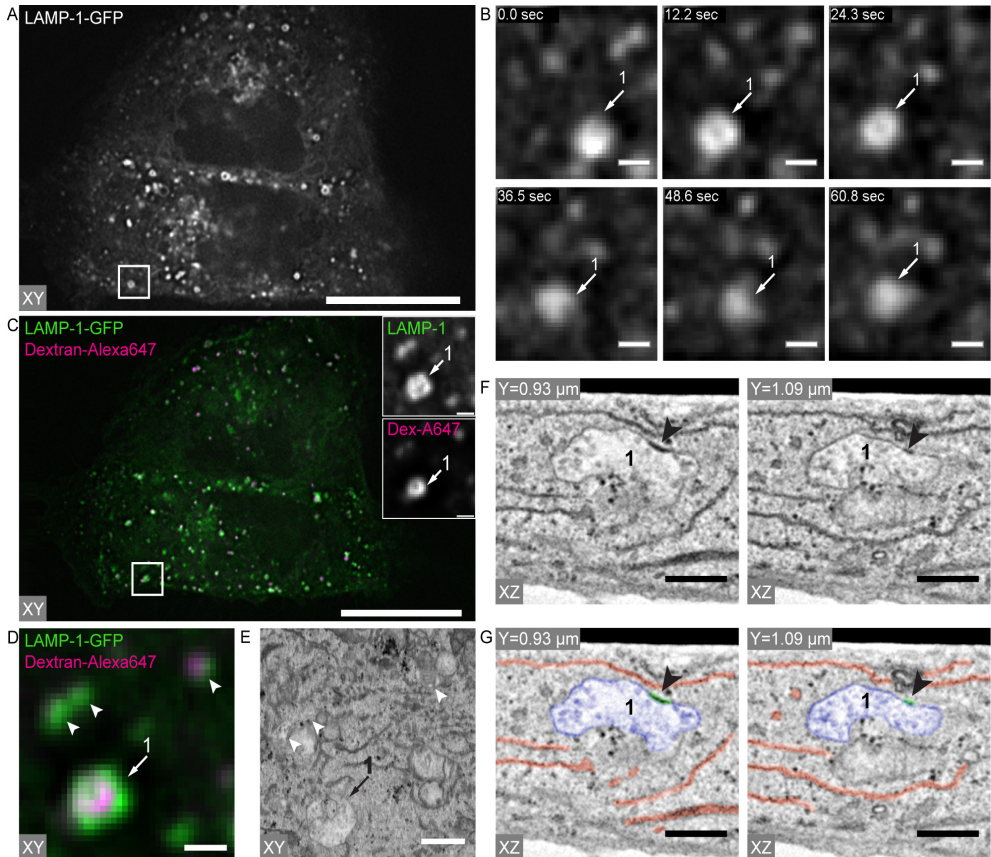


Figure 3: Live-cell CLEM of an early endosome. (A) Still from supplementary movie 2 at the start of live-cell imaging, showing the distribution of LAMP-1-GFP spots throughout the cell. The ROI selected for FIB-SEM, containing spot 1, is highlighted (white square). (B) Magnified stills of the ROI (area in white square in A) showing LAMP-1-GFP-positive spot 1 at distinct time points. (C) Slice from Z-stack after fixation showing the imaging plane with the ROI (white square). Inserts: enlargement of the ROI showing spot 1 in the GFP and dextran channels. (D) Enlarged fluorescent image of the ROI shown in the white squares in A and C (white squares) and containing spot 1 to a size that corresponds to the FIB-SEM image in 3E. Arrowheads indicate LAMP-1-GFP spots that were not tracked live, but could be correlated to the FIB-SEM dataset shown in E. (E) FIB-SEM reconstruction of the ROI containing spot 1 in the same orientation as the FM image in D. Arrowheads indicate endo-lysosomal compartments that that could be correlated to the FM data shown in D. (F) Individual slices from the FIB-SEM dataset showing morphological characteristics of spot 1. Arrowheads point to the presence of a clathrin coat. (G) Same image as in F, colorized to highlight spot 1 (early endosome) (blue), ER (red) and clathrin coat (green). Supplementary movie 3 shows all FIB-SEM slices through the entire ROI, zooming in on spot 1 and providing a reconstruction of the 3D structure of spot 1, including the dissection of intraluminal vesicles and clathrin coat. Table 3 shows the collection of parameters gathered on spot 1. Scale bars for A,C: 25  $\mu\text{m}$ ; B, D, E: 1  $\mu\text{m}$ ; F,G:500 nm.

## Live-cell CLEM of late endosome-lysosome interactions

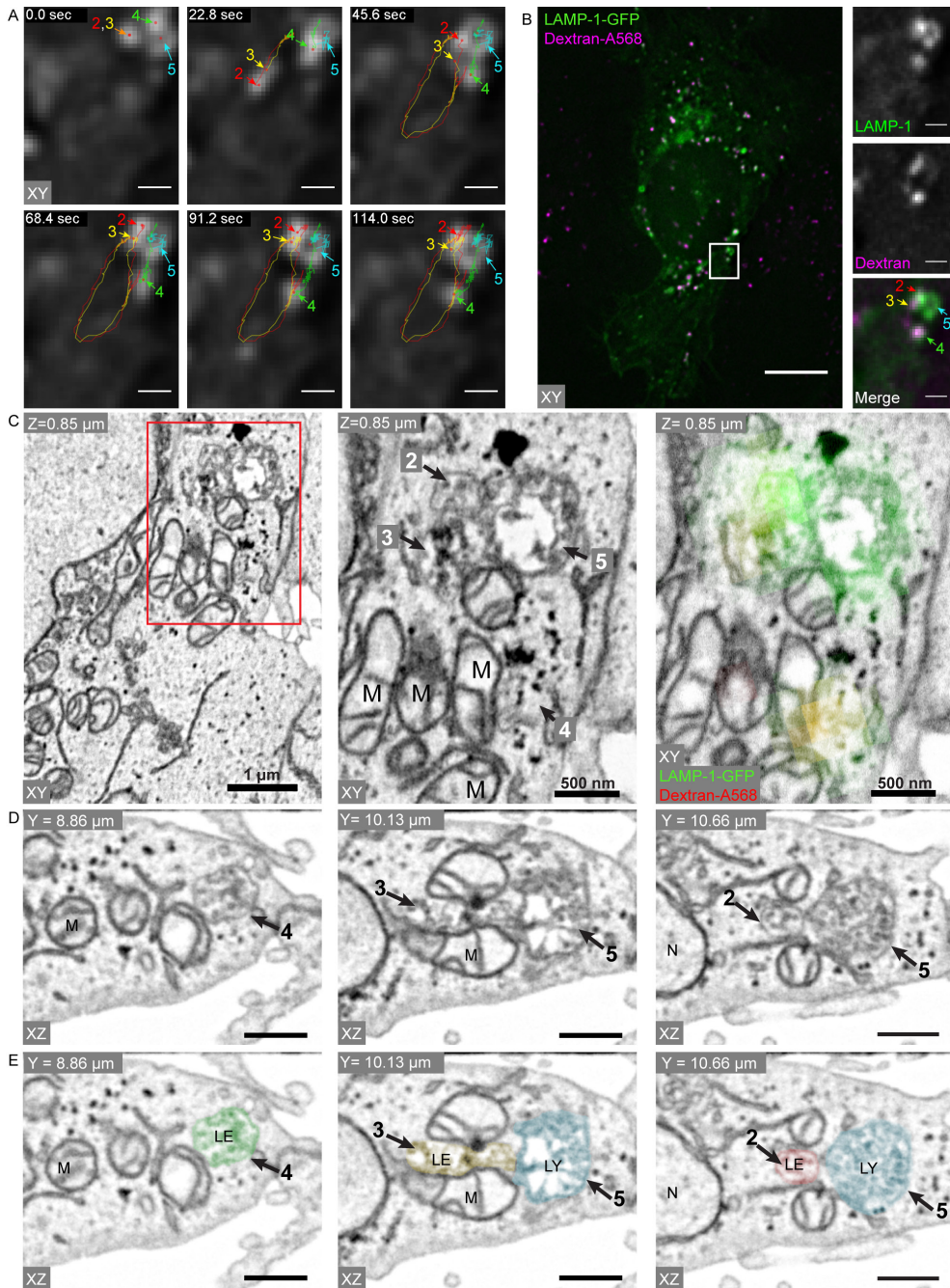
Next we analyzed 4 LAMP-1-GFP positive organelles over a period of 2 minutes (figure 4A). For clarity we use a continuous numbering of the imaged compartments throughout our figures (summarized in table 3), which is why we refer to these spots as spot 2-5. Based on their morphology, we discriminated 3 condensed LAMP-1-GFP positive dots (spots 2-4) and a larger (approximately 0.8  $\mu\text{m}$ ), ring-shaped structure (spot 5) (supplementary movie 4). These larger-sized ring structures were regularly observed and are characteristic for LAMP-1-GFP expressing cells.

Spots 2-4 were highly motile, and moved closely around the ring-shaped spot 5, which displayed a more stationary position (table 3). In the first 30 seconds of imaging spot 4 was so close to spot 5 that they could not be discerned by fluorescence microscopy (figure 4A). Spots 2 and 3 initially moved freely, but after 60 seconds associated with spot 5 until fixation 1 minute later. Interestingly, we could still identify local spots of intense GFP signal on spot 5, indicating that spots 2 and 3 moved along with spot 5 for 60 seconds, while retaining their identities. After fixation, we found that spots 2-4 were all positive for dextran (figure 4B), while the ring-shaped spot 5 was negative.

The FIB-SEM data revealed that spots 2, 3 and 4 have a very similar morphology (table 3, figure 4C). The 3 compartments were small (diameters between 0.3 and 0.5  $\mu\text{m}$ ) and irregularly shaped. Their lumens contained both electron-lucent and electron-dense regions, the latter indicating the presence of degraded material. Furthermore, the spots contained between 12 and 32 ILVs that occupied most of the volume of the compartment, resulting in tightly filled compartments (figure 4D, 4E). Unlike the EE shown in figure 3, spots 2-4 lacked a clathrin coat. Together, these characteristics identify spots 2-4 as late endosomes. Spot 5, which in live-cell imaging showed very different dynamics as spots 2-4, appeared in the FIB-SEM as a relatively large (0.77x0.95x0.95 $\mu\text{m}$ ), irregular formed vacuole with both electron-lucent and electron-dense content, approximately 50 ILVs, and a large electron lucent region (figure 4D, middle and right panel, 4E). This morphology is characteristic for lysosomes and autolysosomes, which both can appear as large vacuoles with irregular content (table 1). Interestingly, we found late endosomal spots 2 and 3 closely opposed to the limiting membrane of (auto)lysosomal spot 5, but without membrane fusion profiles, neither between the 2 late endosomal spots 2 and 3 nor between late endosomes 2 and 3 and (auto)lysosome spot 5. This is consistent with the live-cell imaging observation that the fluorescence of spots 2

Figure 4: Live-cell CLEM of multiple organelles in one sample. (A) Stills from supplementary movie 4 showing the tracks of 4 LAMP-1-GFP spots (spot 2-5) during 114 sec imaging. Spots 2 and 3 are highly dynamic and move back and forward to spot 5. Spot 4 moves away from spot 5 to remain stationary over a period of 60 seconds. Spot 5 is mainly stationary, and shows a typical appearance of LAMP-1-GFP positive ring surrounding a dark lumen. (B) Slice from Z-stack after fixation showing the overall distribution of both LAMP-1-GFP (green) and dextran-A568 (magenta) in the cell. Inset: enlargement of the ROI displayed in A showing the presence of dextran (magenta) in spots 2-4 but not spot 5. (C) Slice from the reconstructed FIB-SEM dataset in same orientation as the LM images in A and B. The left panel shows the location of spots 2-5 (indicated by the red rectangle) present in the ROI shown in A. The middle and right panels show an enlargement of the ROI indicated with the red rectangle in the left panel. In the right panel the fluorescence labeling is overlaid on the EM structure using the same color coding as in A. (D) Representative FIB-SEM slices of spots 2-5. (E) Same images as in D colored to highlight the shape of the correlated spots. Supplementary movie 4 shows all steps from live cell imaging to the reconstruction of the 3D structure of spots 2-5 by FIB-SEM. Based on ultrastructural characteristics spot 2-4 are identified as late endosomes and spot 5 as (auto)lysosome. Table 3 shows the collection of parameters gathered on spots 2-5. Scale bars: A, B (cutouts), C (left panel): 1  $\mu\text{m}$ ; B (full image): 10  $\mu\text{m}$ ; C (middle and right panels) D, E: 500 nm.

Single organelle dynamics linked to 3D structure by correlative live-cell – 3D electron microscopy



2

and 3 shows coordinated movement with spot 5, while remaining visible as distinct entities. Combined, our data indicates that (auto)lysosomes can be contacted by multiple late endosomes, which move together over prolonged periods of time without fusion.

### Live-cell CLEM visualizing the ultrastructural context of endo-lysosomal compartments

In our next experiment, we focused on 5 highly motile LAMP-1-GFP positive spots (spots 6-10, figure 5A, 5B). These spots exhibited different movement patterns, either moving diffusely at low speed (spots 6 and 10) or showing stop-and-go movement [45,46], i.e. bursts of movement followed by a period of no or slow movement (supplementary movie 5, spots 7, 8 and 9). At 80s, Spot 7 interacted with a nearby GFP-positive spot over a period of 10 seconds, after which these two spots could no longer be discerned, indicating a fusion event. At circa 96 seconds spot 10 merged with a nearby fluorescent spot leading to an increase in local fluorescence intensity. Spot 9 became visible only later in the movie, at 64 seconds (supplementary movie 5).

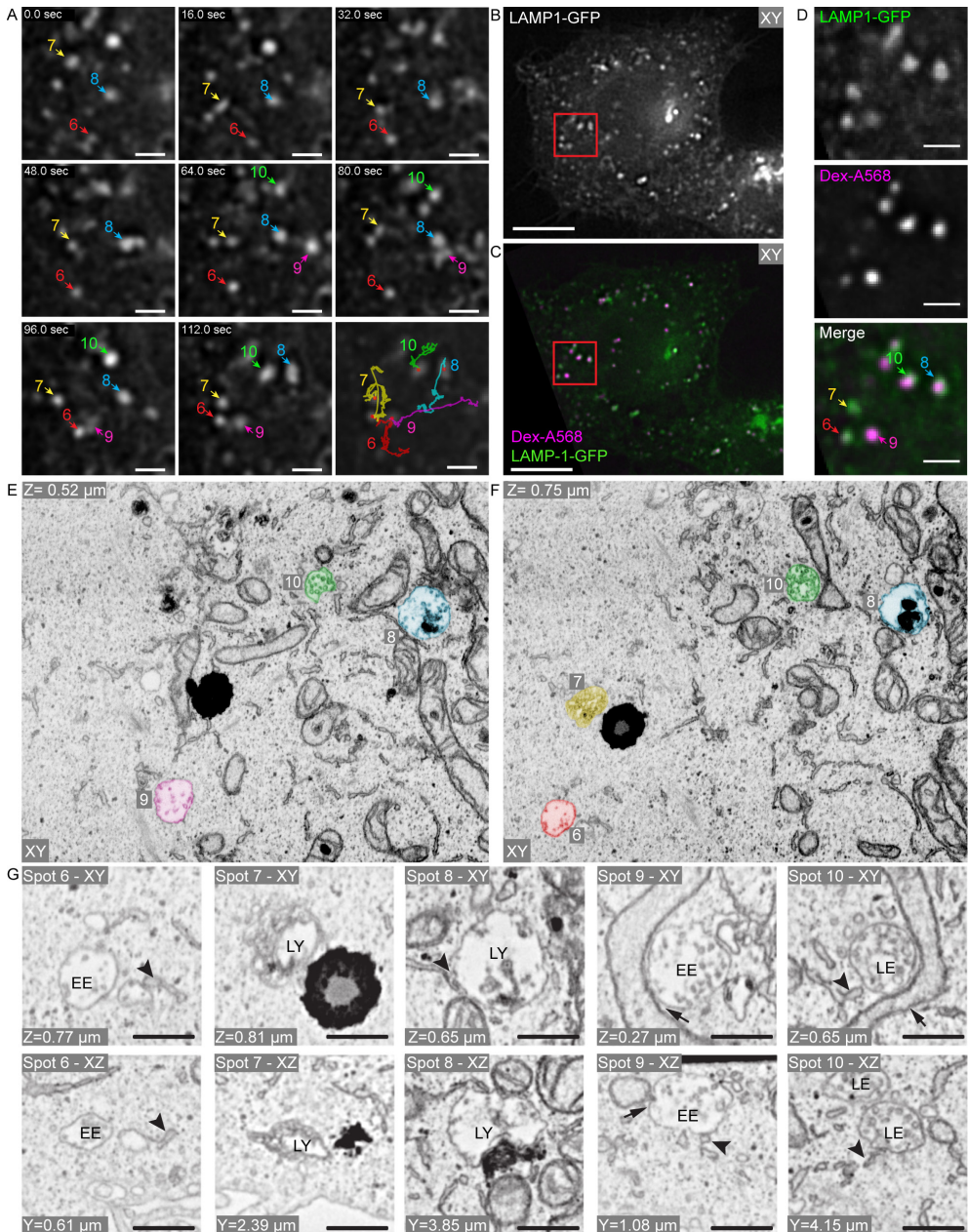
After fixation, we found that spots 8, 9, and 10 contained high levels of dextran, whereas spots 6 and 7 were only mildly positive (figure 5C, 5D). In the fluorescent Z-stack, spots 9 and 10 were present in several 200 nm slices above and below the live-cell imaging plane, suggesting a large size for these compartments, or, alternatively, the presence of multiple compartments located on top of each other. The live cell data on spots 6-10 are further summarized in table 3.

In the FIB-SEM data, we retraced spots 6-10 as morphologically diverse structures (figure 5E, 5F). Spot 6 appeared as an irregularly shaped compartment, measuring 0.55  $\mu\text{m}$  in X, 0.41  $\mu\text{m}$  in Y and 0.54  $\mu\text{m}$  in Z. The lumen of spot 6 was mostly electron-lucent with approximately 25 ILVs (figure 5G). These characteristics identify spot 6 as an early endosome (table 3). Interestingly, these data show that early endosomes do not always contain a clathrin coat during maturation. This type of information is difficult to extract from 2D EM data, since clathrin coats cover only limited areas of the endosomal vacuole, which in 2D EM may be present outside the section. The presence of a clathrin coat is probably dependent on cargo supply.

Spot 7 was identified as an irregularly shaped compartment measuring 0.55  $\mu\text{m}$  in X, 0.41  $\mu\text{m}$  in Y, and 0.54  $\mu\text{m}$  in Z, containing approximately 50 ILVs and small regions of electron-dense material, as well as a large electron-lucent region (figure 5G). Based

Figure 5: Live-cell CLEM provides context information to dynamic endo-lysosomal compartments. (A) Stills from supplementary movie 5 showing the tracks of 5 LAMP-1-GFP spots (spot 6-10) during 112 seconds of imaging. Spots 7-9 exhibit typical stop-and-go movement. The lower right panel shows the tracks of spots 6-10 overlaid over the final frame of live-cell imaging data before fixation. (B) Still from supplementary movie 5 showing the distribution of LAMP-1-GFP just prior to fixation. The ROI selected for FIB-SEM is indicated by the red square. (C) Slice from the Z-stack after fixation showing the distribution of LAMP-1-GFP (green) and dextran (magenta). The ROI selected for FIB-SEM (shown in A) is indicated by the red square. (D) Magnification of the ROI (imaged in A and indicated by the red squares in B and C) showing the distribution patterns of LAMP-1-GFP and dextran in spots 6-10. (E) Pseudocolored virtual slice of the FIB-SEM reconstruction of the ROI showing spots 8, 9 and 10 in the same orientation as the FM images in A – C. (F) Pseudocolored virtual slice of the FIB-SEM reconstruction of the ROI, located 230 nm above slice shown in E, showing spots 6, 7, 8 and 10. (G) Representative FIB-SEM slices of spots 6-10 in both XY and XZ orientation. Based on ultrastructural characteristics we made the following identifications: Spot 6 early endosome; spot 7 (auto)lysosome; spot 8 lysosome, spot 9 and 10 late endosomes. Contact sites with ER (arrowheads) and mitochondria (arrows) are indicated. Table 3 shows the collection of parameters gathered on spots 6-10. Scale bars: A, D: 2  $\mu\text{m}$ ; B, C: 10  $\mu\text{m}$ ; E, F: 1  $\mu\text{m}$ ; G: 500 nm.

Single organelle dynamics linked to 3D structure by correlative live-cell – 3D electron microscopy



2

on these typical morphological characteristics we classified spot 7 as lysosome or autolysosome. Interestingly, while its morphology is very similar to (auto)lysosomal spot 5 from figure 3, the dynamics of spot 7 are vastly different. Spot 5 was mostly immotile, whereas spot 7 traveled relatively fast over a large distance. This shows that individual lysosomes/autolysosomes can display variable dynamic behavior. Further studies using multiple marker proteins are required to define whether these dynamic differences represent different lysosomal sub-populations.

Spot 8 appeared as a spherical compartment measuring 0.83  $\mu\text{m}$  in X, 0.76  $\mu\text{m}$  in Y, 0.90  $\mu\text{m}$  in Z. The lumen of spot 8 contained an electron-lucent region with approximately 60 scattered ILVs, as well as an electron-dense region containing membrane whorls (figure 5G). This identified spot 8 as a lysosome. Spot 9 appeared as a large, spherical compartment measuring 0.71  $\mu\text{m}$  in X, 0.61  $\mu\text{m}$  in Y, 0.74  $\mu\text{m}$  in Z. Its lumen was packed with approximately 100 ILVs, of different sizes (figure 5G). This identified spot 9 as an intermediate stage between early and late endosome. Finally, at spot 10, we found 2 irregularly shaped compartments in close proximity to each other. Both compartments were similar in size (0.49  $\mu\text{m}$  in X, 0.5  $\mu\text{m}$  in Y, and 0.60  $\mu\text{m}$  in Z versus 0.69  $\mu\text{m}$  in X, 0.6  $\mu\text{m}$  in Y, and 0.49  $\mu\text{m}$  in Z) and morphology, with an electron-lucent lumen densely filled with ILVs (figure 5G). We classified both spots as late endosomes. Thus, spot 10 did not represent one compartment but consisted of two late endosomes. By live-cell imaging, we observed an increase in fluorescence of spot 10 at circa 96 seconds, indicative of a fusion event. In the FIB-SEM however, we observed no membrane fusion profile between the 2 late endosomes identified as spot 10. These data indicate that a local increase in fluorescence observed by diffraction-limited live-cell imaging can either represent a fusion event or the close proximity of two compartments, which move closely together and cannot be discerned as individual compartments.

### **Live-cell CLEM reveals multiple contact sites between LAMP-1-GFP positive compartments and ER**

An important feature of volume EM data as obtained with FIB-SEM is that the correlated fluorescent compartment is visualized in 3D, amidst other, non-fluorescent subcellular structures. In case of endo-lysosomal compartments, interactions with ER through membrane contact sites can affect their identity and mobility[47–50]. Membrane contact sites are defined as regions where organelle membranes are closely apposed (<30 nm), but not fusing[51–53]. The limited thickness of a TEM section prevents efficient studies of membrane contact sites, since only parts of an organelle are visible in a given section. Previous work has demonstrated the feasibility of FIB-SEM to resolve membrane contact sites in 3D[54]. Here, we analyzed our datasets for the presence of contact sites between correlated endo-lysosomal compartments and the ER.

Our FIB-SEM data showed that ER membranes are found in abundance within 30 nm of the limiting membrane of endo-lysosomal compartments. The ER cisternae often follow the limiting membrane of the endo-lysosomal organelles, conforming to their shapes (figure 6C, D, supplementary movie 5). In addition, we regularly found that the tip of an ER cisterna closely apposed the endo-lysosomal organelle. Remarkably, these contact sites were observed regardless of organelle type (figure 6A-D, table 3), and found associated with early endosomes, late endosomes, lysosomes/autolysosomes. The majority of the live-imaged spots had at least one contact site with the ER, while several spots showed multiple contact sites at distinct locations on the compartment (table 3, figure 6E). These data show that ER forms contact

sites occur in abundance with multiple types of endo-lysosomal compartments, and that FIB-SEM provides a powerful tool to study these interactions in 3D.

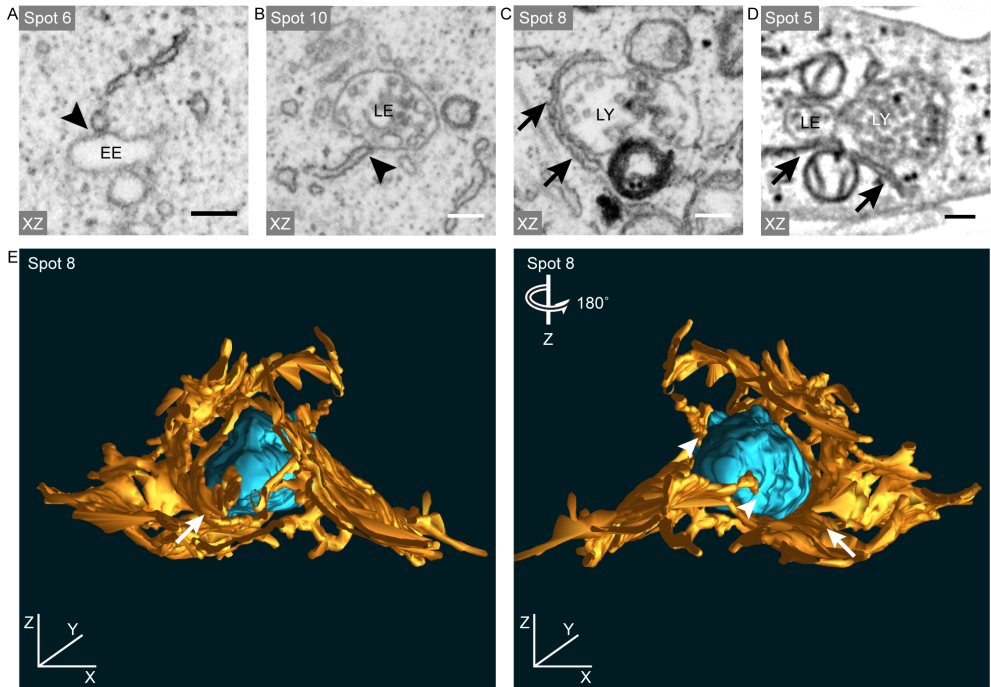


Figure 6: FIB-SEM visualizes ER contact sites with early and late endo-lysosomal compartments (A-D) FIB-SEM slices of spot 5,6, 8 and 10 (same numbering as in figure 5) in XZ direction, showing interactions with the ER. Arrowheads point to contact sites with tips of ER cisternae and arrows to contact sites with ER sheets. (A) Contact site between early endosomal spot 6 and ER. (B) Contact site between late endosomal spot 10 and ER. (C) ER cisternae covering a substantial area of the limiting membrane of lysosomal spot 8. (D) Contact site between (auto)lysosomal spot 5 and an ER sheet. (E) Segmented 3D model of lysosomal spot 8 (cyan) together with the surrounding ER (orange). The multiple contacts sites between spot 8 and ER are indicated. Supplementary movie 5 shows all steps from live cell imaging to the reconstruction of the 3D structure of spots 6-10 by FIB-SEM, and shows the interaction of spot 8 with the ER.

2

Spot #	Avg. Speed ( $\mu\text{m/s}$ )	Peak speed ( $\mu\text{m/s}$ )	Displacement in 110 seconds ( $\mu\text{m}$ )	Movement <sup>†</sup>	Fusion events at timepoint <sup>‡</sup>	Dextran	Size (by FIB-SEM) $\mu\text{m}$ X: 0.80 $\mu\text{m}$ Y: 0.80 $\mu\text{m}$ Z: 1.28	# of ILVs	Morphological hallmarks	Organelle type	ER contact sites <sup>§</sup>
1	0.2	0.739	1.815	Diffusive	-	+	X: 1.28 $\mu\text{m}$ Y: 0.80 $\mu\text{m}$ Z: 1.28	45	Irregularly shaped vacuole. Electron-lucent lumen, loosely packed ILVs. Clathrin patch on limiting membrane.	Early endosome	7
2	0.152	0.975	3.350	Stop-and-go	-	+	X: 0.38 $\mu\text{m}$ Y: 0.29 $\mu\text{m}$ Z: 0.37	32	Mostly globular vacuole with electron-lucent and electron-dense content. Densely packed ILVs.	Late endosome	2
3	0.135	1.102	3.420	Stop-and-go	-	+	X: 0.62 $\mu\text{m}$ Y: 0.43 $\mu\text{m}$ Z: 0.53	22	Rounded to irregularly shaped vacuole with electron-dense content. Densely packed ILVs.	Late endosome	4
4	0.105	0.567	2.310	Diffusive	-	+	X: 0.53 $\mu\text{m}$ Y: 0.46 $\mu\text{m}$ Z: 0.54	12	Rounded vacuole with electron-dense content. Densely packed ILVs.	Late endosome	3
5	0.128	0.73	0.489	Diffusive	-	-	X: 0.77 $\mu\text{m}$ Y: 0.95 $\mu\text{m}$ Z: 0.83	45	Irregularly shaped vacuole with heterogeneous content, with electron-dense and electron-lucent material.	(Auto) lysosome	6
6	0.185	1.334	3.34	Diffusive	-	+/-	X: 0.55 $\mu\text{m}$ Y: 0.41 $\mu\text{m}$ Z: 0.54	25	Irregularly shaped vacuole. Electron lucent lumen with loosely packed ILVs.	Early endosome	1
7	0.251	2.034	2.098	Stop-and-go	87s	+/-	X: 0.55 $\mu\text{m}$ Y: 0.41 $\mu\text{m}$ Z: 0.54	50	Irregularly shaped vacuole. Heterogeneous content containing electron-dense and electron-lucent regions.	(Auto) lysosome	0
8	0.159	1.172	3.323	Stop-and-go	-	+	X: 0.83 $\mu\text{m}$ Y: 0.76 $\mu\text{m}$ Z: 0.90	60	Irregularly shaped vacuole. Contains heterogeneous ILVs, amorphous material and electron-dense membrane whorls.	Lysosome	4
9	0.204	0.904	5.692 <sup>¶</sup>	Stop-and-go	-	+	X: 0.71 $\mu\text{m}$ Y: 0.61 $\mu\text{m}$ Z: 0.74	100	Irregularly shaped to rounded vacuole with electron-lucent lumen. Many ILVs but loosely packed.	Early/late endosome	5
10	0.197	0.69	1.977 <sup>¶</sup>	Diffusive	92.8s	+	X: 0.49 $\mu\text{m}$ Y: 0.50 $\mu\text{m}$ Z: 0.60	70	Two separate compartments without fusion profile. Both are globular vacuoles containing densely packed ILVs.	2 late endosomes	2

Table 3: Overview of dynamic and morphological characteristics of individual correlated spots.

† Movement is either scored as diffusive (random, non-directional movement) or stop-and-go (alternating periods of fast, directional movement and slow, non-directional movement)

‡ Fusion events are scored when individual LAMP-1-GFP(+) spots become indiscernible.

§ ER contact sites were scored when ER membranes were within 30 nm of limiting membrane of endo-lysosomal compartment.

¶ Spots 9 and 10 were only followed for 58 and 50 seconds respectively.

## Discussion

We present an efficient method to routinely trace individual compartments from live-cell fluorescence all the way to volume EM, a method we refer to as single organelle microscopy. The high spatio-temporal resolution of our method maximizes the number of dynamic and ultrastructural parameters that within one experiment can be integrated onto a single organelle, in 3D. The relatively high throughput of the pipeline allows for quantitative measurements on dynamic behavior and ultrastructural characteristics. Using this method, we provide the proof of principle to directly link dynamic information on the behavior of individual endo-lysosomes to their ultrastructural characteristics in 3D.

Previously, correlative live-cell imaging and volume EM approaches were mainly used to identify a rare or transient structure or event[1,2,7,20,31], without taking into account the intracellular trafficking steps leading to this event. Here we present a cohesive experimental pipeline that integrates key temporal and structural parameters, i.e. live-cell dynamics, architecture and cellular context, on a single organelle over an extended period of time. By live-cell imaging we monitor the dynamic local behavior of individual organelles during several minutes prior to fixation. This allows us to define transient interactions, movement patterns and subcellular positioning, which are important factors to determine the identity and function of endo-lysosomal compartments, and can only be studied in live cells. The resolution of EM is required to establish compartment identity, visualize fusion profiles with other compartments, show interactions with surrounding membrane and non-membrane structures, and to provide unique information on the intra-organelle membrane organization. This is illustrated by the collection of spots in table 3, which clearly shows that the presence of LAMP-1-GFP or dextran alone cannot establish organelle identity. The FIB-SEM has the resolution to capture high resolution ultrastructural information in 3D, visualizing local ultrastructural details, such as clathrin coats, membrane whorls and ILVs. Vice versa, by using live cell imaging we can select small, well-defined ROIs for FIB-SEM imaging, which ensures that the organelles of interest are embedded within the final 3D datasets. This selection of small ROIs through fluorescence combined with the precise, targeted removal of excess material using the gallium beam reduces FIB-SEM imaging and data processing time, increasing the overall throughput of the workflow. Of note, of the 10 LAMP-1-GFP spots analyzed in this paper (selected based on their visibility in the live cell movie), only three meet the morphological criteria of a lysosome. Since LAMP-1-GFP in numerous studies is referred to as an established marker for late endosomes – lysosomes[23,33,55], or even strictly lysosomes[56,57], these data illustrate that defining organelle identity by FM, using over-expressed proteins, may lead to incorrect interpretations.

By live-cell imaging we found that LAMP-1-GFP positive compartments frequently interact with each other over extended periods of time. Volume EM proved essential to interpret the nature of these interactions. For example, in figure 4 we show prolonged contact of late endosomal spots 2 and 3 with (auto)lysosomal spot 5 in live cells, but investigation by FIB-SEM showed no evidence for membrane fusion. A similar observation was made in figure 5, where we found that spot 10 increased in brightness after interaction with another GFP-positive spot, forming a larger, brightly fluorescent compartment. By FIB-SEM we found that spot 10 consisted of 2 closely associated late endosomes which were not fused. Together, our data show that endo-lysosomal compartments can move together during prolonged periods without fusion. Although we did not detect fusion of these compartments in our FIB-

SEM data, this does not exclude the possibility of exchange of material between the tracked organelles, as previous studies established a mechanism known as kiss-and-run, where endo-lysosomal organelles undergo transient fusion events, allowing the exchange of luminal content while retaining two distinct compartments[58].

In addition to visualizing the morphology of endo-lysosomal compartments, volume EM also visualizes all structures surrounding the organelles, revealing compartments not detected by fluorescence microscopy. This is shown in figure 6, where we show diverse LAMP-1-GFP positive compartments in relation to the context of LAMP-1-GFP negative structures, such as ER and mitochondria. Interactions of endo-lysosomal compartments with ER at membrane contact sites are required for a range of processes, including signaling, transport of metabolites, endo-lysosomal transport and compartment maturation[47,48,51,52,59–61]. Membrane contact sites are morphologically identified as closely apposed membranes (<30 nm), and molecularly by the presence of tethers[50,52,53], meaning EM is essential to study these domains in detail. In figure 6 we demonstrate the feasibility of using FIB-SEM to determine the level of interaction between previously live-imaged endo-lysosomal compartments and ER (table 3) in 3D, indicating volume EM provides sufficient resolution to examine the presence and structure of inter-organelle contacts.

In our studies we performed chemical fixation *in situ* by adding fixative to the imaging chamber during imaging. While chemical fixation is considered a slow process due to the limited penetration rate of glutaraldehyde and formaldehyde, we found that the relative position of compartments barely changed between the last frame of the live-cell movie and the fluorescent Z-stack recorded after fixation, indicating that chemical fixation is sufficiently fast for our application, and allowing us to link the dynamic information obtained by live-cell imaging to ultrastructure in 3D. Processing steps for EM are also known to introduce alterations in a sample, like shrinkage, which may affect the morphology of individual compartments[62–65]. Interestingly, measurements on the distance between organelles in fluorescence and FIB-SEM revealed very limited changes in the XY direction (as shown in supplementary figure 1). In Z, the distances of organelles relative to the coverslip were 300-400 nm shorter in FIB-SEM than would be expected from the FM data, which is within the axial resolution limit of FM (approximately 500 nm). For approaches that rely on serial sectioning, this could hamper the retracing of organelles between FM and EM. However, since FIB-SEM captures the full volume of the ROI rather than individual slices, this did not cause any pronounced difficulties in correlating the live-imaged compartments in Z. Thus, the collected FIB-SEM volume can rapidly be examined for the presence and relative positioning of the live-imaged organelles in the X, Y and Z-axis.

In the data presented here we use LAMP-1-GFP and dextran for fluorescent imaging, but our method can be extended all types of fluorescent probes, for example to examine the functional state of organelles. Enzyme activity, the presence of ions, and changes in pH are important determinants for endo-lysosomal function. Several fluorescent probes are available to examine these properties (LysoTracker, Magic Red Cathepsin substrates, calcium sensors), but the nature of these probes prevents imaging in fixed material, since fixation perturbs membrane integrity, inactivates enzymes and neutralizes pH or ion gradients[31,66]. With live-cell CLEM, functional information can be obtained in live cells and correlated to the underlying 3D ultrastructure. Furthermore, we can extend our method to include specialized FM approaches to study transient close-range interactions (FRET) and compartment dynamics and membrane trafficking (FRAP). Use of super-resolution techniques

would further increase the flexibility of the pipeline, providing more detailed information of subcellular structures with greater spatiotemporal resolution in live cells[67]. The increased lateral and axial resolution of super-resolution FM would provide not only more accurate fluorescence localization but would also serve to increase the registration accuracy between live imaging and volume EM.

It is becoming increasingly clear that endo-lysosomal trafficking, positioning and organelle interaction are important parameters for lysosomal maturation, membrane interactions and functioning[68,69]. Moreover, defective regulation of endosomal trafficking is seen in many neurological disorders, like Huntington's disease, Alzheimer and Charcot–Marie–Tooth type 2B[55,70,71], and subpopulations of lysosomes are linked to axon formation and cancer progression[72,73]. To be able to understand the function and regulation of these dynamic interactions it is required that ultrastructural and molecular characteristics are directly linked to parameters that can only be derived from live cells, such as organelle dynamics, positioning, enzyme activities. Since our approach integrates information on the dynamics, molecular composition and ultrastructural context of a single compartment, it is highly suited for multi-parameter examination of individual organelles, in healthy and diseased states.

In conclusion, we present a flexible platform to combine available fluorescence microscopy approaches with 3D ultrastructural visualization that reliably links organelle dynamics and ultrastructure, a method we refer to as single organelle microscopy. In addition, we provide a method that allows the selection of ROIs for efficient and targeted FIB-SEM imaging.

## Materials and methods

### Cell culture and transfection

Hela cells were cultured in a 37°C, 5% CO<sub>2</sub> incubator, in T75 culture bottles (Corning). Cells were maintained in Dulbecco's Modified Eagle's Medium (DMEM) (Gibco) supplemented with 10% fetal bovine serum (FBS), 2 mM L-glutamin, 100U/ml penicillin, 100 µg/ml streptomycin (referred to as completed DMEM). Cells were passaged when confluency reached 85-90%, and tested for mycoplasma infection every 4 weeks. Transfections were performed using Effectene transfection reagent (Qiagen) according to manufacturer's instructions.

For correlative live-cell imaging, we used 25 mm diameter photo-etched gridded coverslips (Ibidi GmbH). The coverslips were coated with two layers of carbon (total thickness 20 nm) to promote cell adhesion and improve their dissociation from Epon resin, using an Edwards 306 auto vacuum evaporator using thick carbon wire (Agar scientific, AGE428). Following carbon coating, the coverslips were heated to 120°C overnight. The sterilized coverslips were transferred to 6-well culture plates (Corning) and UV sterilized for at least 30 minutes, after which Hela cells were seeded at a density of  $1.5 \times 10^5$  cells/dish on day 1 under regular culture conditions. On day 2, cells were transiently transfected with a construct encoding LAMP1-GFP at 37°C for five hours, after which they were treated with 500 µg/ml dextran-Alexa conjugates (Alexa568 or Alexa 647, Life technologies) in complete medium supplemented with 30 mM HEPES, to mark degradative compartments. 30 minutes after dextran addition, cells were incubated at 20°C for two hours outside of an incubator to apply a Golgi exit block.

Prior to live-cell imaging, cells were washed three times with phenol-red free DMEM supplemented with 2% FBS, 2 mM L-glutamin, 100U/ml penicillin, 100 µg/ml streptomycin (referred to as live imaging medium), to remove unbound dextran-Alexa conjugates. The coverslips were mounted in a live-cell imaging holder which was filled with 1 ml live imaging medium.

### Live-cell imaging and in-situ fixation

Live imaging was performed on a Deltavision RT widefield microscope (GE Healthcare) equipped with a conditioned imaging chamber set to 37°C and 5% CO<sub>2</sub>. Time-lapse imaging was performed using a 100x/1.4 NA oil immersion objective and images were recorded on a Cascade II EM-CCD camera (Photometrics) with a gain value of 290 using the Acquire3D module in Softworx 6.5.2. An image of the GFP channel was recorded every 400 ms with an exposure time of 100ms.

Cells were stabilized in the imaging chamber for 15 minutes prior to image acquisition, to recover from the Golgi exit block. Live-cell imaging was performed to track LAMP1-GFP labeled compartments for 2 minutes, after which the cells were fixed *in situ* by addition of 1 ml of fixative containing 4% paraformaldehyde (Sigma) and 0.05% glutaraldehyde (25% solution in dH<sub>2</sub>O, Merck) in 1x PHEM (60 mM PIPES, 25 mM HEPES, 10 mM EGTA, and 2 mM MgCl<sub>2</sub>, pH=6.9) buffer to the imaging holder with the camera still active, to obtain images until the cells are fixed. After fixation a Z-stack was recorded for all fluorophores. Using the etched pattern on the coverslip, the position and orientation of the imaged cell was recorded by phase contrast at a low magnification.

### Postfixation, dehydration and resin embedding

Following primary fixation, the coverslips were transferred to 35mm dishes and

postfixed in 2.5% glutaraldehyde and 2% paraformaldehyde in 0.1M sodium cacodylate buffer (CB). Samples in fig. 2 and 3 were postfixed using 1% OsO<sub>4</sub> with 0.8% K<sub>3</sub>Fe(III)(CN)<sub>6</sub> in 0.1M CB for 1 hour on ice. Coverslips were washed 5 times in 0.1M CB, and then treated with 1% tannic acid (Mallinckrodt Pharmaceuticals) in ddH<sub>2</sub>O for 1 hour on ice. Samples were washed 5 times using ddH<sub>2</sub>O and stained using 1% uranyl acetate in ddH<sub>2</sub>O for 1 hour, in the dark at room temperature. After thorough rinsing using ddH<sub>2</sub>O, the coverslips were passed through a graded ethanol:ddH<sub>2</sub>O series for dehydration (50%, 70%, 90%, 96%, 100% for 2 x 5 minutes each, and 100% with acidified dimethoxypropane for 6 x 5 minutes). Samples were stepwise infiltrated with Epon resin (25%, 50%, 75% in ethanol for 1 hour each), followed by two infiltration steps using 100% Epon resin, first for 1h, then 16h. Final embedding of the coverslips in 100% Epon resin was done in 35mm dishes, and the resin was polymerized for 72 hours at 60°C.

For further improvement of electron contrast, the samples in figure 4 and 5 were poststained with 1% OsO<sub>4</sub> with 1.5% K<sub>4</sub>Fe(II)(CN)<sub>6</sub> in 0.065M CB for 1 hour on ice. Coverslips were washed 6 times in ddH<sub>2</sub>O, followed by treatment with 1% thiocarbonylhydrazide (Sigma) at 30°C for 15 minutes, after which the coverslips were washed 6 times in ddH<sub>2</sub>O. The coverslips were then treated with 1% OsO<sub>4</sub> in ddH<sub>2</sub>O on ice for 30 minutes followed by 6 washes in ddH<sub>2</sub>O. The samples were then treated with 2% uranyl acetate in ddH<sub>2</sub>O for 30 minutes in the dark, followed by 6 washes in ddH<sub>2</sub>O. The samples were stained using Walton's lead aspartate (pH 5.6) for 30 minutes at 60°C [74]. Samples were washed twice with ddH<sub>2</sub>O and subjected to a graded ethanol dehydration series and infiltrated with Epon resin in the way described above.

### **Resin block processing and FIB-SEM tomography**

After polymerization, excess material surrounding the carbon-coated part of the coverslip is removed using a small handsaw, resulting in a small slab of resin with the carbon-coated coverslip attached. The coverslip is removed from the resin surface by repeatedly dipping the sample in liquid nitrogen and ddH<sub>2</sub>O at RT, after which the glass was removed with a clean razor blade. The exposed surface was cleaned using ddH<sub>2</sub>O.

The resin-embedded cells are mounted on 12 mm aluminium stubs for SEM using carbon adhesive discs (Agar Scientific), and the sides of the resin block were covered with conductive carbon cement (Agar Scientific) to establish a conductive path to reduce charging effects. To further improve conductivity, the surface of the sample was coated with a 4 nm layer of Pt using a Cressington 208HR sputter coater. Samples were imaged with a Scios FIB-SEM (figures 1-4) or a Helios G3 UC FIB-SEM (figure 5) (Thermo Scientific, Eindhoven, The Netherlands) under high vacuum conditions. The grid pattern embedded in the resin surface was used to retrace the cell of interest, after which the cell contour in SEM was compared with the fluorescence Z-stack to determine the ROI. Using the FIB, a 500 nm thick layer of Pt was deposited over the ROI, at an acceleration voltage of 30kV and a current of 1 nA. Trenches flanking the ROI were milled at an acceleration voltage of 30kV, using a high current (5-7 nA), followed by a staircase pattern in front of the ROI to expose the imaging surface. Fine polishing was done with the ion beam set to 30 kV with a beam current of 0.5 nA, resulting in a smooth imaging surface. Serial imaging was then performed using the in-column backscattered electron detector (imaging settings per experiment are detailed in supplementary table 1).



## Image processing

Wide-field time-lapse series and Z-stacks were deconvolved using Softworx 6.5.2 (GE Healthcare). Manual tracking and annotation of organelles was performed using the mTrackJ plugin for Fiji<sup>75</sup>.

FIB-SEM images were imported as image stack in Fiji ([www.fiji.sc](http://www.fiji.sc))[76] and aligned to each other using TrakEM2[77]. The aligned stack was rotated 90° along its X axis to visualize the FIB-SEM data in the same orientation as the fluorescence Z-stack. The FIB-SEM data was manually correlated with the fluorescence data by using endo-lysosomal compartments as landmarks. This pattern of landmarks and the distances between them was used to register the positions of organelles between FM and EM images. Aligned stacks were also exported and converted to the MRC file format for use in IMOD[78] to perform manual segmentation, 3D modeling and movie generation. Movies were prepared and generated using Adobe Premiere Pro CC 2017 (Adobe Systems) and saved as .MP4 files with h.264 compression.

## Acknowledgements

We acknowledge C. de Heus and G. Posthuma for assistance with cell culture and specimen preparation and C.T.H. Schneijdenberg and S. Matveev for assistance with the FIB-SEM systems. We thank Gerhard Blab for the fruitful discussions and input on correlative strategy.

## Funding

This work was supported by funding in the NWO-TTW perspective program Microscopy Valley (Project 12715), granted to Hans Gerritsen and Judith Klumperman.

## Author contributions

J. Klumperman, J. Fermie, and N. Liv designed the study, analyzed the data and wrote the manuscript. J. Fermie carried out live-cell imaging and FIB-SEM data collection. C. ten Brink provided technical support for live-cell imaging and fluorescence microscopy. E.G. van Donselaar and W.H. Müller optimized and performed sample preparation. N.L. Schieber and Y. Schwab provided support for sample preparation, image processing and data analysis. H.C. Gerritsen, W.H. Müller, and Y. Schwab reviewed the manuscript.

## References

1. Karreman MA, Mercier L, Schieber NL, et al. Fast and precise targeting of single tumor cells in vivo by multimodal correlative microscopy. *J Cell Sci.* 2016;129(2):444-456.
2. Correlative Light and Volume Electron Microscopy: Using Focused Ion Beam Scanning Electron Microscopy to Image Transient Events in Model Organisms. *Methods Cell Biol.* 2012;111:357-382.
3. Rijnsoever C Van, Oorschot V, Klumperman J. Correlative light-electron microscopy (CLEM) combining live-cell imaging and immunolabeling of ultrathin cryosections. *Nat Methods.* 2008;5(11):973-980.
4. Polishchuk RS, Polishchuk E V, Marra P, et al. Correlative light-electron microscopy reveals the tubular-saccular ultrastructure of carriers operating between Golgi apparatus and plasma membrane. *J Cell Biol.* 2000;148(1):45-58.
5. Jun S, Ke D, Debiec K, et al. Direct visualization of HIV-1 with correlative live-cell microscopy and cryo-electron tomography. *Structure.* 2011;19(11):1573-1581.
6. Verkade P. Moving EM: The Rapid Transfer System as a new tool for correlative light and electron microscopy and high throughput for high-pressure freezing. *J Microsc.* 2008;230(2):317-328.
7. Olmos Y, Hodgson L, Mantell J, Verkade P, Carlton JG. ESCRT-III controls nuclear envelope reformation. *Nature.* 2015;522(7555):236-239.
8. Heiligenstein X, Heiligenstein J, Delevoye C, et al. The CryoCapsule: Simplifying correlative light to electron microscopy. *Traffic.* 2014;15(6):700-716.

9. Spiegelhalter C, Tosch V, Hentsch D, et al. From dynamic live cell imaging to 3D ultrastructure: novel integrated methods for high pressure freezing and correlative light-electron microscopy. *PLoS One*. 2010;5(2):e9014.
10. Gaudin R, Berre S, Cunha de Alencar B, et al. Dynamics of HIV-Containing Compartments in Macrophages Reveals Sequestration of Virions and Transient Surface Connections. *PLoS One*. 2013;8(7).
11. Polishchuk RS, San Pietro E, Di Pentima A, Teté S, Bonifacino JS. Ultrastructure of long-range transport carriers moving from the trans-Golgi network to peripheral endosomes. *Traffic*. 2006;7(8):1092-1103.
12. Titze B, Genoud C. Volume scanning electron microscopy for imaging biological ultrastructure. *Biol Cell*. 2016;108(11):307-323.
13. Horstmann H, Körber C, Sätzler K, Aydin D, Kuner T. Serial section scanning electron microscopy (S3EM) on silicon wafers for ultra-structural volume imaging of cells and tissues. *PLoS One*. 2012;7(4):1-8.
14. Denk W, Horstmann H. Serial block-face scanning electron microscopy to reconstruct three-dimensional tissue nanostructure. *PLoS Biol*. 2004;2(11).
15. Heymann JAW, Hayles M, Gestmann I, Giannuzzi LA, Lich B, Subramaniam S. Site-specific 3D imaging of cells and tissues with a dual beam microscope. *J Struct Biol*. 2006;155(1):63-73.
16. Kizilyaprak C, Bittermann AG, Daraspe J, Humbel BM. FIB-SEM Tomography in Biology. Kuo J, ed. 2014;1117:541-558.
17. Peddie CJ, Collinson LM. Exploring the third dimension: volume electron microscopy comes of age. *Micron*. 2014;61:9-19.
18. Xu CS, Hayworth KJ, Lu Z, et al. Enhanced FIB-SEM systems for large-volume 3D imaging. *Elife*. 2017;6:1-36.
19. Narayan K, Danielson CM, Lagarec K, et al. Multi-resolution correlative focused ion beam scanning electron microscopy: Applications to cell biology. *J Struct Biol*. 2014;185(3):278-284.
20. Murphy GE, Narayan K, Lowekamp BC, et al. Correlative 3D imaging of whole mammalian cells with light and electron microscopy. *J Struct Biol*. 2011;176(3):268-278.
21. Russell MRG, Lerner TR, Burden JJ, et al. 3D correlative light and electron microscopy of cultured cells using serial blockface scanning electron microscopy. *J Cell Sci* 2017;130(1):278-291
22. Settembre C, Fraldi A, Medina DL, Ballabio A. Signals from the lysosome: a control centre for cellular clearance and energy metabolism. *Nat Rev Mol Cell Biol*. 2013;14(5):283-296.
23. Huotari J, Helenius A. Endosome maturation. *EMBO J*. 2011;30(17):3481-3500.
24. Saftig P, Klumperman J. Lysosome biogenesis and lysosomal membrane proteins: trafficking meets function. *Nat Rev Mol Cell Biol*. 2009;10(9):623-635.
25. Klumperman J, Raposo G. The complex ultrastructure of the endolysosomal system. *Cold Spring Harb Perspect Biol*. 2014;6(10):1-22.
26. Reggiori, F. Klumperman, J. (2016) Lysosome Biogenesis and Autophagy. In: F. R. Maxfield, J. M. Willard and S. Lu (Eds), *Lysosomes: Biology, Diseases, and Therapeutics* (pp. 7-31). USA: John Wiley & Sons, Inc.
27. Mari M, Bujny M V., Zeuschner D, et al. SNX1 defines an early endosomal recycling exit for sortilin and mannose 6-phosphate receptors. *Traffic*. 2008;9(3):380-393.
28. Pols MS, Ten Brink C, Gosavi P, Oorschot V, Klumperman J. The HOPS Proteins hVps41 and hVps39 Are Required for Homotypic and Heterotypic Late Endosome Fusion. *Traffic*. 2013;14(2):219-232.
29. Murk JLAN, Humbel BM, Ziese U, et al. Endosomal compartmentalization in three dimensions: implications for membrane fusion. *Proc Natl Acad Sci U S A*. 2003;100(23):13332-13337.
30. Van Meel E, Klumperman J. Imaging and imagination: Understanding the endo-lysosomal system. *Histochem Cell Biol*. 2008;129(3):253-266.
31. Bright NA, Davis LJ, Luzio JP. Endolysosomes Are the Principal Intracellular Sites of Acid Hydrolase Activity. *Curr Biol*. 2016;26(17):2233-2245.
32. Pu J, Guardia CM, Keren-Kaplan T, Bonifacino JS. Mechanisms and functions of lysosome positioning. *J Cell Sci*. 2016;129(23):4329-4339.
33. Falcón-Pérez JM, Nazarian R, Sabatti C, Dell'Angelica EC. Distribution and dynamics of Lamp1-containing endocytic organelles in fibroblasts deficient in BLOC-3. *J Cell Sci*. 2005;118(Pt 22):5243-5255.
34. Peden AA, Oorschot V, Hesser BA, Austin CD, Scheller RH, Klumperman J. Localization of the AP-3 adaptor complex defines a novel endosomal exit site for lysosomal membrane proteins. *J Cell Biol*. 2004;164(7):1065-1076.
35. Pols MS, van Meel E, Oorschot V, et al. hVps41 and VAMP7 function in direct TGN to late endosome transport of lysosomal membrane proteins. *Nat Commun*. 2013;4(May 2012):1361.
36. Makarow M. Endocytosis in *Saccharomyces cerevisiae*: internalization of alpha-amylase and fluorescent dextran into cells. *EMBO J*. 1985;4(7):1861-1866.
37. Griffiths G, Pfeiffer S, Simons K, Matlin K. Exit of newly synthesized membrane proteins from the trans cisterna of the Golgi complex to the plasma membrane. *J Cell Biol*. 1985;101(3):949-964.

38. Friedman PL, Ellisman MH. Enhanced visualization of peripheral nerve and sensory receptors in the scanning electron microscope using cryofracture and osmium-thiocarbohydrazide-osmium impregnation. *J Neurocytol.* 1981;10(1):111-131.
39. Willingham C, Rutherford A. Use of Osmium-Thiocarbohydrazide-Osmium and Ferrocyanide-reduced Methods Contrast and Preservation in to. *J Histochem Cytochem.* 1984;32(4):455-460.
40. Sachse M, Urbé S, Oorschot V, Strous GJ, Klumperman J. Bilayered clathrin coats on endosomal vacuoles are involved in protein sorting toward lysosomes. *Mol Biol Cell.* 2002;13(4):1313-1328.
41. Raiborg C, Malerød L, Pedersen NM, Stenmark H. Differential functions of Hrs and ESCRT proteins in endocytic membrane trafficking. *Exp Cell Res.* 2008;314(4):801-813.
42. Piper RC, Katzmann DJ. Biogenesis and Function of Multivesicular Bodies. *Annu Rev Cell Dev Biol.* 2007;23(1):519-547.
43. Sachse M, Ramm G, Strous G, Klumperman J. Endosomes: multipurpose designs for integrating housekeeping and specialized tasks. *Histochem Cell Biol.* 2002;117(2):91-104.
44. Janvier K, Bonifacino JS. Role of the endocytic machinery in the sorting of lysosome-associated membrane proteins. *Mol Biol Cell.* 2005;16(9):4231-4242.
45. Jordens J, Fernandez-Borja M, Marsman M, et al. The Rab7 effector protein RILP controls lysosomal transport by inducing the recruitment of dynein-dynactin motors. *Curr Biol.* 2001;11(21):1680-1685.
46. Flores-Rodriguez N, Rogers SS, Kenwright DA, Waigh TA, Woodman PG, Allan VJ. Roles of dynein and dynactin in early endosome dynamics revealed using automated tracking and global analysis. *PLoS One.* 2011;6(9).
47. Wijdeven RH, Janssen H, Nahidiazar L, et al. Cholesterol and ORP1L-mediated ER contact sites control autophagosome transport and fusion with the endocytic pathway. *Nat Commun.* 2016;7(May):11808.
48. Raiborg C, Wenzel EM, Stenmark H. ER-endosome contact sites: molecular compositions and functions. *EMBO J.* 2015;34(1848):1848-1858.
49. Friedman JR, Dibenedetto JR, West M, Rowland AA, Voeltz GK. Endoplasmic reticulum-endosome contact increases as endosomes traffic and mature. *Mol Biol Cell.* 2013;24(7):1030-1040.
50. Alpy F, Rousseau A, Schwab Y, et al. STARD3 or STARD3NL and VAP form a novel molecular tether between late endosomes and the ER. *J Cell Sci.* 2013;126(23):5500-5512.
51. Gatta AT, Levine TP. Piecing Together the Patchwork of Contact Sites. *Trends Cell Biol.* 2016;20(8):359-366.
52. Prinz WA. Bridging the gap: Membrane contact sites in signaling, metabolism, and organelle dynamics. *J Cell Biol.* 2014;205(6):759-769.
53. Phillips MJ, Voeltz GK. Structure and function of ER membrane contact sites with other organelles. *Nat Rev Mol Cell Biol.* 2015;17(2):69-82.
54. Wu Y, Whiteus C, Xu CS, et al. Contacts between the endoplasmic reticulum and other membranes in neurons. *Proc Natl Acad Sci.* 2017;114(24):E4859-E4867.
55. Gowrishankar S, Yuan P, Wu Y, et al. Massive accumulation of luminal protease-deficient axonal lysosomes at Alzheimer's disease amyloid plaques. *Proc Natl Acad Sci.* 2015;112(28):E3699-E3708.
56. Sardiello M, Palmieri M, di Ronza A, et al. A gene network regulating lysosomal biogenesis and function. *Science.* 2009;325(5939):473-477.
57. Kimura S, Noda T, Yoshimori T. Dissection of the Autophagosome Maturation Process by a Novel Reporter Protein, Tandem Fluorescent-Tagged LC3. *Autophagy.* 2007;3(5):452-460.
58. Bright NA, Gratian MJ, Luzio JP. Endocytic Delivery to Lysosomes Mediated by Concurrent Fusion and Kissing Events in Living Cells. *Curr Biol.* 2005;15(4):360-365.
59. Jongsma MLM, Berlin I, Wijdeven RHM, et al. An ER-Associated Pathway Defines Endosomal Architecture for Controlled Cargo Transport. *Cell.* 2016;166(1):152-166.
60. Rowland AA, Chitwood PJ, Phillips MJ, Voeltz GK. ER Contact Sites Define the Position and Timing of Endosome Fission. *Cell.* 2014;159(5):1027-1041.
61. Eden ER, White IJ, Tsapara A, Futter CE. Membrane contacts between endosomes and ER provide sites for PTP1B-epidermal growth factor receptor interaction. *Nat Cell Biol.* 2010;12(3):267-272.
62. Hiroshi K. A Study of Cellular Swelling and Shrinkage during Fixation, Dehydration and Embedding in Various Standard Media. *J Electron Microscop (Tokyo).* 1962;11(3):135-138.
63. Jensen C, Bajer A. Effects of dehydration on the microtubules of the mitotic spindle. Studies in vitro and with the electron microscope. *J Ultrastruct Res.* 1969;26(5):367-386.
64. Weibel ER, Knight BW. A morphometric study on the thickness of the pulmonary air-blood barrier. *J Cell Biol.* 1964;21(3):367-396.
65. Murk JLAN, Posthuma G, Koster AJ, et al. Influence of aldehyde fixation on the morphology of endosomes and lysosomes: Quantitative analysis and electron tomography. *J Microsc.* 2003;212(1):81-90.
66. Penttilä A, Kalimo H, Trump BF. Influence of glutaraldehyde and/or osmium tetroxide on cell volume, ion content, mechanical stability, and membrane permeability of Erlich ascites tumor cells. *J Cell Biol.*

- 1974;63(1).
67. Nixon-Abell J, Obara CJ, Weigel A V, et al. Increased spatiotemporal resolution reveals highly dynamic dense tubular matrices in the peripheral ER. *Science* (80- ). 2016;354(6311):aaf3928-aaf3928.
  68. van Bergeijk P, Hoogenraad CC, Kapitein LC. Right Time, Right Place: Probing the Functions of Organelle Positioning. *Trends Cell Biol.* 2016;26(2):121-134.
  69. Korolchuk VI, Saiki S, Lichtenberg M, et al. Lysosomal positioning coordinates cellular nutrient responses. *Nat Cell Biol.* 2011;13(4):453-460.
  70. Pal A, Severin F, Hoepfner S, Zerial M. Regulation of Endosome Dynamics by Rab5 and Huntingtin-HAP40 Effector Complex in Physiological versus Pathological Conditions. *Methods Enzymol.* 2008;438(7):239-257.
  71. Verhoeven K, De Jonghe P, Coen K, et al. Mutations in the small GTP-ase late endosomal protein RAB7 cause Charcot-Marie-Tooth type 2B neuropathy. *Am J Hum Genet.* 2003;72(3):722-727.
  72. Hämälistö S, Jäättelä M. Lysosomes in cancer - living on the edge (of the cell). *Curr Opin Cell Biol.* 2016;39:69-76.
  73. Mohamed MM, Sloane BF. Cysteine cathepsins: multifunctional enzymes in cancer. *Nat Rev Cancer.* 2006;6(10):764-775.
  74. Walton J. Lead an en Bloc Contrast Stain Particularly Ultrastructural Enzymology ' Useful for. *J Histochem Cytochem.* 1979;27(10):1337-1342.
  75. Meijering E, Dzyubachyk O, Smal I. Methods for cell and particle tracking. *Methods Enzymol.* 2012;504:183-200.
  76. Schindelin J, Arganda-Carreras I, Frise E, et al. Fiji: an open-source platform for biological-image analysis. *Nat Methods.* 2012;9(7):676-682.
  77. Cardona A, Saalfeld S, Schindelin J, et al. TrakEM2 software for neural circuit reconstruction. *PLoS One.* 2012;7(6).
  78. Kremer JR, Mastronarde DN, McIntosh JR. Computer visualization of three-dimensional image data using IMOD. *J Struct Biol.* 1996;116(1):71-76.
  79. Futter CE, Gibson A, Allchin EH, et al. In polarized MDCK cells basolateral vesicles arise from clathrin- $\gamma$ -adaptin-coated domains on endosomal tubules. *J Cell Biol.* 1998;141(3):611-623.
  80. Stoorvogel W, Oorschot V, Geuze HJ. A novel class of clathrin-coated vesicles budding from endosomes. *J Cell Biol.* 1996;132(1-2):21-33.
  81. Raiborg C, Grønvdal Bache K, Mehlum A, Stang E, Stenmark H. Hrs recruits clathrin to early endosomes. *EMBO J.* 2001;20(17):5008-5021.
  82. Klumperman J, Hille A, Veenendaal T, et al. Differences in the endosomal distributions of the two mannose 6-phosphate receptors. *J Cell Biol.* 1993;121(5):997-1010.
  83. Yamashiro DJ, Tycko B, Fluss SR, Maxfield FR. Segregation of transferrin to a mildly acidic (pH 6.5) para-golgi compartment in the recycling pathway. *Cell.* 1984;37(July):789-800.
  84. Hopkins CR, Trowbridge IS. Internalization and processing of transferrin and the transferrin receptor in human carcinoma A431 cells. *J Cell Biol.* 1983;97(2).
  85. Willingham MC, Hanover JA, Dickson RB, Pastan I. Morphologic characterization of the pathway of transferrin endocytosis and recycling in human KB cells. *Proc Natl Acad Sci U S A.* 1984;81(1):175-179.
  86. Futter CE, Pearse A, Hewlett LJ, Hopkins CR. Multivesicular endosomes containing internalized EGF-EGF receptor complexes mature and then fuse directly with lysosomes. *J Cell Biol.* 1996;132(6).
  87. van Deurs B, Holm PK, Kayser L, Sandvig K, Hansen SH. Multivesicular bodies in Hep-2 cells are maturing endosomes. *Eur J Cell Biol.* 1993;61(2):208-224.
  88. de Wit H, Lichtenstein Y, Geuze HJ, Kelly RB, van der Sluijs P, Klumperman J. Synaptic vesicles form by budding from tubular extensions of sorting endosomes in PC12 cells. *Mol Biol Cell.* 1999;10(12):4163-4176.
  89. Murk JLAN, Posthuma G, Koster AJ, et al. Influence of aldehyde fixation on the morphology of endosomes and lysosomes: quantitative analysis and electron tomography. *J Microsc.* 2003;212(1):81-90.
  90. Griffiths G, Hoflack B, Simons K, Mellman I, Kornfeld S. The mannose 6-phosphate receptor and the biogenesis of lysosomes. *Cell.* 1988;52(3):329-341.
  91. Murk JLAN, Lebbink MN, Humbel BM, et al. 3-D Structure of Multilaminar Lysosomes in Antigen Presenting Cells Reveals Trapping of MHC II on the Internal Membranes. *Traffic.* 2004;5(12):936-945.
  92. Eskelinen E-L. Fine Structure of the Autophagosome. *Methods Mol Biol.* 2008;445:11-28
  93. Eskelinen E-L. Maturation of Autophagic Vacuoles in Mammalian Cells. *Autophagy.* 2005;1(1):1-10.
  94. Dunn WA. Studies on the mechanisms of autophagy: formation of the vacuole. *J Cell Biol.* 1990;110(June):1923-1933.
  95. Liou W, Geuze HJ, Slot JW. Improving structural integrity of cryosections for immunogold labeling. *Histochem Cell Biol.* 1996;106(1):41-58.

## Supplementary material

**Supplementary movies are part of the published article, and accessible through Traffic: <https://onlinelibrary.wiley.com/doi/10.1111/tra.12557>**

Supplementary movie 2:

Epifluorescence time-lapse movie of a region of a HeLa cell shown in figure 3, transfected with LAMP-1-GFP and treated with dextran-Alexa647, showing the dynamic nature of spot 1. Images were captured in the GFP channel for a period of 2 minutes at a rate of 0.45s/frame. Images were deconvolved using Softworx 6.5.2 and manually traced using MTrackJ (colored traces). The movie is played back at a rate of 12 frames per second (5.4x real time). Scalebar: 2  $\mu$ m.

Supplementary movie 3:

FIB-SEM slices in XZ orientation and segmentation of part of the HeLa cell previously live imaged in movie 2 and figure 3. Segmentation of spot 1 shows its limiting membrane (green), intraluminal vesicles (purple) and bilayered clathrin coat (cyan). Images were captured at a lateral pixel size of 6 nm and 10 nm slice thickness, using the in-lens backscattered electron detector with inverted contrast, and manually segmented in IMOD 4.9. The dataset shown is 11  $\mu$ m wide.

Supplementary movie 4:

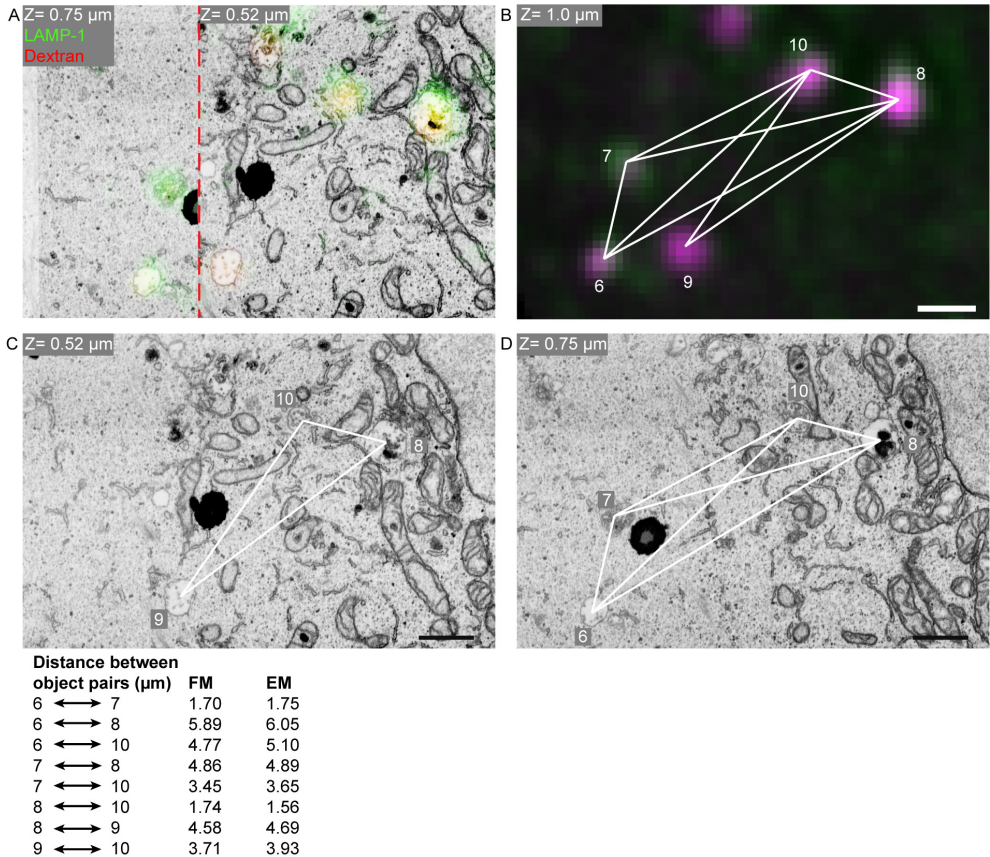
Combined epifluorescence time-lapse movie and FIB-SEM reconstruction of the same ROI as shown in figure 4, showing a region of a HeLa cell transfected with LAMP-1-GFP and treated with dextran-Alexa568. The fluorescence section shows a time-lapse recording of spots 2-5, showing their dynamic nature, followed by a slice from the Z-stack of the same, fixed cell showing the presence of dextran. The subsequent FIB-SEM reconstruction shows the morphology and position of the correlated LAMP-1-GFP positive compartments and their surrounding organelles. Live-cell images were captured in the GFP channel for a period of 2 minutes at a rate of 0.4s/frame. Images were deconvolved using Softworx 6.5.2 and manually traced using MTrackJ (colored traces). Live-cell data is played back at a rate of 12 frames per second (4.8x real time). 3D EM reconstruction and segmentation was performed using IMOD 4.9. Scalebar: 2  $\mu$ m.

Supplementary movie 5:

Combined epifluorescence time-lapse movie and FIB-SEM reconstruction of the ROI examined in figure 5, showing a region of a HeLa cell transfected with LAMP-1-GFP and treated with dextran-Alexa568. The fluorescence data shows the dynamic behavior of spots 6-10, as well as the presence of dextran in the same ROI. The FIB-SEM reconstruction shows correlation of FM data to the volume EM data, as well as ER in close proximity to spot 8. Images were captured in the GFP channel for a period of 2 minutes at a rate of 0.4s/frame. Images were deconvolved using Softworx 6.5.2 and manually traced using MTrackJ (colored traces). The movie is played back at a rate of 15 frames per second (6x real time). 3D EM reconstruction and segmentation was performed using IMOD 4.9. Scalebar: 2  $\mu$ m.

	<b>Figure 3</b>	<b>Figure 4</b>	<b>Figure 5</b>
Microscope	FEI Scios	FEI Scios	FEI Helios G3 UC
Acceleration voltage (kV)	2	2	2
Beam current (nA)	0.2	0.2	0.2
Pixel dwell time ( $\mu$ s)	15	10	10
Lateral pixel size (nm)	6	5	5
Slice thickness (nm)	10	10	5
Slices	1065	1120	1176
Volume of dataset (xyz $\mu$ m)	14.8 x 4.6 x 10.6	17.7 x 5.9 x 11.2	15.4 x 4.2 x 5.8

Supplementary table 1: Image acquisition parameters of 3D datasets

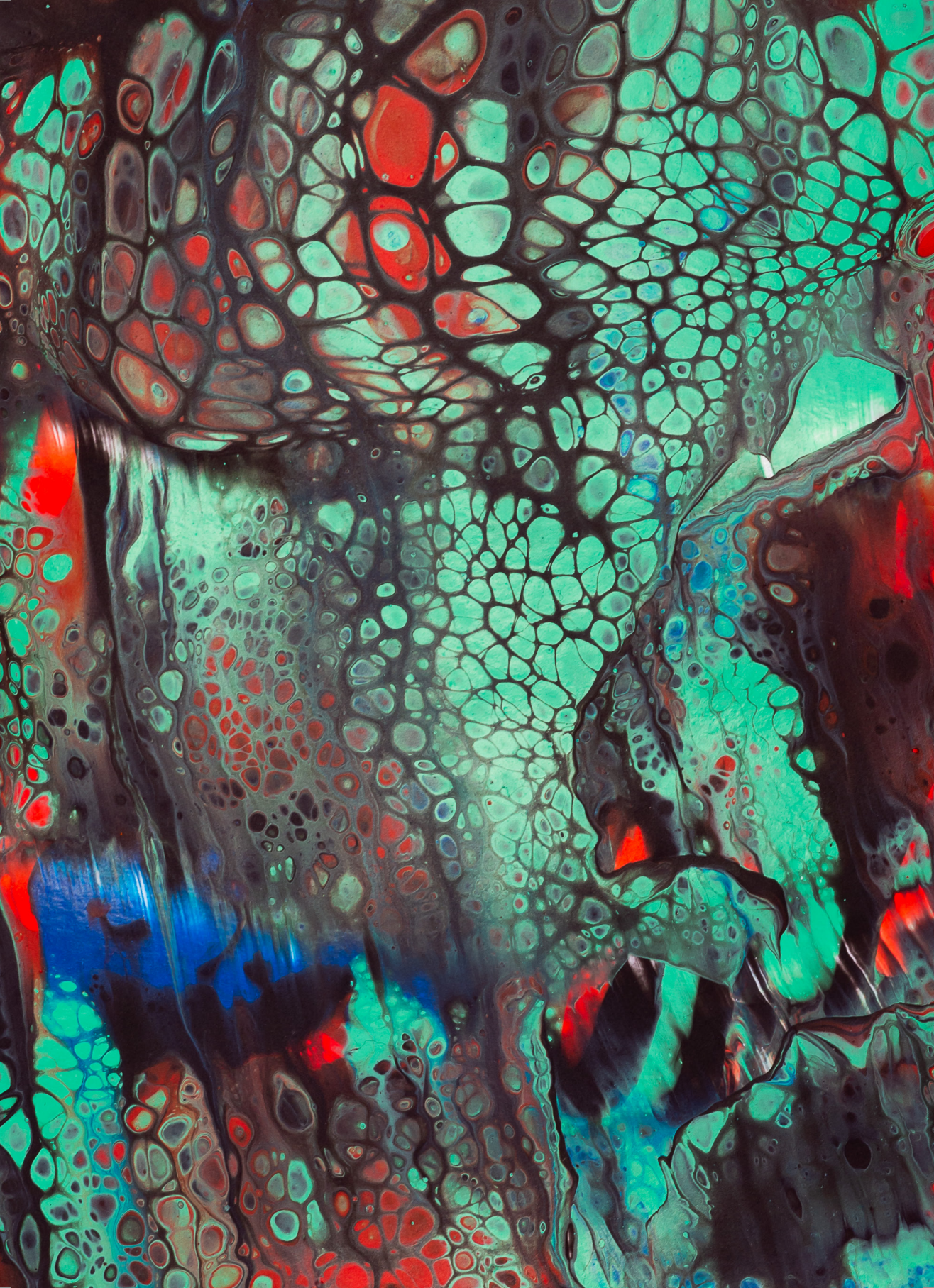


Supplementary figure 1:

Representation of correlation procedure. The live-cell imaged spots of figure 5 are used to demonstrate registration of FM and EM data in 3D. (A) Slice from Z-stack showing the previously live-imaged organelles. The distances between individual spots are measured to form a pattern of landmarks. (B, C) Slices from the FIB-SEM data corresponding to the fluorescence ROI shown in S1A. The FIB-SEM volume is examined to define the Z planes in which the locations of the organelles most closely match the landmark pattern defined in the fluorescent data. Upon retrieval of organelles of interest, the distances between organelles are measured in the FIB-SEM data, to confirm correct registration of datasets. (D) Overlay of LAMP-1-GFP and dextran fluorescence over matching FIB-SEM slices. The image is a composite of two different virtual FIB-SEM slices (marked by dotted line) to be able to visualize all organelles in a single image.

Single organelle dynamics linked to 3D structure by correlative live-cell – 3D electron microscopy

2



# Functional characterization of endo-lysosomal compartments by correlative light electron microscopy

---

## Chapter 3

---

Job Fermie<sup>1,2</sup>, Nalan Liv<sup>1</sup>, Reini van der Welle<sup>1</sup>, Corlinda ten Brink<sup>1</sup>, Cilia de Heus<sup>1</sup>, Wally Müller<sup>3</sup>, Hans Gerritsen<sup>2</sup>, Judith Klumperman<sup>1</sup>

1. Section Cell Biology, Center for Molecular Medicine, University Medical Center Utrecht, Utrecht University, Heidelberglaan 100, 3584CX Utrecht, The Netherlands
2. Section Molecular Biophysics, Debye Institute for Nanomaterials Science, Utrecht University, 3508 TA Utrecht, Netherlands.
3. Section Cryo-EM, Department of Chemistry, Utrecht University, Padualaan 8, 3584 CH Utrecht, The Netherlands

Manuscript in preparation

## Abstract

Fluorescent biosensors are valuable tools to monitor protein activities and the functional state of organelles in live cells. However, their information is limited in resolution and lacks ultrastructural context information. Protein activities are confined to organelle zones with a distinct membrane morphology, which can only be seen by electron microscopy (EM). EM, however, intrinsically lacks information on protein activities. The lack of methods to integrate these two imaging modalities has hampered understanding the functional organization of organelles. In this chapter we introduce 'functional correlative microscopy' (functional CLEM) to directly infer functional information from live cells to EM with nanometer resolution. We label live cells with fluorescent biosensors after which they are processed for EM using focused ion beam scanning electron microscopy (FIB-SEM) or electron tomography (ET). By high precision correlation we correlate within a single dataset hundreds of fluorescent spots enabling quantitative analysis of the data. We employ our method to monitor essential functional parameters of late endo-lysosomal compartments, i.e. pH, calcium, enzyme activities and cholesterol content. Our data reveal a steep functional difference in enzyme activity between late endosomes and lysosomes and unexpectedly high calcium levels in late endosomes. In contrast to previous studies most lysosomes contain active cathepsins. The functional distribution of cathepsins is preserved after a block in fusion by knockout of HOPS component VPS41. The presented CLEM workflows are compatible with of a large repertoire of probes and pave the way for large scale functional studies of all types of cellular structures.

## Introduction

The function of intracellular organelles is intrinsically determined by their structure, since specific activities are carried out in restricted membrane subdomains or organelle zones[1]. Understanding these structure-function relationships requires an integrated approach in which the spatio-temporal localization and activation of molecules is directly linked to sub-organelle membrane organization. In the last century new techniques in light microscopy (LM) and electron microscopy (EM) have led to a choice of imaging techniques that target specific molecular, functional or ultrastructural parameters. However, no microscope can yet provide a complete read-out of all parameters simultaneously. Our current understanding of the fundamental processes of life is therefore largely based on averages of dynamic, functional data from LM studies and averages of ultrastructural data from EM studies. The links between these imaging modalities are mostly indirect, which causes a major gap in our knowledge on the functional organization of individual organelles. In our group we develop Correlative Light and Electron Microscopy (CLEM) techniques that blend fluorescence microscopy (FM) and EM readouts[2]. By combining FM and EM on the same sample a novel, multiparameter imaging tool is created in which function and form are integrated at the resolution level of single organelles. Here we apply CLEM to image functional probes by FM in live or fixed cells and convert these data to EM.

We apply our method to the endo-lysosomal system, a dynamic network of interacting compartments with defined roles in protein processing. Lysosomes are the major degradative compartments of the cell with a key role in nutrient sensing and transcriptional regulation[3,4]. The biogenesis of lysosomes involves multiple fusion and fission events between biosynthetic carriers, early and late endosomes, lysosomes and autophagosomes. Fusion of late endosomes with pre-existing

lysosomes results in the formation of endolysosomal hybrid compartments from which a new pool of lysosomes can reform[5]. Functionally, the distinct endo-lysosomal compartments are determined by multiple molecular parameters, such as the presence of active degradative proteases, calcium content and an acidic pH[6]. A low pH (4,5 – 5.0) ensures optimal activation of the more than 50 lysosomal hydrolases involved in lysosomal degradation. Moreover, progression from early endosomes to lysosomes requires microtubule dependent transport from the cell periphery to the Golgi region and interactions with other membrane systems, such as the endoplasmic reticulum[6–10]. A full understanding of endo-lysosomal compartments can therefore only be obtained by an integrated understanding of their molecular composition, functional status, dynamics, position and subcellular context.

Currently, CLEM is mostly used to rapidly screen samples to select regions of interest (ROIs) for high-resolution EM examination. However, with the increase in accuracy of correlation exciting new applications come into reach using CLEM to transfer fluorescent information directly to EM with nanometer resolution[11]. Of particular interest are functional probes or biosensors, which monitor functional changes or detect biomarkers in live cells. Biosensors are available for a range of endo-lysosomal processes, including pH[12], lysosomal enzyme activity[13–16], reactive oxygen species[17], and presence of metal ions[18–22]. However, they have seen limited use as CLEM probes[16,23–25] due to the lack of accurate correlation methods[26]. Here we present two complementary correlative workflows to simultaneously correlate multiple functional parameters from live cells to 3D EM at the level of single organelles [11,27–30]. Our methods open new ways to obtain quantitative, high throughput functional data with EM resolution.

## Results

### Outline of CLEM workflows

A major challenge in CLEM approaches is to link live cell FM to 3D EM, thereby literally inferring dynamic information to static EM pictures[27,29,31–34]. We selected a variety of probes that are routinely applied to analyze functional characteristics of endo-lysosomal compartments in live cells by FM (table 1). We applied these probes in two functional CLEM workflows using focused ion beam scanning electron microscopy (FIB-SEM) or electron tomography (ET), respectively (figure 1). Each workflow has its specific benefits, which are addressed below.

Probe name	Probe description	Activation of fluorescence	Expected localization	Fluorescence retained in cryosections
<b>Dextran Alexa 488 and 647</b>	General tracers of endocytosis	-	All endocytic compartments, but mostly the degradative pathway to lysosomes	YES
<b>LysoTracker Green (DND-26)</b>	Membrane-permeable, weakly basic amine, conjugated to a fluorophore. Protonation at low pH selectively traps the probe in acidic compartments due to the loss of membrane permeability.	Always fluorescent, but selectively accumulates in acidic compartments.	Acidic compartments <pH6	NO
<b>Magic Red cathepsin B</b>	Membrane-permeable probe consisting of a Cresyl violet fluorophore flanked by two amino acid bait sequences for cathepsin B.	Fluorophore release after cleavage of bait sequences	Endo-lysosomal compartments with active cathepsin B	NO
<b>SIR-Lysosome cathepsin D</b>	Silicon Rhodamine-labeled pepstatin A, a membrane-permeable specific inhibitor of aspartate proteases. Detection of active cathepsin D.	Always fluorescent, but needs to irreversibly bind to the active form of Cathepsin D to prevent wash out.	Endo-lysosomal compartments with active cathepsin D	NO
<b>Oregon Green BAPTA-1 Dextran</b>	Calcium chelator BAPTA-1 conjugated to Oregon Green and dextran. Taken up by endocytosis.	15-fold fluorescence increase upon calcium binding	Calcium-rich compartments	NO
<b>TopFluor-Cholesterol</b>	BODIPY-conjugated cholesterol analog. Taken up by endocytosis.	-	Marks cholesterol rich compartments and membranes	YES

Table 1: Functional probes for endo-lysosomal organelles used in this study.

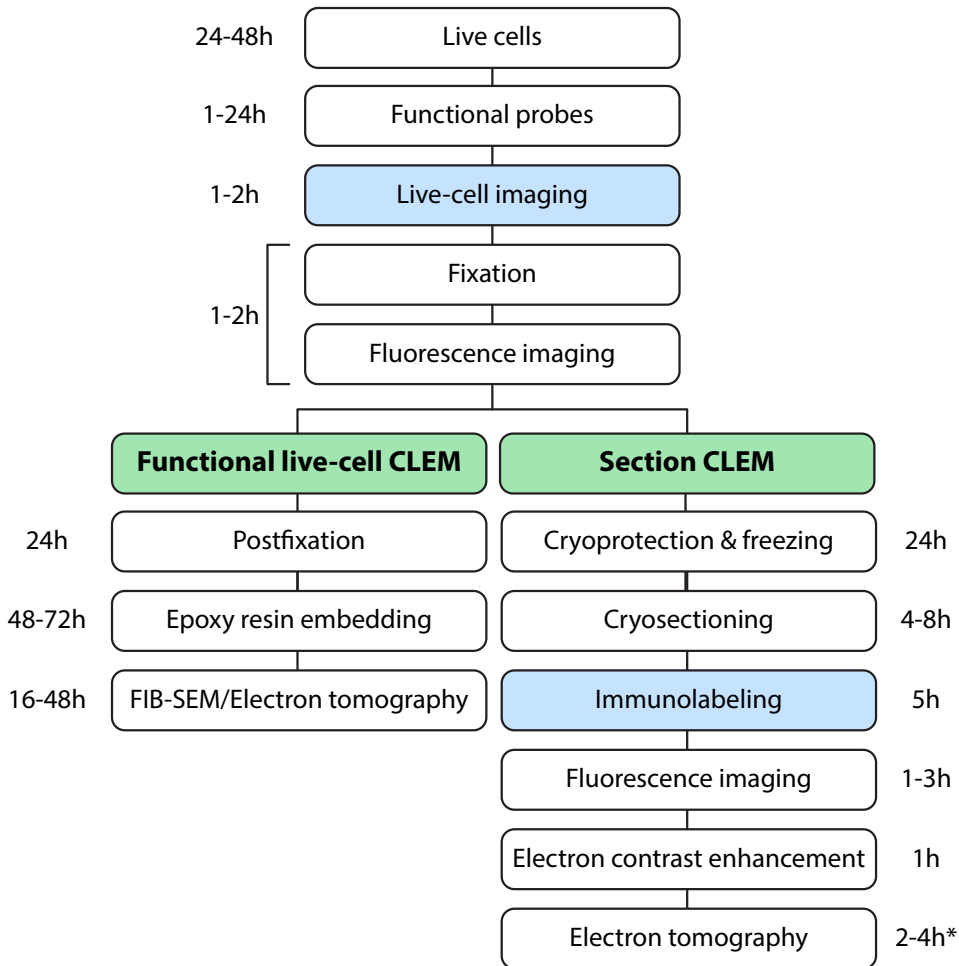


Figure 1: Graph depicting the two workflows used in this chapter annotated for the time needed per step. Optional steps are indicated in blue. Both workflows are compatible with live-cell imaging. \*Time needed to collect a single tomogram. On average, each following tomogram adds 2-3h of imaging and reconstruction time.

### Functional 3D live cell CLEM

Recently, we developed a 3D live cell CLEM protocol to correlate live cell FM movies to 3D FIB-SEM images, which is presented in chapter 2 [29]. In brief, we imaged live HeLa cells transfected with a fluorescent lysosomal membrane protein, GFP-LAMP-1, and obtained movement tracks of GFP-LAMP-1 positive compartments. Then we fixed cells and collected fluorescent z-stacks to obtain information on the 3D constellation of the tracked compartments. The samples were then embedded in Epon resin for FIB-SEM analysis. Here we aimed to adapt this protocol to image functional probes of which the fluorescence depends on live cell activities.

A pre-requisite for 3D live cell CLEM is that fluorescent probes remain visible after fixation in order to obtain the z-stack. To test for this, we analyzed how a panel of frequently used functional probes (listed in table 1) retained staining

intensity and localization after fixation in PHEM buffer containing 4% PFA and 0.1% glutaraldehyde, the preferred fixative for live cell CLEM studies[29]. We observed that Magic Red cathepsin B fluorescent signals remained correctly visible for 15-30 minutes after fixation, after which the fluorescent pattern became less punctate and weaker. SiR-Lysosome, LysoTracker and Oregon Green 488 BAPTA-1 dextran (BAPTA-dextran) retained proper localization until several days after fixation, albeit with a gradual loss of fluorescence intensity. Therefore, as a routine procedure, we imaged samples directly after fixation by FM, without further washing steps. This strategy proved to work well for all the probes used in this chapter, resulting in sufficient and localized fluorescence intensity suitable for 3D CLEM.

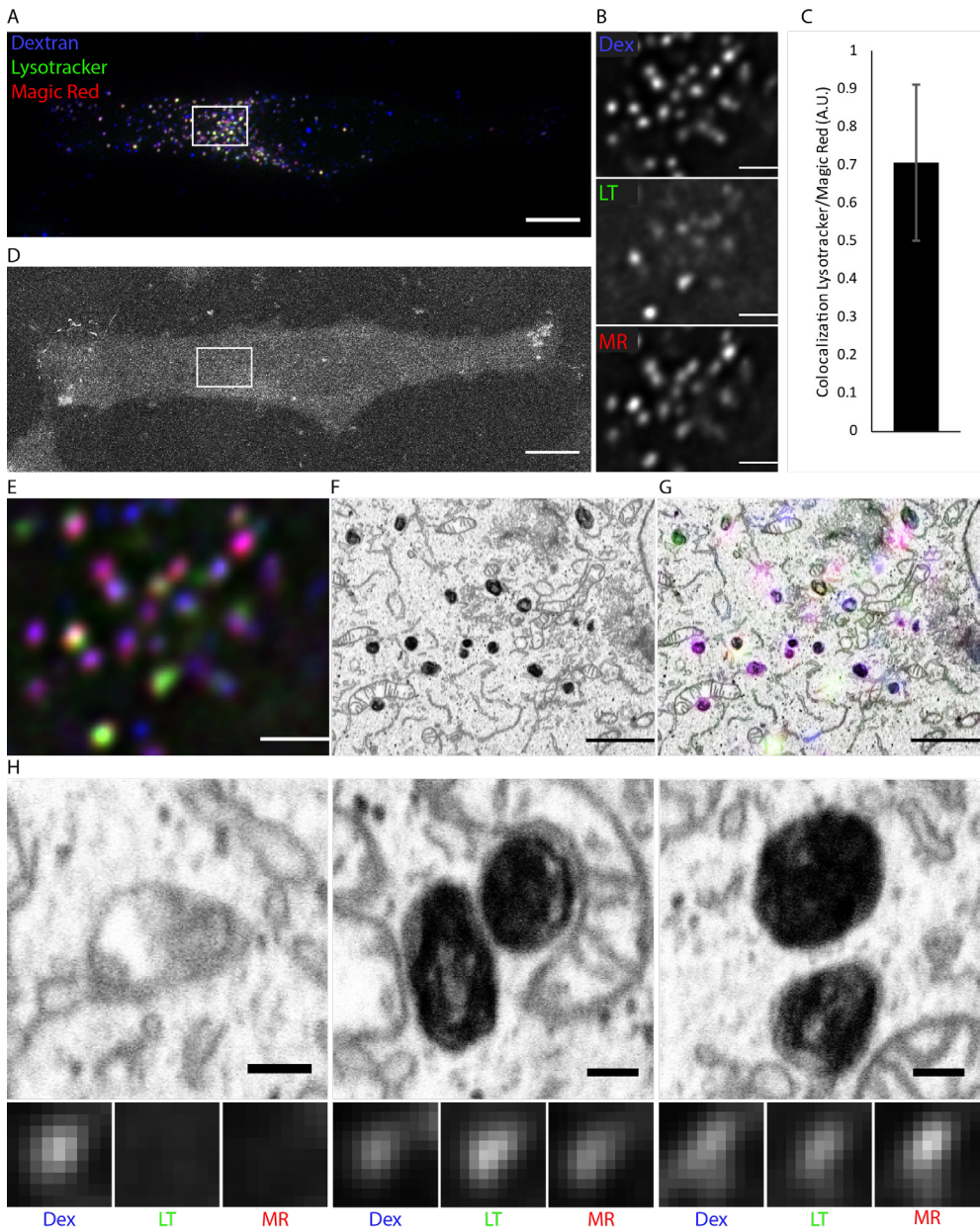
### Functional 3D live cell CLEM shows that lysosomes are the predominant sites for low pH and lysosomal enzyme activity

Based on a body of literature there is general consensus on the overall morphological appearance of early endosomes, late endosomes and lysosomes, as is illustrated in the introduction of this thesis. In short, early endosomes are discernable by an irregularly shaped vacuole with electron lucent lumen, little content and they often contain a flat cytoplasmic clathrin coat[35]. Late endosomes are distinguished by the presence of numerous intraluminal vesicles, whereas lysosomes contain degradation products and membrane whorls. Endolysosomes, which are hybrid organelles formed by fusion between late endosomes and lysosomes, show a combination of these morphological characteristics[6,23]. Here we use 3D live cell CLEM to directly link these morphological definitions to their functional status.

The functional performance of lysosomes is determined by multiple parameters, most notably pH, activity of lysosomal enzymes, protein and lipid composition, and the presence of small elements like calcium. In a first experiment (dataset 1/figure 2) we applied functional probes to simultaneously analyze pH and activity of lysosomal enzymes, and combined this with an endocytic marker. HeLa cells were grown on gridded glass coverslips and simultaneously incubated with Magic Red cathepsin B and dextran-Alexa 647 for 2 hours. During the last 15 minutes LysoTracker Green was added. Dextran is taken up by endocytosis and via early and late endosomes transported to lysosomes. LysoTracker and Magic Red cathepsin B enter cells via diffusion and monitor acidic compartments ( $\text{pH} < 6$ ) and activity of the lysosomal enzyme cathepsin B, respectively (table 1). By FM (figure 2 A, B) we found that the LysoTracker and Magic Red cathepsin B signals largely co-localized (figure 2C), which is in concert with the notion that a low pH is required to optimally activate lysosomal proteases. Most of the LysoTracker and Magic Red-positive spots also contained endocytosed dextran, indicating that they were reached by endocytic cargo within 2 hours (figure 2 A,B). In addition, we found a pool of compartments

Figure 2: Functional correlative live and volume electron microscopy dataset 1. A, Maximum intensity projection of fixed HeLa cell treated with dextran Alexa 647 (Dex), LysoTracker Green (LT) and Magic Red cathepsin B (Magic Red, MR). The ROI selected for CLEM is marked by the white square. C, Magnified slice from Z-stack showing the ROI. D, SEM micrograph showing the basal surface of same cell as in A. The ROI selected for CLEM is highlighted in white. E, Merged fluorescent slice showing all fluorescent probe signals in the ROI. F, Slice from FIB-SEM reconstruction of the ROI. G, Overlay of fluorescent functional probes over FIB-SEM data. LysoTracker (green) and Magic Red cathepsin B (red) signals predominantly localize to dense lysosomes. Dextran Alexa 647 (Dex) is found in early and late endosomes as well as lysosomes. H, FIB-SEM images showing examples of single organelles with their functional labels. Left panel: organelle that by FM only labels for dextran and by EM is characterized as late endosome. Middle and right panels: in total 4 organelles that by FM label for Magic Red cathepsin B (MR), LysoTracker (LT) and Dextran and by EM are identified as electron-dense lysosomes. Scale bars: A, D: 10  $\mu\text{m}$ ; B, E-G: 2  $\mu\text{m}$ ; H: 200 nm. Additional information is provided in supplementary figure S1.

Functional characterization of endo-lysosomal compartments by correlative light electron microscopy



3

that only contained endocytosed dextran, which we in previous studies identified as early or late endosomes[23,29].

Following FM imaging, samples were post-fixed using the optimized contrasting protocol described in chapter 2, after which cells were processed for FIB-SEM using the strategy described in figure 1. All fluorescently labeled compartments (n = 35) present in the selected ROI (figure 2D) were retraced in the FIB-SEM data (figure 2E-G, supplementary figure 1B-D). By EM morphology, 31 compartments were characterized as lysosomes and 4 as late endosomes. Since this number of late endosomes was very low, we restricted the functional analysis of single organelles to the lysosomal population. Correlation of the FM to the FIB-SEM data showed that 80% of all lysosomes were positive for dextran, and 71% and 90% for LysoTracker and Magic Red cathepsin B, respectively (supplementary figure 1A). Thus, the majority (70-90%) of the compartments that by EM are defined as 'classical' lysosomes, i.e. with an electron dense lumen and prevalent membrane whorls (figure 2H), by CLEM display a low pH (<6), contain active cathepsin B and are positive for dextran after 2 hours uptake.

We then extended our studies to a larger, second experimental set up (dataset 2) in which we in addition to Magic Red cathepsin B also included SiR-Lysosome, a probe to measure cathepsin D activity (table 1), and again dextran (2 hours uptake). Although the assays of Magic Red cathepsin B and SiR-Lysosome cathepsin D are based on different chemical principles (table 1), we found by FM a high degree of overlap (81%) between these two probes (figure 3A-C). We imaged 2 ROIs of this experiment by FIB-SEM and correlated a total of 242 compartments from FM to EM (figure 3D-E). By EM morphology, 66 compartments were characterized as late endosomes, 39 as endolysosomal hybrids and 145 as lysosomes (figure 3F). Strikingly, 58% of the organelles present in this relatively large dataset is defined as lysosome (figure 3 F), which is similar to a previous study in which we randomly screened 300 endo-lysosomal compartments in ultrathin cryosections of HeLa cells (figure 4 in [36]).

By CLEM analysis, we found that 93% of the morphologically defined late endosomes and 94% of the endolysosomal hybrids were positive for dextran, whereas 73% of the lysosomes were reached by this probe after 2 hours (figure 3G). The remaining lysosomal population is either not yet reached by dextran or represents organelles that do not fuse with late endosomes. Interestingly, our data show that only 23-33% of the morphologically characterized late endosomes is labeled for active cathepsin B or D, respectively, whereas 84-92% of the lysosomes show these activities (Figure 3H-I). The hybrid endolysosomal organelles, representing late endosomes and lysosomes after heterotypic fusion, are intermediate for cathepsin B and D enzyme activity (figure 3H-I), with respectively 60% and 80% positive compartments. These single organelle data show that within each class of organelles the percentage of compartments with active cathepsin D is higher than for cathepsin B. This might indicate that there is more active cathepsin D present in HeLa cells, or that cathepsin D is activated at an earlier stage, or that the SiR-Lysosome cathepsin D probe is more sensitive than Magic Red cathepsin B. Regardless of these differences an important implication of these functional studies is that the majority of lysosomal enzymes is activated at the stage of endolysosomes, i.e. after fusion of late endosomes with lysosomes, and that enzymes retain their activity in bona fide lysosomes with a classical lysosomal morphology.

We then integrated the information of all 3 probes at the level of single compartments.

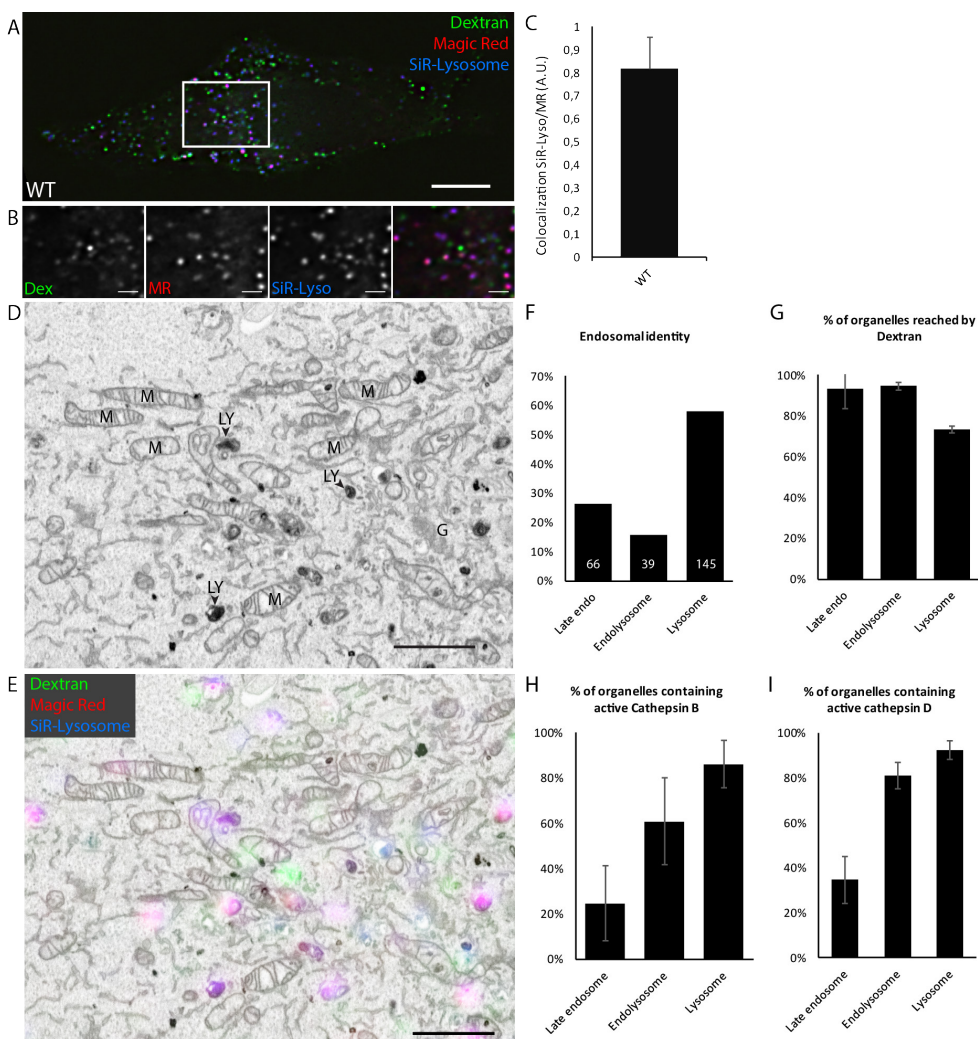


Figure 3: Functional correlative live and volume electron microscopy dataset 2. A, Fluorescent micrograph showing wildtype HeLa cells treated with dextran Alexa 488, Magic Red cathepsin B (Magic Red, MR) and SiR-Lysosome cathepsin D (SiR-Lyso). ROI for CLEM is indicated by white square. B, Magnified images of ROI. C, Quantification of co-localization of the Magic Red cathepsin B and SiR-Lysosome cathepsin D fluorescence shows high level of overlap. D, Slice from FIB-SEM reconstruction of the ROI. M, mitochondria; LY, lysosomes; G, Golgi. E, Overlay of FIB-SEM slice and functional fluorescent data. Dextran is found in late endosomes and lysosomes, while SiR-Lysosome cathepsin D and Magic Red cathepsin B are primarily found in lysosomes. F, Composition of endo-lysosomal system present in ROI as defined by ultrastructural characteristics in FIB-SEM data. G-I, Single organelle microscopy of compartments present in ROI. G, Most late endosomal and endolysosomal compartments contain dextran and circa 70% of the lysosomes is positive. H and I; A minority of late endosomes is positive for active cathepsin B and D, while the majority of lysosomal compartments are enzymatically active. Scale bars: A; 10 microns; B, D, E; 2 microns.

This showed that in wildtype cells the major population of morphologically defined late endosomes (74.2%) is positive for dextran but lacks cathepsin B or D activity (table 2). By contrast, the predominant pools of endolysosomes (74%) and lysosomes (64.8%) contain both dextran and active cathepsins. The FM datasets (figure 3) show that cathepsin B and cathepsin D activity display highly overlapping localization patterns (82%), which in dataset 1 largely overlaps with LysoTracker and in dataset 2 with endocytosed dextran. The CLEM analysis shows that the predominant compartments labeled by this triple set of probes are endolysosomes and lysosomes (table 2, supplementary table 1).

Dextran	Enzyme activity	Late endosomes n = 66	Endolysosomes n=39	Lysosomes n = 145
+	-	66.7%	20.5%	8.3%
-	+	6.1%	5.1%	26.9%
+	+	27.2%	74.4%	64.8%

Table 2: Dataset 2. Numbers indicate the percentages of endo-lysosomal subtypes that by CLEM are labeled with the functional probes. Data were obtained in wild type HeLa cells incubated with dextran (2 hours), Magic Red cathepsin B and SiR-Lysosome cathepsin D. Enzyme activity for a compartment is defined as being positive for either or both Magic Red cathepsin B or SiR-Lysosome cathepsin D. Full data of all individual probes is collected in supplementary table 1.

### Functional 3D live cell CLEM of Vps41 KO cells shows a block in cargo transfer from late endosomes to endolysosomes

The large number of compartments analysed by the functional live cell CLEM approach allows for quantitative studies on the endo-lysosomal system. Here we provide a proof-of-principle by applying functional CLEM to study the role of the Homotypic fusion and vacuole Protein Sorting (HOPS) protein VPS41 on endo-lysosomal organization and function. HOPS is a tethering complex that regulates fusion between lysosomes with late endosomes and autophagosomes.[37–40] Previously we showed by immuno-EM[36] that siRNA mediated knockdown of VPS41 causes a defect in late endosome – lysosome fusion, resulting in an increase in late endosomes and a decrease in lysosome numbers[36],[41]. The number of Magic Red cathepsin B-positive puncta in VPS41 depleted cells remained similar if not slightly elevated. In seeming contrast, our present correlations show that most late endosomes lack cathepsin B activity (figure 3, table 2). This raises the question what the cathepsin B puncta in VPS41 knockdown cells do represent.

To address this question by our correlative imaging method we generated VPS41 knockout (KO) HeLa cells using CRISPR/Cas9 mediated genome editing as described in the method section. VPS41 KO cells were incubated with dextran (2 hours), Magic Red cathepsin B and SiR-Lysosome cathepsin D (figure 4 A, B), under the same conditions as the wildtype HeLa cells analyzed in dataset 2/figure 3. FM of the VPS41 KO cells showed a significant increase in the number of Magic Red cathepsin B puncta (figure 4C). Also, we found a marked decrease in co-localization of endocytosed dextran with Magic Red cathepsin B (figure 4D), indicative for the defect in HOPS-dependent fusion delaying delivery of endocytosed cargo to

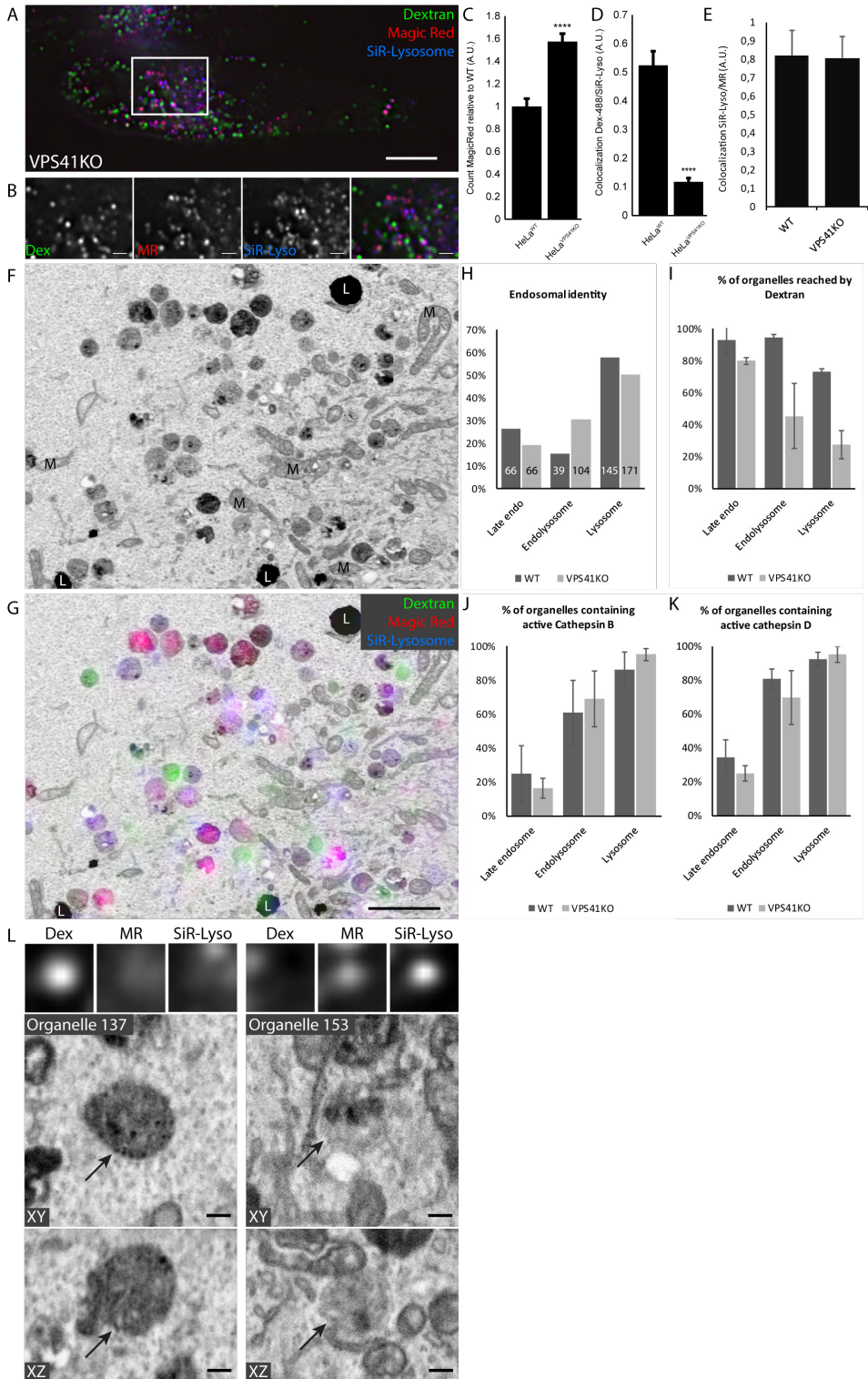
lysosomes[36]. The Magic Red cathepsin B and SIR-Lysosome cathepsin D patterns were strongly overlapping (Figure 4E), which is similar as in wildtype cells.

The correlating FIB-SEM datasets (figure 4, table 3) contained a total of 341 organelles and clearly showed that the overall morphology of the endo-lysosomal population had changed in VPS41 KO cells. Within the selected ROI we found an accumulation of heterogeneous endo-lysosomal compartments (compare figure 3D to figure 4F) of which by morphology 66 compartments were characterized as late endosomes, 104 as endolysosomal hybrids and 171 as lysosomes (figure 4H). This indicates a noticeable increase in the occurrence of endolysosomal hybrid organelles as compared to wildtype cells: from 15.6% to 30.5% (figure 4H). Of note, in Vps41 siRNA HeLa cells we also found an increase in late endosomes, but in this case no distinction between late endosomes and endolysosomes was made[36]. Our current data indicate that a significant portion of these late endosomes are in fact endolysosomal hybrid compartments.

By single organelle analysis in VPS41 KO cells we found that the majority of endolysosomal hybrid compartments (>60%) as well as of the 'classical' lysosomes (>90%) was enzymatically active (figure 4 J, K), whereas only a minority of late endosomes displayed cathepsin activity (figure 4 J, K). The compartmentalization of active cathepsins to mainly endolysosomes and lysosomes in VPS41 KO cells is similar to wildtype cells and indicates that even though the composition of the endo-lysosomal system has changed, the functional status of endosomal subtypes remains the same. It also shows that the onset of activation of lysosomal enzymes in Vps41 KO cells, remains mainly localized in endolysosomes, despite the endocytic trafficking defects.

CLEM analysis of the dextran distribution showed a clear reduction in the delivery of dextran to morphologically-defined lysosomes in VPS41 KO cells. In wildtype cells 73% of the lysosomal population was reached after 2 hours uptake, in VPS41 KO cells this was only 28% (figure 4I). Previously, we found by immunoEM that the percentage of lysosomes containing endocytosed BSA5nm decreased from ~60% in control cells to ~13% in Vps41 depleted cells[36]. Now, by using an entirely different approach based on correlation of FM and FIB-SEM data, we find a similar outcome, illustrating the efficacy of our approach. The percentage of dextran-positive endolysosomes also decreased significantly in VPS41 KO cells, from 95% to 54.8%. Late endosomes in VPS41 KO cells were still readily reached by dextran (94% positive in wildtype and 80% in VPS41 KO cells).

These data show that VPS41 KO cells accumulate endolysosomes that generally display cathepsin activity but are less well reached by dextran. Surprisingly, when we integrated all assays onto the level of single organelles we found a clear separation of either dextran-positive (20.5%) or cathepsin-positive (45.2%) endolysosomal compartments in VPS41 KO cells. Only 18.3% still contained both activities, instead of the 74.4% in wildtype cells. These data show a clear decrease in the delivery of dextran to cathepsin-positive endolysosomal hybrid compartments. It is somewhat surprising though that the steady-state number of these hybrid compartments increases. This could be either caused by a longer fusion process and/or a delay in lysosome reformation from the hybrid organelles. It is a realistic scenario that the lack of VPS41 causes a delay in endosome maturation affecting these processes. The lysosomal pool in VSP41 KO cells was more homogeneous. Whereas in wildtype cells, most lysosomes (64.8%) contained both dextran and cathepsin, in VPS41 KO cells 71.9% of all lysosomes displayed cathepsin activity but lacked dextran. This



3

Figure 4: VPS41 knockout alters distribution of dextran but not cathepsins. A, FM showing VPS41 KO cells incubated with dextran-Alexa 488 (for 2 hours), Magic Red cathepsin B (Magic Red, MR) and SiR-Lysosome cathepsin D (SiR-Lyso). ROI for CLEM indicated by white square. B, Magnified ROI showing partial overlap between dextran and functional probes. C, FM analysis of Magic Red cathepsin B signal in VPS41 KO and wild-type cells shows significantly more Magic Red cathepsin B spots in VPS41 KO cells. D, Colocalization analysis of dextran and SiR-Lysosome cathepsin D. VPS41 KO causes a significant decrease in colocalization. E, Colocalization analysis of Magic Red cathepsin B and SiR-Lysosome cathepsin D. No changes are seen under VPS41 KO conditions. F, FIB-SEM slice of the ROI shown in A, showing perturbed endosomal morphology with accumulated electron dense compartments. L, lipid droplet; M, mitochondrion. G, FIB-SEM slice overlaid with functional data, showing separation of dextran-positive and enzymatically-active compartments. H, Identification of endo-lysosomal organelles in wildtype and VPS41 KO datasets shows a substantial increase of endolysosomal hybrids in VPS41 KO cells. I, Analysis of dextran delivery to lysosomal compartments. Less lysosomes are reached by dextran in VPS41 KO cells. J, K Analysis of the effect of VPS41 KO on the localization of functional probes. VPS41 KO lysosomes contain active cathepsins B and D. L, Correlative analysis of endolysosomal hybrids in VPS41 KO cells showing heterogeneity in morphology and dextran and cathepsin labeling. Scale bars: A; 10 microns; B, D, E; 2 microns, L; 200 nm.

clearly reflects the effect of HOPS depletion on the delivery of cargo to lysosomes. VPS41 KO had no marked effect on the functionality of late endosomes. In both wildtype and VPS41 KO cells the major pool of late endosomes was positive for dextran and negative for cathepsin activity (66.7 versus 74.3%, respectively). Thus, the most prominent functional changes caused by VPS41 KO were seen in the endolysosomal and lysosomal populations.

Overall these data indicate that VPS41 KO cells accumulate endolysosomes that are either positive for dextran or cathepsin activity. The decrease in dextran-positive endolysosomes and especially dextran-positive lysosomes (table 3, supplementary table 2) clearly shows that the block in HOPS function causes a delay in the delivery of endocytosed cargo to enzymatically active compartments. The CLEM data also imply that the increase in fluorescent puncta for Magic Red cathepsin B and SiR-Lysosome cathepsin D in Vps41 KO cells is caused by an increase in number of enzymatically active endolysosomal hybrid organelles.

Dextran	Enzyme activity	Late endosomes n = 66	Endolysosomes n=104	Lysosomes n = 171
+	-	74.3%	36.5%	4.1%
-	+	19.7%	45.2%	71.9%
+	+	6.0%	18.3%	24.0%

Table 3: Distribution of functionally labeled organelles in VPS41 knockout HeLa cells incubated with dextran (2 hours), Magic Red cathepsin B and SiR-Lysosome. Fractions are calculated per organelle type. Enzyme activity for a compartment is defined as being positive for either or both Magic Red cathepsin B or SiR-Lysosome cathepsin D. Full data of all individual probes is collected in supplementary table 2.

### Functional 3D live cell CLEM marks most late endosomes positive for calcium

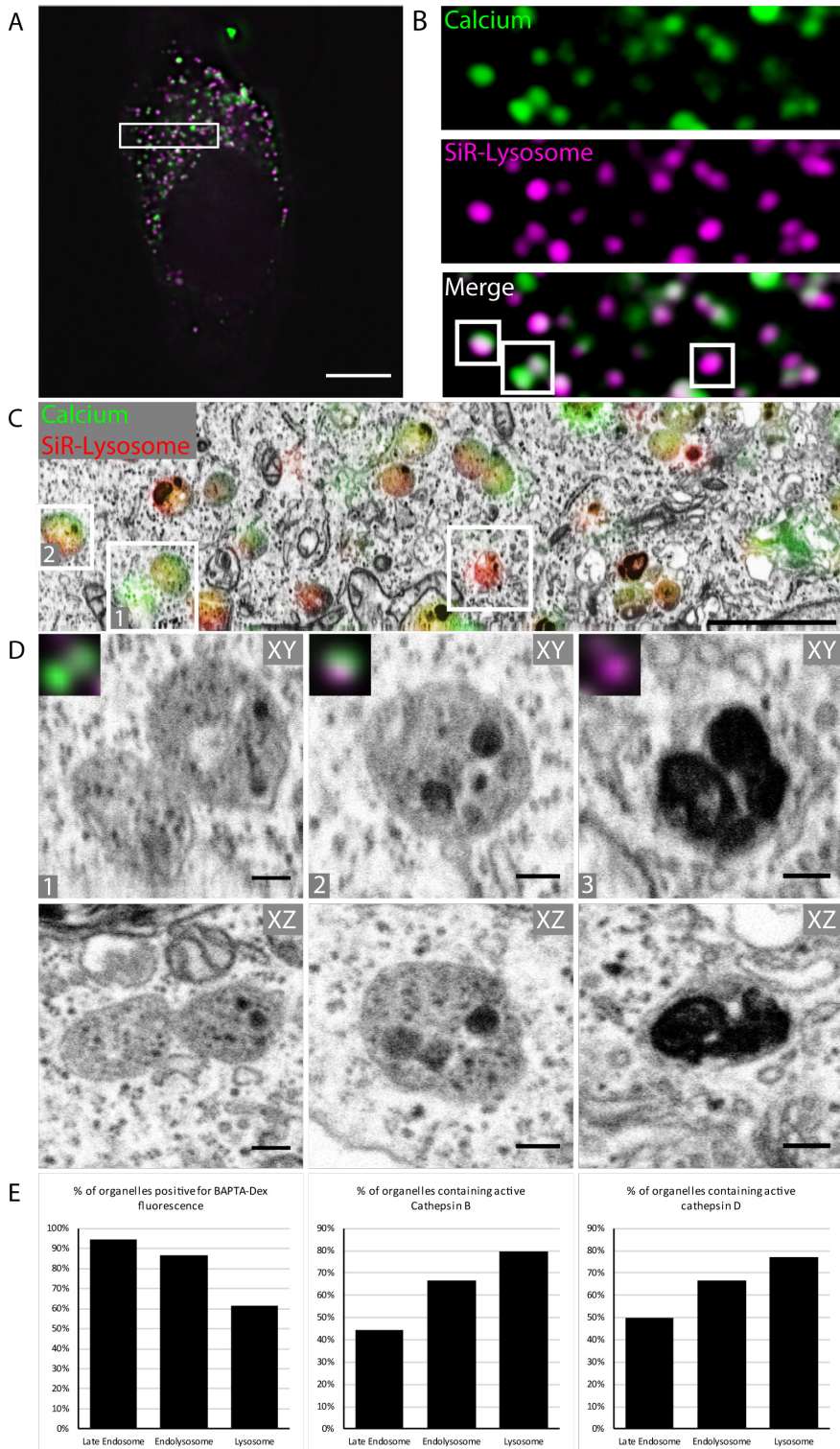
We next studied the applicability of our CLEM approach for calcium measurements (dataset 3). Calcium is required for a number of processes, including endo-lysosomal positioning, fusion and exocytosis [42–45]. Calcium indicators are probes that exhibit an increase in fluorescence upon binding Ca<sup>2+</sup>. The BAPTA-dextran probe is generally used to examine cytosolic calcium levels after microinjection [46,47], however, since dextrans of similar MW are taken up by endocytosis (as in figure 2), we reasoned that it could also be used to trace calcium in endo-lysosomal compartments. To test this, we incubated HeLa cells with a combination of dextran-Alexa568, BAPTA-dextran and SiR-Lysosome cathepsin D, after which cells were fixed and imaged by FM (supplementary figure 2A). We found that 3 hours uptake of BAPTA-dextran gave an optimal, punctate fluorescence signal, which largely overlapped with dextran-Alexa568 and partially with SiR-Lysosome cathepsin D (supplementary figure 2B). This indicates that BAPTA-dextran is taken up by endocytosis and follows the same route as dextran-Alexa568. Moreover, since BAPTA-dextran shows a punctate staining pattern the probe can be used to monitor the presence of calcium within endo-lysosomal compartments.

After establishing the feasibility of the approach, we incubated cells with BAPTA-dextran for 3 hours and combined this with SiR-Lysosome cathepsin D and Magic Red cathepsin B. We imaged the cells by FM and then prepared them for FIB-SEM. As in supplementary figure 2A, FM showed that BAPTA-dextran partially overlapped with SiR-Lysosome cathepsin D (figure 5A, B). In the correlating FIB-SEM dataset we found 77 endo-lysosomal compartments, which by EM morphology were defined as late endosomes (22), endolysosomal hybrids (11) and lysosomes (44). Overall, we found that the signal of BAPTA-dextran is easily retraced between FM and FIB-SEM. Consistent with previous studies showing an increase in calcium concentration upon maturation of endo-lysosomal compartments [48,49] most BAPTA-dextran positive spots correlated to bona-fide lysosomes and a smaller fraction to endolysosomes and late endosomes (figure 5C, D, table 3). However, when we performed single organelle analysis, this showed that 91% of all late endosomes were positive for BAPTA-dextran versus only 61% of the lysosomes. There was no apparent difference in morphology or location of lysosomes that were either positive or negative for the BAPTA-dextran (figure 5F).

These data show that the vast majority of late endosomes is positive for calcium, indicating that calcium is an important requirement for late endosome functioning. The percentage of lysosomes positive for calcium was lower, but since lysosomes represent the largest population of late endo-lysosomal compartments in HeLa cells [36], they are rightfully considered as the major population of calcium containing organelles.

Figure 5: Functional imaging of calcium in endo-lysosomal compartments. A, FM of cells labeled with BAPTA-dextran (calcium) and SiR-Lysosome cathepsin D. ROI for CLEM marked in white. B, Magnified view of ROI with selected compartments (white boxes). C, Slice from reconstructed FIB-SEM data overlaid with FM information. Both SiR-Lysosome cathepsin D and calcium signals localize to endo-lysosomal compartments. D, XY and XZ slices from the FIB-SEM data showing representative organelles with corresponding fluorescence data. Box 1: 2 calcium-rich late endosomes with minimal SiR-Lysosome cathepsin D activity. Box 2: endolysosome with electron dense cargo, positive for calcium and SiR-Lysosome cathepsin D. Box 3: lysosome containing dense membrane whorls displaying cathepsin D activity but no calcium. E, Correlative analysis of functional probes to morphology. BAPTA-dextran is predominantly visible in late endosomes, while active cathepsins are mainly found in endolysosomes and lysosomes. Scalebars: A; 10  $\mu$ m, B-C; 2  $\mu$ m, D; 200 nm.

Functional characterization of endo-lysosomal compartments by correlative light electron microscopy



3

## Probe distributions

Thus far, for each quantification we used the morphological definition of tens-to-hundreds of classified compartments and added the functional data on top, the method we refer to as single organelle microscopy. This gives solid data on how the probes are distributed within different endo-lysosomal subtypes. To establish the distribution of a given probe over the entire endo-lysosome population, i.e. take a probe as starting point and plot the morphological data on top, requires higher sample sizes that reflect the random distribution of the different classes of organelles. We therefore combined datasets 1-3 to provide sufficient sample size. As shown in figure 6, this resulted in a graph of how the different probes are relatively distributed over the different organelle subtypes. We conclude that in wildtype HeLa cells, cathepsin B and cathepsin D activity is predominantly contained within endolysosomes and lysosomes, whereas substantial fractions of dextran and calcium are found in late endosomes.

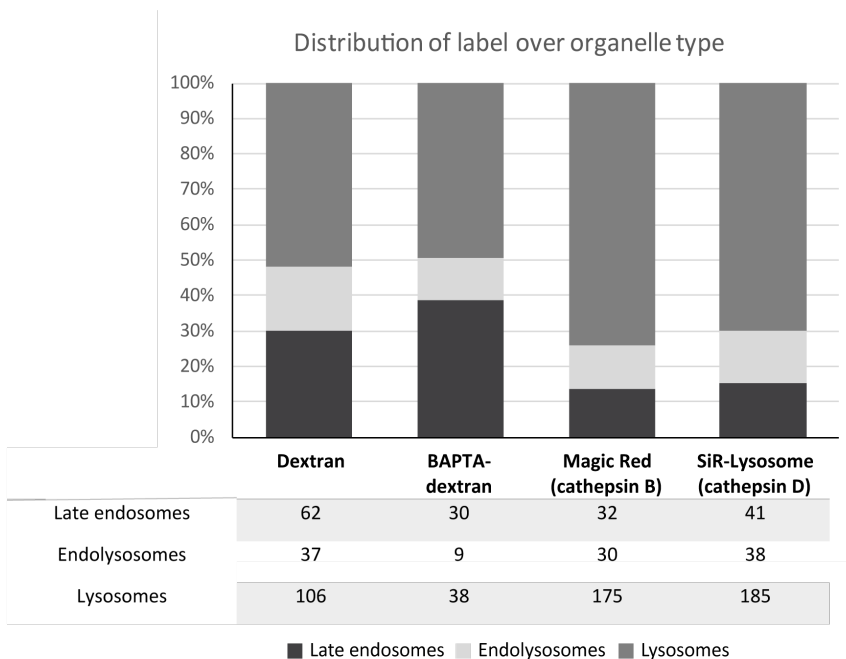


Figure 6: Summarizing graph of all functional data obtained for wildtype cells using correlative functional imaging. The numbers of labeled organelles per probe are shown below the graph.

## Functional 3D section CLEM

The advantage of the FIB-SEM approach is that a single sample contains hundreds of organelles for correlation between FM and EM. A drawback is that FIB-SEM is not (yet) compatible with labeling of specific proteins. As second functional 3D CLEM approach we introduced Tokuyasu cryosections, the technique of choice for immuno-EM[50]. For CLEM applications, cryosections are hydrated and thawed to room temperature, after which they are labeled with antibodies tagged with a fluorescent and an electron dense marker[51]. Sections are first viewed by FM and subsequently by EM or electron tomography (ET)[28,51,52], after which the images are correlated. Recently, we developed a method to correlate cryosections from FM to EM with 5 – 30 nm accuracy[11]. This high precision method overcomes the need

to use electron dense labels for EM and opens a whole new field of applications, since we can now directly use the fluorescent signal to label EM images.

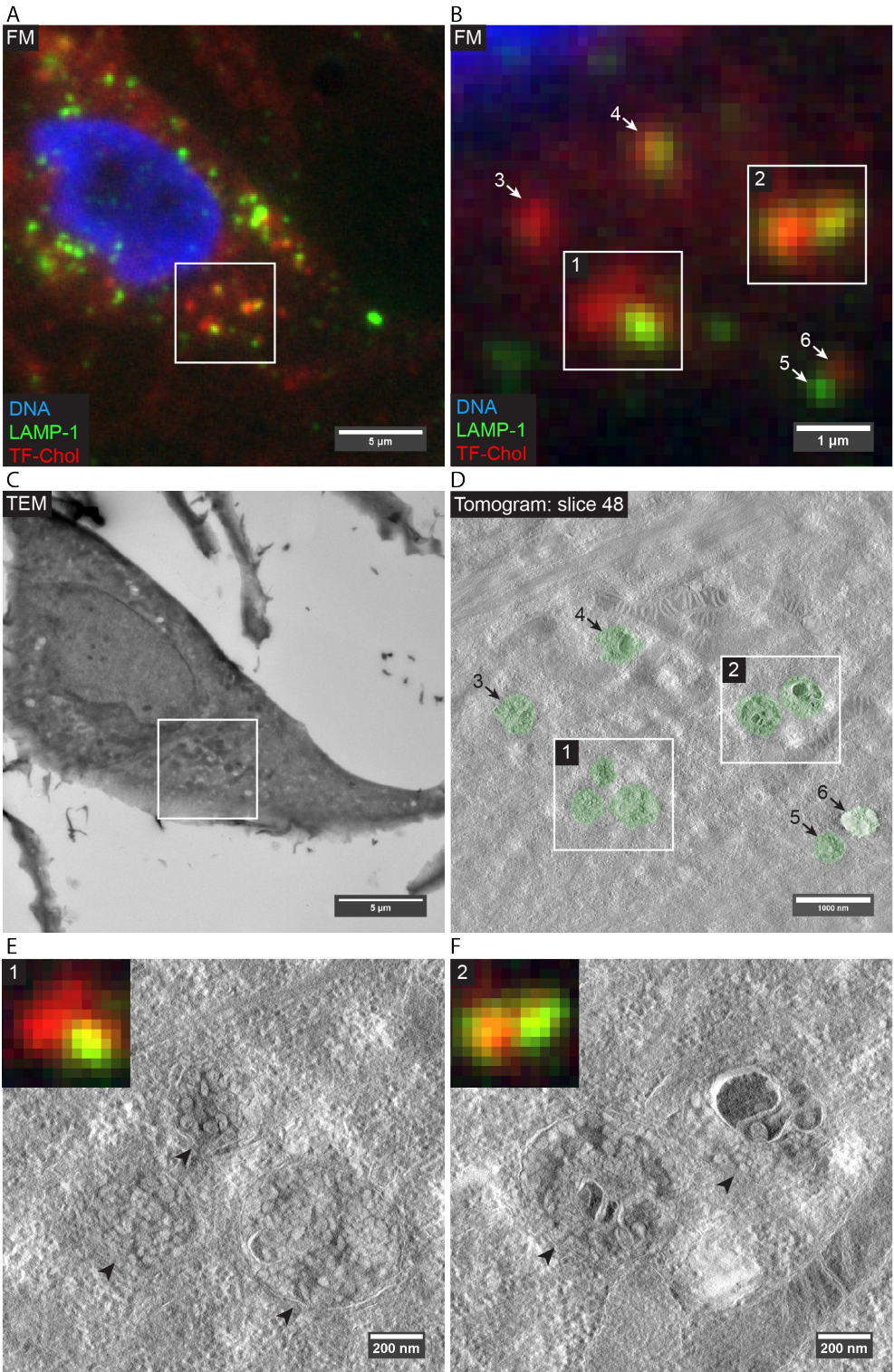
For section CLEM application we tested the functional probes listed in table 1 for their ability to retain fluorescent in thawed, hydrated cryosections. This showed that dextran Alexa 647, dextran Alexa 488 and TopFluor-cholesterol (TF-Chol) retained sufficient fluorescence for correlative experiments (figure 5A). LysoTracker and Magic Red cathepsin B signals disappeared upon fixation, probably by leaking from cells after permeabilization by fixatives. SiR-Lysosome cathepsin D and BAPTA-dextran signals were not visible in cryosections, presumably due to the exposure of the fluorescent groups to cryogenic temperatures.

### Localization of endo-lysosomal cholesterol by functional 3D section CLEM

Based on table 1 we decided to use TF-Chol as proof of principle for an 'EM-labelless' functional section CLEM approach. The localization of lipids by EM is notoriously difficult, due to their poor retention by fixatives[53,54], which is why probes for lipid localization in EM are highly warranted. TF-Chol has been used to study delivery of cholesterol from HDL particles[55] and also to study cholesterol homeostasis after viral infections[25], but not in conjunction with immuno-localization of endosomal markers or for CLEM. The probe is taken up by endocytosis but only retained in endo-lysosomal compartments when bound to cholesterol. Hence, it relies on live cells to obtain its proper localization.

TF-Chol was added to live HeLa cells for 16 hours, after which cells were fixed, cryoprotected with 2.3 M sucrose, frozen in liquid nitrogen, and sectioned into semi-thin (300 nm) cryosections[50]. We made use of the unique immuno-labeling properties of cryosections by combining TF-Chol with immuno-fluorescence-gold labeling for the lysosomal membrane protein LAMP-1 (figure 7A). Following immuno-labelling, grids were treated with Hoechst 33342 and imaged using widefield FM. TF-Chol distributed over discrete punctae that partially colocalized with LAMP-1 (figure 7B). Following FM imaging, the sections were stained with uranyl acetate and embedded in methylcellulose/uranyl acetate, as described [50]. ROIs identified in FM could easily be retraced using overview transmission EM (figure 7C) and were then examined using ET (figure 7D). A small sized tomogram (5 x 5 micrometer) showed that TF-Chol fluorescence correlates to endosomal structures characterized by large numbers of intraluminal vesicles (figure 7E, F), i.e. typical for late endosomes. These are qualitative data. In order to obtain statistically relevant numbers on the distribution of endocytosed cholesterol over distinct endo-lysosomal compartments the experiment needs to be extended statistically significant numbers of organelles.

Figure 7 (next page): TopFluor-cholesterol localizes to endo-lysosomal compartments A, FM of 300 nm cryosections of HeLa cells treated with TF-chol and immunolabeled for LAMP-1. LAMP-1 labeling partially overlaps with TF-chol fluorescence. The ROI selected for tomography is marked with a white square. B, magnified ROI from A showing spots of interest for tomography. Spots 1 and 2 are further examined in E and F. C, TEM micrograph of the same cryosections as shown in A. ROI for tomography based on fluorescent data is marked with a white square. D, electron tomogram of the ROI. The fluorescent spots of interest are identified as endo-lysosomal compartments based on the morphological features. E, F; TF-chol reaches both late endosomes and lysosomes, which are identified by the accumulation of intraluminal vesicles and electron-dense amorphous content, respectively.



3

## Discussion

Fluorescent biosensors are a highly informational class of probes that can be used to examine the functional state of cells and organelles. Functional information of sub-cellular structures is most useful when interpreted in the ultrastructural context. However, function and morphology are commonly examined in separate populations without a direct link between the two and without integrating functional and form parameters. Here, we present 'functional CLEM' methods as a powerful tool to correlate functional biosensor assay data to 3D ultrastructure.

The first approach presented in this chapter is an adaption of our previously established workflow to monitor GFP-tagged proteins in live cells and by 3D FIB-SEM[29]. We validated an array of functional probes commonly applied in FM for application in this correlative setting (table 1) by assessing their ability to retain fluorescence when cells are fixed after live cell imaging. The tested probes all retained fluorescence for at least 30 minutes after fixation, which allowed us to collect fluorescent Z-stack images needed for correlative 3D-EM and register the functional data of individual fluorescent spots to 3D ultrastructure, as demonstrated in figure 2.

We applied this 3D CLEM method to analyze function-form relationships of single endo-lysosomal organelles, by which we focused on late endocytic compartments. Lysosomes form by fusion of late endosomes with pre-existing lysosomes resulting in endolysosomes from which lysosomes are reformed in a lysosome regeneration cycle[6]. LysoTracker and active cathepsin B and D by FM largely overlapped in discrete punctae, which by EM mostly correlated to classical lysosomes. Vice versa, single organelle microscopy revealed that the vast majority of lysosomes was labeled for the combination of LysoTracker and cathepsin activities. The percentage of late endosomes displaying this combination of markers was significantly lower (22-33%). The majority of late endosomes was positive for calcium, whereas this ion was found in 61% of the imaged lysosomes. Dextran loaded for 2 hours was seen in the majority of endosomes (94%) and a lower percentage of lysosomes (73%), which reflects the time needed to reach deeper into the endo-lysosomal pathway. The endolysosomal hybrid compartments displayed an intermediate functional phenotype between late endosomes and lysosomes.

These quantitative data reveal a stepwise increase in lysosomal hydrolase activity from late endosomes to lysosomes, i.e. much more endolysosomes and lysosomes than late endosomes are positive for cathepsins, which nicely correlates to a low pH and in EM to a classical lysosomal morphology. This sets endolysosomes and lysosomes functionally apart from late endosomes by the presence of a low pH and degradation power. The high level of co-localization between LysoTracker and cathepsin activities in direct correlation to lysosomal morphology shows that these probes are bona fide markers for lysosomes, by which Magic Red cathepsin B shows a more restricted localization than SIR-lysosome cathepsin D. The data also imply that endolysosomes are the first sites in the endocytic pathway that consistently display cathepsin activity. This is in agreement with live-cell microscopy studies from the Luzio lab, showing that the onset of acid hydrolase activity occurs after fusion events that lead to the formation of endolysosomes[23,56]. In contrast to these studies, however, we find that endolysosomes are not the principal sites of hydrolase activity, since the huge majority of classical dense lysosomes also displays enzyme activity. Since lysosomes are much more abundant than the endolysosomal hybrid compartments, lysosomes are the most abundant compartments in the cell

displaying enzyme activity.

The Luzio lab defined a pool of acid hydrolase-inactive, non-acidic lysosomes as terminal storage compartments important for lysosome regeneration. We indeed found a pool of cathepsin-negative lysosomes (figures 3 and 5). However, whereas the Luzio lab[23] by FM found that circa half of dextran labeled lysosomes lacked active cathepsin B, in our hands by CLEM correlation this pool was only 8.3% of all lysosomes. The discrepancy is most likely explained by different applications of the probes. We used the standard concentration of MR cathepsin B for 15 minutes, whereas the Luzio lab used a 10x diluted solution for 2 minutes. It is therefore conceivable that we detected enzyme activities that remain below detection threshold in the milder conditions. Furthermore, the Luzio lab used a 4 hr pulse/20 hr chase protocol for dextran, whereas we added this probe 2 hours continuously. The pool of dextran labeled compartments will therefore be different between the two approaches. These observations stress the need for controlled experimental conditions when using functional probes and strengthens the importance of CLEM to distinguish functionally different compartments at the ultrastructural level. Of note, the differences in enzyme detection threshold could be used to our advantage to mark high versus low activity organelles. Functional data obtained by FM only should be interpreted with great caution as to the type and percentage of total organelles that is visualized.

Fusion of late endosomes with pre-existing lysosomes is a tightly controlled process that involves the HOPS tethering complex[38,40,57]. We used 3D CLEM to study the effect of KO of the HOPS component VPS41 on the distribution of endocytosed cargo and active lysosomal hydrolases. The high throughput imaging by FIB-SEM allowed us to compare the functionality of multiple hundreds of endo-lysosomal organelles in HeLa wildtype versus VPS41 KO cells. This showed that in VPS41 KO cells only a small portion of lysosomes was reached by endocytosed dextran after 2 hours uptake. Previous studies using an entirely different approach based on immuno-EM labeling[36] led to the same conclusion, showing the power and accuracy of the CLEM approach applied here. The dextran-negative lysosomes do contain active lysosomal hydrolases, which also require HOPS dependent fusion to reach the lysosomes. This indicates that VPS41 KO results in a delay rather than a block in late endosome – lysosome fusion, allowing endogenous lysosomal enzymes, with much longer half-lives than 2 hours, to eventually reach lysosomes. Interestingly, activation of lysosomal enzymes remained largely restricted to endolysosomes and lysosomes and did not spill over to late endosomes. Thus, despite the trafficking defects in VPS41 KO cells the functional compartmentalization of lysosomal enzyme activity is strictly retained. Finally, we found an accumulation of endolysosomal hybrid compartments that were either positive for dextran or for cathepsin activity. A remaining question is whether these represent normal endolysosomal intermediates or reflect a defect in endosomal maturation caused by Vps41 KO.

The advantage of the FIB-SEM approach is that a single sample contains hundreds of organelles for correlation between FM and EM. A drawback is that FIB-SEM is not (yet) compatible with labeling of specific proteins. As second functional 3D CLEM approach we used semi-thin (300 nm) Tokuyasu cryosections, which we first viewed by FM and then by electron tomography (ET)[28,51,52] (figure 5) (section CLEM). Cryosections are made at cryogenic temperature from deeply frozen samples, which obviates the need for resin embedding and OsO4 fixation or contrasting. This strongly increases epitope preservation, which is why cryosections are the technique of choice for immuno-EM[37] and antibody-based section CLEM [27,28,51]. Since

FM imaging is done before staining with heavy metals, this brings the additional advantage that many fluorescent probes (e.g. GFP, mCherry, Alexa dyes) retain fluorescence at a higher level than in epoxy resins (e.g. EPON) or acrylate resins (e.g. Lowicryl) [58–62]. Furthermore, in the FM there is no background from the embedding media, which is a major problem when using epoxy resin embedded samples for section CLEM[63]. Lastly, since the absence of embedding media allows fluorescent probes to penetrate deep into the section, cryosections produce a high fluorescent yield[64]. Cryosections, however, lack the rigidness and contrast required for FIB-SEM, which is why we use ET to collect 3D images[28,52]. ET has a smaller field of view and a longer acquisition time, therefore lower throughput than FIB-SEM, but provides better image contrast and a higher resolving power (2-5 nm versus 5-10 nm in SEM).

Also for the functional section CLEM approach, samples need to be processed through the steps for Tokuyasu cryosections prior to FM. Not all probes retain visible through this process (table 1). As a consequence, application of this method is more constrained than the live cell to FIB-SEM approach. Fluorescent signals in cryosections are likely lost during the process of cryoprotection (by 2.3M sucrose) or freezing of samples, which could alter the fluorophore. Alternatively, the preparation steps required for labeling of thawed cryosections may cause washout of probes[65].

We used the section CLEM approach to study the localization of endocytosed TF-Chol in combination with Immunolabeling of LAMP-1. We found that TF-Chol added to the medium primarily accumulated in late endosomal-lysosomal compartments, as defined by the presence of LAMP-1 and morphology by ET. The data show the potency of cryosections for functional CLEM using high resolution 3D EM images in combination with Immunolabeling. The applicability of this approach will be broadened by the development of additional probes that retain their fluorescence in thawed cryosections.

Previously, we showed that GFP can be followed by live tracking before preparation to CLEM (Fermie et al. Traffic 2018)[27,29]. A similar use can be added to the probes presented in this paper to study the functional status of a given organelle over time. For example, fluorescent live-cell imaging with functional probes has been broadly used to examine endosome or phagosome maturation[66,67] or neuronal signaling[68]. Additionally, most biosensors have well-defined spectra, compatible for imaging in combination with other fluorescent probes or tags. Probe design is an important and rapid development field for FM, which by CLEM can now also be used in the interest of EM studies. Recent developments include probes for more types of chemicals inside lysosomes[69] and a panel of specific probes for other cell organelles like mitochondria, endoplasmic reticulum and the Golgi network[70]. When all these techniques are combined, the functional CLEM workflows presented in this paper can integrate information on protein localization, functional status, dynamics and 3D ultrastructure, all in a single sample and at the level of single organelles.

## Methods

### Cell culture

Hela cells were cultured at 37°C, 5% CO<sub>2</sub> incubator, in T75 culture bottles (Corning). Cells were maintained in Dulbecco's Modified Eagle's Medium (DMEM; Gibco) supplemented with 10% fetal bovine serum (FBS), 2 mM L-glutamin, 100 U/mL penicillin, 100 µg/mL streptomycin (referred to as complete DMEM). During live-cell imaging, cells were kept in phenol red-free DMEM supplemented with 2% fetal bovine serum (FBS), 2 mM L-glutamin, 100 U/mL penicillin, 100 µg/mL streptomycin (referred to as imaging medium).

### Chemicals and reagents

SiR-Lysosome kit (SC012) was purchased through Spirochrome. Magic Red cathepsin B (ICT938) was purchased through Bio-Rad Antibodies. DQ-Green BSA (D12050), LysoTracker Red DND-99 (L7528), Oregon Green BAPTA-1 dextran (O6798), dextran Alexa Fluor 488 (D22910), dextran Alexa Fluor 568 (D22912) and dextran Alexa Fluor 647 (D22914) were purchased through Thermo Fisher Scientific. TopFluor Cholesterol (810255) was purchased from Avanti Polar Lipids. LAMP1 was detected with a mouse anti-human LAMP-1 (CD107a) monoclonal antibody, purchased from BD Pharmingen (Vianen, The Netherlands).

### Characterization of various probes

For the experiment in figure 2, cells were grown to a density of 2×10<sup>5</sup> cells per coverslip. Cells were incubated with MR Cathepsin B (according to manufacturer's protocol) and dextran Alexa 647 (500 µg/ml) for 2 hours in complete DMEM at 37°C, 5% CO<sub>2</sub> conditions, followed by a rinse with medium and 15 minutes incubation with LysoTracker Red DND-99 (100 nM) in complete DMEM at 37°C, 5% CO<sub>2</sub>. Following LysoTracker addition, cells were fixed in 1× PHEM buffer containing 4% PFA and 0.1% glutaraldehyde.

For the characterization of the BAPTA-dextran, cells were seeded overnight in an 8 well µ-Slide (Ibidi GmbH, 80826). Cells were incubated with BAPTA-dextran (250 µg/ml), dextran Alexa 568 (250 µg/ml) and SiR-Lysosome (500 nM) for 3 hours, after which cells were fixed with 4% PFA in 1×PHEM for 15 minutes. Following fixation, slides were washed with 1×PHEM and imaged in buffer.

For the CLEM experiment in figure 3, cells were grown to a density of 2×10<sup>5</sup> cells per coverslip. Cells were incubated overnight with BAPTA-dextran (250 µg/ml) in complete DMEM, followed by a 3 hour incubation with SiR-Lysosome in complete DMEM. Cells were then incubated with Magic Red cathepsin B for 15 minutes before fixation in 1× PHEM buffer containing 4% PFA and 0.1% glutaraldehyde.

For the functional comparison of WT and VPS41 KO cells, cells were treated with SiR-Lysosome (500 nM) and dextran Alexa 488 (250 µg/ml) in complete medium for 3 hours, followed by a 15 minute incubation with Magic Red cathepsin B (half of manufacturer's recommendation). Cells were stringently washed in imaging medium and imaged live in a 37°C, 5% CO<sub>2</sub> conditioned environment on the microscope. Afterwards, cells were fixed in prewarmed 1× PHEM containing 4% PFA and 0.1% glutaraldehyde, and immediately imaged in fixative to make a z-stack.

### Fluorescence imaging for CLEM

Cells cultured for correlative LM/FIB-SEM were grown on Gridded Glass Coverslips with 500 µm grid size (Ibidi GmbH, 10816). Fluorescence imaging of fixed cells was

performed using a Deltavision RT widefield microscope system (GE Healthcare) equipped with a 100×/1.4NA oil immersion lens and a Cascade II EM-CCD camera (Photometrics), as well temperature and CO<sub>2</sub> controllers. Multi-channel Z-stacks were captured and deconvolved using Softworx 6.5.2 (GE Healthcare). Colocalization analysis of fluorescence data was performed using Volocity (Perkin Elmer).

### **Sample contrasting and resin embedding**

Material for electron microscopy was stained using previous protocols for enhanced electron contrast, as previously described. After fluorescent imaging, cells were postfixed with 1% OsO<sub>4</sub> with 1.5% K<sub>4</sub>Fe(II)(CN)<sub>6</sub> in 1× PHEM for 1 hour on ice, followed by washing steps in ddH<sub>2</sub>O and contrast enhancement with 1% thiocarbohydrazide in ddH<sub>2</sub>O at 30°C for 15 minutes. Cells were then washed in ddH<sub>2</sub>O and further postfixed with 1% OsO<sub>4</sub> in ddH<sub>2</sub>O on ice for 30 minutes. Cells were washed in ddH<sub>2</sub>O and stained with 2% uranyl acetate in ddH<sub>2</sub>O at room temperature, followed by further washing steps with ddH<sub>2</sub>O. Finally, cells were stained with Walton's lead aspartate (pH 5.6) for 30 minutes at 60°C. Finally, samples were subjected to a graded ethanol series for dehydration. After dehydration, samples were embedded in Epon resin (ratio: 12g Glycid Ether 100, 8g dodeceny succinic anhydride, 5.5g methyl nadic anhydride, 560 µL N-benzyl dimethylamine).

### **Focused ion beam scanning electron microscopy**

After Epon polymerization, the resin blocks were removed from the coverslips and prepared for FIB-SEM imaging as in Fermie et al. with slight modifications[29]. If liquid nitrogen was insufficient to remove the glass coverslip and resin block, the coverslip was dissolved by immersing the blocks in 48% hydrofluoric acid for 15 to 20 minutes, followed by stringent washing in dH<sub>2</sub>O and overnight bakeout at 65°C to guarantee resin strength. As conductive coating of the resin surface, 6 nm gold was used instead of platinum. This had no effect on the imaging procedure.

Samples were imaged in a Scios FIB-SEM (Thermo Scientific, Eindhoven, The Netherlands) under high vacuum conditions. Individual cells were retraced based on their coordinates on the grid pattern, after which ROIs within the cells were chosen based on their fluorescence data. Using the FIB set to 30 kV, a 500 nm Pt layer was deposited over the ROI at a 1 nA current, after which trenches were milled along the sides and a staircase pattern along the front face of the ROI at 7-15 nA. Fine polishing of the front (imaging) surface was performed at 1 nA. Serial imaging was performed using Auto Slice&View (Thermo Fisher Scientific, Eindhoven, The Netherlands).

### **Data correlation and analysis**

Serial images collected by FIB-SEM were aligned using TrakEM2[71]. If needed, aligned FIB-SEM datasets were processed to correct for rotational differences between the fluorescence Z-stack and the EM volume. This was achieved through the Rotate module present in TransformJ, using quantic B-spline interpolation and isotropic resampling[72].

Features in the FIB-SEM dataset are coarsely aligned to parts of the fluorescence Z-stack (e.g. membrane protrusions, nucleus). We then used individual compartments as landmarks for refined correlation between FM and FIB-SEM throughout the EM volume. After correlation, we scored all correlated compartments for presence or absence of fluorescent signals in order to examine functional properties.

### CRISPR/Cas9 knockout of VPS41

Hela cells were transiently transfected with pSpCas9(BB)-2A-GFP (PX458)[73] encoding sgRNAs targeting VPS41 using X-tremeGENE (Merck) according to the manufacturers recommendation. sgRNAs were designed using CRISPOR (<http://crispor.tefor.net/>)[74] and target coding sequences in the N-terminal region encoded by the third coding exon. The sgRNA used was sgRNA2 AAGTATTTTCAGTTACCCCAT. GFP-positive cells were sorted using a FACSAria II flow cytometer (BD) and plated in 10 cm dishes. Colonies were picked from these plates after 1 week and expanded. To confirm VPS41 absence, total cell lysates were analyzed by Western blotting using mouse anti-VPS41 (SC-377271, Santa Cruz).

### Immunolabeling and electron tomography of TopFluor-cholesterol labeled cells

Hela cells were grown in 60 mm plastic culture dishes and incubated in medium containing TF-Chol overnight. Afterwards, they were fixed in 0.1 M phosphate buffer (pH 7.4) containing 2% paraformaldehyde and 0.2% glutaraldehyde. Fixed cells were scraped from the dishes, pelleted in 12% gelatin, cryoprotected in 2.3 M sucrose and plunge frozen according to previous protocols [27,50]. 300 nm thick cryosections were picked up on formvar coated copper grids, after which they were immunolabeled for LAMP-1 followed by secondary labeling with Alexa647-conjugated goat-anti-mouse antibodies (Thermo Scientific, A21235) and gold-conjugated Protein A (Cell Microscopy Core, UMC Utrecht, The Netherlands). Sections were then labeled using Hoechst 33342 to label nuclei. The grids were washed with dH<sub>2</sub>O and sandwiched between a microscope slide and a no. 1 coverslip in 2% methylcellulose in dH<sub>2</sub>O. Sections were imaged in a Deltavision RT widefield fluorescence microscope (GE Healthcare, U.S.A.) equipped with a Cascade II EM-CCD camera (Photometrics, U.S.A.). Grids were first imaged at 40× magnification to form a map of the section, after which regions of interest were selected using 100× magnification. After imaging the grids were removed from the microscope slide, thoroughly rinsed with H<sub>2</sub>O and contrasted for EM and embedded in methylcellulose containing uranyl acetate, according to previous protocol [50]. After drying, regions of interest were imaged using a Tecnai 20 TEM (Thermo Fischer Scientific) operating at 200 kV, equipped with an Eagle 4K×4K CCD camera running Xplore3D (Thermo Fischer Scientific) software. Single tilt image series were automatically collected with 1° tilt increments from -60° to +60°. Tomographic reconstructions were generated using IMOD [75].

### Acknowledgements

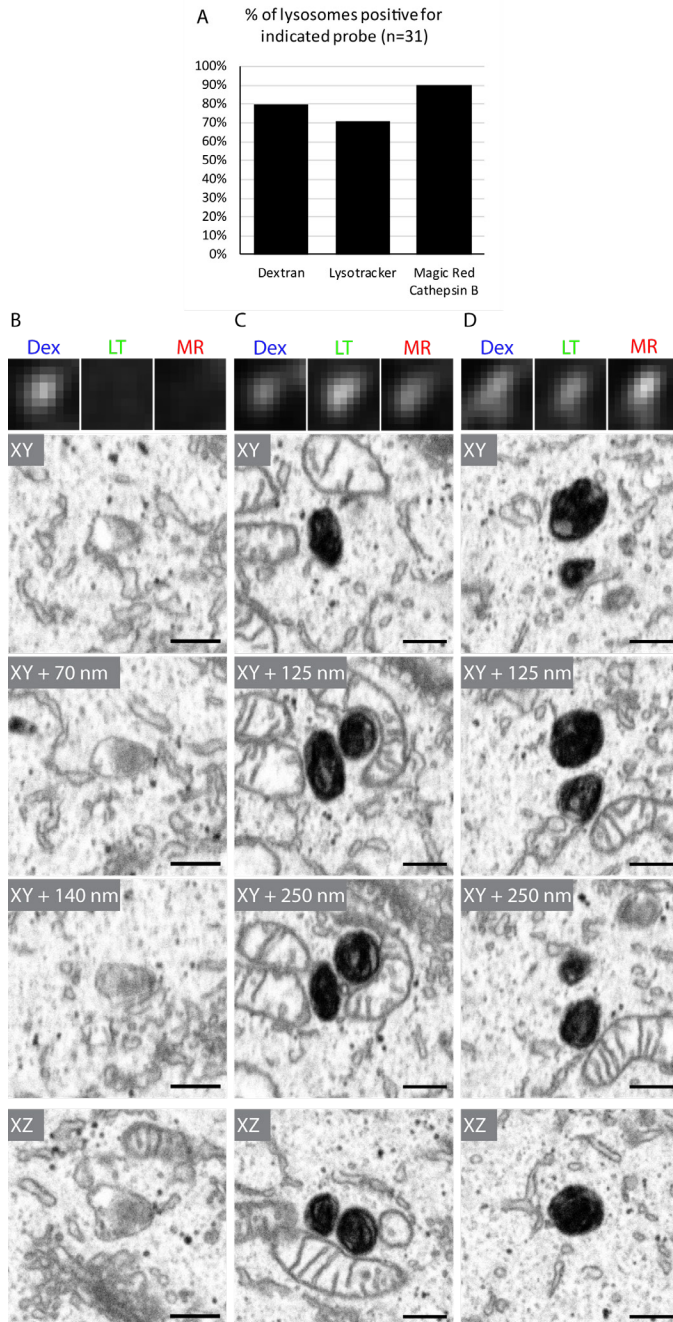
We thank Fried Zwartkruis and Susan Zwakenberg (University Medical Center Utrecht) for the assistance with the CRISPR/Cas9 gRNA design and generation of VPS41 KO Hela cell lines. We would also like to thank George Posthuma (University Medical Center Utrecht) for assistance with electron microscopy and specimen preparation. We express thanks to Chris Schneijdenberg (Utrecht University) for assistance with FIB-SEM imaging, and Elly van Donselaar (Utrecht University/ University Medical Center Utrecht) for establishing the optimized EM staining protocols.

## References

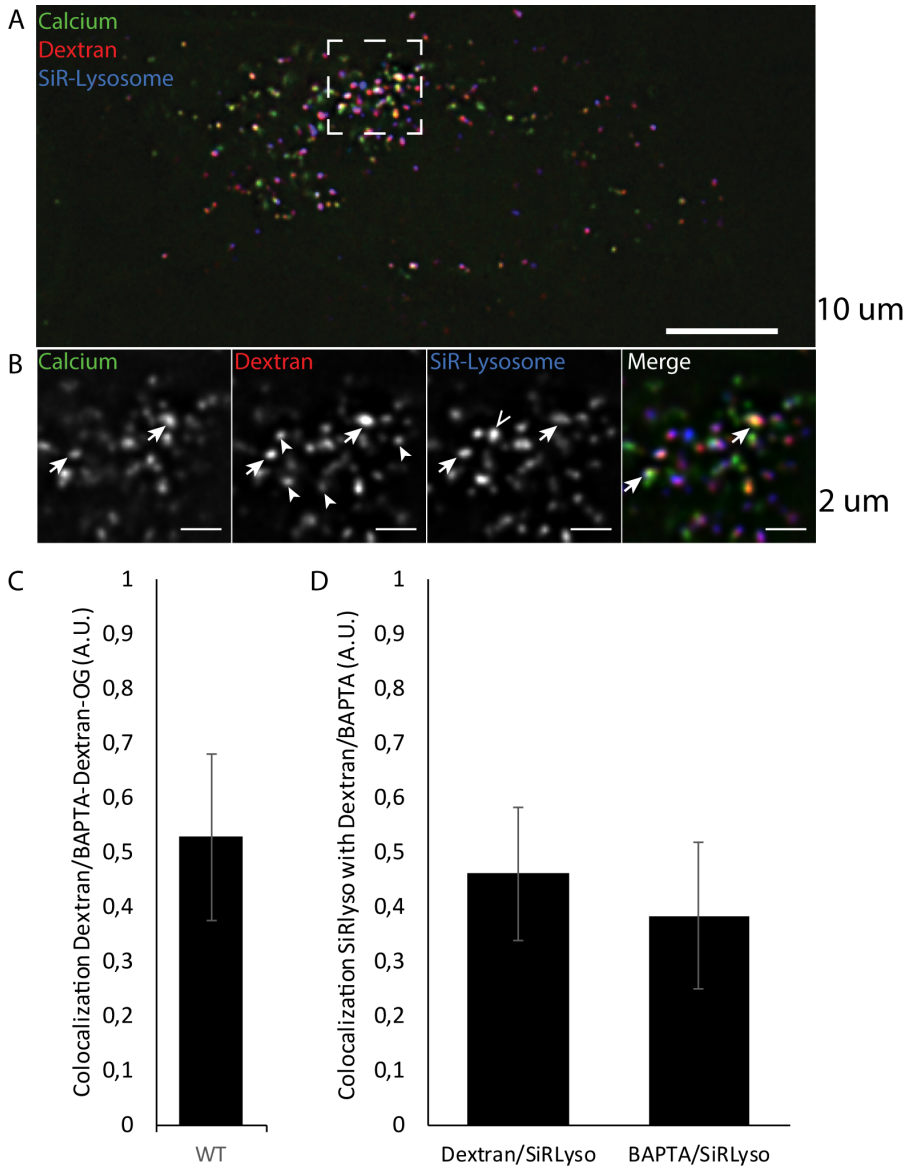
1. Sasaki K, Yoshida H. Organelle Zones. *Cell Struct Funct* 2019;
2. de Boer P, Hoogenboom JP, Giepmans BNG. Correlated light and electron microscopy: ultrastructure lights up! *Nat Methods* 2015;12:503–13.
3. de Duve C. The lysosome turns fifty. *Nat Cell Biol* 2005;7:847–849.
4. Settembre C, Fraldi A, Medina DL, Ballabio A. Signals from the lysosome: a control centre for cellular clearance and energy metabolism. *Nat Rev Mol Cell Biol* 2013;14:283–96.
5. Reggiori F, Klumperman J. Lysosome Biogenesis and Autophagy. In: *Lysosomes: Biology, Diseases, and Therapeutics*. Hoboken, NJ, USA: John Wiley & Sons, Inc.; 2016. p. 7–31.
6. Huotari J, Helenius A. Endosome maturation. *EMBO J* 2011;30:3481–500.
7. Korolchuk VI, Saiki S, Lichtenberg M, Siddiqi FH, Roberts EA, Imarisio S, Jahreis L, Sarkar S, Futter M, Menzies FM, O’Kane CJ, Deretic V, Rubinsztein DC. Lysosomal positioning coordinates cellular nutrient responses. *Nat Cell Biol* 2011;13:453–60.
8. Pu J, Guardia CM, Keren-Kaplan T, Bonifacino JS. Mechanisms and functions of lysosome positioning. *J Cell Sci* 2016;129:4329–4339.
9. van Bergeijk P, Hoogenraad CC, Kapitein LC. Right Time, Right Place: Probing the Functions of Organelle Positioning. *Trends Cell Biol* 2016;26:121–134.
10. Neeffes J, Jongsma MML, Berlin I. Stop or Go? Endosome Positioning in the Establishment of Compartment Architecture, Dynamics, and Function. *Trends Cell Biol* 2017;27:580–594.
11. Mohammadian S, Fokkema J, Agronskaia A V, Liv N, de Heus C, van Donselaar E, Blab GA, Klumperman J, Gerritsen HC. High accuracy, fiducial marker-based image registration of correlative microscopy images. *Sci Rep* 2019;9:3211.
12. Canton J, Grinstein S. *Measuring phagosomal pH by fluorescence microscopy*. Elsevier Ltd; 2017.
13. Van Noorden CJF, Jonges TGN, Van Marle J, Bissell ER, Griffini P, Jans M, Snel J, Smith RE. Heterogeneous suppression of experimentally induced colon cancer metastasis in rat liver lobes by inhibition of extracellular cathepsin B. *Clin Exp Metastasis* 1997;16:159–167.
14. Kallemeijn WW, Li KY, Witte MD, Marques ARA, Aten J, Scheij S, Jiang J, Willems LI, Voorn-Brouwer TM, Van Roomen CPAA, Ottenhoff R, Boot RG, Van Den Elst H, Walvoort MTC, Florea BI, Codée JDC, Van Der Marel GA, Aerts JMFG, Overkleeft HS. Novel activity-based probes for broad-spectrum profiling of retaining  $\beta$ -exoglucosidases in situ and in vivo. *Angew Chemie - Int Ed* 2012;51:12529–12533.
15. Herrera Moro Chao D, Kallemeijn WW, Marques ARA, Orre M, Ottenhoff R, van Roomen C, Foppen E, Renner MC, Moeton M, van Eijk M, Boot RG, Kamphuis W, Hol EM, Aten J, Overkleeft HS, Kalsbeek A, Aerts JMFG. Visualization of Active Glucocerebrosidase in Rodent Brain with High Spatial Resolution following In Situ Labeling with Fluorescent Activity Based Probes. *PLoS One* 2015;10:e0138107.
16. Van Elsland DM, Bos E, De Boer W, Overkleeft HS, Koster AJ, Van Kasteren SI. Detection of bioorthogonal groups by correlative light and electron microscopy allows imaging of degraded bacteria in phagocytes. *Chem Sci* 2016;7:752–758.
17. Gomes A, Fernandes E, Lima JLFC. Fluorescence probes used for detection of reactive oxygen species. *J Biochem Biophys Methods* 2005;65:45–80.
18. Miyawaki A, Llopis J, Heim R, McCaffery JM, Adams JA, Ikura M, Tsien RY. Fluorescent indicators for  $\text{Ca}^{2+}$  based on green fluorescent proteins and calmodulin. *Nature* 1997;388:882–887.
19. Zhong XZ, Yang Y, Sun X, Dong XP. Methods for monitoring  $\text{Ca}^{2+}$  and ion channels in the lysosome. *Cell Calcium* 2017;64:20–28.
20. McCue H V, Wardyn JD, Burgoyne RD, Haynes LP. Generation and characterization of a lysosomally targeted, genetically encoded  $\text{Ca}^{2+}$ -sensor. *Biochem J* 2013;449:449–57.
21. Qin Y, Sammond DW, Braselmann E, Carpenter MC, Palmer AE. Development of an Optical  $\text{Zn}^{2+}$  Probe Based on a Single Fluorescent Protein. *ACS Chem Biol* 2016;11:2744–2751.
22. Han Y, Goldberg JM, Lippard SJ, Palmer AE. Superiority of SpiroZin2 Versus FluoZin-3 for monitoring vesicular  $\text{Zn}^{2+}$  allows tracking of lysosomal  $\text{Zn}^{2+}$  pools. *Sci Rep* 2018;8:15034.
23. Bright NA, Davis LJ, Luzio JP. Endolysosomes Are the Principal Intracellular Sites of Acid Hydrolase Activity. *Curr Biol* 2016;26:2233–2245.
24. Rohrl C, Meisslitzer-Ruppitsch C, Bittman R, Li Z, Pabst G, Prassl R, Strobl W, Neumuller J, Ellinger A, Pavelka M, Stangl H. Combined Light and Electron Microscopy Using Diaminobenzidine Photooxidation to Monitor Trafficking of Lipids Derived from Lipoprotein Particles. *Curr Pharm Biotechnol* 2012;13:331–340.
25. Stoeck IK, Lee J-Y, Tabata K, Romero-Brey I, Paul D, Schult P, Lohmann V, Kaderali L, Bartenschlager R. Hepatitis C virus replication depends on endosomal cholesterol homeostasis. *J Virol* 2017;92:JV1.01196-17.
26. Pols MS, van Meel E, Oorschot V, ten Brink C, Fukuda M, Swetha MG, Mayor S, Klumperman J. hVps41 and

- VAMP7 function in direct TGN to late endosome transport of lysosomal membrane proteins. *Nat Commun* 2013;4:1361.
27. Rijnsoever C Van, Oorschot V, Klumperman J. Correlative light-electron microscopy (CLEM) combining live-cell imaging and immunolabeling of ultrathin cryosections. *Nat Methods* 2008;5:973–980.
  28. Mari M, Geerts WJC, Reggiori F. Immuno- and correlative light microscopy-electron tomography methods for 3D protein localization in yeast. *Traffic* 2014;15:1164–1178.
  29. Fermie J, Liv N, ten Brink C, van Donselaar EG, Müller WH, Schieber NL, Schwab Y, Gerritsen HC, Klumperman J. Single organelle dynamics linked to 3D structure by correlative live-cell imaging and 3D electron microscopy. *Traffic* 2018;354–369.
  30. Fokkema J, Fermie J, Liv N, van den Heuvel DJ, Konings TOM, Blab GA, Meijerink A, Klumperman J, Gerritsen HC. Fluorescently Labelled Silica Coated Gold Nanoparticles as Fiducial Markers for Correlative Light and Electron Microscopy. *Sci Rep* 2018;8:13625.
  31. Polishchuk RS, San Pietro E, Di Pentima A, Teté S, Bonifacino JS. Ultrastructure of long-range transport carriers moving from the trans-Golgi network to peripheral endosomes. *Traffic* 2006;7:1092–1103.
  32. Bushby AJ, Mariggi G, Armer HEJ, Collinson LM. Correlative light and volume electron microscopy: using focused ion beam scanning electron microscopy to image transient events in model organisms. *Methods Cell Biol* 2012;111:357–82.
  33. Karreman MA, Mercier L, Schieber NL, Solecki G, Allio G, Winkler F, Ruthensteiner B, Goetz JG, Schwab Y. Fast and precise targeting of single tumor cells in vivo by multimodal correlative microscopy. *J Cell Sci* 2016;129:444–56.
  34. Russell MRG, Lerner TR, Burden JJ, Nkwe DO, Pelchen-Matthews A, Domart M-C, Durgan J, Weston A, Jones ML, Peddie CJ, Carzaniga R, Florey O, Marsh M, Gutierrez MG, Collinson LM. 3D correlative light and electron microscopy of cultured cells using serial blockface scanning electron microscopy. *J Cell Sci* 2017;130:278–291.
  35. Sachse M, Urbé S, Oorschot V, Strous GJ, Klumperman J. Bilayered clathrin coats on endosomal vacuoles are involved in protein sorting toward lysosomes. *Mol Biol Cell* 2002;13:1313–28.
  36. Pols MS, Ten Brink C, Gosavi P, Oorschot V, Klumperman J. The HOPS Proteins hVps41 and hVps39 Are Required for Homotypic and Heterotypic Late Endosome Fusion. *Traffic* 2013;14:219–232.
  37. Nickerson DP, Brett CL, Merz AJ. Vps-C complexes: gatekeepers of endolysosomal traffic. *Curr Opin Cell Biol* 2009;21:543–551.
  38. Balderhaar HJK, Ungermann C. CORVET and HOPS tethering complexes - coordinators of endosome and lysosome fusion. *J Cell Sci* 2013;126:1307–16.
  39. van der Beek J, Jonker C, van der Welle R, Liv N, Klumperman J. CORVET, CHEVI and HOPS - multisubunit tethers of the endo-lysosomal system in health and disease. *J Cell Sci* 2019;132:jcs189134.
  40. Solinger J a, Spang A. Tethering complexes in the endocytic pathway: CORVET and HOPS. *FEBS J* 2013;280:2743–57.
  41. Swetha MG, Sriram V, Krishnan KS, Oorschot VMJ, ten Brink C, Klumperman J, Mayor S. Lysosomal membrane protein composition, acidic pH and sterol content are regulated via a light-dependent pathway in metazoan cells. *Traffic* 2011;12:1037–1055.
  42. Lloyd-Evans E, Waller-Evans H, Peterneva K, Platt FM. Endolysosomal calcium regulation and disease. *Biochem Soc Trans* 2010;38:1458–1464.
  43. Medina DL, Di Paola S, Peluso I, Armani A, De Stefani D, Venditti R, Montefusco S, Scotto-Rosato A, Prezioso C, Forrester A, Settembre C, Wang W, Gao Q, Xu H, Sandri M, Rizzuto R, De Matteis MA, Ballabio A. Lysosomal calcium signalling regulates autophagy through calcineurin and TFEB. *Nat Cell Biol* 2015;17:288–99.
  44. Grimm C, Bartel K, Vollmar AM, Biel M. Endolysosomal cation channels and cancer—a link with great potential. *Pharmaceuticals* 2018;11:1–8.
  45. Di Paola S, Scotto-Rosato A, Medina DL. TRPML1: The Ca(2+)retaker of the lysosome. *Cell Calcium* 2018;69:112–121.
  46. White C, McGeown G. Imaging of changes in sarcoplasmic reticulum [Ca<sup>2+</sup>] using Oregon Green BAPTA 5N and confocal laser scanning microscopy. *Cell Calcium* 2002;31:151–159.
  47. Christensen K, Myers JT, Swanson J. pH-dependent regulation of lysosomal calcium in macrophages. *J Cell Sci* 2002;115:599–607.
  48. Morgan AJ, Davis LC, Galione A. Imaging approaches to measuring lysosomal calcium. Elsevier Ltd; 2015.
  49. Yang J, Zhao Z, Gu M, Feng X, Xu H. Release and uptake mechanisms of vesicular Ca<sup>2+</sup>-stores. *Protein Cell* 2018;10:1–12.
  50. Slot JW, Geuze HJ. Cryosectioning and immunolabeling. *Nat Protoc* 2007;2:2480–2491.
  51. Vicidomini G, Gagliani MC, Canfora M, Cortese K, Frosi F, Santangelo C, Di Fiore PP, Boccacci P, Diaspro A, Tacchetti C. High Data Output and Automated 3D Correlative Light-Electron Microscopy Method. *Traffic*

- 2008;9:1828–1838.
52. Zeuschner D, Geerts WJC, van Donselaar E, Humbel BM, Slot JW, Koster AJ, Klumperman J. Immuno-electron tomography of ER exit sites reveals the existence of free COPII-coated transport carriers. *Nat Cell Biol* 2006;8:377–383.
  53. Möbius W, Ohno-Iwashita Y, van Donselaar EG, Oorschot VMJ, Shimada Y, Fujimoto T, Heijnen HFG, Geuze HJ, Slot JW. Immuno-electron microscopic localization of cholesterol using biotinylated and non-cytolytic perfringolysin O. *J Histochem Cytochem* 2002;50:43–55.
  54. Edgar JR, Manna PT, Nishimura S, Banting G, Robinson MS. Tetherin is an exosomal tether. *Elife* 2016;5:1–19.
  55. Hölttä-Vuori M, Sezgin E, Eggeling C, Ikonen E. Use of BODIPY-Cholesterol (TF-Chol) for Visualizing Lysosomal Cholesterol Accumulation. *Traffic* 2016;17:1054–1057.
  56. Bright NA, Reaves BJ, Mullock BM, Luzio JP. Dense core lysosomes can fuse with late endosomes and are re-formed from the resultant hybrid organelles. *J Cell Sci* 1997;110.
  57. Nickerson DP, Brett CL, Merz AJ. Vps-C complexes: gatekeepers of endolysosomal traffic. *Curr Opin Cell Biol* 2009;21:543–551.
  58. Peddie CJ, Liv N, Hoogenboom JP, Collinson LM. *Integrated Light and Scanning Electron Microscopy of GFP-Expressing Cells*. 1st ed. Elsevier Inc.; 2014.
  59. Peddie CJ, Blight K, Wilson E, Melia C, Marrison J, Carzaniga R, Domart MC, O’Toole P, Larjani B, Collinson LM. Correlative and integrated light and electron microscopy of in-resin GFP fluorescence, used to localise diacylglycerol in mammalian cells. *Ultramicroscopy* 2014;143:3–14.
  60. Chong MK, Chua AJS, Tan TTT, Tan SH, Ng ML. *Microscopy techniques in flavivirus research*. *Micron* 2014;59:33–43.
  61. Kaufmann R, Schellenberger P, Seiradake E, Dobbie IM, Jones EY, Davis I, Hagen C, Grünewald K. Super-resolution microscopy using standard fluorescent proteins in intact cells under cryo-conditions. *Nano Lett* 2014;14:4171–4175.
  62. Kim D, Deerinck TJ, Sigal YM, Babcock HP, Ellisman MH, Zhuang X. Correlative Stochastic Optical Reconstruction Microscopy and Electron Microscopy. *PLoS One* 2015;10:e0124581.
  63. Karreman M a, Agronskaia A V, van Donselaar EG, Vocking K, Fereidouni F, Humbel BM, Verrips CT, Verkleij AJ, Gerritsen HC. Optimizing immuno-labeling for correlative fluorescence and electron microscopy on a single specimen. *J Struct Biol* 2012;180:382–6.
  64. Hassink G, Slotman J, Oorschot V, Van Der Reijden BA, Monteferrario D, Noordermeer SM, Van Kerkhof P, Klumperman J, Strous GJ. Identification of the ubiquitin ligase Triad1 as a regulator of endosomal transport. *Biol Open* 2012;1:607–14.
  65. Möbius W, Posthuma G. Sugar and ice: Immuno-electron microscopy using cryosections according to the Tokuyasu method. *Tissue Cell* 2018;0–1.
  66. Modi S, Swetha MG, Goswami D, Gupta GD, Mayor S, Krishnan Y. A DNA nanomachine that maps spatial and temporal pH changes inside living cells. *Nat Nanotechnol* 2009;4:325–330.
  67. Thekkan S, Jani MS, Cui C, Dan K, Zhou G, Becker L, Krishnan Y. A DNA-based fluorescent reporter maps HOCl production in the maturing phagosome. *Nat Chem Biol* 2018;1.
  68. Grienberger C, Konnerth A. *Imaging Calcium in Neurons*. *Neuron* 2012;73:862–885.
  69. Zhu J-L, Xu Z, Yang Y, Xu L. Small-molecule fluorescent probes for specific detection and imaging of chemical species inside lysosomes. *Chem Commun* 2019;
  70. Zhu H, Fan J, Du J, Peng X. *Fluorescent Probes for Sensing and Imaging within Specific Cellular Organelles*. *Acc Chem Res* 2016;49:2115–2126.
  71. Cardona A, Saalfeld S, Schindelin J, Arganda-Carreras I, Preibisch S, Longair M, Tomancak P, Hartenstein V, Douglas RJ. TrakEM2 software for neural circuit reconstruction. *PLoS One* 2012;7.
  72. Meijering E, Dzyubachyk O, Sma I. *Methods for cell and particle tracking*. 1st ed. Elsevier Inc.; 2012.
  73. Ran FA, Hsu PD, Wright J, Agarwala V, Scott DA, Zhang F. Genome engineering using the CRISPR-Cas9 system. *Nat Protoc* 2013;8:2281–2308.
  74. Haeussler M, Schönig K, Eckert H, Eschstruth A, Mianné J, Renaud J-B, Schneider-Maunoury S, Shkumatava A, Teboul L, Kent J, Joly J-S, Concordet J-P. Evaluation of off-target and on-target scoring algorithms and integration into the guide RNA selection tool CRISPOR. *Genome Biol* 2016;17:148.
  75. Kremer JR, Mastronarde DN, McIntosh JR. Computer visualization of three-dimensional image data using IMOD. *J Struct Biol* 1996;116:71–6.



Supplementary figure 1: Supplementary data on the correlated organelles of dataset 1. A, analysis of labeling density of endo-lysosomal probes. All three probes label the majority of lysosomes found in dataset 1. B, additional virtual slices of the late endosome shown in Figure 2H, left panel, in both XY and XZ planes. C, additional virtual slices of the two lysosomes shown in figure 2H, middle panel, in both XY and XZ planes. D, additional virtual slices of the two lysosomes shown in figure 2H, right panel, in both XY and XZ planes. Distances indicated in B-D are shifts in Z, relative to the first plane shown in the figure. Scale bars: B-D; 400 nm.



Supplementary figure 2: Evaluation of BAPTA-dextran as endocytosed calcium probe. A, examination of BAPTA-dextran as endosomal calcium sensor. Cells were loaded with BAPTA-dextran (calcium), dextran-Alexa568 (dextran) and SiR-Lysosome cathepsin D. BAPTA fluorescence is seen in compartments containing dextran and SiR-Lysosome. B, magnified fluorescence image of labeled cell from A, showing overlap of probes. BAPTA-dextran follows the same endocytic route as Dex-A568 and reaches lysosomal compartments (arrows). Not all compartments reached by endocytic cargo contain calcium (closed arrowheads). A small population of lysosomes is not reached by either BAPTA-dextran or dextran-A568, which are highly enriched for SiR-Lysosome (open arrowheads). C, analysis of colocalization of dextran-Alexa568 with BAPTA-dextran. A substantial fraction of overlap is seen between both probes. D, colocalization analysis of dextran and BAPTA-dextran with SiR-Lysosomes. Both probes overlap with SiR-Lysosomes, indicating they reach mature endo-lysosomal and lysosomal compartments. Scale bars: A; 10  $\mu$ m, B; 2  $\mu$ m.

<b>Dextran</b>	<b>MRB</b>	<b>SiRLyso</b>	<b>Late endosomes n= 66</b>	<b>Endolysosomes n = 39</b>	<b>Lysosomes n=145</b>
+	-	-	66,7%	20,5%	8,3%
-	+	-	0,0%	0,0%	0,0%
-	-	+	0,0%	0,0%	0,7%
+	+	-	0,0%	0,0%	0,0%
+	-	+	10,6%	23,1%	6,9%
-	+	+	6,1%	5,1%	26,2%
+	+	+	16,7%	51,3%	57,9%

Supplementary table 1: Single Organelle Microscopy. Combined labeling distributions per organelle type. Correlated organelles of dataset 2/figure 3.

<b>Dextran</b>	<b>MRB</b>	<b>SiRLyso</b>	<b>Late endosomes n= 66</b>	<b>Endolysosomes n = 104</b>	<b>Lysosomes n=171</b>
+	-	-	74.2%	36.5%	4.1%
-	+	-	0.0%	0.0%	0.0%
-	-	+	7.6%	0.0%	0.6%
+	+	-	1.5%	1.0%	0.0%
+	-	+	3.0%	1.9%	0.0%
-	+	+	12.1%	45.2%	71.3%

Supplementary table 2: Single Organelle Microscopy. Combined labeling distributions per organelle type. Correlated organelles of VPS41 KO cells (table 3/figure 4).





# A bimodal endocytic probe for three-dimensional correlative light and electron microscopy

---

## Chapter 4

---

Job Fermie<sup>1,2</sup>, Tineke Veenendaal<sup>1</sup>, Cilia de Heus<sup>1</sup>, Viola Oorschot<sup>1,3</sup>, Suzanne van Dijk<sup>1</sup>, Lin Yang<sup>4</sup>, Wei Li<sup>4</sup>, Wally Müller<sup>5</sup>, George Posthuma<sup>1</sup>, Hans Gerritsen<sup>2</sup>, Judith Klumperman<sup>1</sup>, Nalan Liv<sup>1</sup>

1. Section Cell Biology, Center for Molecular Medicine, University Medical Center Utrecht, Utrecht University, Utrecht, The Netherlands
2. Section Molecular Biophysics, Debye Institute for Nanomaterials Science, Utrecht University, Utrecht, The Netherlands
3. Present address: Monash Micro Imaging, Monash University, Melbourne, Victoria, Australia
4. Lab of Electron microscopy, Institute of Genetics & Developmental Biology, Chinese Academy of Sciences, Beijing, China
5. Section Cell Biology & Mycology, Department of Biology, Utrecht University, Utrecht, The Netherlands

Manuscript in preparation

## Abstract

Correlative light and electron microscopy (CLEM) can infer molecular, functional and dynamic information to ultrastructure by linking information of different imaging modalities. One of the main challenges in CLEM is the accurate registration of fluorescent signals to electron microscopy (EM), especially in 3D-CLEM. Here, we present fluorescent BSA-gold (fBSA-Au), a bimodal endocytic tracer as fiducial marker for 2D and 3D CLEM applications. fBSA-Au consists of colloidal gold (Au) particles stabilized with fluorescent bovine serum albumin (BSA). The conjugate is efficiently endocytosed and distributed throughout cells, and highly visible in both fluorescence microscopy (FM) and EM. We demonstrate the use of fBSA-Au in several 2D and 3D CLEM applications using Tokuyasu cryosections and resin-embedded material. As a fiducial marker, fBSA-Au facilitates rapid retracing of regions of interest between FM and EM modalities and enables accurate (50-150 nm) correlation of fluorescence to EM data. Compared to fiducials applied after sectioning, fBSA-Au has the advantage that it is present in endocytic organelles and does not obscure any cellular ultrastructure. The broad applicability and visibility makes fBSA-Au an excellent endocytic fiducial marker for 2D and 3D CLEM applications.

## Introduction

The ability to characterize the spatial and temporal characteristics of organelles and proteins is crucial in many areas of cell biology. These properties are commonly examined by use of fluorescence microscopy (FM). FM is highly sensitive, has a large toolbox to simultaneously analyze multiple cellular parameters and can be used to examine the dynamics of processes in live cells. A limitation, however, is its inability to record the ultrastructural context underlying the localization patterns. To obtain this information, electron microscopy (EM) is the method of choice. Its greater resolving power is uniquely suited to locate proteins within the cellular context, thanks to its ability to directly visualize membranes and other subcellular structures. However, specific proteins or structures of interest cannot always be discerned by morphology alone and additional, electron-dense labeling methods are required to visualize them. Various labeling methods are available for EM, such as immunolabeling with colloidal gold [1,2] or peroxidase-based methods generating osmiophilic precipitates [3–5]. These strategies do have limitations though, as the electron-dense precipitates generated by peroxidase reactions can obscure ultrastructural detail and immunolabels have an inherently limited penetration into specimens [6,7]. The level of penetration can be improved by permeabilization using detergents, but at the cost of ultrastructural preservation. A strategy to overcome these drawbacks is correlative light and electron microscopy (CLEM), which integrates the data from FM and EM on a single sample. This way, CLEM can use the large reporter diversity and sensitivity from FM to provide localization information, and infer this information to high-resolution morphological data, without the limitations of EM labeling.

One of the main challenges in CLEM is to accurately retrace fluorescent label from the FM to the corresponding structure in EM. Retracing specific fluorescent cells or subcellular structures within a large dataset requires reference points that must be easily identifiable in both modalities. These can be naturally formed landmarks such as branching blood vessels and unique cell shapes [8], or artificial marks on the sample support [9–12] or the sample itself [8,13–15]. Yet, these landmarks do not provide the required registration accuracy to correlate fluorescence signals to

individual subcellular structures. In addition, they may not always be present in quantities sufficient for accurate registration. For these applications, correlation is ideally achieved through artificial fiducials [16–19]. Fiducials are particles easily visible in both FM and EM, which are small enough to not obscure morphological details (<100 nm). A variety of particles has been developed and used in correlative methods, achieving correlation accuracies well below 100 nm [17–20]. These approaches work most efficiently in 2D CLEM applications, by which the fiducials are commonly applied to the surface of a substrate, i.e. on a coverslip or the formvar layer of an EM grid. However, with the increasing popularity of live-cell and 3D CLEM applications, there is a pressing need for strategies to distribute fiducials in 3D, which is as of yet unaddressed.

To guarantee accurate registration in 3D CLEM applications, fiducials should be present throughout the entire volume of interest. The endosomal system naturally provides a 3D network of vesicular structures throughout the cell, and is easily reached and manipulated from the extracellular environment. This triggered us to explore the endosomal system as means to distribute fiducials throughout the cell. Endocytic tracers such as dextran, albumins or nanoparticles conjugated to fluorophores or colloidal gold are commonly used to mark endosomal compartments. One of the most applied endocytic probes, bovine serum albumin (BSA), efficiently labels early endosomes, late endosomes and (auto)lysosomes, and can be conjugated to a variety of fluorophores and colloidal particles[21–23]. BSA conjugates to fluorophores or gold particles have been used in the past for either FM or EM approaches. These conjugates are highly visible and show no cytotoxicity, even after prolonged chase times[23–25]. We reasoned that fluorescently labeled BSA conjugated to electron dense particles could function as an efficient fiducial for 3D CLEM, but no such probe is available to date.

Here, we present an endocytic tracer consisting of 5 or 10 nm colloidal gold stabilized with fluorescently labeled BSA, hereafter named fBSA-Au<sup>5</sup> and fBSA-Au<sup>10</sup>, respectively. We demonstrate the applicability of fBSA-Au as fiducial marker in a variety of 3D CLEM approaches using Tokuyasu CLEM and resin-embedding CLEM. We show that the small size of the conjugate enables efficient endocytosis, whereas the high atomic number of the gold colloids ensures good visibility in the EM. Importantly, the bimodal nature of the tracer guarantees accurate registration of FM and EM data, by which endocytic compartments containing multiple fluorescent-gold colloids serve as fiducial landmarks. Finally, the uniform size of the gold particles ensures excellent compatibility with immunoEM (double) labeling strategies[26]. These benefits make fBSA-Au a highly useful tool for both 2D and 3D CLEM.

## Results:

### fBSA-Au particles are stable and mono disperse

As electron-dense core of the bimodal probe, we chose to use colloidal gold particles nominally sized at 5 and 10 nm, because of their small size and high visibility in EM. The small size guarantees efficient endocytosis and compatibility with other immunoEM methods. Using the protocol developed by Slot et al.[26,27], we synthesized mono disperse colloidal particles of different sizes (figure 1A, D, G). The resulting gold colloids were stabilized with BSA-Alexa555 (Thermo Scientific) and purified using centrifugation on a glycerol gradient to filter out unbound BSA-Alexa555. This process yielded BSA-conjugated particles of uniform size, with fBSA-Au<sup>5</sup> averaging  $5.8 \pm 0.7$  nm and fBSA-Au<sup>10</sup> averaging  $8.6 \pm 0.5$  nm, as measured

in transmission electron microscopy (TEM) (figure 1G). Interesting enough, BSA binding to the particles could not be detected using TEM. This is likely the result of the low electron contrast of the BSA, which is poorly visible in EM without heavy metal contrasting.

Stabilization of the gold particles with BSA-Alexa555 resulted in a detectable shift in size distribution, indicating binding of BSA-Alexa555 to the gold particles without forming aggregates of larger sizes. To test clustering behavior, size distributions of the particles were recorded using dynamic light-scattering (DLS) (figure 1C, F). Here, we found that both the 'bare' and 'functionalized' particles remain non-clustered in solution. Furthermore, we found that fBSA-Au conjugates remain stable in solution over extended periods of time, showing no signs of clustering or precipitation after several months of storage at 4°C. Together, these data show that colloidal gold particles can be functionalized with BSA-Alexa555, after which the resulting conjugates remain monodisperse, uniformly sized and stable in solution.

### fBSA-Au is efficiently endocytosed and transported by the endosomal system

Following characterization of the size and clustering behavior of the conjugates, we tested their feasibility for CLEM experiments. To be useful as endocytic CLEM probe, the probes should be non-toxic to cells, efficiently endocytosed and brightly fluorescent throughout the experiment.

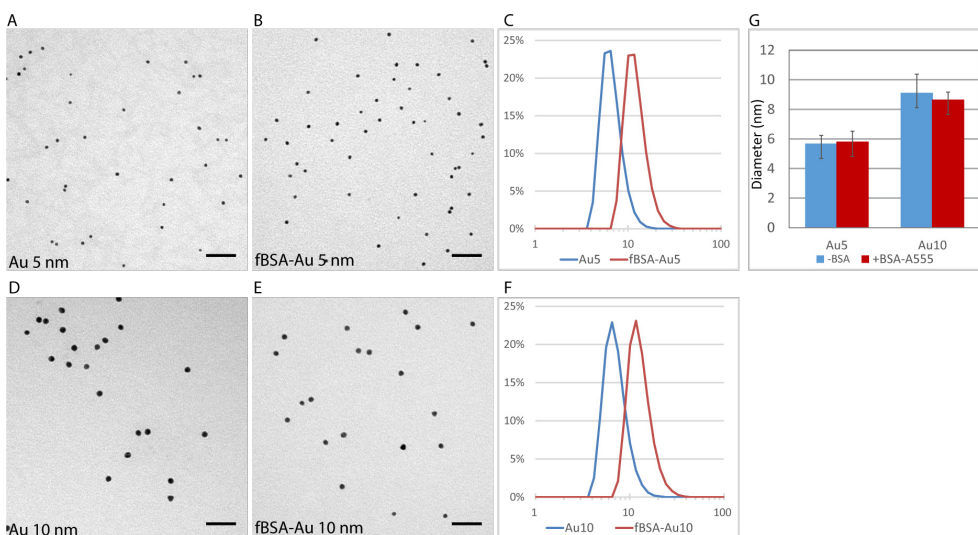


Figure 1: Characterization of synthesized fBSA-Au conjugates. (A) Representative TEM micrographs of 5 nm colloidal gold, showing the monodisperse nature of the particles before and (B) after BSA functionalization. (C) DLS measurements showing the size distribution of 5 nm colloidal gold and BSA-Alexa555 functionalized particles. Functionalization causes a shift in size distribution, but does not induce larger aggregates. (D) Representative TEM micrographs of 10 nm colloidal gold before and (E) after BSA functionalization. (F) DLS measurements showing the size distribution of 10 nm colloidal gold and BSA-Alexa555 functionalized particle. BSA functionalization causes a shifted size distribution, but does not induce larger aggregates. (G) Sizing of Au5 and Au10 particles determined by TEM. Both Au5 and Au10 are homogeneously sized. Unlike in DLS measurements, the apparent size of the functionalized particles does not increase after BSA functionalization, likely due to the poor visibility of the electron-lucent BSA. Graph depicts mean +/- S.D. Scale bars: A, B, D, E: 50 nm.

We first examined the uptake efficiency and localization of internalized fBSA-Au<sup>5</sup> using FM. After endocytosis, BSA conjugates are predominantly targeted to the degradative path of the endosomal system, where they accumulate in late endosomes and lysosomes. We incubated HeLa cells with fBSA-Au<sup>5</sup> for 3 hours to label the entire endosomal pathway, including lysosomes which are the terminal compartments of the endocytic route[23,28]. Following uptake, cells were fixed and immunolabeled for EEA1 and LAMP-1 to mark early endosomal and late endosomal/lysosomal compartments respectively. This showed that internalized fBSA-Au<sup>5</sup> is visible as strongly fluorescent spots that colocalize with both EEA1 and LAMP-1 (figure 2A), indicating that fBSA-Au<sup>5</sup> is efficiently taken up by cells and transported to both early and late endocytic compartments.

To examine whether fBSA-Au<sup>10</sup> is also transported to lysosomes and reaches the same compartments as the generic endocytosis marker Dextran, we incubated HeLa cells with both Dextran488 and fBSA-Au<sup>10</sup> for 3 hours[29]. Following incubation, cells were fixed and examined by FM. We found that fBSA-Au<sup>10</sup>, like fBSA-Au<sup>5</sup>, is readily taken up resulting in the appearance of brightly fluorescent spots. The majority of fBSA-Au<sup>10</sup> positive spots also contained Dextran488 (figure 2B). This indicates that use of fBSA-Au<sup>10</sup> is compatible with application of the commonly used endocytic marker Dextran and that both probes follow the same route to lysosomes.

Finally, we examined whether the fBSA-Au probes could be used in live cell imaging, which requires bright and stable fluorescence of the administered probe. After incubating cells for 3 hours fBSA-Au<sup>5</sup>, coverslips were live imaged with widefield FM. This showed that fBSA-Au<sup>5</sup> positive spots actively moved inside the cells (figure 2C, supplementary video 1) and remained brightly fluorescent over 250 acquired frames during live-cell imaging. We conclude from these combined studies that fBSA-Au is an appropriate endocytic probe suitable for FM studies, including live-cell imaging.

### **fBSA-Au is an efficient fiducial for 2D on-section CLEM**

After validating the endocytosis of fBSA-Au<sup>5</sup> and fBSA-Au<sup>10</sup>, we tested the feasibility of these conjugates for CLEM experiments. First, we tested a 2D on-section CLEM setup using ultrathin Tokuyasu cryosections, the most sensitive method for immun-EM[9,15,30,31]. Since cryosections show no fluorescent background signal caused by resin, they are uniquely suitable for imaging by both FM and EM. Moreover, since epitopes are generally well preserved in this approach, CLEM applications using cryosections often involve on-section labeling with a fluorescently tagged antibody, followed by colloidal gold conjugated to Protein A. The fluorescent labeling is thereby used to select regions of interest (ROIs) for subsequent EM imaging. The fluorescence signal obtained from cryosections is, however, limited by the thickness of the sections, which is circa 70 nm. Therefore, fBSA-Au<sup>5</sup> fluorescence must be sufficiently intense to be used as fiducial in this approach.

HeLa cells were incubated with fBSA-Au<sup>5</sup> for 3 hours, after which samples were prepared for cryosectioning and immunolabeling according a well-established protocol[2]. fBSA-Au<sup>5</sup> was chosen for this and following experiments as its small size enables easy distinction from commonly used 10 or 15 nm-sized immunogold labels. Sections were immunolabeled with monoclonal CD63 antibodies, a marker for late endosomes and lysosomes, followed by secondary labeling with Alexa488-tagged rabbit antibodies and 10nm sized protein-A-gold. By FM we found that the Alexa555 fluorophore of fBSA-Au<sup>5</sup> withstood the aldehyde fixation, cryoprotection and plunge freezing steps required for preparation of cryosections. The fBSA-Au<sup>5</sup>

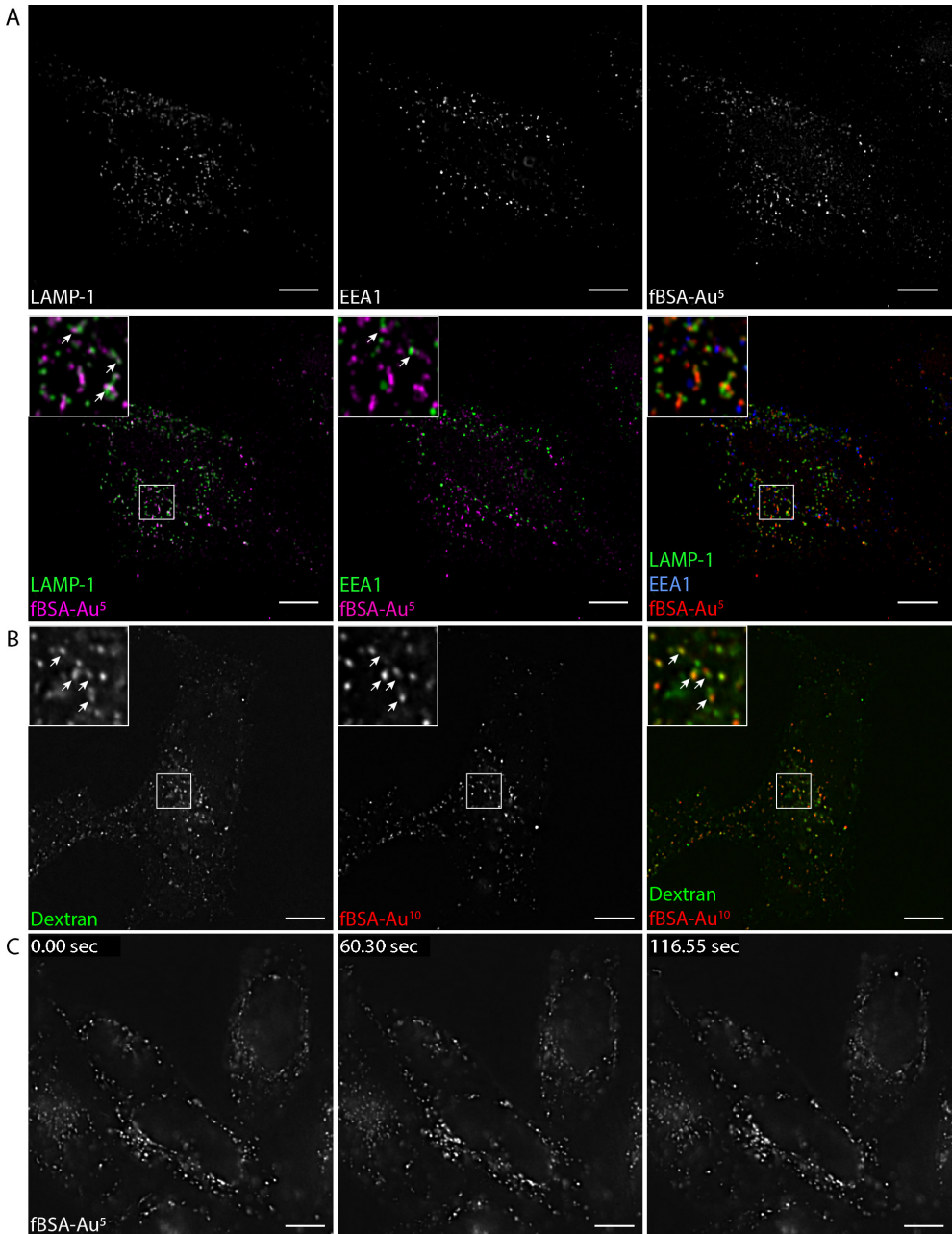


Figure 2: fBSA-Au is a highly fluorescent, efficiently internalized endocytic tracer. (A) Fluorescence images of fixed HeLa cells incubated with fBSA-Au<sup>5</sup> and immunolabeled for EEA1 and LAMP-1. fBSA-Au<sup>5</sup> is visible in both EEA1 and LAMP1 positive compartments, i.e. throughout the endosomal system. (B) Fluorescence images of fixed HeLa cells incubated with fBSA-Au<sup>10</sup> and Dextran-Alexa488. fBSA-Au<sup>10</sup> is readily endocytosed and largely co-localizes with Dextran (indicated by arrows). (C) Stills from supplementary video 1 of live HeLa cells loaded with fBSA-Au<sup>5</sup>. fBSA-Au<sup>5</sup> has sufficient fluorescence intensity to employ time-lapse experiments with high temporal resolution. Scale bars: A-C: 10  $\mu$ m.

signal was clearly visible by FM of the 70 nm thin sections, where it largely colocalized with CD63 labeling (figure 3A). We then selected ROIs for imaging in TEM, and retraced Alexa555 fluorescence spots to EM ultrastructure (figure 3B, C). We performed an initial correlation based on recognizable features on the grid, such as nuclei and unique cell shapes (figure 3A, B), to find back labeled structures in both FM and EM. Here, we found that Alexa555 labeled compartments in FM always contained 5 nm gold upon EM inspection. The reverse was also valid: gold-containing endosomes and lysosomes identified in EM always contained Alexa555 fluorescence when correlated back to FM image (see Figure 3D). This showed that fBSA-Au<sup>5</sup> fluorescence precisely correlated to endosomal compartments containing Au<sup>5</sup>.

Notably, the intensity of the fBSA-Au<sup>5</sup> fluorescent spots correlated well to the number of gold particles present in a compartment; bright fluorescent spots correlated to compartments with large numbers of gold particles, whereas small, yet readily detectable fluorescent spots correlated to individual particles or small clusters of gold (figure 3D). This fluorophore-gold correlation is made possible since both fluorescent and gold signal are from the same section, containing precisely the same number of fBSA-Au<sup>5</sup> particles.

To establish the resolution of the correlation approach, we selected the center of fBSA-Au<sup>5</sup> fluorescence for a given organelle on FM images and the center of the same organelle in EM images. By this we reached sub-organelle accuracy registration. For example, manual picking of 15 pairs of FM and EM fBSA-Au<sup>5</sup> signals followed by semi-automated correlation with a previously established correlation algorithm, ec-CLEM[32] (supplementary figure 1), resulted in a registration accuracy between 60-130nm. Importantly, this high accuracy of correlation also enabled us to retrace organelles labeled for CD63 but lacking fBSA-Au<sup>5</sup> (figure 3).

These data show that the fBSA-Au probe correlates with 100% efficiency between the FM and EM modalities, and by both distribution and intensity can be reliably used as a fiducial marker to overlay FM to EM images. Importantly, mapping the constellation of multiple fBSA-Au labeled compartments provides the resolution to retrace fluorescently-labeled structures that lack fBSA-Au, which allows a broad application of the probe to endo-lysosomal as well as other structures. We conclude that the avid visibility in FM and EM and its compatibility to combine with immunogold labeling makes fBSA-Au<sup>5</sup> a highly suitable bimodal probe and fiducial marker for 2D section CLEM, with a particular high accuracy thanks to the inherent wide distribution of particles within the cells.

### **fBSA-Au as a fiducial in correlative FM and electron tomography**

Here, we extend the application of fBSA-Au as fiducial marker to correlative FM and electron tomography (ET), using semi-thin (circa 350 nm) cryosections. ET provides a unique tool to view 3D nanometer-scale detail within the cellular context, and comprises the tilting of a sample around 1 or 2 axes, after which a 3D reconstruction is generated based on back projection algorithms[33].

HeLa cells were incubated with fBSA-Au<sup>5</sup> for 3 hours and fixed, after which ~350 nm cryosections were prepared. The sections were thawed and immunolabeled for the lysosomal marker LAMP-1 followed by secondary labeling with Alexa488-tagged rabbit antibodies and 10 nm sized protein-A-gold. By FM, fBSA-Au<sup>5</sup> was readily detected as distinct spots that partially colocalized with LAMP-1 (figure 4A). The overall fluorescence intensity of fBSA-Au<sup>5</sup> was higher than in 70 nm cryosections

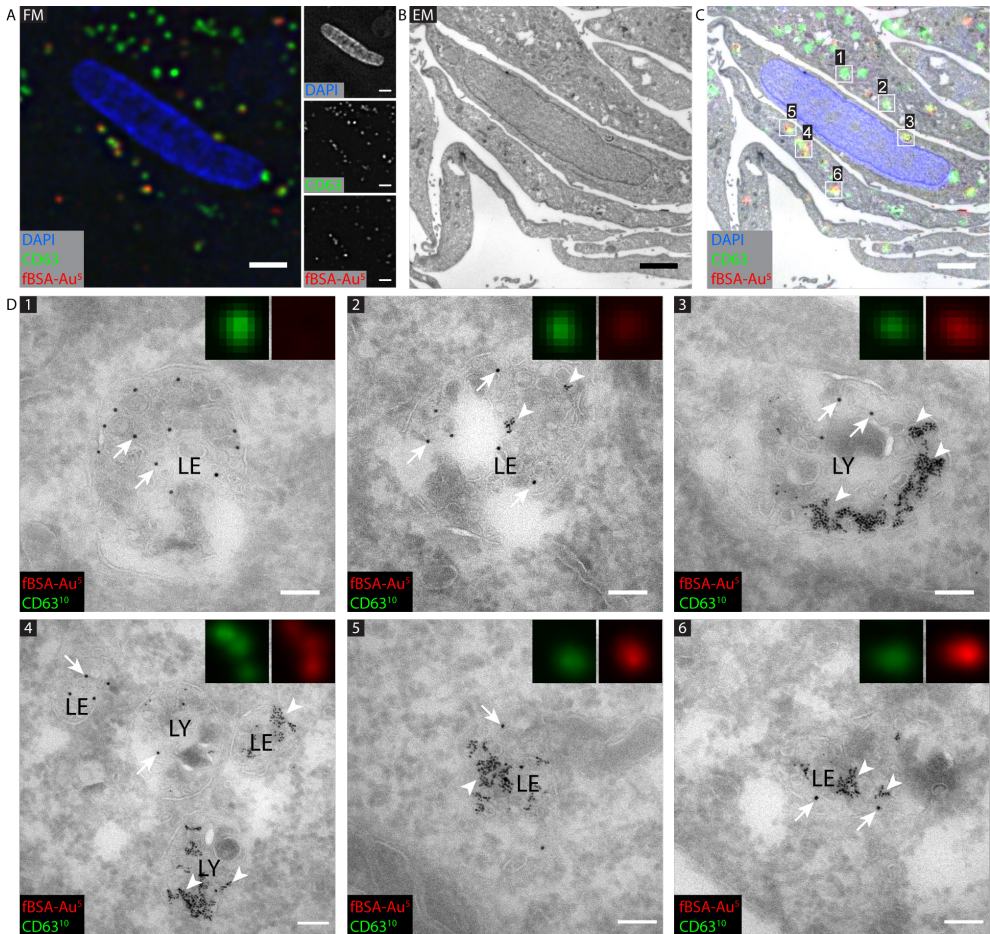


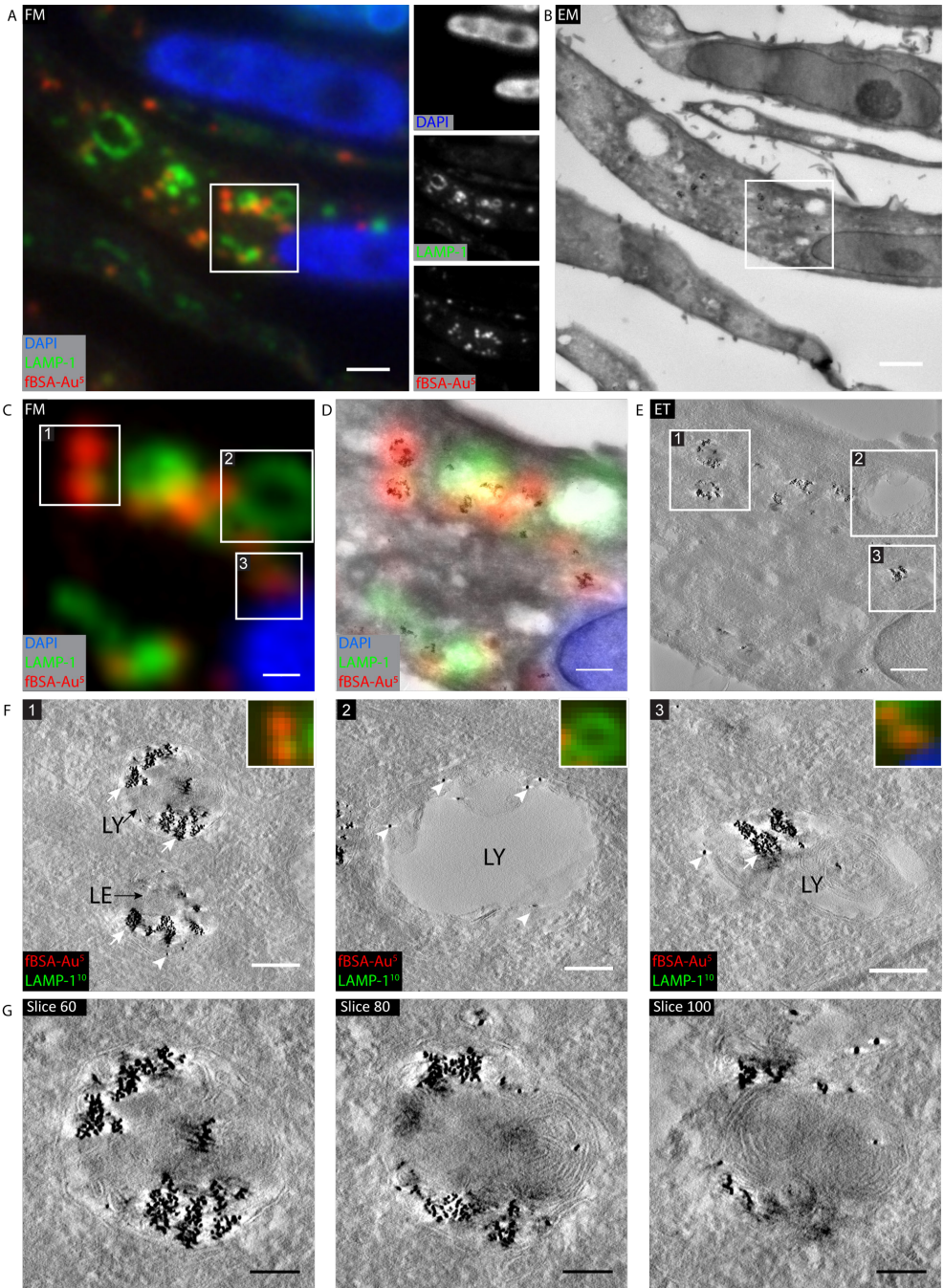
Figure 3: CLEM of CD63 positive, fBSA-Au5 containing compartments in HeLa cells. (A) FM image of ultrathin cryosection. Region of interest (ROI) with CD63 immuno-labeling (Alexa488 and Au10) and Alexa555 fluorescence of internalized fBSA-Au5. (B) EM of ROI. (C) Overlay of FM and EM images, showing high registration accuracy between modalities. (D) High magnification EM of fBSA-Au5 (arrowheads) containing organelles labeled for CD63 (10 nm gold, arrows). All selected compartments are positive for CD63 (10 nm gold, arrows). Inserts: magnified zoom-ins of CD63 and fBSA-Au5 fluorescence of the selected compartments. The intensity of fBSA-Au5 Alexa555 fluorescence corresponds to the number of gold particles present per compartment. (1) and (2) Late endosomes (LE) containing many intraluminal vesicles for CD63 (10 nm gold, arrows) and no (1) or little (2) fBSA-Au5 label. (3) lysosome (LY) with clusters of fBSA-Au5 gold particles. (4) Several late endosomes and lysosomes containing varying levels of fBSA-Au5. (5) and (6) Late endosomes heavily loaded with fBSA-Au5 correlating to intense red fluorescence. Scale bars: A-C: 2  $\mu$ m; D: 100 nm.

(figure 3 and figure 4), which corresponds to a higher number of fBSA-Au<sup>5</sup> particles in the increased Z-volume of 350 nm.

We then selected regions with fBSA-Au<sup>5</sup> fluorescence for correlation to ET. It is of particular importance to select the proper ROI before starting image acquisition, since ET can be performed only on small-sized ROIs. In semi-thin sections, however, the increased thickness causes more scattering of electrons and obscures visibility of structures by 2D TEM. This hampers screening of the sample for retracing ROIs. We found that retracement of the ROI was greatly facilitated by the presence of fBSA-Au<sup>5</sup>, since the electron-dense gold particles were well visible in the flat, peripheral areas of the cells. After identifying ROIs in 2D TEM, 3D images were collected by ET (figure 4B-D) and individual organelles were retraced from FM to 3D EM. The correlation accuracy of this approach ranged between 60 and 200 nm as determined using ec-CLEM, which is at the same level as for 2D CLEM. These data show that in semi-thin sections the fBSA-Au<sup>5</sup> probe can be used at the mesoscale – to find back cells – and the nanometer level, to retrace individual organelles.

After collection of the tilt series and tomogram reconstruction, we examined the morphology of the correlated structures and distribution of gold particles in the ROIs. Of note, in contrast to fBSA-Au<sup>5</sup> added to whole cells for internalization, the antibody-based LAMP-1 labeling is applied onto sections. The antibodies can penetrate into cryosections – as opposed to resin embedded materials – but gold particles mostly remain at the section surface [6,7]. Hence, there is little correlation between the intensities of FM and EM labeling of LAMP-1. ROI 1 shows a collection of fBSA-Au<sup>5</sup> particles present in a late endosome and a lysosome. Multiple virtual slices through the lysosome (figure 4) shows that fBSA-Au<sup>5</sup> is evenly distributed through the organelle. ROI 2 contains a large, LAMP-1-positive organelle that is negative for fBSA-Au<sup>5</sup> (figure 4G, panel 2). The corresponding ET image shows sparse LAMP-1 gold-labeling from the section surface. Thus, thanks to the accurate CLEM procedure enabled by fBSA-Au<sup>5</sup>, these LAMP-1 positive organelles can be detected by FM and registered to EM, despite the low level of immunogold-labeling and absence of fBSA-Au<sup>5</sup> signal. These data show that the intensity of the FM signal coming from semi-thin sections and the accuracy of the correlation procedure overcomes the need to tag antibodies with an additional gold tag. ROI 3 shows another example of a typical lysosome containing ample fBSA-Au<sup>5</sup> particles.

The 5 nm gold particles are visible throughout the volume of the tomograms (figure 4F, G), thanks to the internalization of fBSA-Au<sup>5</sup> prior to fixation. This allowed correlation of structures throughout the section (figure 4G), which is an important improvement over fiducials that reside on the surface of sections. Together, these findings show that fBSA-Au<sup>5</sup> is a powerful probe to use as endocytic fiducial marker in 3D CLEM, with high visibility and enabling fast retracing of ROIs with high registration accuracy. By using semi-thin sections the FM signal for fBSA-Au<sup>5</sup> as well as the antibody-based staining immunolabel is markedly increased over ultrathin sections. This increases the sensitivity of the immunolabeling procedure and allows for detection of low levels of protein that that may be missed in ultrathin sections.



4

Figure 4: 3D CLEM of 350 nm cryosections using electron tomography (ET). HeLa cells were incubated with fBSA-Au5 fiducials and immunogold labeled for LAMP-1 (10 nm gold). (A) FM image of 350 nm thick cryosection with the selected ROI for ET highlighted by white box. Insets show separate channels for the used fluorophores. (B) EM of same region as shown in (A). At this magnification, clusters of endocytosed fBSA-Au5 gold particles are visible, allowing rapid correlation from FM to EM. ROI selected for ET is shown in white box. (C) Magnified crop from (A) showing ROI for ET. Numbers refer to same spots as shown in E and F. (D) Zoom-in to ROI with overlaid fluorescence information. fBSA-Au5 fluorescence strictly corresponds to fBSA-Au5 gold particles. (E) Virtual slice from tomogram of ROI highlighting selected organelles. (F) Zoom-ins of selected organelles. Panel 1: late endosome (LE) and lysosome (LY) with large amounts of fBSA-Au5 gold particles (white arrows) and minimal LAMP-1 labeling (white arrowheads). Panel 2: LAMP-1 labeled lysosome devoid of endocytosed fBSA-Au5. This slice is from the surface of the section, since LAMP-1 representing gold particles do not penetrate into the section. Panel 3: LAMP-1 labeled lysosome with high level of endocytosed fBSA-Au5 gold. (G) Virtual sections through the lysosome shown in panel 1 of (F), showing distribution of gold throughout compartment. Scale bars: A,B; 2  $\mu$ m; C-E: 500 nm; F: 200 nm; G: 100 nm.

### fBSA-Au as an endocytic fiducial for correlative live-FM and electron tomography of resin-embedded cells

In CLEM approaches using resin embedding, fluorescence signals are generally recorded in 3D in live or fixed samples, before EM sample preparation. After this, the material is contrasted and embedded in epoxy or acrylic resin. Ultrathin or semi-thin serial sections are then collected from the resin blocks either for TEM or ET, and correlated to the original fluorescence data. This type of approach is sensitive to distortions caused by the staining, dehydration and embedding steps, which challenges retracing individual compartments between FM and EM. These 3D CLEM approaches also introduce an additional level of challenge for FM and EM correlation, especially in the z-dimension, due to the disparity in axial resolution between FM and EM. We reckoned that fBSA-Au fiducials would significantly ease the serial section targeting and the subsequent correlation procedure for correlative FM and ET in X, Y, and Z, due to their unique 3D distribution.

To test this, HeLa cells were grown and imaged on patterned glass coverslips, allowing easy relocation of cells of interest between FM and EM. This approach has been introduced by Polischuk et al. [11] and is commonly used in the correlative microscopy field for volume imaging [34,35]. Cells were incubated for 3 hours with fBSA-Au<sup>5</sup>, then fixed, after which a series of fluorescent Z-stacks was collected (figure 5A).

FM images of whole cells readily showed the presence of endocytosed fBSA-Au<sup>5</sup> (figure 5B-D). The positions of cells were recorded relative to the pattern on the coverslips to facilitate X-Y correlation of the target cells in the EM. To examine the endosomal organelles containing the endocytosed fBSA-Au<sup>5</sup>, we selected perinuclear regions from these cells, and recorded the FM Z-stacks, since these regions best demonstrate the 3D cellular distribution of the fBSA-Au<sup>5</sup>. After FM, the coverslips were stained with heavy metals and embedded in resin, serial semi-thin (250 nm) sections were cut and collected for ET (figure 5A). To select the serial ET section containing the correlated ROI in FM, we used the depth information from FM Z-stack to assess the distance of ROI from the bottom of the coverslip. Based on this data, we were able to select the correct section and retrace the ROI in TEM, and acquire high-resolution tomograms of fBSA-Au<sup>5</sup> containing compartments.

In the tomograms, we could easily distinguish the individual organelles selected in FM (figure 5E, F). Most fluorescent spots that were retraced by ET, were endo-lysosomal compartments with clusters of gold particles (figure 5G, H). However, we also found that faint fluorescent spots correlated to endosomal organelles

containing only few gold particles (figure 5H, organelle 3). This highlights the strong sensitivity of the fBSA-Au<sup>5</sup> probe.

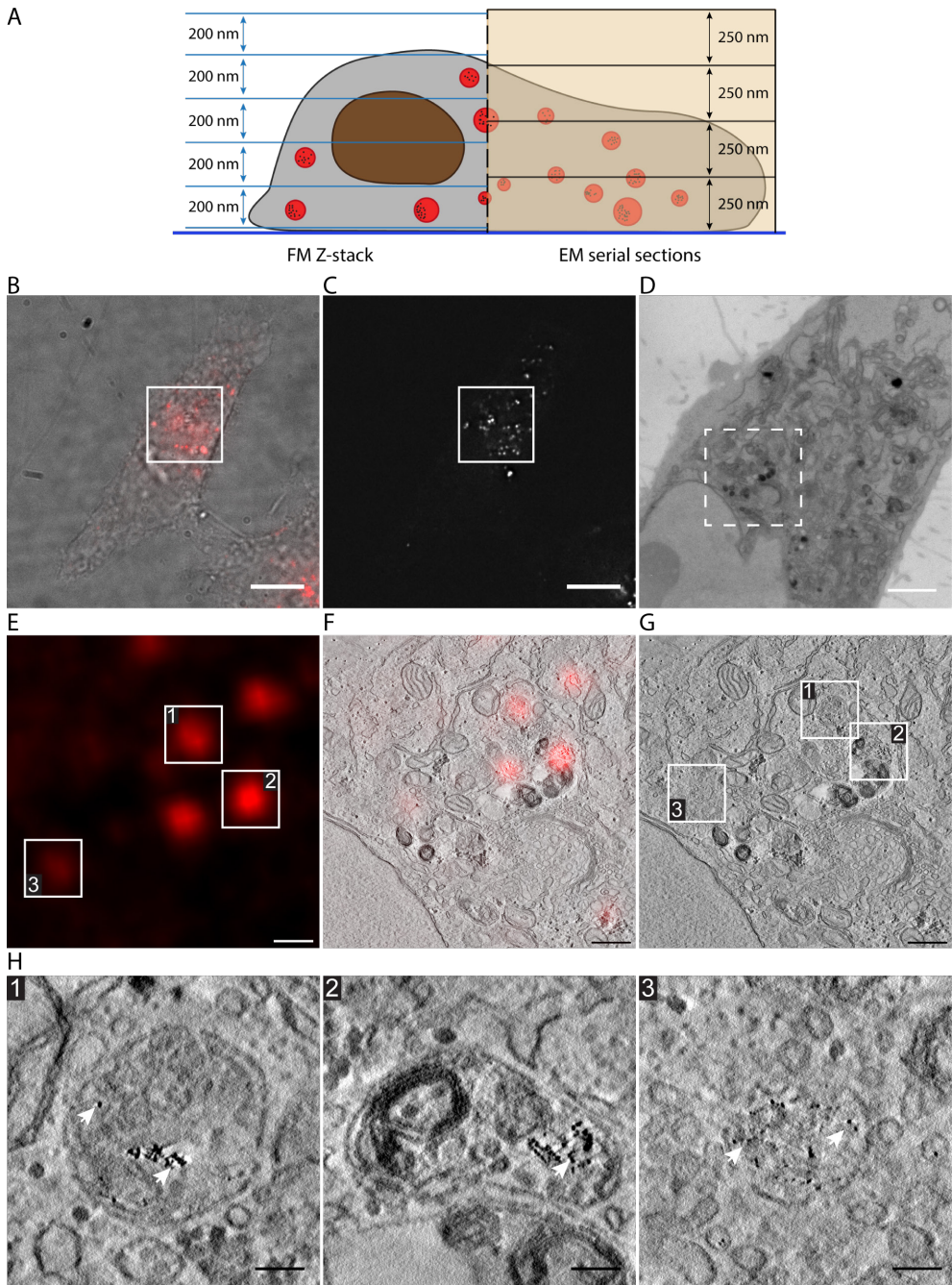
We conclude that endocytosed fBSA-Au is highly suitable for resin-based 3D CLEM approaches: first by providing the information required to select the correct Z-layer for EM imaging for ET, and second by using fBSA-Au as fiducial marker to provide high correlation accuracy in 3D. The proof of concept example provided here focuses on the application of fBSA-Au<sup>5</sup> as fiducial for endo-lysosomal organelles, but the bimodal visibility is also highly usable for other CLEM studies. In these cases, endosomes containing fBSA-Au<sup>5</sup> can be used as 3D reference points with a unique constellation to register FM data from other organelles than the endo-lysosomal system to their corresponding ultrastructure. The applicability extends to live-cell CLEM approaches [23,35], since the endocytosed fiducials are visible during every step of correlative imaging, all the way from live cells to the final tomograms (figures 2, 5). Finally, each serial section can be correlated to form a complete 3D FM and 3D EM dataset after reconstruction.

## Discussion

Bimodal fiducial markers are of great importance for correlative microscopy methods since they enable an accurate registration of fluorescence information over morphology [16,17]. In this chapter, we synthesized and demonstrated fBSA-Au, a conjugate of AlexaFluor-labeled BSA and 5 or 10 nm sized colloidal gold particles, and describe its application as 3D bimodal endocytic probe and fiducial marker. Endocytic markers are an attractive source and solution for correlative fiducials, since they efficiently distribute throughout cells, resulting in a well-defined 3D pattern of landmarks usable for correlation. We demonstrate that fBSA-Au<sup>5</sup> and fBSA-Au<sup>10</sup> are stable in solution, efficiently endocytosed, non-toxic, brightly fluorescent and with sufficient electron contrast for detection in TEM. Furthermore, the probe is versatile, since it can be synthesized with differently sized gold particles and distinct fluorophores. We show that endocytosed fBSA-Au is taken up effectively by the cells, colocalizes with common endosomal markers such as EEA1, CD63 and LAMP1, and reaches the same population of organelles as do established endocytic tracers such as Dextran or fluorescent BSA.

The properties of fBSA-Au render it broadly applicable for 2D and 3D CLEM, and compatible both with resin EM and cryosectioning approaches. We show that fBSA-Au provides ample fluorescence signal for imaging in intact cells in both live and fixed conditions, thanks to the accumulation of multiple fBSA-Au particles into the confined space of endosomes and lysosomes. In addition, fBSA-Au is readily detectable even in FM of thin (70 nm) Tokuyasu cryosections. The high electron contrast and uniformly sized gold particles make them well visible in EM and reliable

Figure 5: fBSA-Au<sup>5</sup> serves as a bimodal endocytic probe for CLEM using pre-embedding fluorescence and resin sections. (A) Schematic of the imaging strategy employed in figure 5. A fluorescent Z-stack with 200 nm intervals is collected of cells loaded with fBSA-Au<sup>5</sup> after fixation but prior to resin embedding. After resin embedding, 250 nm thick sections were cut for ET (B) DIC image of HeLa cell incubated with fBSA-Au<sup>5</sup> for 3 hours (Fluorescence overlay in red). (C) Fluorescence signal of fBSA-Au<sup>5</sup> shown in A. ROI for CLEM is highlighted with white box. (D) TEM micrograph of 250 nm thick section from HeLa cells, showing the ROI from A and B. ROI for ET is indicated in dashed white box. (E) Fluorescence signal of region corresponding to the ET ROI with spots of interest. (F) Virtual slice from tomogram overlaid with fluorescence data. (G) Virtual slice from tomogram showing 3 selected organelles. (H) Magnified virtual slices of the selected organelles, containing fBSA-Au<sup>5</sup>, visible by the 5nm gold particles (arrows). Organelles 1 and 2 are late endo-lysosomes, while organelle 3 is a late endosome. Arrows indicate clusters of gold particles. Scalebars: B, C: 10  $\mu$ m; D: 2  $\mu$ m; E, F, G: 500 nm; H: 100 nm.



reference points to correlate data from FM and EM, in both 2D and 3D. Moreover, since the gold particles of fBSA-Au's are of well-defined size, its use is compatible with immunogold labeling, which is especially valuable when using cryosection CLEM. The excellent visibility in EM ensures compatibility with current and future automated CLEM procedures and registration software [32,36,37]. Furthermore, the well-controlled nature of the synthesis process allows the formation of arbitrarily sized gold particles, which should allow results similar to the fBSA-Au<sup>5</sup> shown here, for any particle size. Combining the uncompromised FM and EM properties, we found that the probe functions well for CLEM, enabling live-cell imaging and easy registration of data in both 2D and 3D applications. The high signal intensity

Bimodal nanoparticles are a useful tool in cell biology, either as bimodal fiducial for CLEM or as an endocytic probe to reveal the identity of endocytic compartments. Fluorescently labeled silica nanoparticles have been used as endocytosed tracers in both FM and EM [16,23]. However, their relatively large size limits efficiency of endocytosis, and is prone to obscure morphological features within endosomes, hampering their ultrastructural identification. The fBSA-Au probes presented here are significantly smaller (5-15 nm diameter vs 60-100 nm for silica particles) which allows higher levels of endocytosis and retains visibility of morphological features in endosomes. Quantum dots are another type of nanoparticles often used in cell biology and CLEM approaches[20,38,39]. Like fBSA-Au, they can be functionalized with physiologically relevant molecules, and are small in size (5-30 nm). However, their low electron density makes them poorly visible in electron micrographs, in contrast to the excellent EM visibility of fBSA-Au. Moreover, quantum dots remain invisible in cryosections due to the reversed contrasting protocol.

A limitation in the development of bimodal fiducials is that fluorophores can be quenched when they are in close proximity to colloidal heavy metal particles[40–42]. Usually, spacers are incorporated to prevent this quenching, especially when larger sized metal particles are used, but these probes still suffer from a limited fluorescence signal. Thanks to the synthesis strategy of fBSA-Au, where Alexa-labeled BSA proteins are bound to colloidal gold particles, we are able to achieve high fluorescence signal despite using relatively large gold particles. In our case, the bulk of BSA molecules provides enough space between the gold and the fluorophores to retain sufficient fluorescence. Additionally, commercially available BSA-Alexa555 is labeled with Alexa555 at a 5:1 molar density (5 moles of dye per 1 mole protein). This high labeling density combined with the bulk of BSA should provide a sufficiently large fraction of unquenched fluorophores visible in FM.

One of the challenges with bimodal probes is to ensure colocalization of fluorescence signal and the electron dense particle[42]. For fBSA-Au<sup>5</sup>, the challenge primarily lies in the degradation of BSA as it is trafficked to lysosomes, the enzymatically active end-point of the endocytic pathway (as discussed in chapter 3). Degradation of BSA will lead to a dissociation of the Alexa label and the gold particles, which may lead to labeling discrepancies in correlative approaches. In previous studies, degradation of BSA was seen by the aggregation and clustering of gold particles in lysosomes [28,43]. Similar clustering was observed in lysosomes in the experiments here, indicating the degradation of BSA-Alexa555 (figures 3 and 4). However, our CLEM experiments show no labeling discrepancies between FM and EM; gold particles were seen in any dye-labeled compartment, and fluorescence was detected in all compartments containing gold colloids. This overlap confirms that at least within a period of 3 hours uptake the localization and fluorescence of the Alexa dye is retained in endocytic compartments, even after the degradation of BSA, and

throughout the process of fixation, sectioning and labeling.

We have demonstrated the use of fBSA-Au in 2D and 3D room temperature CLEM approaches using TEM or ET. We envision, however, that fBSA-Au is also compatible with SEM based volume CLEM approaches and even cryo-EM. Volume CLEM enables examination of cellular processes in an extended 3D, ultrastructural context. FM is inferred to large volume data obtained with 3D EM techniques like focused ion beam scanning EM (FIB-SEM) and serial blockface scanning EM (SBF-SEM). In these larger volumes, accurate registration of FM and EM data is crucial. Accurate registration strategies based on fiducial markers are currently well-developed for 2D CLEM[17,37] but lag behind for volume CLEM due to a lack of fiducials that can easily be distributed throughout the ROI in 3D. We surmise that the distribution of fBSA-Au<sup>5</sup> throughout the endocytic system makes it an excellent fiducial marker for volume CLEM approaches. Care must be taken to ensure its visibility in SEM imaging, due to the possible masking of the gold particles caused by harsher contrasting regimes often employed for backscatter imaging in SEM, and its lower resolution compared to TEM. Other types of fiducial markers with bigger size and distinctive structures can be more suitable for these applications [16]. Promising advances to overcome this challenge have however been made using multi-color EM [44], making identification of colloidal nanoparticles in cells possible.

For cryo-EM, accurate selection of ROIs for cryo-ET is of extreme importance due to the fragile nature of frozen hydrated material[45]. The use of fluorescence to determine ROIs prior to imaging is rapidly gaining traction thanks to maturing cryo-FM setups[46–49]. By using 3D bimodal probes like fBSA-Au, ROIs selected in FM can be verified in EM by the presence of fBSA-Au loaded compartments in the thinned lamellae. Since nearly all cells show a significant level of endocytosis, with the exception of erythrocytes, the use of endocytosed fBSA-Au is widely applicable. We predict that fBSA-Au is compatible with cryo-FM and cryo-EM of plunge frozen or high-pressure frozen material since fluorophores generally retain their fluorescence and exhibit reduced bleaching under cryogenic temperatures[47,50,51]. If this is not the case for AlexaFluor 555 we will incorporate a cryo-compatible fluorophore into fBSA-Au, as many different fluorescently labeled BSA species are commercially available.

Overall, we conclude that fBSA-Au is a powerful and easy-to-use 3D fiducial marker that can be used in an array of CLEM applications since it is stable, efficiently endocytosed and compatible with a variety of established LM and EM techniques. Its abundant yet compartmentalized distribution, not obscuring any morphological details, and high correlation accuracy makes it especially suited to address questions at the subcellular level requiring nanometer retraction efficiency.

## Materials and methods

### Antibodies and reagents

LAMP-1 was detected with a mouse anti-human LAMP-1 (CD107a) monoclonal antibody, purchased from BD Pharmingen (Vianen, The Netherlands). CD63 labeling was performed with a mouse anti-human CD63 monoclonal antibody, clone CLB-gran/12,435 (Sanquin reagents, Amsterdam, The Netherlands). EEA1 was detected using a rabbit anti-human EEA1 antibody (Cell Signalling, C45B10). Primary antibodies were detected with secondary fluorescently (Alexa488/647) labeled antibodies, purchased from Thermo Scientific. Protein A gold 10 nm was made in-house (Cell Microscopy Core, UMC Utrecht, The Netherlands). Alexa555-conjugated

BSA was bought from Thermo Scientific (A34786). Tannic acid was purchased from Mallinckrodt. Chloroauric acid trihydrate was purchased from Merck (#1.01582). Paraformaldehyde (95% wt/vol) was purchased from Sigma. Glutaraldehyde (8% wt/vol; EM grade) was purchased from Polysciences.

### **fBSA-Au<sup>5</sup> and fBSA-Au<sup>10</sup> complex synthesis**

5 or 10 nm colloidal gold particles were synthesized by reduction of chloroauric acid with tannic acid and sodium citrate, according to protocols developed by Slot and Geuze [27]. Reagent ratios were adjusted to obtain 5 or 10 nm sized colloid gold particles. Following synthesis, the colloid particles were stabilized with an excess of AlexaFluor 555-labeled BSA, as described previously for other proteins[26,27]. For additional stabilization, 0.1% BSA (final concentration) was added to the solution. The complexes were centrifuged on a 10-30% glycerol gradient centrifugation to remove aggregates and excess protein. The purified fraction was diluted in PBS and stored with the addition of sodium azide. Prior to use in cell culture, the required volume of fBSA-Au was dialyzed against PBS overnight at 4°C to remove the sodium azide and residual contaminants.

Measurements for sizing of synthesized gold colloids were performed by diluting gold colloids or fBSA-Au to OD=5 in dH<sub>2</sub>O. Formvar and carbon-coated copper grids were placed on 5  $\mu$ l drops of diluted solutions for 5 minutes. Grids were washed once on drops of dH<sub>2</sub>O, after which excess liquid was drained using filter paper. After drying, the gold particles were then imaged in TEM at magnifications >80,000 $\times$ . Micrographs containing gold particles were analyzed using the particle size analyzer developed by Ralph Sperl[52]. At least 100 gold particles are measured per condition except for non-functionalized Au<sup>10</sup> (n=46). Data is represented as Mean  $\pm$  S.D (figure 1).

### **Cell culture**

HeLa cells were cultured in Dulbecco's Modified Eagle's Medium (DMEM; Gibco) supplemented with 10% heat-inactivated fetal bovine serum (FBS), 2mM L-glutamine, 100 U/ml penicillin, 100  $\mu$ g/ml streptomycin (complete DMEM). Cells were grown under 5% CO<sub>2</sub>/air atmosphere at 37°C.

### **Immunofluorescence labelling and imaging of endocytosed fBSA-Au**

Cells grown on glass coverslips were treated with BSA-Alexa-Au<sup>5</sup> in culture medium at OD<sub>5</sub>, and incubated for 3 hours at 37°C. Cells were fixed with 4% paraformaldehyde in PBS for 1 hour, and permeabilized with 0.1% Triton X-100 in PBS. Blocking was performed using 1% bovine serum albumin (BSA) in PBS. Immunolabeling for LAMP-1 and EEA-1 was performed by incubating coverslips in PBS containing the corresponding antibodies and 1% BSA. Labeling was visualized using Alexa-tagged secondary antibodies. After secondary labeling, coverslips were washed with PBS and dH<sub>2</sub>O, and mounted to microscope slides using Prolong Gold or Diamond (Thermo Scientific).

### **Correlative microscopy of resin-embedded samples**

For correlation of fluorescence microscopy and EM of resin-embedded cells, imaging was performed prior to sample preparation in EM. Cells were grown on carbon-coated, gridded coverslips prepared as in [35], and treated with fBSA-Au<sup>5</sup> diluted to OD<sub>5</sub> in complete DMEM for 3 hours. Cells were washed in 1 $\times$  PHEM buffer to remove excess fBSA-Au<sup>5</sup>, and fixed using 4% formaldehyde and 0.2% glutaraldehyde in 1 $\times$  PHEM buffer. Using FM, Z-stacks of cells of interest were obtained for the

Alexa555 signal. The position of cells relative to the pattern etched in the coverslip was registered using polarized light.

To prepare specimens for electron microscopy, the imaged coverslips were postfixed using osmium tetroxide and uranyl acetate, dehydrated using a graded ethanol series, and embedded in Epon resin. Resin was polymerized for 48 hours at 65°C. After polymerization, the glass coverslip was removed from the Epon block by dissolving it in hydrogen fluoride, after which the exposed Epon surface was thoroughly cleaned with distilled water and left to harden overnight at 63°C. Areas of the resin block containing imaged cells were cut out using a clean razor blade, and glued to empty Epon sample stubs, with the basal side of the cells facing outwards. From these blocks, 70 and 250 nm thick sections were cut and collected on formvar and carbon coated copper support grids (50 mesh or slot grids). Grids with 250 nm thick sections were seeded with tomography fiducials by placing the grids on drops of demiwater containing 1:100 diluted protein-A-gold 10 nm for 5 minutes. Afterwards, grids were rinsed 3 times on distilled water and blotted dry with filter paper.

### **Sample preparation and light microscopic imaging of cryosections**

For CLEM on thin (70 nm) and thick (350 nm) cryosections, cells were grown in 60 mm culture dishes, treated with fBSA-Au5 diluted to OD5 in complete DMEM for 3 hours at 37°C and fixed with 2% formaldehyde and 0.2% glutaraldehyde in 0.1M phosphate buffer (pH 7.4). Samples were cryoprotected, sectioned and immunolabeled according to previous protocol [2,9], with minor modifications. Following incubation with primary antibodies, the grids were labeled with Alexa-488 labeled secondary antibodies, followed by incubation with protein-A gold conjugates (10 nm). The grids were washed with dH<sub>2</sub>O and sandwiched between a microscope slide and a no. 1 coverslip in 2% methylcellulose in dH<sub>2</sub>O. Sections were imaged in a Deltavision RT widefield fluorescence microscope (GE Healthcare, U.S.A.) equipped with a Cascade II EM-CCD camera (Photometrics, U.S.A.). Grids were first imaged at 40× magnification to form a map of the section, after which regions of interest were selected using 100× magnification. After imaging the grids were removed from the microscope slide, thoroughly rinsed with H<sub>2</sub>O and contrasted for EM and embedded in methylcellulose containing uranyl acetate, according to previous protocol [2].

### **Electron microscopy of resin sections and cryosections**

Thin cryosections were imaged in a Tecnai 12 TEM (Thermo Fischer Scientific, Eindhoven, The Netherlands) equipped with a Veleta 2k×2k CCD camera (EMSIS, Munster, Germany), operating at 80 kV. Tilt series of resin sections and labeled thick cryosections were acquired in a Tecnai 20 TEM (Thermo Fischer Scientific) operating at 200 kV, equipped with an Eagle 4K×4K CCD camera running Xplore3D (Thermo Fischer Scientific) software. Single tilt image series were automatically collected with 1° tilt increments from -60° to +60° at microscope magnifications of 11500× or 14500×, resulting in final pixel sizes of 0.96 nm or 0.76 nm, respectively.

### **Tomogram reconstruction**

Tomogram reconstruction was performed using the IMOD software package[33]. Tilt series were aligned using bead tracking of the 10 nm gold particles used for immunolabeling (cryosections) or seeded gold fiducials (resin sections). Tomograms were generated from the aligned data using weighted back projection.

## Correlation of light and electron microscopic images

Registration of thin section fluorescence and EM data was performed using ec-CLEM [32]. Here, multiple corresponding pairs of fluorescent spots and gold particles were manually selected, after which the software automatically applies the correct scaling and transformation steps and generates overlays of FM and EM data. We used only linear transformation options to achieve the overlays shown in the figures.

For correlation of FM and ET data, registration was first performed using ec-CLEM by overlaying FM data over a regular TEM image of the ROI, collected before the start of tilt imaging. The transformed fluorescence images were then overlaid over tomogram slices corresponding to the region of the regular TEM image.

## References

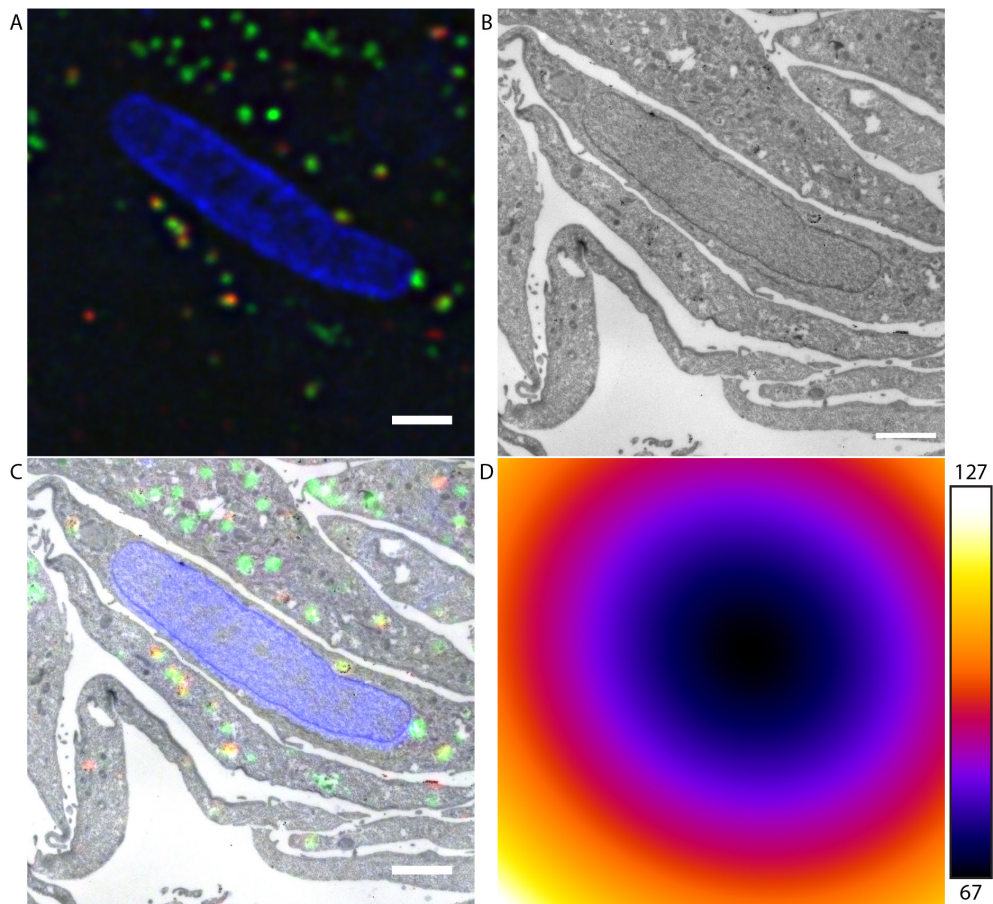
1. Horisberger M, Rosset J. Colloidal gold, a useful marker for transmission and scanning electron microscopy. *J Histochem Cytochem* 1977;25:295–305.
2. Slot JW, Geuze HJ. Cryosectioning and immunolabeling. *Nat Protoc* 2007;2:2480–2491.
3. Deerinck TJ, Martone ME, Lev-Ram V, Green DPL, Tsien RY, Spector DL, Huang S, Ellisman MH. Fluorescence photooxidation with eosin: A method for high resolution immunolocalization and in situ hybridization detection for light and electron microscopy. *J Cell Biol* 1994;126:901–910.
4. Gaietta GM, Deerinck TJ, Ellisman MH. Labeling tetracysteine-tagged proteins with biarsenical dyes for live cell imaging. *Cold Spring Harb Protoc* 2011;6:44–47.
5. Martell JD, Deerinck TJ, Sancak Y, Poulos TL, Mootha VK, Sosinsky GE, Ellisman MH, Ting AY. Engineered ascorbate peroxidase as a genetically encoded reporter for electron microscopy. *Nat Biotechnol* 2012;30:1143–1148.
6. Stierhof Y-D, Schwarz H, Frank H. Transverse sectioning of plastic-embedded immunolabeled cryosections: Morphology and permeability to protein A-colloidal gold complexes. *J Ultrastruct Mol Struct Res* 1986;97:187–196.
7. Stierhof YD, Schwarz H. Labeling properties of sucrose-infiltrated cryosections. *Scanning Microsc Suppl* 1989;3:35–46.
8. Karreman MA, Mercier L, Schieber NL, Solecki G, Allio G, Winkler F, Ruthensteiner B, Goetz JG, Schwab Y. Fast and precise targeting of single tumor cells in vivo by multimodal correlative microscopy. *J Cell Sci* 2016;129:444–56.
9. Rijnsoever C Van, Oorschot V, Klumperman J. Correlative light-electron microscopy (CLEM) combining live-cell imaging and immunolabeling of ultrathin cryosections. *Nat Methods* 2008;5:973–980.
10. Verkade P. Moving EM: The Rapid Transfer System as a new tool for correlative light and electron microscopy and high throughput for high-pressure freezing. *J Microsc* 2008;230:317–328.
11. Polishchuk RS, Polishchuk E V., Marra P, Alberti S, Buccione R, Luini A, Mironov AA. Correlative light-electron microscopy reveals the tubular-saccular ultrastructure of carriers operating between Golgi apparatus and plasma membrane. *J Cell Biol* 2000;148:45–58.
12. Müller-Reichert T, Srayko M, Hyman A, O’Toole ET, McDonald K. Correlative Light and Electron Microscopy of Early *Caenorhabditis elegans* Embryos in Mitosis. *Methods Cell Biol* 2007;2007:101–119.
13. Bishop D, Nikić I, Brinkoetter M, Knecht S, Potz S, Kerschensteiner M, Misgeld T. Near-infrared branding efficiently correlates light and electron microscopy. *Nat Methods* 2011;8:568–70.
14. Bushby AJ, Mariggi G, Armer HEJ, Collinson LM. Correlative light and volume electron microscopy: using focused ion beam scanning electron microscopy to image transient events in model organisms. *Methods Cell Biol* 2012;111:357–82.
15. Vicidomini G, Gagliani MC, Canfora M, Cortese K, Frosi F, Santangelo C, Di Fiore PP, Boccacci P, Diaspro A, Tacchetti C. High Data Output and Automated 3D Correlative Light-Electron Microscopy Method. *Traffic* 2008;9:1828–1838.
16. Fokkema J, Fermie J, Liv N, van den Heuvel DJ, Konings TOM, Blab GA, Meijerink A, Klumperman J, Gerritsen HC. Fluorescently Labelled Silica Coated Gold Nanoparticles as Fiducial Markers for Correlative Light and Electron Microscopy. *Sci Rep* 2018;8:13625.
17. Kukulski W, Schorb M, Welsch S, Picco A, Kaksonen M, Briggs JAG. Correlated fluorescence and 3D electron microscopy with high sensitivity and spatial precision. *J Cell Biol* 2011;192:111–119.
18. Watanabe S, Punge A, Hoppel G, Willig KI, Hobson RJ, Davis MW, Hell SW, Jorgensen EM. Protein localization in electron micrographs using fluorescence nanoscopy. *Nat Methods* 2011;8:80–4.

19. Kopek BG, Shtengel G, Xu CS, Clayton D a, Hess HF. Correlative 3D superresolution fluorescence and electron microscopy reveal the relationship of mitochondrial nucleoids to membranes. *Proc Natl Acad Sci U S A* 2012;109:6136–41.
20. Giepmans BNG, Deerinck TJ, Smarr BL, Jones YZ, Ellisman MH. Correlated light and electron microscopic imaging of multiple endogenous proteins using Quantum dots. *Nat Methods* 2005;2:743–749.
21. Hanaki KI, Momo A, Oku T, Komoto A, Maenosono S, Yamaguchi Y, Yamamoto K. Semiconductor quantum dot/albumin complex is a long-life and highly photostable endosome marker. *Biochem Biophys Res Commun* 2003;302:496–501.
22. Geoffroy JS, Becker RP. Endocytosis by endothelial phagocytes: uptake of bovine serum albumin-gold conjugates in bone marrow. *J Ultrastructure Res* 1984;89:223–239.
23. Zhang Y, Hensel M. Evaluation of nanoparticles as endocytic tracers in cellular microbiology. *Nanoscale* 2013;5:9296.
24. Chithrani BD, Ghazani AA, Chan WCW. Determining the size and shape dependence of gold nanoparticle uptake into mammalian cells. *Nano Lett* 2006;6:662–668.
25. Connor EE, Mwamuka J, Gole A, Murphy CJ, Wyatt MD. Gold nanoparticles are taken up by human cells but do not cause acute cytotoxicity. *Small* 2005;1:325–327.
26. Slot JW, Geuze HJ. Sizing of protein A-colloidal gold probes for immunoelectron microscopy. *J Cell Biol* 1981;90:533–536.
27. Slot JW, Geuze HJ. A new method of preparing gold probes for multiple-labeling cytochemistry. *Eur J Cell Biol* 1985;38:87–93.
28. Pols MS, Ten Brink C, Gosavi P, Oorschot V, Klumperman J. The HOPS Proteins hVps41 and hVps39 Are Required for Homotypic and Heterotypic Late Endosome Fusion. *Traffic* 2013;14:219–232.
29. Makarow M. Endocytosis in *Saccharomyces cerevisiae*: internalization of alpha-amylase and fluorescent dextran into cells. *EMBO J* 1985;4:1861–1866.
30. Vicidomini G, Gagliani MC, Cortese K, Krieger J, Buescher P, Bianchini P, Boccacci P, Tacchetti C, Diaspro A. A novel approach for correlative light electron microscopy analysis. *Microsc Res Tech* 2009;73:NA-NA.
31. Mari M, Geerts WJC, Reggiori F. Immuno- and correlative light microscopy-electron tomography methods for 3D protein localization in yeast. *Traffic* 2014;15:1164–1178.
32. Paul-Gilloteaux P, Heiligenstein X, Belle M, Domart MC, Larijani B, Collinson L, Raposo G, Salamero J. EC-CLEM: Flexible multidimensional registration software for correlative microscopies. *Nat. Methods* 2017;14:102–103.
33. Kremer JR, Mastrorarde DN, McIntosh JR. Computer visualization of three-dimensional image data using IMOD. *J Struct Biol* 1996;116:71–6.
34. Russell MRG, Lerner TR, Burden JJ, Nkwe DO, Pelchen-Matthews A, Domart M-C, Durgan J, Weston A, Jones ML, Peddie CJ, Carzaniga R, Florey O, Marsh M, Gutierrez MG, Collinson LM. 3D correlative light and electron microscopy of cultured cells using serial blockface scanning electron microscopy. *J Cell Sci* 2016;jcs.188433.
35. Fermie J, Liv N, ten Brink C, van Donselaar EG, Müller WH, Schieber NL, Schwab Y, Gerritsen HC, Klumperman J. Single organelle dynamics linked to 3D structure by correlative live-cell - 3D electron microscopy. *Traffic* 2018;1–16.
36. Sjollem KA, Giepmans BNG. Automated Annotating Label in Nanotomy. *Imaging Microsc* 2016;4:45–46.
37. Mohammadian S, Fokkema J, Agronskaia A V., Liv N, de Heus C, van Donselaar E, Blab GA, Klumperman J, Gerritsen HC. High accuracy, fiducial marker-based image registration of correlative microscopy images. *Sci Rep* 2019;9:3211.
38. Peckys DB, Bandmann V, de Jonge N. Correlative fluorescence and scanning transmission electron microscopy of quantum dot-labeled proteins on whole cells in liquid. 1st ed. Elsevier Inc.; 2014.
39. Liv N, van Oosten Slingeland DSB, Baudoin J-P, Kruit P, Piston DW, Hoogenboom JP. Electron Microscopy of Living Cells During in Situ Fluorescence Microscopy. *ACS Nano* 2016;10:265–73.
40. Kandela I, Meyer D, Oshel P, Rosa-Molinar E, Albrecht R. Fluorescence Quenching by Colloidal Heavy Metals: Implications for Correlative Fluorescence and Electron Microscopy Studies. *Microsc Microanal* 2003;9:1194–1195.
41. Kandela IK, Albrecht RM. Fluorescence Quenching by Colloidal Heavy Metals Nanoparticles: Implications for Correlative Fluorescence and Electron Microscopy Studies. *Scanning* 2007;29:152–161.
42. Miles BT, Greenwood AB, Benito-Alifonso D, Tanner H, Galan MC, Verkade P, Gersen H. Direct Evidence of Lack of Colocalisation of Fluorescently Labelled Gold Labels Used in Correlative Light Electron Microscopy. *Sci Rep* 2017;7:44666.
43. Bright NA, Reaves BJ, Mullock BM, Luzio JP. Dense core lysosomes can fuse with late endosomes and are re-formed from the resultant hybrid organelles. *J Cell Sci* 1997;110.
44. Scotuzzi M, Kuipers J, Wensveen DI, De Boer P, Hagen KCW, Hoogenboom JP, Giepmans BNG. Multi-



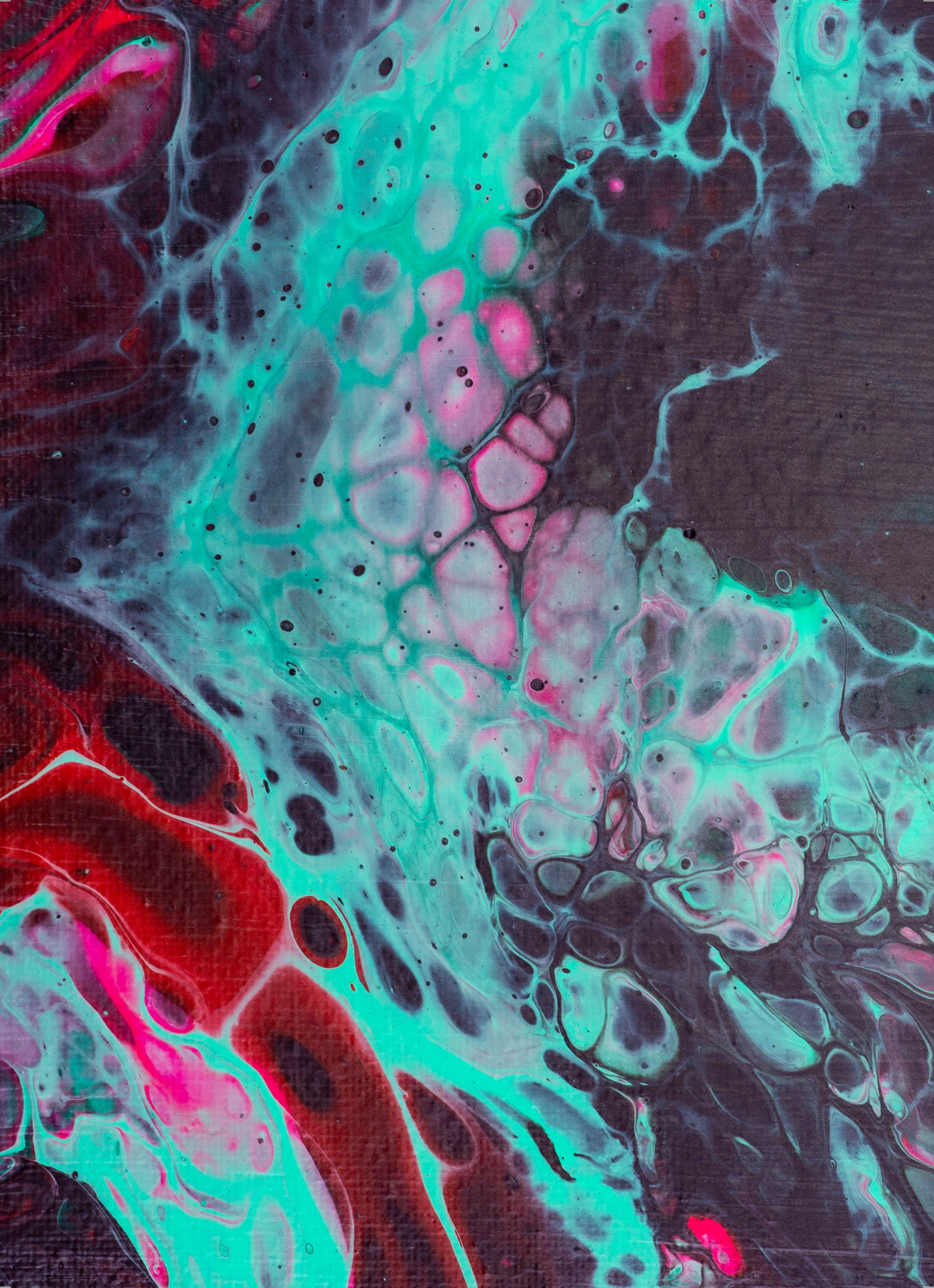
- color electron microscopy by element-guided identification of cells, organelles and molecules. *Sci Rep* 2017;7:45970.
45. Villa E, Schaffer M, Plitzko JM, Baumeister W. Opening windows into the cell: focused-ion-beam milling for cryo-electron tomography. *Curr Opin Struct Biol* 2013;23:771–7.
  46. Schwartz CL, Sarbash VI, Ataullakhanov FI, McIntosh JR, Nicastro D. Cryo-fluorescence microscopy facilitates correlations between light and cryo-electron microscopy and reduces the rate of photobleaching. *J Microsc* 2007;227:98–109.
  47. Kaufmann R, Hagen C, Grünewald K. Fluorescence cryo-microscopy: current challenges and prospects. *Curr Opin Chem Biol* 2014;20:86–91.
  48. Schellenberger P, Kaufmann R, Siebert CA, Hagen C, Wodrich H, Grünewald K. High-precision correlative fluorescence and electron cryo microscopy using two independent alignment markers. *Ultramicroscopy* 2014;143:41–51.
  49. van Driel LF, Valentijn JA, Valentijn KM, Koning RI, Koster AJ. Tools for correlative cryo-fluorescence microscopy and cryo-electron tomography applied to whole mitochondria in human endothelial cells. *Eur J Cell Biol* 2009;88:669–684.
  50. Kaufmann R, Schellenberger P, Seiradake E, Dobbie IM, Jones EY, Davis I, Hagen C, Grünewald K. Super-resolution microscopy using standard fluorescent proteins in intact cells under cryo-conditions. *Nano Lett* 2014;14:4171–4175.
  51. Weisenburger S, Jing B, Renn A, Sandoghdar V. Cryogenic localization of single molecules with angstrom precision. In: Verma P, Egner A, editors. *Nanoimaging and Nanospectroscopy*. International Society for Optics and Photonics; 2013. p. 88150D.
  52. Sperling R. Particle Size Analyzer macro for ImageJ [Internet]. 2009; Available from: <https://code.google.com/archive/p/psa-macro/>

## Supplementary data



Supplementary figure 1: fBSA-Au as fiducial enables high registration accuracy. (A) FM data of region of interest. (B) EM region of interest. (C) Overlay of FM and EM data. (D) Quantification of registration error using ec-CLEM, showing regions of high accuracy (67 nm registration error) and lower accuracy (127 nm registration error). Scalebars 2  $\mu\text{m}$ .

4



# Fluorescently labelled silica coated gold nanoparticles as fiducial markers for correlative light and electron microscopy

Jantina Fokkema<sup>1</sup>, Job Fermie<sup>1,2</sup>, Nalan Liv<sup>2</sup>, Dave J. van den Heuvel<sup>1</sup>, Tom O. M. Konings<sup>1</sup>, Gerhard A. Blab<sup>1</sup>, Andries Meijerink<sup>3</sup>, Judith Klumperman<sup>2</sup>, Hans C. Gerritsen<sup>1</sup>

1. Section Molecular Biophysics, Debye Institute for Nanomaterials Science, Utrecht University, Utrecht, The Netherlands
2. Section Cell Biology, Center for Molecular Medicine, University Medical Center Utrecht, Utrecht University, Utrecht, The Netherlands
3. Section Condensed Matter and Interfaces, Debye Institute for Nanomaterials Science, Utrecht University, Utrecht, The Netherlands

---

## Chapter 5

---

This chapter is published as:

Fokkema J, Fermie J, Liv N, van den Heuvel DJ, Konings TO, Blab GA, Meijerink A, Klumperman J, Gerritsen HC. Fluorescently Labelled Silica Coated Gold Nanoparticles as Fiducial Markers for Correlative Light and Electron Microscopy. Scientific reports. 2018 Sep 11;8(1):13625.

## Abstract

Gold nanoparticles coated with a fluorescently labelled (rhodamine B) silica shell are presented as fiducial markers for correlative light and electron microscopy (CLEM). The synthesis of the particles is optimized to obtain homogeneous, spherical core-shell particles of arbitrary size. Next, particles labelled with different fluorophore densities are characterized to determine under which conditions bright and (photo) stable particles can be obtained. 2D and 3D CLEM examples are presented where optimized particles are used for correlation. In the 2D example, fiducials are added to a cryosection of cells whereas in the 3D example cells are imaged after endocytosis of the fiducials. Both examples demonstrate that the particles are clearly visible in both modalities and can be used for correlation. Additionally, the recognizable core-shell structure of the fiducials proves to be very powerful in electron microscopy: it makes it possible to irrefutably identify the particles and makes it easy to accurately determine the center of the fiducials.

## Introduction

The field of correlative light and electron microscopy, or CLEM, has expanded rapidly during the last decade. Especially in biology it turns out to be very useful to combine these two techniques. Light microscopy or fluorescence microscopy (FM) is used to visualize, localize and track specific fluorescent molecules in cells over large areas with high sensitivity, while electron microscopy (EM) provides high resolution ultrastructural information of cells and materials [1,2]. This opens up the possibility to visualize rare transient events or specific cells within complex tissues [3,4].

For the best results in CLEM experiments, data from the different modalities should be registered with the highest possible precision. This is complicated by the vastly different fields of view of FM and EM, as well as the different contrast mechanisms of these techniques. FM requires bright and stable fluorophores, while EM relies on differences in electron density for contrast, and frequently requires heavy metal staining to visualize biological structures. Since fluorescent probes (i.e. molecules or proteins) are typically not electron dense, fluorescent labels can generally not be used for correlation.

Particles visible in both modalities (fiducial markers) can be used to overcome this problem. The viability of this approach has been demonstrated in literature by using fluorescent latex beads [5–7] or quantum dots [8–10]. However, a shared problem of these candidate particles is their relatively low EM contrast, making visualization and localization in heavily EM stained samples difficult or even impossible. An alternative approach to register data between modalities is via a double labelling procedure. Here, proteins of interest are labelled with a fluorescent probe, followed by labelling with antibodies or protein A conjugated with colloidal gold [11,12]. A disadvantage of this approach is that correlation is indirect and based on the assumption that both labels fully colocalize. Despite great successes achieved by this approach, Miles et al. recently demonstrated that this assumption not always holds true, thereby stressing the importance of finding a more direct way for registering FM and EM data [13].

In this work, nanocomposite core-shell particles based on a gold core and a fluorescently labelled silica shell (figure 1) are deployed as fiducial markers. The gold core provides contrast for EM and fluorophores covalently incorporated in the silica shell for FM. Rhodamine B is chosen as fluorophore because it was demonstrated

by Karreman et al. [14] that rhodamine like fluorophores behave well under the dry and vacuum conditions encountered in EM. Using a red emitting fluorophore is also advantageous because excitation at longer wavelengths results in reduced autofluorescence [15]. To obtain the fiducials, first, an optimized synthesis of the nanocomposite particles to obtain spherical and highly monodisperse particles of arbitrary size is presented. Next, a thorough study is performed to optimize the fluorophore labelling density within the fluorescently labelled silica to obtain bright and (photo)stable particles. Finally, the particles are tested as fiducials in a 2D and a 3D CLEM experiment.

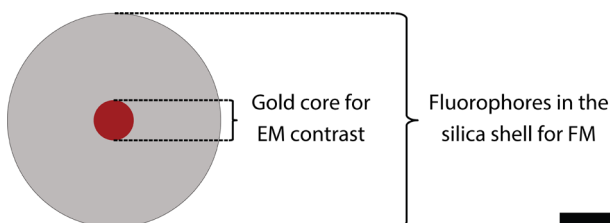


Figure 1: A schematic representation of the here presented fiducial markers. The scale bar indicates 20 nm.

## Results

A series of  $\sim 90$  nm diameter particles with relative concentrations of 0 to 30 dyes were synthesized, see table 1 and SI-1,2. Transmission electron microscopy (TEM) measurements were carried out to determine particle sizes at different stages of the synthesis. Representative images of particles are shown in figure 2. The images illustrate that the particles are successfully coated with a very thin silica layer after the first growth step (a). The silica layer becomes thicker and more homogeneous after growth of the rhodamine B labelled silica layer (b) and the second stabilization layer (c). It is important to note that silica grows selectively onto the existing particles, i.e. no secondary nucleation takes place. Average particle diameters and standard deviations at the different stages of the synthesis were determined from TEM images. Average particle sizes are almost identical for all samples at different stages of the reaction justifying the assumption that the volume of rhodamine B labelled silica per particle is similar for all samples. By ensuring that the number of particles is the same in all reactions, it is ensured that we are truly studying fluorophore labelling density effects.

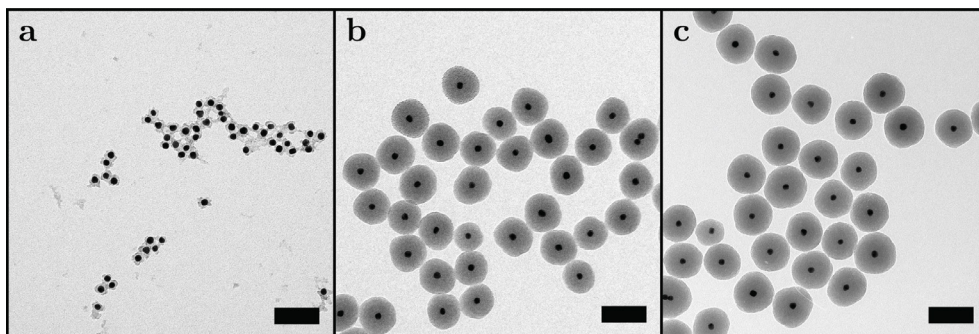


Figure 2: Representative TEM images at different stages of the silica coating procedure; (a) after growth of the first stabilization layer; (b) after growth of the rhodamine B labelled silica layer; (c) after growth of the second stabilization layer. The scale bars indicate 100 nm.

To calculate the average fluorophore separations, fluorophore labelling efficiencies were determined. This was performed via absorption measurements after dissolution of the silica shell of the particles as described by Imhof et al [16]. Next, the average separation between fluorophores was calculated as the cube root of volume available per fluorophore. This value increases from 7.7 nm for the highest to 28.5 nm for the lowest labelling density (see table 1). The estimated average number and corresponding error  $\sqrt{N}$  of fluorophores per particle ranges from 12 for the lowest to 558 for the highest labelling density and is also included in this table.

[Dye]	Total particle diameter				Labelling efficiency (%)	Average separation (nm)	Fluorophores per particle (a.u.)
	RITC layer		Stab. layer				
	d (nm)	$\sigma$ (nm)	d (nm)	$\sigma$ (nm)			
30	79	4.5	89	4.9	3.7	7.7	558 $\pm$ 24
25	86	5.4	88	4.8	4.1	7.9	662 $\pm$ 26
20	83	5.0	88	5.4	4.5	8.2	530 $\pm$ 23
15	82	4.3	88	4.8	4.3	9.2	358 $\pm$ 19
12.5	82	4.3	87	5.0	3.8	10.2	265 $\pm$ 16
10	82	4.7	89	4.5	3.2	11.7	175 $\pm$ 13
7.5	83	4.8	89	4.7	3.5	12.4	151 $\pm$ 12
5	81	4.7	88	5.1	2.9	15.2	77 $\pm$ 9
2.5	83	5.6	89	5.3	2.7	19.6	39 $\pm$ 6
1	82	4.8	89	4.5	2.2	28.5	12 $\pm$ 4
0	76	4.8	89	5.4	N/A	N/A	N/A

Table 1: Particle sizes determined from TEM after growth of the rhodamine B labelled silica layer and growth of the second stabilization layer and corresponding fluorophore labelling efficiencies and average separations between fluorophores. All samples were based on 15 nm ( $\sigma = 1.4$  nm) diameter gold cores coated with a thin silica shell to obtain a total diameter of 25 nm ( $\sigma = 2.7$  nm). In this table, d is the average particle diameter and  $\sigma$  is the standard deviation of this average value, both were determined by measuring diameters of 100 particles.

## Spectral measurements and radiative decay curves

To study fluorophore density effects, excitation and emission spectra and radiative decay curves were recorded (see figure 3 a and b). Both spectra exhibit a small blue shift with increasing fluorophore density that is accompanied by an increase in the height of the shoulder around 520 nm in the excitation spectrum. Radiative (or fluorescence) decay curves were measured using the time-correlated single-photon counting technique after excitation with a pulsed laser [17]. These curves reveal faster decays with increasing labelling density which is indicative for fluorescence quenching. The radiative decay of particles labelled with the lowest dye labelling density, [Dye] = 2.5, is already slightly faster than the decay of the fluorophore, rhodamine B isothiocyanate (RITC), in ethanol. This can be attributed to a change in the local medium of the fluorophores, silica versus ethanol, and the APTES-dye coupling.

Similar observations at increasing fluorophore densities in solid matrices were made by Genovese et al. (rhodamine B in pluronic silica) [18] and Imhof et al. (fluorescein in Stöber silica) [16] and for fluorophores on antibodies by Szabó et al [19]. An explanation for these observations can be found by taking into account concentration effects including self-quenching. Increasing the fluorophore density results in the formation of an increased number of dimers [20,21] or other species

acting as quenching centers. Additionally, resonance energy transfer (homo-FRET) between fluorophores becomes more efficient because the average separation between fluorophores shortens [17]. This combination of energy transfer and quenching successfully explains the effects of fluorophore concentration on the fluorescence quantum yield of fluorophores in solution [22,23] and can also be applied to the work presented here. When increasing the fluorophore density in the particles, energy transfer between fluorophores becomes possible and the number of quenching centers within the particles increases. This energy transfer allows the excited state to migrate within the particle which makes it possible for the excited state to migrate from an unquenched fluorophore to a nearby quenching center, thereby contributing to quenching of fluorescence.

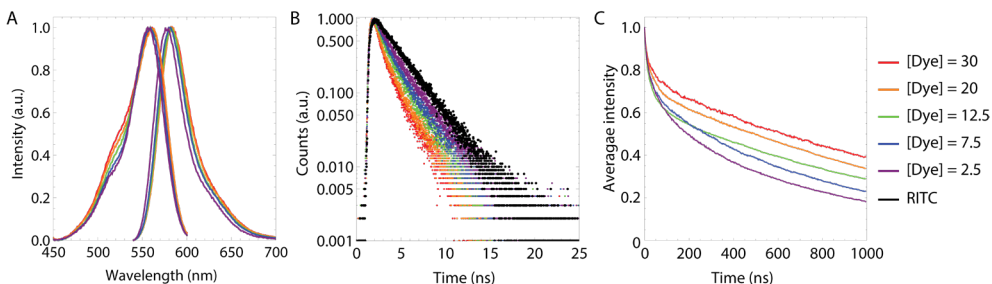


Figure 3: (a) Emission spectra recorded after excitation at 520 nm (right) and excitation spectra recorded at 610 nm (left). (b) Radiative decay curves after pulsed excitation at 509 nm and detection at maximum emission. (c) Normalized bleaching curves measured at an excitation intensity of 6.0 W cm<sup>-2</sup>.

### Single particle intensity and (photo)chemical stability

Widefield fluorescence microscopy measurements were performed to determine the single particle intensity and photostability of the particles. In figure 4a the average single particle intensity is plotted as a function of the relative dye concentration. It can be seen that initially the single particle intensity increases with increasing dye concentration. After this first increase, the single particle intensity remains more constant and eventually a small drop in intensity is observed. This optimum can be explained by the counterbalance between increasing the number of fluorophores versus the increase in self quenching which becomes more evident when the single particle intensity is plotted as a function of the average fluorophore separation, see figure 4b. At large separations (>15 nm) the single particle intensity increases when the number of fluorophores per particle increases (i.e. shortening of the average separation) because the fluorophores do not sense each other. Next, a more constant regime between 10-15 nm with an optimum around 12 nm is observed. This constant regime can be explained by the counterbalance between increasing the number of fluorophores versus the increase in self quenching. Finally, when average separations drop below 10 nm self-quenching becomes dominant which results in the aforementioned drop of intensity.

The photostability of the particles was studied by measuring their photobleaching behavior. From the photobleaching curves in figure 3c it becomes clear that, generally speaking, the intensity loss reduces when the fluorophore density increases. This can be explained by the shortening of the radiative decay lifetime at higher fluorophore densities. The fluorophores spend less time in the excited state, thereby decreasing the bleach rate. In addition, photobleaching reduces the effective dye concentrations which decreases the effect of concentration quenching thereby counterbalancing bleaching.



Another observations made throughout the experiments was that particles with a relative dye concentration above 15 tend to cluster over time (gray area, figure 4). This clustering can result from a reduction of the negative zeta potential caused by the incorporation of positively charged fluorophores and amine groups. For CLEM applications non-clustered particles are preferred, therefore these high concentrations should be avoided.

Based on the results included in this section, a relative fluorophore concentration of 10 (separation 11.7 nm) was chosen as the optimum labelling density. The average single particle intensity is maximum around this concentration. In terms of bleaching, it might be desirable to go for a higher labelling density. However, because of particle stability, a relative fluorophore concentration well below 15 (separation 9.2 nm) is desired.

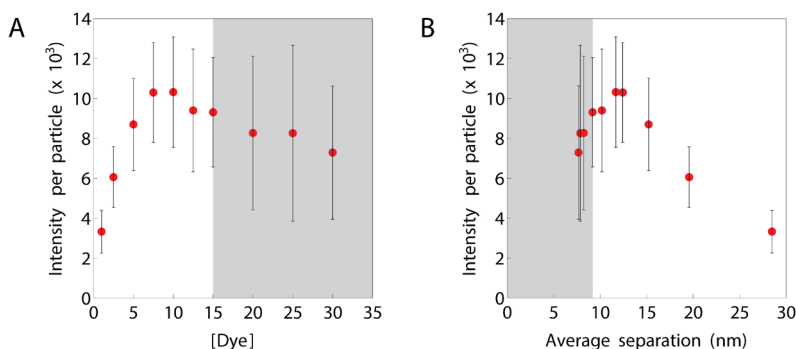
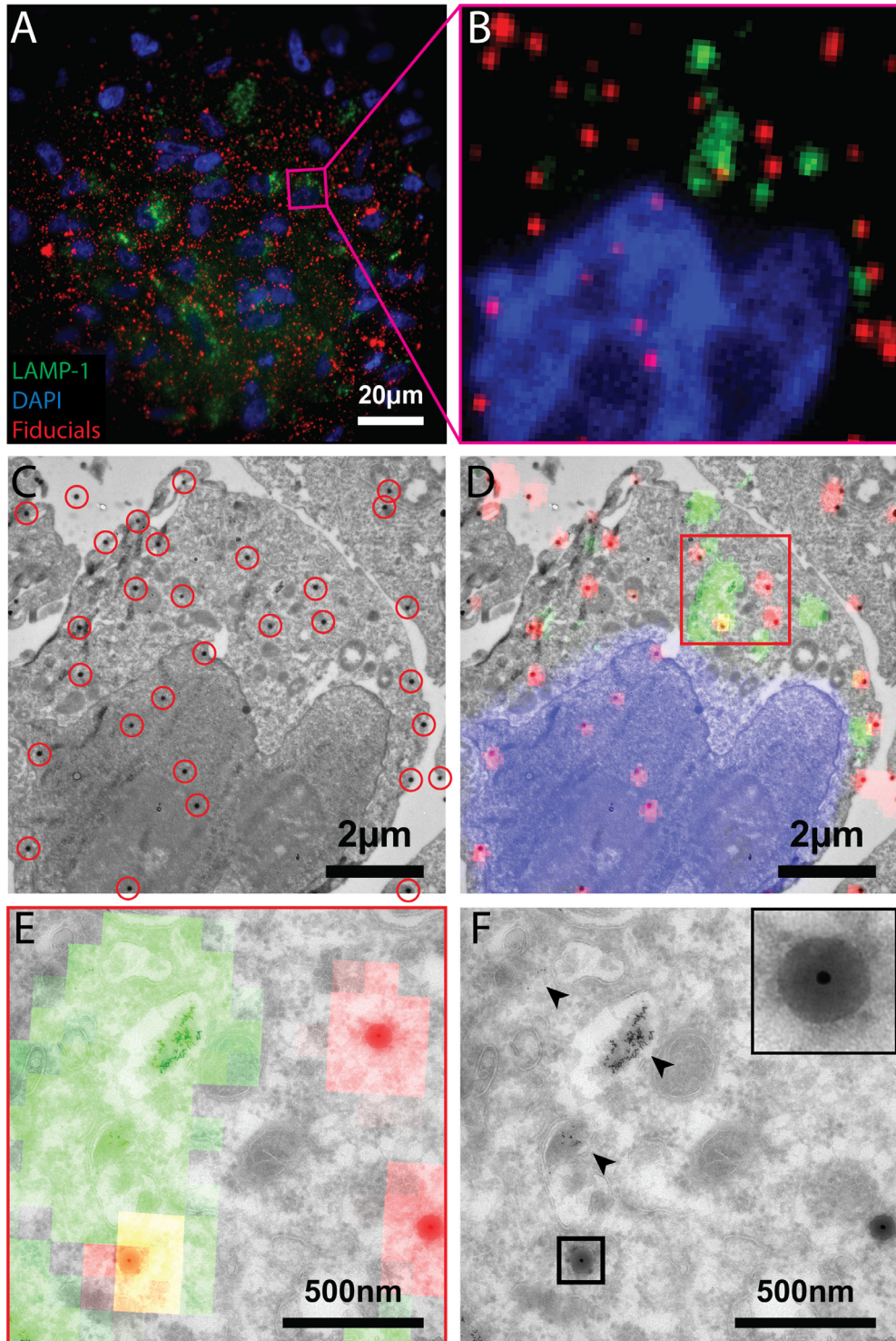


Figure 4: Average single particle intensity plotted as a function of the relative dye concentration (a) and as a function of the average fluorophore separation (b). The standard deviation in this plot corresponds to the standard deviation of the normal distribution that was fitted to the data to obtain the mean intensity. The area in gray corresponds to non-stable particles.

## 2D CLEM experiment: Widefield and TEM imaging of fiducials on thin cryosections

The nanocomposite particles with the optimum dye concentration were first tested as fiducials in a 2D CLEM experiment. This experiment was performed by the addition of the particles to a cryosection of cells on a TEM grid in a correlative workflow. Results of this experiment are included in figure 5 and demonstrate that the fiducials are clearly visible in both modalities. The FM/EM overlay included in (d) and (e) is purely based on the positions of the particles and is used to correlate LAMP-1-GFP fluorescence to the ultrastructure of late endosomes and lysosomes. The inset in figure 5f clearly shows the core-shell structure of the fiducials. This core-shell structure was also apparent at the lower magnification TEM image in figure 5 and proved to be very useful to identify the fiducials; additional images are included in the supplementary information (SI-3).

Figure 5: 2D CLEM experiment of 81.9 nm diameter fiducials on top of a 70 nm thick cryosection of HT1080 cells stably expressing LAMP-1-GFP. (a) Widefield fluorescence microscopy image. (b) Region selected for TEM imaging. (c) TEM image of the selected region (fiducials encircled in red). (d) Overlay of FM and EM data based on the positions of the particles. In (f) and (f) higher magnification CLEM and TEM images of the in (d) highlighted region are included. The GFP fluorescence perfectly overlaps with the position of late endosomes and lysosomes, which were identified in TEM by their ultrastructural characteristics and the presence of endocytosed BSA-Au5 (arrowheads). In the inset of (f) one of the fiducials is enlarged, highlighting the core-shell structure of the particles.



5

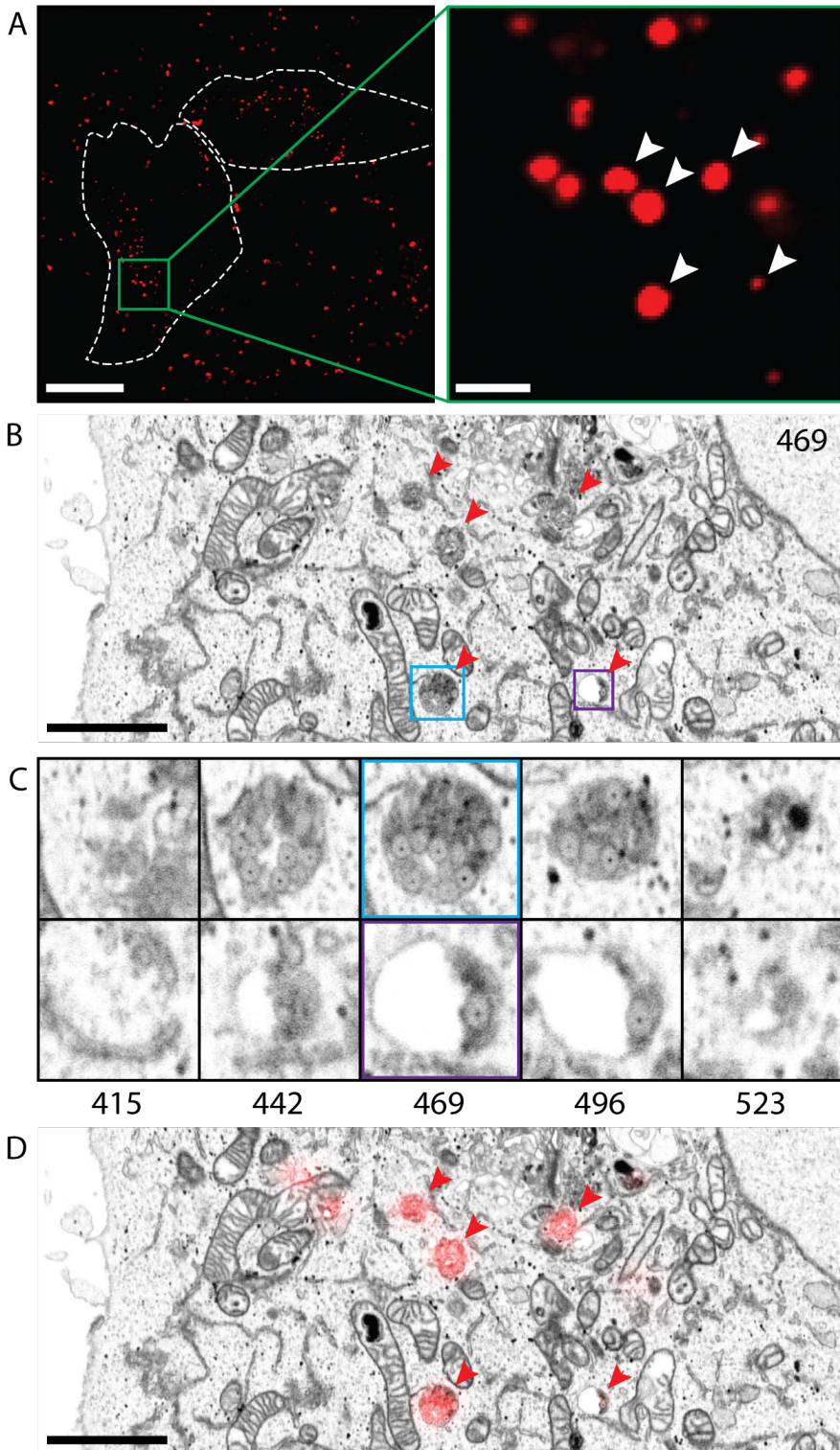
The core-shell also proved to be very useful to accurately determine the center of the fiducials and having a distinguishable well defined structure opens up possibilities for automatic registration of the particles. It should be noted that the EM magnification should be high enough to observe the core-shell structure of the fiducials. At too low magnifications, the core-shell structure is no longer visible which complicates discriminating fiducials from dirt and automatic registration of the fiducials.

### 3D CLEM experiment: Endocytosed nanoparticles as fiducials for correlative confocal fluorescence and 3D electron microscopy

In biological samples, correlating regions of interest (ROIs) between fluorescence and electron imaging can prove challenging due to the heterogeneous content of the cell and limited resolution of fluorescence imaging. Several organelles can be located within the same fluorescent spot, causing the risk of misidentification. The use of fiducials improves the registration accuracy between FM and EM, and can aid in alleviating this issue, especially when imaging in 3D. Due to their unique gold core silica shell architecture, we hypothesized that the nanoparticles could function as well-defined fiducials to correlate fluorescence and 3D electron imaging data. Previous research on silica particles has demonstrated that, under the right conditions, cells readily take up silica particles through endocytosis without cytotoxic effects [24–27] indicating that endocytosed particles could serve as a useful and functional fiducial.

To examine the viability of the nanoparticles as 3D fiducials, we incubated HeLa cells with the nanoparticles diluted in medium, allowing uptake of the particles into the cells. After three hours the samples were fixed and imaged using confocal fluorescence microscopy. Endocytosed nanoparticles were detected throughout the cells (figure 6a), indicating successful endocytosis. Following fluorescence imaging, we selected a region of a cell containing both large, bright spots and smaller, dimly fluorescent spots for FIB-SEM imaging (figure 6a, inset). Samples were postfixed, stained and embedded for imaging by focused ion beam scanning electron microscopy (FIB-SEM). In FIB-SEM, samples are imaged by scanning the surface of a ROI using the electron beam, after which a thin layer is ablated from the surface using the FIB. This cycle is repeated until the ROI has been imaged, allowing 3D reconstruction of a sample. FIB-SEM on biological samples requires relatively severe staining with heavy metals to obtain sufficient detail of cellular structures, which comes at the risk of obscuring fiducials, and exaggerating biological features that may be mistaken for fiducials. In our FIB-SEM data, we found that the combination of electron-dense gold core and electron-lucent silica shell made for easy, unequivocal identification of the compartments containing nanoparticles,

Figure 6: 3D CLEM experiment of 99.2 nm diameter fiducials after cellular uptake in HeLa cells. (a) Confocal fluorescence microscopy slice of cells after fixation. White areas indicate coarse outlines of two cells. The enlarged region highlighted in green is chosen as ROI for FIB-SEM imaging. The white arrowheads indicate fiducials visible in the corresponding FIB-SEM slice shown in (b). (b) Virtual slice of the reconstructed FIB-SEM data, corresponding to the focal plane used for fluorescence imaging. Red arrowheads indicate compartments visualized in fluorescence microscopy, which contain various amounts of fiducials. The organelles encircled in blue and purple containing fiducials are enlarged in (c). (c) FIB-SEM slices through organelles of interest at different heights of both compartments, clearly showing the different amounts of fiducials present. The numbers below the figures correspond to the number of the FIB-SEM slices. (d) Overlay of FM and EM data based on the positions of the fiducials indicated by the arrowheads in (a) and (b). The scale bars in (a) correspond to 20 and 2  $\mu\text{m}$ , the scale bar in (b) and (d) corresponds to 2  $\mu\text{m}$ .



5

even in heavily stained samples, allowing easy correlation of fluorescence and FIB-SEM data.

The nanoparticles were found in endocytic compartments (figure 6b), and could be resolved at an individual particle level. The unique structure of the particles proved helpful in identification, meaning that any fluorescent spot seen in the confocal data could be linked to corresponding particles detected using FIB-SEM (figure 6b). Interestingly, brightly fluorescent spots were correlated to compartments containing up to 40 particles (figure 6c, blue outline), whereas only 1 or 2 nanoparticles could be found in compartments corresponding to dimly fluorescent spots (figure 6c, purple outline), indicating a high level of sensitivity. Thanks to the high resolution and small sectioning distance employed by FIB-SEM, even single particles could be detected, and fitted to the fluorescent data.

In the FM (figure 6a) and FIB-SEM data, particles, and clusters of particles were also observed outside the cells. Thorough testing, including Dynamic Light Scattering measurements, proved that initially non-clustered particles were presented to the cells. The observation of clusters outside the cells can be explained by taking into account that this data is recorded after 3 hours of uptake, after the addition of fixative and after overnight fixation. Within this time frame, particles still present in the medium can aggregate, in particular after the addition of fixative. This aggregation is not expected to affect the initial uptake of the particles but this could complicate automatic registration strategies.

Combined, our data shows that the nanoparticles are taken up by HeLa cells and are useable as 3D fiducials, owing to their bright fluorescence and ease of identification in FIB-SEM data.

## Conclusions and outlook

15 nm gold particles coated with a fluorescently labelled silica shell (rhodamine B isothiocyanate (RITC)) were successfully synthesized. A relative dye concentration of 10, corresponding to an average fluorophore-fluorophore separation of 11.7 nm yielded optimum brightness and (photo)stability. Particles labelled with this optimum dye concentration were successfully used as fiducials in a 2D CLEM experiment to correlate widefield FM and TEM images by addition of the fiducials to a cryosection of cells on a TEM grid, demonstrating high registration accuracy in both FM and EM. After endocytosis of the fiducials by HeLa cells, the particles could also be used as well-defined fiducials to correlate confocal fluorescence microscopy and FIB-SEM. In both experiments, the unique core-shell signature of the fiducials proved very useful to identify the fiducials and to accurately determine the center of the fiducials. This was especially evident in the FIB-SEM data, where a fiducial with only an electron-lucent shell or only a small electron-dense core would be at risk of being misidentified as a cellular structure.

In future research, automatic registration procedures can be explored were the distinct core-shell structure of the here presented particles can be used to detect the fiducials in EM. Furthermore, we plan to use the offset between EM and FM positions of the fiducials to correct for FM/EM sample distortions. This opens up the possibility to use the fiducials to test and quantify the accuracy of different data correlation methods. Such a method can for example include nonlinear effects such as sample deformation caused by shrinkage of the sample in EM. Furthermore, the unique architecture of the nanoparticles can aid in devising automated correlation strategies, based on accurate localization of the nanoparticles within complex

biological specimens. Finally, we note that due to the silica shell the particles are non-toxic and compatible with live cell imaging experiments, opening up imaging strategies for live-cell correlative imaging.

## Materials and Methods

### Synthesis of the fiducial markers

The fiducial markers used in this study were synthesized via a multistep procedure, experimental details are included in the supplementary information (SI-1,2). Briefly, gold particles with a diameter around 15 nm were synthesized via the sodium citrate reduction [28,29]. After polyvinylpyrrolidone (PVP) functionalization [30], the particles were transferred to ethanol and coated with a very thin non fluorescent silica layer using a seeded growth procedure based on the traditional Stöber method [31–33]. This layer stabilizes the particles and acts as a spacer between the gold and the fluorophores. Next, the particles were coated with a rhodamine B labelled silica layer. By coupling the fluorophores to (3-Aminopropyl)triethoxysilane (APTES) molecules prior to the synthesis, fluorophores were covalently incorporated within the silica matrix [16,34]. Finally, to keep the particles stable, the particles were coated with a second thin silica layer. To optimize the fluorophore labelling density, particles labelled with different fluorophore densities were synthesized by varying the amount of APTES-fluorophore complex added during growth of the fluorescent silica layer. The particles were characterized to find the optimum labelling density in terms of particle brightness and (photo)chemical stability.

### Determination of the fluorophore incorporation efficiency

Immediately after synthesis of the particles, 3 mL of the reaction mixture was transferred to a 5 mL eppendorf tube. This solution was centrifuged 15 minutes at 15.000 rcf to separate the particles from the reaction mixture. The supernatant was collected and stored. The particles were redispersed in 3 mL absolute ethanol and centrifugation and redispersion in ethanol was repeated two more times. 1.5 mL particle solution and 1.5 mL of a 0.4 M sodium hydroxide solution in water were transferred to a clean 5 mL eppendorf tube. After homogenization, solutions were stored for 48 hours to ensure complete dissolution of the silica shell of the particles. Next, the solutions were centrifuged 30 minutes at 20.000 rcf to remove the non-dissolved gold cores from the solution. Supernatants, ranging from transparent and colorless for the blanco (Dye] = 0] to transparent pink for high labelling densities (Dye] = 30] were separated from the red to black pellets and stored. Absorption spectra of all solutions were recorded on a HP8953A spectrophotometer in 1 cm quartz cuvettes. If necessary, samples were diluted with a 1:1 (volume ) mixture of ethanol and 0.4 M sodium hydroxide solution.

### Spectral and radiative decay measurements

Bulk excitation and emission spectra and radiative decay measurements of the particles suspended in ethanol were recorded in 1 cm quartz cuvettes using an Edinburg Instruments FLS920 fluorescence spectrometer. In all measurements, fluorescence was detected at an angle of 90° to the exciting beam. Furthermore, a 530 nm longpass filter was placed between the sample and the detector in all measurements to remove residual excitation light. To record excitation and emission spectra, a 450 W xenon lamp and a double excitation monochromator with a grating blazed at 500 nm was used for excitation. Spectra were recorded with a Hamamatsu H74220-60 photo sensor module with a grating blazed at 500 nm. For the radiative decay measurements a picosecond pulsed diode laser (EPL-515) emitting at 509.8

nm with a 50 ns pulse period and a 204.4 ps pulse width was used for excitation. Radiative decay curves were recorded with a Hamamatsu R928 PMT detector with a grating blazed at 500 nm.

### Single particle measurements

Measurements were carried out on a Nikon Eclipse Ti widefield microscope equipped with a 40x 0.75 NA Nikon air objective. A Nikon TI-ND6-PFS perfect focus unit was used to retain sample focus during the measurements. A mercury arc lamp in conjunction with a 510-560 nm excitation filter, a 565 nm long pass dichroic mirror and a 590 nm long pass emission filter ensured proper illumination and detection wavelengths. An excitation intensity of 6.0 W/cm<sup>2</sup> was used in all experiments. Finally, an Andor NEO sCMOS camera was used to record images. Single particle intensities were determined using ThunderSTORM [35]. For the single particle intensity measurements, the obtained data was directly analyzed in Mathematica. To obtain the average single particle intensities, for every sample, data obtained from at least 20 images was plotted in a histogram. The first peak in this histogram was attributed to the single particle intensity and a normal distribution was fitted to this peak to obtain the mean intensity and the standard deviation. For the bleaching measurements, a second analysis was performed in MatLab to trace the intensity of single particles from frame to frame. Furthermore, the data was filtered based on the single particle intensities determined from the first frame to remove clusters from the data set. The filtered data was averaged per frame to obtain bleaching curves.

### Cell culture

HeLa cells and HT1080 cells stably expressing LAMP-1-GFP were cultured in a 37°C, 5% CO<sub>2</sub> incubator, in T75 culture bottles (Corning). Cells were maintained in Dulbecco's Modified Eagle's Medium (DMEM; Gibco) supplemented with 10% fetal bovine serum, 2 mM L-glutamine, 100 U/mL penicillin, 100 µg/mL streptomycin (referred to as complete DMEM). Cells were passaged when confluency reached 85% to 90%.

### 2D CLEM: Widefield and TEM imaging of fiducials on thin cryosections

HT1080 cells stably expressing LAMP-1-GFP were incubated in complete DMEM containing 5 nm diameter colloidal gold particles conjugated to bovine serum albumin (BSA-Au5 for 3 hours. Following incubation, cells were processed for cryosectioning according to previous protocol [12]. Briefly, cells were chemically fixed using formaldehyde and glutaraldehyde, scraped from the culture substrate and pelleted in 12% gelatin. Samples were infiltrated overnight in 2.3 M sucrose for cryoprotection, and plunge frozen in liquid nitrogen. 70 nm thick cryosections were sectioned and picked up on copper support grids coated with formvar and carbon. Sections were treated with DAPI (4 µg/mL) diluted in PBS to label nuclei. After labelling, sections were washed with PBS, incubated with a diluted solution (1/500) of the fiducial markers in water, followed by rinses with PBS and dH<sub>2</sub>O. The grids were sandwiched between a microscope slide and a #1.5 coverslip in a drop of 50% glycerol in dH<sub>2</sub>O. Fluorescence imaging for DAPI, GFP and the fluorescent nanoparticles was performed with a Deltavision RT Core widefield microscope (GE Healthcare) equipped with a Cascade II EM-CCD camera (Photometrics), using a 100x/1.4 NA objective. Following fluorescent imaging, the sections were washed in dH<sub>2</sub>O, stained with uranyl acetate and embedded in methylcellulose as previously described [12]. ROIs determined in FM were retraced and imaged in a Tecnai T12

TEM (Thermo Scientific). Following imaging, the x and y positions of the fiducials in fluorescence data were registered using ThunderSTORM [35]. Fiducials not properly resolved in ThunderSTORM were not considered as reference points for registration of data. In TEM data, positions of the fiducials were registered manually using the center of the gold core. Correlation of fluorescence and TEM data based on the positions of the particles was performed using eC-CLEM [36].

### **3D CLEM: Confocal and FIB-SEM imaging of endocytosed nanoparticles**

Hela cells were grown on gridded glass coverslips, prepared as described by Fermie et al [37]. Cells were incubated with fiducial markers at a concentration of 1  $\mu\text{g/ml}$  dissolved in complete DMEM and incubated for 3 hours, and fixed overnight in 1x PHEM buffer (60 mM PIPES, 25 mM HEPES, 10 mM EGTA, 2 mM  $\text{MgCl}_2$ , pH = 6.9) containing 4% paraformaldehyde (Sigma) and 0.1% glutaraldehyde (Merck) at 4°C. Following fixation, coverslips with cells were washed in 1x PHEM buffer and mounted in live-cell coverslip holders filled with 1x PHEM buffer to prevent dehydration of the samples. Fluorescence imaging was performed using a Zeiss LSM700 CLSM equipped with 63x/1.4 NA oil immersion objective. Nanoparticles were excited using the 555 nm laser line at 2% power. Z-stacks were collected with 200 nm step size. The position of cells relative to the grid of the coverslips was recorded using polarized light. Cells were prepared for electron microscopy according to protocol described earlier [38] with minor modifications. Briefly, samples were postfixed using 1% osmium tetroxide (w/v) with 1.5% potassium ferrocyanide (w/v) for 1 h on ice, incubated with 1% thiocarbonylhydrazide in dH<sub>2</sub>O (w/v) for 15 min, followed by 1% osmium tetroxide in dH<sub>2</sub>O for 30 min. Samples were stained en-bloc with 2% uranyl acetate in dH<sub>2</sub>O for 30 minutes and stained with Walton's lead aspartate for 30 min at 60°C. Dehydration was performed using a graded ethanol series. Samples were embedded in Epon resin and polymerized for 48-60 h at 65°C. Polymerized resin blocks were removed from the glass coverslips using liquid nitrogen, mounted on aluminum stubs and rendered conductive using conductive carbon paint and a sputter coated layer of 5 nm Pt. Following sample preparation, automated serial imaging was performed using a Scios FIB-SEM (Thermo Scientific), according to previously described workflow [37]. Briefly, trenches were prepared surrounding the region of interest using the FIB, after which automated serial imaging was performed using 5 nm isotropic voxels. Electron microscopy images were collected at an acceleration voltage of 2kV and a current of 0.2 nA, using the T1 backscattered electron detector. Following imaging, correlation of fluorescence and FIB-SEM data was achieved by manual registration using Fiji and ec-CLEM [36]. FIB-SEM images are presented with inverted contrast, to resemble TEM contrast.

### **Acknowledgements**

The authors thank Cilia de Heus (University Medical Center Utrecht) for her help with the preparation of EM samples.

### **Author contributions statement**

J.Fo. conceived the experiments; J.Fo. synthesized the particles and performed spectral and decay measurements; D.J.H. and J.Fo. performed single particle measurements; J. Fo., T.O.M.K. and G.A.B. analyzed the single particle measurements; J.Fe. and N.L. conducted the 2D and 3D CLEM experiments; J. Fo, J.Fe. and N.L. wrote the manuscript with input from the other authors; A.M., J.K. and H.C.G. supervised the project and provided funding. All authors have approved the final version of the manuscript.

## References

1. de Boer P, Hoogenboom JP, Giepmans BNG. Correlated light and electron microscopy: ultrastructure lights up! *Nat Methods* 2015;12:503–13.
2. Narayan K, Subramaniam S. Focused ion beams in biology. *Nat Methods* 2015;12:1021–1031.
3. Olmos Y, Hodgson L, Mantell J, Verkade P, Carlton JG. ESCRT-III controls nuclear envelope reformation. *Nature* 2015;522:236–9.
4. Karreman MA, Mercier L, Schieber NL, Solecki G, Allio G, Winkler F, Ruthensteiner B, Goetz JG, Schwab Y. Fast and precise targeting of single tumor cells in vivo by multimodal correlative microscopy. *J Cell Sci* 2016;129:444–56.
5. Kukulski W, Schorb M, Welsch S, Picco A, Kaksonen M, Briggs JAG. Correlated fluorescence and 3D electron microscopy with high sensitivity and spatial precision. *J Cell Biol* 2011;192:111–119.
6. Schellenberger P, Kaufmann R, Siebert CA, Hagen C, Wodrich H, Grünewald K. High-precision correlative fluorescence and electron cryo microscopy using two independent alignment markers. *Ultramicroscopy* 2014;143:41–51.
7. Schorb M, Briggs J a G. Correlated cryo-fluorescence and cryo-electron microscopy with high spatial precision and improved sensitivity. *Ultramicroscopy* 2013;1–9.
8. Masich S, Östberg T, Norlén L, Shupliakov O, Daneholt B. A procedure to deposit fiducial markers on vitreous cryo-sections for cellular tomography. *J Struct Biol* 2006;156:461–468.
9. Brown E, Verkade P. The use of markers for correlative light electron microscopy. *Protoplasma* 2010;244:91–97.
10. Giepmans BNG, Deerinck TJ, Smarr BL, Jones YZ, Ellisman MH. Correlated light and electron microscopic imaging of multiple endogenous proteins using Quantum dots. *Nat Methods* 2005;2:743–749.
11. Oorschot V, de Wit H, Annaert WG, Klumperman J. A Novel Flat-embedding Method to Prepare Ultrathin Cryosections from Cultured Cells in Their In Situ Orientation. *J Histochem Cytochem* 2002;50:1067–1080.
12. Slot JW, Geuze HJ. Cryosectioning and immunolabeling. *Nat Protoc* 2007;2:2480–2491.
13. Miles BT, Greenwood AB, Benito-Alifonso D, Tanner H, Galan MC, Verkade P, Gersen H. Direct Evidence of Lack of Colocalisation of Fluorescently Labelled Gold Labels Used in Correlative Light Electron Microscopy. *Sci Rep* 2017;7:44666.
14. Karreman M a, Agronskaia A V, van Donselaar EG, Vocking K, Fereidouni F, Humbel BM, Verrips CT, Verkleij AJ, Gerritsen HC. Optimizing immuno-labeling for correlative fluorescence and electron microscopy on a single specimen. *J Struct Biol* 2012;180:382–6.
15. Billinton N, Knight AW. Seeing the Wood through the Trees: A Review of Techniques for Distinguishing Green Fluorescent Protein from Endogenous Autofluorescence. *Anal Biochem* 2001;291:175–197.
16. Imhof A, Megens M, Engelberts JJ, de Lang DTN, Sprik R, Vos WL. Spectroscopy of Fluorescein (FITC) Dyed Colloidal Silica Spheres. *J Phys Chem B* 2002;103:1408–1415.
17. Lakowicz JR. Principles of fluorescence spectroscopy. Springer; 2006.
18. Genovese D, Rampazzo E, Zaccheroni N, Montalti M, Prodi L. Collective Properties Extend Resistance to Photobleaching of Highly Doped Plus NPs. *Eur J Inorg Chem* 2017;2017:5094–5097.
19. Szabó Á, Szendi-Szalmári T, Ujlaky-Nagy L, Rádi I, Vereb G, Szöllösi J, Nagy P. The Effect of Fluorophore Conjugation on Antibody Affinity and the Photophysical Properties of Dyes. *Biophys J* 2018;114:688–700.
20. López Arbeloa I, Ruiz Ojeda P. Dimeric states of rhodamine B. *Chem Phys Lett* 1982;87:556–560.
21. Setiawan D, Kazaryan A, Martoprawiro MA, Filatov M. A first principles study of fluorescence quenching in rhodamine B dimers: how can quenching occur in dimeric species? *Phys Chem Chem Phys* 2010;12:11238.
22. Penzkofer A, Lu Y. Fluorescence quenching of rhodamine 6G in methanol at high concentration. *Chem Phys* 1986;103:399–405.
23. López Arbeloa F, Ruiz Ojeda P, López Arbeloa I. Dimerization and trimerization of rhodamine 6G in aqueous solution. Effect on the fluorescence quantum yield. *J Chem Soc Faraday Trans 2 Mol Chem Phys* 1988;84:1903–1912.
24. Jin Y, Kannan S, Wu M, Zhao JX. Toxicity of Luminescent Silica Nanoparticles to Living Cells. *Chem Res Toxicol* 2007;20:1126–1133.
25. Chu Z, Huang Y, Tao Q, Li Q. Cellular uptake, evolution, and excretion of silica nanoparticles in human cells. *Nanoscale* 2011;3:3291.
26. Zhu J, Liao L, Zhu L, Zhang P, Guo K, Kong J, Ji C, Liu B. Size-dependent cellular uptake efficiency, mechanism, and cytotoxicity of silica nanoparticles toward HeLa cells. *Talanta* 2013;107:408–415.
27. Annika Mareike Gramatke I-LH, Gramatke AM, Joksimovic R, Sokolowski M, Gradzielski M, Haase A. Size and Cell Type Dependent Uptake of Silica Nanoparticles. *J Nanomed Nanotechnol* 2014;05.
28. Turkevich J, Stevenson PC, Hillier J. A study of the nucleation and growth processes in the synthesis of

- colloidal gold. *Discuss Faraday Soc* 1951;11:55.
29. Perrault SD, Chan WCW. Synthesis and Surface Modification of Highly Monodispersed, Spherical Gold Nanoparticles of 50–200 nm. *J Am Chem Soc* 2009;131:17042–17043.
  30. Graf C, Vossen DLJ, Imhof A, Van Blaaderen A. A general method to coat colloidal particles with silica. *Langmuir* 2003;19:6693–6700.
  31. Giesche H. Synthesis of monodispersed silica powders I. Particle properties and reaction kinetics. *J Eur Ceram Soc* 1994;14:189–204.
  32. Giesche H. Synthesis of monodispersed silica powders II. Controlled growth reaction and continuous production process. *J Eur Ceram Soc* 1994;14:205–214.
  33. Stöber W, Fink A, Bohn E. Controlled growth of monodisperse silica spheres in the micron size range. *J Colloid Interface Sci* 1968;26:62–69.
  34. Verhaegh NAM, Blaaderen A van. Dispersions of Rhodamine-Labeled Silica Spheres: Synthesis, Characterization, and Fluorescence Confocal Scanning Laser Microscopy. *Langmuir* 1994;10:1427–1438.
  35. Ovesný M, Křížek P, Borkovec J, Švindrych Z, Hagen GM. ThunderSTORM: a comprehensive ImageJ plug-in for PALM and STORM data analysis and super-resolution imaging. *Bioinformatics* 2014;30:2389–2390.
  36. Paul-Gilloteaux P, Heiligenstein X, Belle M, Domart MC, Larijani B, Collinson L, Raposo G, Salamero J. EC-CLEM: Flexible multidimensional registration software for correlative microscopies. *Nat. Methods* 2017;14:102–103.
  37. Fermie J, Liv N, ten Brink C, van Donselaar EG, Müller WH, Schieber NL, Schwab Y, Gerritsen HC, Klumperman J. Single organelle dynamics linked to 3D structure by correlative live-cell imaging and 3D electron microscopy. *Traffic* 2018;354–369.
  38. Deerinck TJ, Bushong E, Thor A, Ellisman MH. NCMIR Methods for 3D EM: A New Protocol for Preparation of Biological Specimens for Serial Block-Face SEM. SBEM Protoc v7\_01\_2010 Available online <https://ncmir.ucsd.edu/sbem-protocol> (accessed 17 Oct 2018) 2018;

## Appendix for chapter 5: supplementary information

### Synthesis of the fiducial markers

The particles were synthesized via the multistep procedure depicted schematically in figure S1. In the first step, citrate stabilized gold nanoparticles with a diameter of approximately 15 nm were synthesized in water via the extensively studied citrate reduction or Turkevich method [28,29]. Next, the particles were coated with a nonionic polymer, polyvinylpyrrolidone or PVP, so that they could be transferred into ethanol following the procedure described by Graf et al [30]. Once the particles were transferred to ethanol, they were coated with a fluorescently labelled silica shell via a seeded growth procedure similar to the procedure described by H. Giesche [31,32]. This seeded growth procedure is based on the traditional Stöber method [33] to synthesize silica particles of a specific size obtained via the addition of silica precursor, TEOS, to mixtures of water, ammonia and alcohol.

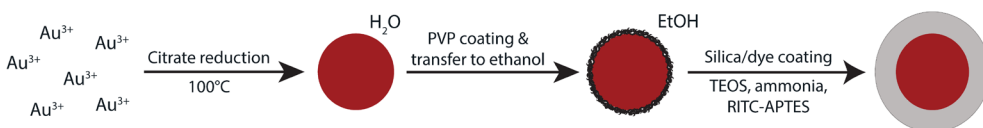


Figure S1: A schematic representation of the synthesis of the (rhodamine B labelled) silica coated gold nanoparticles

Fluorescent dyes were covalently incorporated within the silica matrix during shell growth following the procedures described by A. Imhof et al. [16] for fluorescein isothiocyanate (FITC) and Verhaegh et al. [34] for rhodamine B isothiocyanate (RITC). Covalent incorporation is ensured by linking a fluorophore with an active amine reactive group such as an isothiocyanate group with an aminosilane; (3-aminopropyl) triethoxysilane or APTES. After coupling, this complex was introduced during the silica shell growth and part of it was incorporated within the silica shell.

### Materials

Hydrogen tetrachloroaurate(III)trihydrate or chloroauric acid (ACS reagent) was obtained from ACROS Organics. Sodium citrate tribasic dihydrate, tetraethyl orthosilica or TEOS (reagent grade, 98%), polyvinylpyrrolidone or PVP (Average Mw 10.000 g mol<sup>-1</sup>), ammonium hydroxide solution (ACS reagent, 28-30% NH<sub>3</sub> basis), rhodamine B isothiocyanate (mixed isomers) or RITC, 99% (3-Aminopropyl) triethoxysilane or APTES, dialysis tubing cellulose membrane (av. flat width 33 mm) and Vivaspin 20 centrifugal concentrator tubes (MWCO 100.000 Da) were purchased from Sigma-Aldrich. Absolute ethanol was purchased from Merck.

All glassware and stirring beans used for the gold synthesis were rinsed with aqua regia and milli-Q water prior to use. All remaining glassware was extensively cleaned with soap, water and ethanol prior to use. Milli-Q water was used in all the experiments.

### Methods

#### Synthesis of 15 nm diameter gold cores

Gold and citrate stock solutions were prepared by transferring 0.1 g chloroauric acid and 0.1 g sodium citrate to two separate vials. 10 mL water was added to both vials to obtain 1% (w/v) stock solutions. In a typical synthesis, 300 mL water and 3 mL of the 1% (w/v) gold solution were transferred to a two necked round bottomed flask equipped with a condenser. This flask was placed in a  $140^\circ\text{C}$  oil bath to ensure

homogeneous heating and was heated until boiling under constant vigorous stirring (600 rpm). When boiling commenced, 9 mL of the 1% (w/v) sodium citrate solution was added. Within the first few minutes after sodium citrate addition, the color of the solution gradually changed from blue to purple to deep red indicating particle formation. After 15 minutes boiling no change in color was observed anymore and the deep red solution was cooled down to room temperature.

### **PVP functionalization and transfer of the particles to ethanol**

120  $\mu\text{L}$  of a 10% (w/v) PVP solution (1 g in 10 mL water) was added per 5 mL of gold nanoparticle solution under constant stirring. The obtained solution was stirred for at least 12 hours to ensure functionalization of the gold nanoparticles. After 12 hours, the solution was centrifuged 15 minutes at 15.000 rcf in 5 mL eppendorf tubes. The supernatant (water) was removed as much as possible with a glass pipette and the particles were redispersed in an equal amount of ethanol. Homogenization of the sample was ensured by placing the obtained solution in a sonication bath (~1 minute).

### **APTES-dye coupling**

To perform the APTES-dye coupling reaction, 10 mg RITC and 1 mL absolute ethanol were transferred to a vial. This solution was stirred and 8.3  $\mu\text{L}$  APTES was added. The vial was wrapped in aluminum foil to protect the fluorophore from photobleaching and stirred for 16 hours. The APTES-dye ratio during this coupling reaction was calculated such that there was a two times excess of APTES compared to the amount of fluorophore. Different dilutions of this dye solution in absolute ethanol were used to synthesize particles labelled with different dye labelling densities. Solutions with relative dye concentrations ranging from 0 to 30 (labelled as [Dye] = 0 - 30) were prepared by preparing dilutions of 0 to 30 vol% of APTES-dye solution in ethanol. For example, to obtain a relative dye concentration of 30, 300  $\mu\text{L}$  APTES-dye solution (30 vol%) and 700  $\mu\text{L}$  absolute ethanol (70 vol%) were transferred to a vial.

### **Coating of the gold nanoparticles with a fluorescently labelled silica shell**

15 mL solution of PVP stabilized gold nanoparticles was transferred to a 20 mL closed vial. Under continuous stirring (700 rpm), 1500  $\mu\text{L}$  28-30% ammonium hydroxide solution was added to this solution. Next, 30  $\mu\text{L}$  of a 10 vol% of TEOS solution in absolute ethanol was added to grow a first, very thin, silica layer. This layer helps to stabilize the particles since the immediate addition of APTES-dye solution results in the formation of clusters of gold nanoparticles. Furthermore, this layer serves as a spacer layer between the gold cores and the fluorophores embedded in the silica shell. 60 minutes after the first TEOS addition an additional 150  $\mu\text{L}$  of the 10 vol% TEOS solution was added. After approximately one minute of stirring, 150  $\mu\text{L}$  of diluted APTES-dye solution was added as well. Both additions were repeated with 300  $\mu\text{L}$  after 90 minutes of stirring. Finally, after another 90 minutes, 60  $\mu\text{L}$  of 10 vol% TEOS was added to grow a final stabilization layer around the fluorescently labelled particles.

60 minutes after the final addition, the reaction mixture was transferred to a dialysis bag inside a 40 mL vial filled with ethanol. The solution was gently stirred and the ethanol was replaced three times in a time span of 36 hours. After 36 hours, further cleaning of the particles was performed via repeated centrifugation in 100.000 MWCO vivaspin tubes.

### A calibration line to synthesize particles of a desired size

To synthesize particles of a desired size, a multistep silica coating of the gold nanoparticles was performed. Increasing volumes of TEOS were added to 5 mL of PVP functionalised gold nanoparticles in a solution of water, ammonia and absolute ethanol. 90 minutes after every addition, TEM samples were prepared. In figure S2 representative TEM images of these samples are shown.

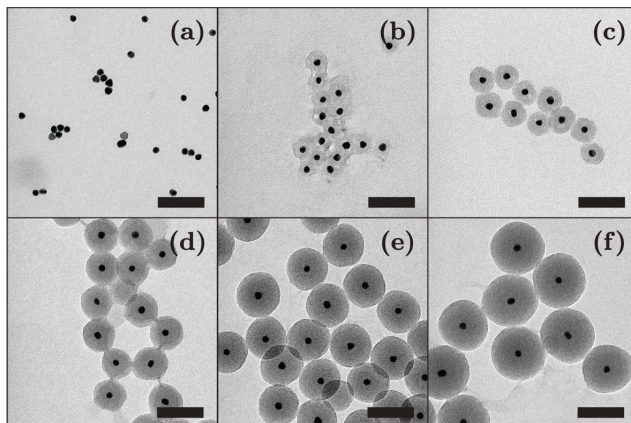


Figure S2: Representative TEM images of samples taken at different stages of silica coating. Sample (a) is prepared before TEOS addition. From (b) to (f) volumes of 20, 40, 80, 160 and 320  $\mu\text{L}$  of 10 vol% TEOS are added.

From the TEM images it becomes clear that the silica shell is already homogeneous after the first TEOS addition (b). Furthermore, one can conclude that the thickness of the silica shell is increasing from (b) to (f) after every TEOS addition. Average particle diameters of all samples were determined by measuring the diameter of 100 particles, corresponding size histograms are presented in figure S3a. In figure S3b the average particle diameters are plotted versus the cube root of the total volume of added 10 vol% TEOS. From this plot it becomes evident that there is a linear relationship between these two parameters after the first TEOS addition. This is also in line with expectations since TEOS is converted directly into silica. Therefore, if silica grows only on the existing particles, there should be a linear relationship between the volume of added TEOS and the increase in volume of the particles. This linear relationship demonstrates that particles with every desired size can be synthesized with high control simply by varying the amount of added TEOS. From figure S3b it can be derived how much TEOS should be added to synthesize particles of a desired size starting from the same solution of gold particles.

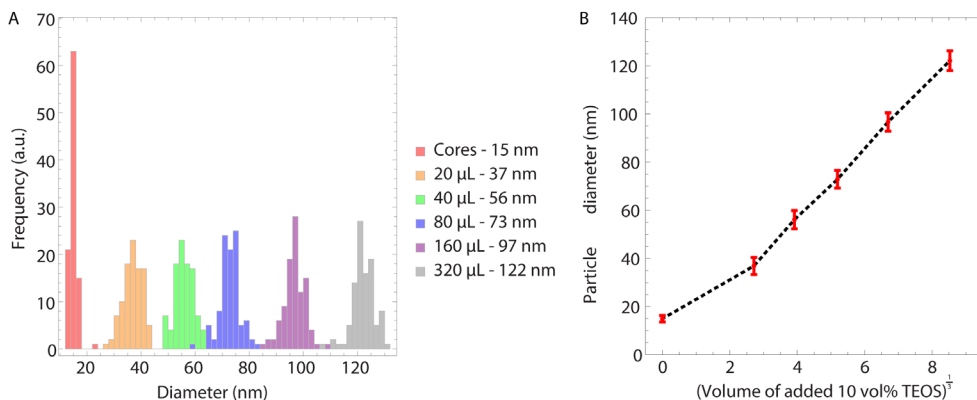


Figure S3: Size histograms (a) and a plot (b) showing the linear relationship between the cube root of the added volume of TEOS and the particle diameter.

## 2D-CLEM experiment: Recognition of the fiducials

In this section it is demonstrated how the unique signature of the particles can be used to identify the fiducials in EM. To do so, specific areas of the EM image of the 2D-CLEM example presented in the main text are enlarged in figure S4. This demonstrates that already in this low magnification image the core-shell structure can be used to distinguish between fiducials (encircled in green) and other dark spot that are excluded as fiducials (encircled in orange). This is also confirmed by FM data since no fluorescence is observed from the dark spots that are excluded as fiducials.

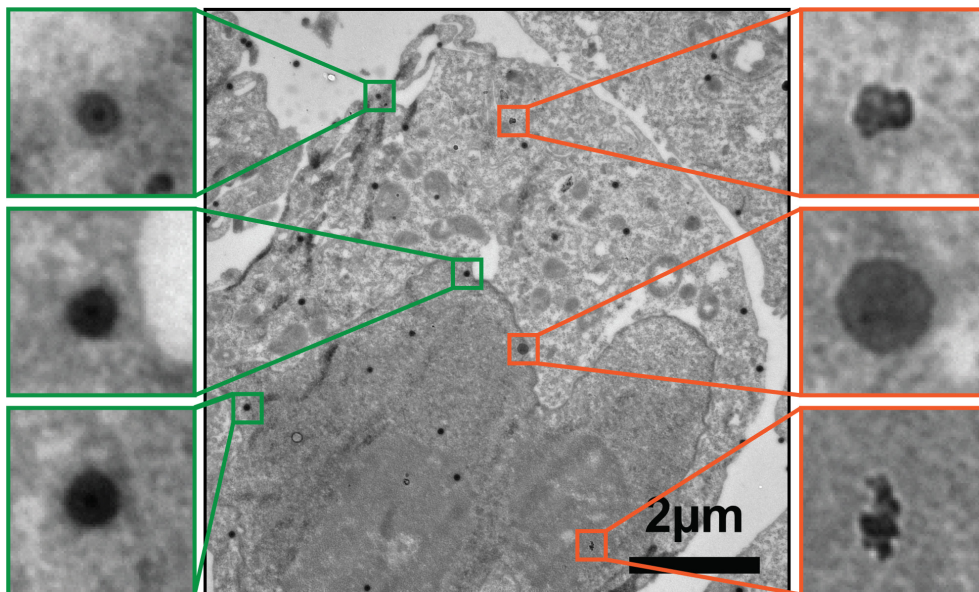


Figure S4: Low magnification TEM image of 81.9 nm diameter fiducials on top of a 70 nm thick cryosection of HT1080 cells stably expressing LAMP-1-GFP.

This becomes even more apparent in the higher magnification EM image of the same region of interest included in figure S5. Again, the particles encircled in green correspond to fiducials whereas regions encircled in orange are excluded as fiducials because of the absence of the distinct core-shell structure.

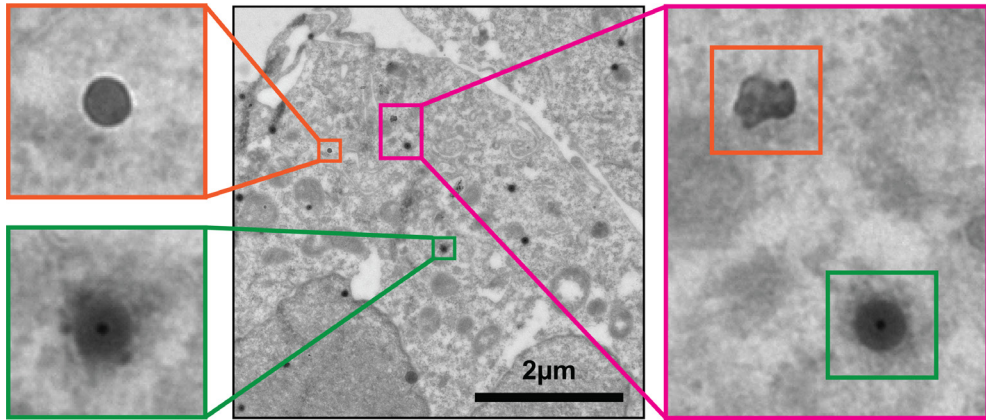
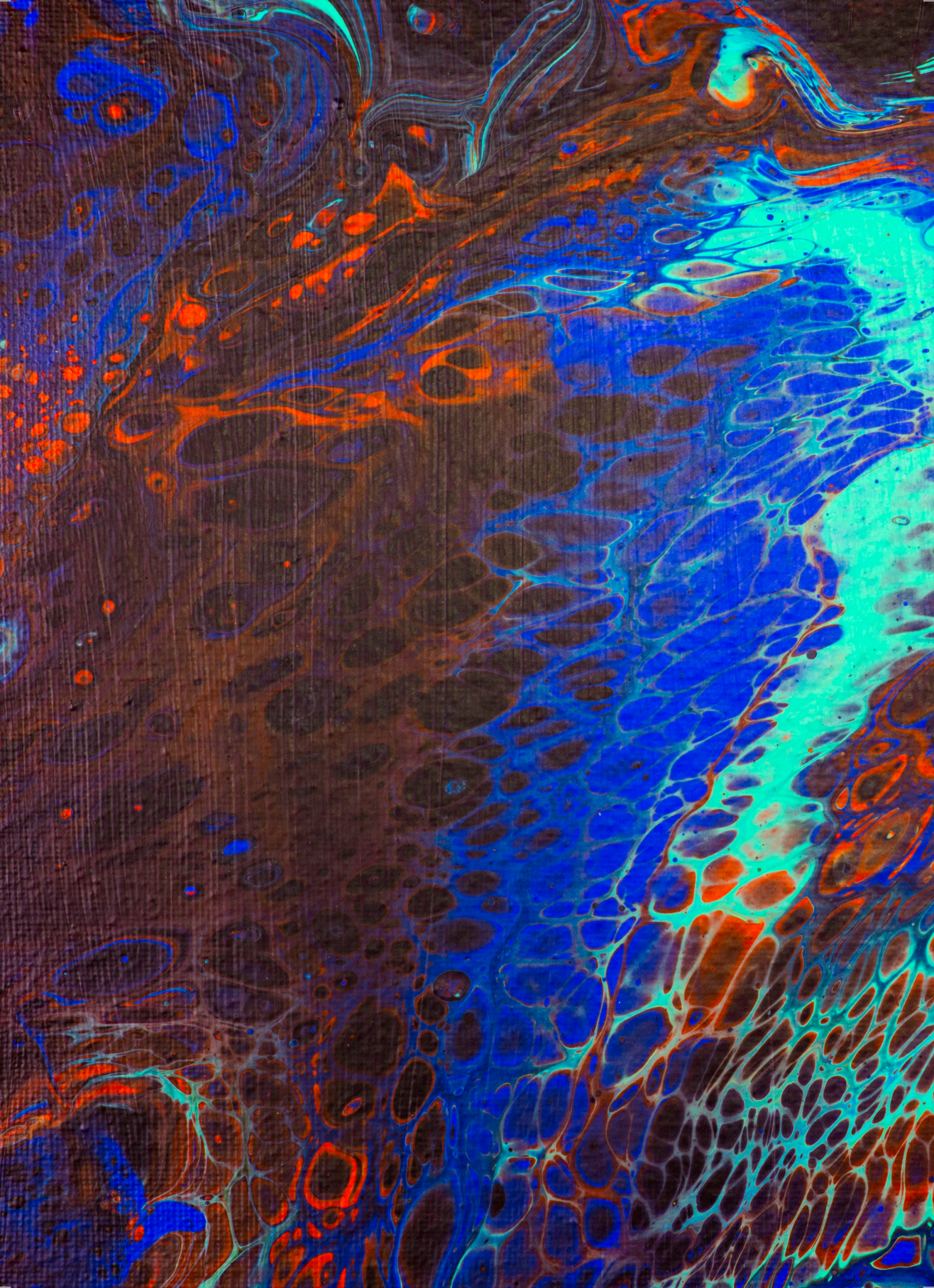


Figure S5: TEM image of 81.9 nm diameter fiducials on top of a 70 nm thick cryosection of HT1080 cells stably expressing LAMP-1-GFP.

Fluorescently labelled silica coated gold nanoparticles as fiducial markers for correlative light and electron microscopy



# Summarizing discussion

Job Fermie<sup>1,2</sup>, Nalan Liv<sup>1</sup>, Wally Müller<sup>3</sup>, Hans Gerritsen<sup>2</sup>, Judith Klumperman<sup>1</sup>

1. Section Cell Biology, Center for Molecular Medicine, University Medical Center Utrecht, Utrecht University, Utrecht, The Netherlands
2. Section Molecular Biophysics, Debye Institute for Nanomaterials Science, Utrecht University, Utrecht, The Netherlands
3. Section Cell Biology & Mycology, Department of Biology, Utrecht University, Utrecht, The Netherlands

---

## Chapter 6

---

## Summary

Correlative live-cell light and electron microscopy (live-cell CLEM) has revolutionized bioimaging, since it is the only approach that infers molecular and dynamic information to ultrastructural context. Live-cell CLEM is used to identify rare or transient events for EM analysis, that are nearly impossible to detect by electron microscopy (EM) alone[1–5]. Live-cell data can also be used to register live-cell dynamics to an ultrastructural snapshot, but this has seen limited application since technical challenges still preclude broader adoption[6–8]. The fixation steps required for optimal ultrastructural preservation can introduce a time gap between the last live frame and the EM snapshots taken after fixation. Due to the resolution mismatch between the fluorescence microscope (FM) and the EM finding back regions of interest (ROI) between modalities in 3D can prove challenging. Finally, accurate overlay of fluorescence and EM data is crucial to interpret the correlated datasets. These challenges must be overcome to efficiently retrace individual organelles between live-cell FM data and EM, especially in a 3D volume.

This thesis explored novel approaches to reliably facilitate live-cell correlative imaging. We demonstrate how correlative live-cell imaging and EM link dynamic and functional properties to ultrastructural context. Furthermore, we demonstrate how CLEM is used to significantly reduce imaging time in the EM by providing a system of reference points for targeting in focused ion beam scanning electron microscopy (FIB-SEM). Finally, we show the potential of different bimodal fiducial particles for (live-cell) CLEM using both 2D and 3D imaging systems.

In chapter 2, we introduce CLEM methods for Single Organelle Microscopy, where we combine live-cell imaging with large-scale 3D EM (volume EM). This combination of techniques enables efficient, quantitative investigation of compositional, dynamic and ultrastructural properties of individual organelles. High-speed live-cell imaging is used to register the dynamic behavior of fluorescently labeled organelles. Cells are fixed in situ to minimize the imaging gap between live data and the subsequent fixed data. Imaging with FIB-SEM then collects 3D ultrastructural data of the previously live-imaged organelles. We demonstrate this approach in cells labeled with the lysosomal marker LAMP-1-GFP. Using Single Organelle Microscopy, we analyze dynamic properties such as speed, displacement and fusion events of endosomal organelles, and link these to ultrastructural features such as intraluminal vesicles and membrane contacts with surrounding organelles. Since FIB-SEM captures all ultrastructural data of a given volume, there is limited chance of missing organelles during registration of datasets, which may happen during serial sectioning. This was used to provide morphological context to the behavior exhibited by the tracked LAMP-1-GFP spots. For example, we found that of the 10 LAMP-1-GFP spots analyzed in chapter 2, only 3 meet the morphological criteria of a lysosome. Since LAMP-1-GFP in numerous studies is referred to as an established marker for late endosomes – lysosomes, or even strictly lysosomes, this data highlights the importance of techniques like CLEM to unequivocally establish organelle identity. In addition, we found that the majority of LAMP-1-GFP organelles maintained one or more membrane contact sites with the endoplasmic reticulum, highlighting the potential of the technique to study interactions between organelles.

We further expand the capabilities of CLEM Single Organelle Microscopy in chapter 3, by using fluorescent reporters and biosensors. By registering parameters such as enzyme activity, pH and calcium content biosensors enable the interrogation of the functional state of cells. By incorporating fluorescent biosensors into a correlative

workflow, functional properties of single organelles can be investigated within ultrastructural context, in a workflow we termed functional CLEM. We show the potential of functional CLEM by validating a panel of broadly used endo-lysosomal biosensors for CLEM. Functional CLEM was then used to quantitatively study the functional state of organelles by examining over 500 endo-lysosomal organelles in wild-type and VPS41 KO cells. VPS41 is part of the HOPS complex required for fusion between late endosomes and lysosomes. In comparison to wild-type cells, in VPS41 KO cells only a small fraction of lysosomes is reached by endocytosed Dextran after two hours of uptake, whereas they were still enzymatically active. The data also show that activation of lysosomal enzymes remains largely restricted to endolysosomal hybrid and lysosomal compartments and is not increased in late endosomes under VPS41 KO conditions. These results exemplify how correlative functional imaging can be used to examine the functional implications of a genetic deletion in an ultrastructural context.

Chapters 4 and 5 focus on the development and use of novel fiducial markers in CLEM. One of the challenges for any correlative approach is the accurate registration of fluorescence to morphology, especially for volume CLEM. In chapter 4, we examine colloidal gold particles functionalized with fluorescent BSA (fBSA-Au) as endocytosed fiducial markers for CLEM. We find that fBSA-Au is readily internalized by cells and highly visible in both FM and EM. Compartments containing fBSA-Au serve as effective fiducials for both 2D and 3D EM approaches.

The use of endocytosed fiducials is further highlighted in chapter 5, where we synthesize and characterize gold-core silica-shell nanoparticles, and utilize these particles as fiducial markers. Not only do these particles allow high-accuracy CLEM overlay, they are also efficiently endocytosed, and are detectable as single particles in both confocal FM and FIB-SEM imaging. Their unique architecture makes them easily detectable in both scanning and transmission EM, where the electron-dense gold core provides a useful reference point. The particles described in chapters 4 and 5 describe two different approaches for efficient fiducials, that aid in rapid and accurate registration of correlative data. For large-scale volume imaging as in FIB-SEM, the silica nanoparticles provide good reference points, due to their large size and greater contrast in material. If immunolabeling or fine ultrastructural detail is desired, fBSA-Au is highly suitable.

## Outlook

Both LM and EM systems have recently drastically improved in the speed and resolution with which large volumes can be imaged. The automation of electron imaging and specimen handling enable high-speed imaging for days or weeks on end [9–11]. This has enabled high throughput imaging, something previously impossible in EM. High throughput EM has greatly broadened the scope in which EM can be used, allowing stitching of entire sections for large fields of view [12,13], and volume imaging to collect ultrastructural information of large, 3D volumes [9,14,15]. Customized systems routinely capture data at a rate of > 25 megapixels per second [11,16], resulting in several terabytes of raw data captured every day, with further increases expected in the near future.

This avalanche of data has revolutionized fields such as connectomics, where large-scale, uninterrupted datasets are crucial to trace the interactions between individual neurons in brain tissue [15–18]. In addition, it adds a facet to EM that was previously too time-consuming to be feasible: to use EM as a quantitative tool, rather than a qualitative one. It enables large-scale comparison between healthy

and diseased phenotypes, comparison between multiple individuals and unbiased measurements of rare structures. For cell biology, this combination of high-speed EM and CLEM is highly attractive, since it allows quantitative investigations of both dynamic and rare processes like membrane contact sites, interactions between organelle populations, and intercellular interactions.

The growth of the data collection rate does pose a problem for the cell biology and imaging fields: the collected data has to be managed in a meaningful manner to be useful for research[19,20]. This challenge goes beyond the simple goal of having sufficient storage space: instead, data should also be presentable in a meaningful manner for publication. Thus, data visualization and curation platforms have been set up to provide easy access to large-scale EM and FM data, such as EMPIAR, PDB, and EMDB[21–23]. These platforms do not only provide a way to present data to a broad audience, but also offer a tool for interested researchers to re-examine datasets. These databases provide a potential for collaborative researchers, as their data can be used as validation tools, or to reduce extensive data duplication.

The sheer volume also poses a challenge for essential data post-processing tasks like stack organization, annotation and segmentation, and this is expected to become even more crucial in the future. Luckily, annotation and segmentation of data is becoming increasingly automated, reducing the need for large-scale human validation of data as systems start achieving accuracy on par with or beyond human annotation[17,24,25]. Automated segmentation of these large datasets will enable quantitative examination of morphological features, something that is as of yet unfeasible in terms of annotation time. Further developments in software are crucial for large-scale CLEM applications, as registration of large-scale fluorescence and EM data is no trivial task. Having software tools that aid in time-consuming steps like ROI selection, registration of data from different modalities, and final segmentation may drastically reduce the complexity of CLEM experiments. The first developments towards automation of CLEM are already becoming visible: for example, tools for large-scale data visualization, automated alignment of data and 3D reconstruction from different modalities are slowly becoming available[26–29], and will become more prevalent in the near future.

Another field revolutionized by the advances of CLEM is cryo-EM. Cryogenic imaging offers the benefit of imaging specimens in near-native, hydrated conditions, at nanometer or angstrom resolution[30]. This approach is currently revolutionizing the way we examine ultrastructure, but is handicapped by the limited throughput of cryo-electron tomography (cryo-ET). Targeting specific ROIs with cryo-ET is highly challenging as frozen samples have poor contrast, are easily damaged by the electron beam, and are inaccessible to exogenous labels. Further difficulty is added by the limited volume of a cryo-electron tomogram, which are generally acquired from material thinned by cryo-FIB-SEM, known as lamellae [31–34]. Thinning material by FIB is time-consuming and sensitive to operator error, further limiting throughput.

The implementation of cryo-CLEM solves an important shortcoming in the process of cryo-EM: by using FM, ROIs are easily identified, and FM can guarantee that the chosen cell actually contains the structure or protein of interest. As a result, cryo-FM and associated correlative strategies have rapidly become established tools in conjunction with cryo-ET [31,35,36]. At this stage, cryo-FM still adds transfer steps to the workflow of cryo-CLEM, but this will likely rapidly change with the adoption of fully integrated solutions where FM and EM data is collected in a single system[37,38]. The integration of microscope modalities increases specimen

throughput, and eliminates steps that contaminate or damage the vulnerable frozen specimens[37,39], driving down the cost per sample and eliminating some of the technical challenges associated with performing cryo-EM.

The increased expertise with cryogenic imaging has also translated to novel applications: while cryo-FIB-SEM is primarily used for the creation of cryo-ET lamellae, cryo-FIB-SEM is also developed as a standalone imaging strategy. The technique is still in its infancy, but has shown potential for automated serial imaging ('Slice & View') without devitrification of samples[40–42]. Future improvements of imaging regimes and data post-processing could very well make cryo-volume imaging a reality, where cryo-FM provides compositional information, which is then linked to ultrastructural data provided by cryo-FIB-SEM.

The difficulty experienced with labeling in cryo-CLEM highlights another facet of CLEM, namely CLEM probes. Labeling and contrasting in CLEM is generally a compromise, with a trade-off between fluorescence signal and electron microscopic detail. Ideally, a specimen should simultaneously be highly fluorescent and sufficiently electron dense, especially for integrated CLEM strategies. Yet, common fluorescent probes are highly sensitive to the preparation required for sufficient morphological detail and provide no electron contrast. This has sparked development towards genetically encoded probes specifically tailored as CLEM probes. So far, protein engineering has been used to introduce the genetic tag mEos4B, which has a reduced sensitivity to the strong fixatives used in EM [43], and remains fluorescent in acrylic resins. Progress is also seen towards bimodal contrast, resulting in peroxidase-based probes fused to fluorescent proteins, such as FLIPPER and miniSOG[44–46]. These constructs are not only fluorescent, but also capable of polymerizing diaminobenzidine, a common osmophilic reagent used for EM contrast. Although the toolbox of specifically tailored CLEM probes is currently limited, we expect that further protein engineering will result in further, more advanced solutions.

### **Concluding remarks**

In conclusion, the field of CLEM is going through an exciting wave of innovation, thanks to a combination of higher resolution and larger-scale FM techniques, efficient alignment schemes and an increase of imaging resolution and speed of EM systems. Another exciting prospect is the broader accessibility of CLEM through community initiatives and platforms for bio-imaging like CORBEL, EuroBioImaging, NEMI and COMULIS[47–50]. Initiatives and consortia like these enable the development of novel CLEM approaches or the inclusion of novel imaging modalities, while also serving as a platform to make CLEM easily accessible to the larger scientific community.

Overall, this thesis highlights the advances necessary to efficiently place live-cell dynamics and molecular composition into ultrastructural context, and demonstrates the benefits of the use of bimodal particles for more efficient CLEM applications. These, and other recent developments have made CLEM into an increasingly powerful tool in cell biology, by tightly interlinking the best that fluorescence and electron imaging have to offer.

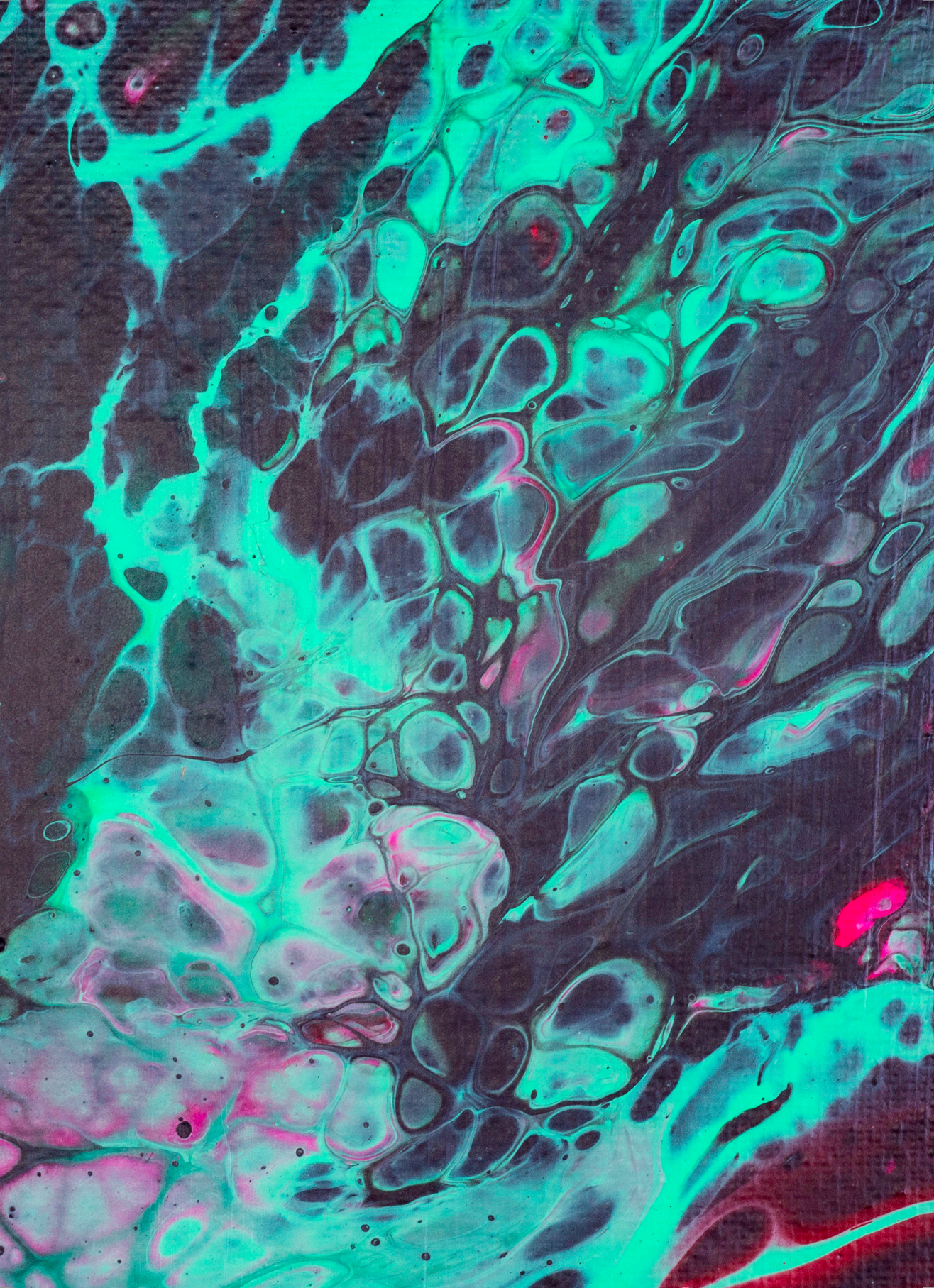
## References

1. Polishchuk RS, Polishchuk E V., Marra P, Alberti S, Buccione R, Luini A, Mironov AA. Correlative light-electron microscopy reveals the tubular-saccular ultrastructure of carriers operating between Golgi apparatus and plasma membrane. *J Cell Biol* 2000;148:45–58.
2. Murphy GE, Narayan K, Lowekamp BC, Hartnell LM, Heymann J a W, Fu J, Subramaniam S. Correlative 3D imaging of whole mammalian cells with light and electron microscopy. *J Struct Biol* 2011;176:268–78.
3. Bushby AJ, Mariggi G, Armer HEJ, Collinson LM. Correlative Light and Volume Electron Microscopy: Using Focused Ion Beam Scanning Electron Microscopy to Image Transient Events in Model Organisms. *Methods Cell Biol* 2012;111:357–382.
4. Olmos Y, Hodgson L, Mantell J, Verkade P, Carlton JG. ESCRT-III controls nuclear envelope reformation. *Nature* 2015;522:236–9.
5. Russell MRG, Lerner TR, Burden JJ, Nkwe DO, Pelchen-Matthews A, Domart M-C, Durgan J, Weston A, Jones ML, Peddie CJ, Carzaniga R, Florey O, Marsh M, Gutierrez MG, Collinson LM. 3D correlative light and electron microscopy of cultured cells using serial blockface scanning electron microscopy. *J Cell Sci* 2017;130:278–291.
6. Polishchuk RS, San Pietro E, Di Pentima A, Teté S, Bonifacino JS. Ultrastructure of long-range transport carriers moving from the trans-Golgi network to peripheral endosomes. *Traffic* 2006;7:1092–1103.
7. Rijnsoever C Van, Oorschot V, Klumperman J. Correlative light-electron microscopy (CLEM) combining live-cell imaging and immunolabeling of ultrathin cryosections. *Nat Methods* 2008;5:973–980.
8. Stepanek L, Pigino G. Microtubule doublets are double-track railways for intraflagellar transport trains. *Science (80- )* 2016;352:721–724.
9. Briggman KL, Bock DD. Volume electron microscopy for neuronal circuit reconstruction. *Curr Opin Neurobiol* 2012;22:154–161.
10. Hayworth KJ, Morgan JL, Schalek R, Berger DR, Hildebrand DGC, Lichtman JW. Imaging ATUM ultrathin section libraries with WaferMapper: a multi-scale approach to EM reconstruction of neural circuits. *Front Neural Circuits* 2014;8:1–18.
11. Eberle AL, Mikula S, Schalek R, Lichtman J, Knothe Tate ML, Zeidler D. High-resolution, high-throughput imaging with a multibeam scanning electron microscope. *J Microsc* 2015;259:114–120.
12. Faas FGA, Cristina Avramut M, van den Berg BM, Mieke Mommaas A, Koster AJ, Ravelli RBG. Virtual nanoscopy: Generation of ultra-large high resolution electron microscopy maps. *J Cell Biol* 2012;198:457–469.
13. Ravelli RBG, Kalicharan RD, Cristina Avramut M, Sjollem KA, Pronk JW, Dijk F, Koster AJ, Visser JTI, Faas FGA, Giepmans BNG. Destruction of tissue, cells and organelles in type 1 diabetic rats presented at macromolecular resolution. *Sci Rep* 2013;3:1–6.
14. Peddie CJ, Collinson LM. Exploring the third dimension: volume electron microscopy comes of age. *Micron* 2014;61:9–19.
15. Xu CS, Hayworth KJ, Lu Z, Grob P, Hassan AM, García-Cerdán JG, Niyogi KK, Nogales E, Weinberg RJ, Hess HF. Enhanced FIB-SEM systems for large-volume 3D imaging. *Elife* 2017;6:1–36.
16. Zheng Z, Lauritzen JS, Perlman E, Robinson CG, Nichols M, Milkie D, Torrens O, Price J, Fisher CB, Sharifi N, Calle-Schuler SA, Kmecova L, Ali IJ, Karsh B, Trautman ET, Bogovic JA, Hanslovsky P, Jefferis GSXE, Kazhdan M, Khairy K, Saalfeld S, Fetter RD, Bock DD. A Complete Electron Microscopy Volume of the Brain of Adult *Drosophila melanogaster*. *Cell* 2018;174:730–743.e22.
17. Takemura SY, Bharioke A, Lu Z, Nern A, Vitaladevuni S, Rivlin PK, Katz WT, Olbris DJ, Plaza SM, Winston P, Zhao T, Horne JA, Fetter RD, Takemura S, Blazek K, Chang LA, Ogundeyi O, Saunders MA, Shapiro V, Sigmund C, Rubin GM, Scheffer LK, Meinertzhagen IA, Chklovskii DB. A visual motion detection circuit suggested by *Drosophila* connectomics. *Nature* 2013;500:175–181.
18. Hildebrand DGC, Cicconet M, Torres RM, Choi W, Quan TM, Moon J, Wetzel AW, Scott Champion A, Graham BJ, Randlett O, Plummer GS, Portugues R, Bianco IH, Saalfeld S, Baden AD, Lillaney K, Burns R, Vogelstein JT, Schier AF, Lee WCA, Jeong WK, Lichtman JW, Engert F. Whole-brain serial-section electron microscopy in larval zebrafish. *Nature* 2017;545:345–349.
19. Patwardhan A, Carazo J-M, Carragher B, Henderson R, Heymann JB, Hill E, Jensen GJ, Lagerstedt I, Lawson CL, Ludtke SJ, Mastronarde D, Moore WJ, Roseman A, Rosenthal P, Sorzano C-OS, Sanz-García E, Scheres SHW, Subramaniam S, Westbrook J, Winn M, Swedlow JR, Kleywegt GJ. Data management challenges in three-dimensional EM. *Nat Struct Mol Biol* 2012;19:1203–1207.
20. Patwardhan A, Ashton A, Brandt R, Butcher S, Carzaniga R, Chiu W, Collinson L, Doux P, Duke E, Ellisman MH, Franken E, Grünewald K, Heriche J-K, Koster A, Kühlbrandt W, Lagerstedt I, Larabell C, Lawson CL, Saibil HR, Sanz-García E, Subramaniam S, Verkade P, Swedlow JR, Kleywegt GJ. A 3D cellular context for the macromolecular world. *Nat Struct Mol Biol* 2014;21:841–845.

21. Berman HM, Westbrook J, Feng Z, Gilliland G, Bhat TN, Weissig H, Shindyalov IN, Bourne PE. The Protein Data Bank. *Nucleic Acids Res* 2000;28:235–242.
22. Iudin A, Korir PK, Salavert-Torres J, Kleywegt GJ, Patwardhan A. EMPIAR: a public archive for raw electron microscopy image data. *Nat Methods* 2016;13:387–388.
23. Patwardhan A, Lawson CL. Databases and Archiving for CryoEM. *Methods Enzymol* 2016;579:393–412.
24. Arganda-Carreras I, Turaga SC, Berger DR, Cireşan D, Giusti A, Gambardella LM, Schmidhuber J, Laptev D, Dwivedi S, Buhmann JM, Liu T, Seyedhosseini M, Tasdizen T, Kametsky L, Burget R, Uher V, Tan X, Sun C, Pham TD, Bas E, Uzunbas MG, Cardona A, Schindelin J, Seung HS. Crowdsourcing the creation of image segmentation algorithms for connectomics. *Front Neuroanat* 2015;9:1–13.
25. Zeng T, Wu B, Ji S. DeepEM3D: approaching human-level performance on 3D anisotropic EM image segmentation. *Bioinformatics* 2017;33:2555–2562.
26. Paul-Gilloteaux P, Heiligenstein X, Belle M, Domart MC, Larijani B, Collinson L, Raposo G, Salamero J. EC-CLEM: Flexible multidimensional registration software for correlative microscopies. *Nat. Methods.* 2017;14:102–103.
27. Mohammadian S, Fokkema J, Agronskaia A V., Liv N, de Heus C, van Donselaar E, Blab GA, Klumperman J, Gerritsen HC. High accuracy, fiducial marker-based image registration of correlative microscopy images. *Sci Rep* 2019;9:3211.
28. Cardona A, Saalfeld S, Schindelin J, Arganda-Carreras I, Preibisch S, Longair M, Tomancak P, Hartenstein V, Douglas RJ. TrakEM2 software for neural circuit reconstruction. *PLoS One* 2012;7.
29. Saalfeld S, Cardona A, Hartenstein V, Tomancak P. CATMAID: collaborative annotation toolkit for massive amounts of image data. *Bioinformatics* 2009;25:1984–1986.
30. Dubochet J, Adrian M, Chang J-J, Homo J-C, Lepault J, McDowell AW, Schultz P. Cryo-electron microscopy of vitrified specimens. *Q Rev Biophys* 1988;21:129–228.
31. Plitzko JM, Rigort A, Leis A. Correlative cryo-light microscopy and cryo-electron tomography: from cellular territories to molecular landscapes. *Curr Opin Biotechnol* 2009;20:83–9.
32. Villa E, Schaffer M, Plitzko JM, Baumeister W. Opening windows into the cell: focused-ion-beam milling for cryo-electron tomography. *Curr Opin Struct Biol* 2013;23:771–7.
33. Rigort A, Bäuerlein FJB, Villa E, Eibauer M, Laugks T, Baumeister W, Plitzko JM. Focused ion beam micromachining of eukaryotic cells for cryoelectron tomography. *Proc Natl Acad Sci U S A* 2012;109:4449–54.
34. Hsieh C, Schmelzer T, Kishchenko G, Wagenknecht T, Marko M. Practical workflow for cryo focused-ion-beam milling of tissues and cells for cryo-TEM tomography. *J Struct Biol* 2014;185:32–41.
35. Briegel A, Chen S, Koster AJ, Plitzko JM, Schwartz CL, Jensen GJ. Correlated Light and Electron Cryo-Microscopy. 2010. p. 317–341.
36. Arnold J, Mahamid J, Lucic V, de Marco A, Fernandez J-J, Laugks T, Mayer T, Hyman AA, Baumeister W, Plitzko JM. Site-Specific Cryo-focused Ion Beam Sample Preparation Guided by 3D Correlative Microscopy. *Biophys J* 2016;110:860–869.
37. Faas FGA, Bárcena M, Agronskaia AV, Gerritsen HC, Moscicka KB, Diebolder CA, van Driel LF, Limpens RWAL, Bos E, Ravelli RBG, Koning RI, Koster AJ. Localization of fluorescently labeled structures in frozen-hydrated samples using integrated light electron microscopy. *J Struct Biol* 2013;181:283–290.
38. Zonneville AC, Van Tol RFC, Liv N, Narvaez AC, Efftig APJ, Kruit P, Hoogenboom JP. Integration of a high-NA light microscope in a scanning electron microscope. *J Microsc* 2013;252:58–70.
39. Gorelick S, Buckley G, Gervinskias G, Johnson TK, Handley A, Caggiano MP, Whisstock JC, Pocock R, de Marco A. PIE-scope, integrated cryo-correlative light and FIB/SEM microscopy. *Elife* 2019;8.
40. Schertel A, Snaidero N, Han HM, Ruhwedel T, Laue M, Grabenbauer M, Möbius W. Cryo FIB-SEM: Volume imaging of cellular ultrastructure in native frozen specimens. *J Struct Biol* 2013;184:355–360.
41. Rigort A, Plitzko JM. Cryo-focused-ion-beam applications in structural biology. *Arch Biochem Biophys* 2015;581:122–130.
42. Vidavsky N, Akiva A, Kaplan-Ashiri I, Rechav K, Addadi L, Weiner S, Schertel A. Cryo-FIB-SEM serial milling and block face imaging: Large volume structural analysis of biological tissues preserved close to their native state. *J Struct Biol* 2016;196:487–495.
43. Paez-Segala MG, Sun MG, Shtengel G, Viswanathan S, Baird M a, Macklin JJ, Patel R, Allen JR, Howe ES, Piszczek G, Hess HF, Davidson MW, Wang Y, Looger LL. Fixation-resistant photoactivatable fluorescent proteins for CLEM. *Nat Methods* 2015;
44. Shu X, Lev-Ram V, Deerinck TJ, Qi Y, Ramko EB, Davidson MW, Jin Y, Ellisman MH, Tsien RY. A genetically encoded tag for correlated light and electron microscopy of intact cells, tissues, and organisms. *PLoS Biol* 2011;9:e1001041.
45. Kuipers J, van Ham TJ, Kalicharan RD, Veenstra-Algra A, Sjollem KA, Dijk F, Schnell U, Giepmans BNG.

- FLIPPER, a combinatorial probe for correlated live imaging and electron microscopy, allows identification and quantitative analysis of various cells and organelles. *Cell Tissue Res* 2015;360:61–70.
46. de Beer MA, Kuipers J, van Bergen en Henegouwen PMP, Giepmans BNG. A small protein probe for correlated microscopy of endogenous proteins. *Histochem Cell Biol* 2018;149:261–268.
  47. CORBEL Project – Coordinated Research Infrastructures Building Enduring Life-science Services [Internet]. [cited 2019 Aug 11];Available from: <https://www.corbel-project.eu/home.html>
  48. Euro-Biolmaging - Research Infrastructure for Imaging Technologies in Biological and Biomedical Sciences [Internet]. [cited 2019 Aug 11];Available from: <http://www.eurobioimaging.eu/>
  49. NEMI – Netherlands Electron Microscopy Infrastructure [Internet]. [cited 2019 Aug 11];Available from: <http://www.e-microscopy.nl/>
  50. COMULIS - Correlated Multimodal Imaging in Life Sciences [Internet]. [cited 2019 Aug 11];Available from: <https://www.comulis.eu/>





---

# Addendum

---

## Nederlandse samenvatting

Er zijn weinig technieken zo invloedrijk geweest in de celbiologie als microscopie. Zowel fluorescentiemicroscopie (FM) als elektronenmicroscopie (EM) zijn van groot belang voor het ophelderen van de structuur en dynamiek van eiwitten, cellen en weefsels.

FM is bij uitstek geschikt om (sub)cellulaire structuren snel te lokaliseren en te bestuderen. Specifieke eiwitten en moleculen kunnen worden gedetecteerd dankzij fluorescente labels, in de vorm van antilichamen of chemische stoffen, of door fusie van het eiwit van interesse met een fluorescent eiwit. Deze laatste aanpak is ook geschikt voor microscopie in levende cellen, waardoor eiwitten, organellen en individuele cellen door zowel de ruimte als tijd gevolgd kunnen worden. De beperking van FM is echter dat alleen de labels worden gevisualiseerd, waardoor de context waarin de fluorescentie wordt gezien (de ultrastructuur) onbekend blijft.

EM maakt gebruik van elektronen in plaats van fotonen. Net als zichtbaar licht in fluorescentie gedragen elektronen zich als golven, maar door hun kortere golflengte is het oplossend vermogen veel groter. Bovendien is EM niet afhankelijk van labels, waardoor de ultrastructuur op nanometerschaal zichtbaar wordt gemaakt. Inmiddels is de techniek zo ver ontwikkeld dat ook visualisatie van complexe interacties tussen cellen en organellen in drie dimensies mogelijk is. Voor EM is het echter noodzakelijk dat materiaal sterk gefixeerd is en vrij van water, waardoor levend materiaal niet in de EM kan worden onderzocht.

Door de sterk verschillende preparateisen van FM en EM kunnen monsters lastig worden uitgewisseld tussen de twee technieken. Desondanks kunnen de technieken toch complementair worden gebruikt. Correlatieve licht en elektronenmicroscopie (CLEM) omvat een set technieken waarbij de sterke punten van FM en EM worden gecombineerd. Hierbij worden eerst fluorescente data van een specimen verzameld, waarna deze worden gekoppeld aan EM observaties op hetzelfde materiaal. Hierdoor is men in staat om bijvoorbeeld eiwitten of enzymactiviteit te lokaliseren in de cellulaire context. Er kan gebruik worden gemaakt van de snelheid van FM om zeldzame kenmerken te identificeren voor onderzoek in de EM, iets wat met alleen EM zeer tijdrovend zou zijn. CLEM kan bovendien gebruikt worden om FM data verworven uit levende cellen te koppelen aan ultrastructuur. Hierdoor kan ook de structurele basis van dynamische processen in de cel worden onderzocht. Mede door deze eigenschappen is CLEM een essentiële techniek binnen celbiologisch onderzoek geworden.

Voor CLEM is nauwkeurige registratie van data uit verschillende microscopen van groot belang. De schaal en resolutie waarmee beelden worden gevormd verschillen sterk tussen FM en EM. Dit resolutieverschil zorgt dat het koppelen van FM en EM data wordt bemoeilijkt. Bovendien kunnen preparaten vervormen tijdens de voorbereiding voor EM, waardoor de regio van interesse (ROI) niet langer op de verwachte plek in het EM preparaat zit. Dit probleem kan worden ondervangen door data te koppelen door middel van referentiepunten die van nature in het monster aanwezig zijn, zoals de unieke vorm van individuele cellen of organellen als de celkern, of unieke vormen in weefsel, zoals bloedvaten. Op deze manier kunnen de datasets met voldoende nauwkeurigheid aan elkaar worden gekoppeld om specifieke cellen te herkennen in weefsel, of grote organellen in een cel te kunnen lokaliseren. Voor registratie met hogere nauwkeurigheid is deze informatie echter niet genoeg. In die gevallen maakt men gebruik van kunstmatige referentiepunten die in zowel licht- als elektronenbeelden zichtbaar zijn, bijvoorbeeld in de vorm van

nanodeeltjes. Goede zichtbaarheid van deze referentiepunten in zowel FM als EM is daarbij essentieel.

Het doel van het onderzoek in dit proefschrift was de ontwikkeling van nieuwe methodes binnen CLEM. De methodes die in dit proefschrift zijn ontwikkeld benaderen meerdere facetten van deze techniek. Het eerste deel beschrijft een techniek om met FM verkregen beelden uit levende cellen te correleren aan 3D EM data. Op deze manier kunnen dynamische en functionele parameters uit levende cellen worden geplaatst in hun ultrastructurele context. Verder introduceert dit proefschrift twee strategieën voor efficiënte correlatie van licht- en elektronenmicroscopische data door het gebruik van fluorescente en elektron-dichte nanodeeltjes als referentiepunten voor CLEM.

Deze nieuw ontwikkelde technieken en nanodeeltjes zijn ingezet voor de karakterisering van het endo-lysosomale systeem. Dit systeem van membraan-omhulde blaasjes is verantwoordelijk voor onder andere het transport van eiwitten, afbraak van materialen uit de extracellulaire ruimte en recycling van receptoren. Daarnaast zijn endosomen en lysosomen onder andere betrokken bij het repareren van de celmembranen bij schade, het herkennen van pathogenen en het reguleren van de beschikbare hoeveelheid voedingsstoffen in de cel. De verschillende onderdelen van het endo-lysosomale systeem kennen een grote diversiteit in moleculaire samenstelling, dynamiek, en structurele kenmerken. Hierdoor is een combinatie FM en EM noodzakelijk om alle verschillende aspecten van het systeem waar te nemen.

## Samenvatting van het proefschrift

**Hoofdstuk 2** beschrijft een nieuwe strategie voor CLEM (live-cell CLEM) om dynamische FM informatie van het endo-lysosomale systeem te correleren aan 3D ultrastructurele data, verkregen uit een scanning EM uitgerust met een gefocuste ionenbundel (FIB-SEM). Met een FIB-SEM kunnen biologische structuren op nanometerschaal in kaart worden gebracht in 3D, wat cruciaal is om de identiteit van endo-lysosomale organellen vast te kunnen stellen. Door de combinatie van FM en FIB-SEM kunnen individuele organellen met grote nauwkeurigheid worden aangewezen voor analyse en kan dynamische informatie efficiënt worden gekoppeld aan structurele data.

In **hoofdstuk 3** wordt de combinatie van FM en 3D EM gebruikt om functionele informatie te integreren in CLEM. De identiteit van endo-lysosomale organellen wordt naast hun structuur en samenstelling ook bepaald door de aanwezigheid van specifieke enzymen, ionen en verschillen in de pH. Fluorescente sensors voor calcium, enzymactiviteit en pH kunnen worden gebruikt om deze parameters te onderzoeken, maar deze zijn niet zichtbaar in een elektronenmicroscop. Dankzij de in hoofdstuk 2 geïntroduceerde live-cell CLEM techniek kunnen deze functionele parameters worden gekoppeld aan ultrastructuur. Met deze aanpak tonen we aan dat deletie van het eiwit VPS41 leidt tot een verstoring van het transport van dextraan en morfologische veranderingen in endo-lysosomale compartimenten teweeg brengt. Ondanks deze verstoringen blijft enzymactiviteit van cathepsine B en cathepsine D, twee lysosomale enzymen, correct gelokaliseerd, wat duidt op een regulatie die onafhankelijk is van het correct functioneren van VPS41.

In het tweede deel van dit proefschrift (**hoofdstukken 4 en 5**) worden nieuwe nanodeeltjes ontwikkeld, welke bijdragen aan een snelle en nauwkeurige registratie van data uit verschillende microscopen. **Hoofdstuk 4** beschrijft de synthese en het

gebruik van nanodeeltjes gevormd uit fluorescent bovine (koe) serum albumine en elektronen-dicht colloïdaal goud (fBSA-Au), welke voor meerdere doelen kan worden ingezet. fBSA-Au wordt efficiënt opgenomen door gekweekte cellen en is zichtbaar in zowel de FM als EM. Dit maakt fBSA-Au geschikt als referentiepunten voor zowel 2D als 3D CLEM, wat wordt gedemonstreerd aan de hand van verschillende CLEM technieken.

In **hoofdstuk 5** worden nanodeeltjes beschreven die zijn opgebouwd uit een kern van 15 nm colloïdaal goud, omgeven door een huls van fluorescente silica. Deze huls kan worden gegroeid tot een arbitraire dikte, waardoor nanodeeltjes van gewenste grootte kunnen worden verkregen. De synthese en karakterisering van deze deeltjes wordt getoond, alsmede hun gebruik voor CLEM. We laten zien dat cellen deze nanodeeltjes opnemen via endocytose. Net als fBSA-Au zijn deze deeltjes daarna zeer goed zichtbaar in zowel FM als EM, wat ze uitermate geschikt maakt als referentiepunten voor zowel 2D als 3D CLEM. Dankzij hun grotere formaat en fBSA-Au en hun compositie zijn ze bovendien geschikt als referentiepunten voor correlatie van FM naar FIB-SEM.

Samenvattend bevat dit proefschrift een verzameling van nieuwe en verbeterde aanpakken voor het correleren van dynamische en functionele FM data in 3D ultrastructuur verkregen via EM. Daarnaast worden twee verschillende soorten nanodeeltjes beschreven die kunnen worden gebruikt als referentiepunten om CLEM data te oriënteren en te koppelen. Deze en andere recente ontwikkelingen maken CLEM tot een steeds krachtigere techniek voor celbiologie, door een intieme koppeling van het beste dat FM en EM te bieden hebben.

## Dankwoord

Zo. Daar ligt het dan, helemaal klaar. Hoewel mijn naam prominent op de voorkant van dit werk staat, had het er niet kunnen liggen zonder de directe dan wel indirecte bijdragen van een hoop mensen, die ik hierbij allemaal wil bedanken.

Ten eerste wil ik graag mijn promotoren Hans en Judith bedanken. **Judith**, voordat ik bij jou aan mijn proefschrift begon had ik al kennis mogen maken met jouw groep en werkzaamheden tijdens een korte stage, wat een enorme drijfveer is geweest om een proefschrift te doen dat zo zwaar op beeldvorming leunde. Ik heb enorm veel geleerd van de vrijheid die je me hebt gegeven tijdens het uitvogelen van de FIB-SEM en andere correlatieve werkwijzen. Het in biologische context plaatsen en vervolgens sterk presenteren van al de data die hieruit voortkwam ging me lastiger af. Dankzij jouw hulp en sturing ben ik gaan inzien dat dit enorm waardevolle vaardigheden zijn, en ik ben blij dat ik ze in dit proefschrift heb kunnen toepassen. **Hans**, mijn biologische projecten stonden wat verder van jouw expertise af, maar toch wist je me altijd te prikkelen om ook over de biofysica achtergrond van biologische vindingen na te denken. Je bent een geweldige mentor voor me geweest, die ervoor zorgde dat ik af en toe ook stil stond bij hoe het met mezelf ging, in plaats van alleen maar over mijn onderzoek en werkzaamheden na te denken.

Dan wil ik ook graag **Nalan** en **Wally**, mijn copromotoren bedanken. **Nalan**, you went from an enthusiastic colleague to an incredible daily supervisor. I thoroughly enjoyed working with you, whether it was on designing new correlative techniques or writing chapters. I am incredibly thankful for all your enthusiasm, input and support in the lab, and I'm honored to be the first PhD you co-supervised. **Wally**, dank je wel voor alle ondersteuning gedurende mijn project, en alle lunchbesprekingen die daaraan te pas kwamen. Ik vond het geweldig om samen met je te kunnen klussen aan de samplevoorbereiding, en later ook samen uit te zoeken hoe we de mooiste afbeeldingen uit het systeem konden krijgen.

I would like to thank all the committee members: **Allard Mosk**, **Dorus Gadella**, **Friedrich Förster**, **Lukas Kapitein**, and **Yannick Schwab**. I want to express my gratitude to all of you for your interest, and look forward to discussing my thesis with all of you during the ceremony.

I would also like to express my gratitude to the PIs present in the Cell Biology over the years. **Madelon**, **Catherine**, **Paul**, **Peter**, **Ger**, **Fulvio**, thank you for all the input during work discussions and meetings, which has helped me shape my projects and thesis.

Het grootste deel van het werk in mijn proefschrift heb ik gedaan samen met de mensen uit de Klumperman-groep, die ik ook graag wil bedanken voor de geweldige ervaringen tijdens mijn promotie.

**Reini**, miss Friday! Waar je ook ging, je zorgde altijd voor een heerlijke hoeveelheid leven in de brouwerij en liet een glimlach in je kielzog achter. Die energie mag je ook zeker meenemen naar mijn promotie, waar je mijn een van mijn paranimfen bent. **Jan**, het was met jou altijd even makkelijk om over data-analyse te kunnen kletsen als over de nieuwste board games. Ik ben superblij dat je een van mijn paranimfen bent! **Ann**, ik heb het geweldig gehad samen met jou op de kamer. Eerst samen met Mario, daarna met z'n tweeën, hadden we een heerlijk rustig kantoor waarin ruimte was voor discussies over projecten, lastige vragen over morfologie, en af en toe ook ruimte om frustratie te uiten als een proef niet het verwachte resultaat opleverde. **Paolo**, although we didn't share too much in terms of projects, I had a



great time with you. Your knowledge of biochemistry and cloning was very nice to have in the lab. **Elisa**, from the moment you joined the lab you brought a lot of life into the group. Your Italian passion will carry you far. **Corlinda**, dank je wel voor alle hulp tijdens zowel mijn masterproject en mijn AIO-periode, en alle handigheidjes voor live-cell imaging die ik van je heb kunnen leren. **Cilia**, het was enorm gezellig om met jou op het lab te werken. Ik heb er ook ontzettend veel plezier in gehad om samen met jou het stuk FIB-SEM op de afdeling op te zetten. **Despina**, dankzij jou is de ezel nu toch echt op, met staart en al! Heel veel dank voor alle steunmomenten en geweldige Griekse anekdotes. **Tineke**, dankzij jou heb ik de fijne kneepjes van het immunolabelen in m'n vingers kunnen krijgen. **Suzanne**, ik heb enorm genoten van jouw rust en vriendelijkheid in het lab. Dank je wel voor alle hulp! **George**, dank je wel voor alle input en training rond de EMs. Altijd had je wel een oplossing als ik weer eens met een raar probleem op de EM aan kwam zetten, en ook van het klussen aan apparatuur was je niet vies. Ik heb daar enorm van geleerd, je enthousiasme en klusdrift waren zeer aanstekelijk. **René**, dank je wel voor alle hulp met het in elkaar zetten van figuren en posters! **Wieke** en **Betty**, lieve dames van het secretariaat, dank jullie wel voor alle gezelligheid in de afgelopen jaren, en alle hulp met het navigeren van het administratieve labyrinth van het UMCU. Ook de dames en heer van het onderwijs, **Maggy**, **Annemarie**, **Koen**, **Rita**, dank jullie wel voor de gezelligheid en hulp bij het geven van het bacheloronderwijs.

In het lab heb ik ook hulp gehad van studenten. **Jouke** en **Brigitte**, dank jullie wel voor alle hulp, het was een toffe ervaring om jullie te begeleiden. Succes met jullie volgende stappen!

Ook in de groep Biofysica zijn er een aantal mensen die ik graag wil bedanken: **Gerhard**, **Dave**, **Jantina**, **Sergey**, **Sajjad** and **Sasha**. **Gerhard**, eigenlijk direct sinds kennismaken heb ik enorm van onze discussies genoten, en ik dank je voor alle input en hulp. We moeten nog steeds een keer een glas whisky drinken nu dit proefschrift klaar is. **Jantina**, heel veel succes met de laatste loodjes! Ik vond het hartstikke gezellig om met jou samen aan de Shiny Particles projecten te werken, en ben blij dat je nu je draai hebt gevonden in het onderwijs.

I would also like to thank the people in Madelon Maurice's group, our sister group within Cell Biology. In no particular order, **Manja**, **Tom**, **Ingrid**, **Cara**, **Alba**, **Allesa**, **Joep**, **Jeroen**, **Felix**, **Peter**, **Stefanie**, thank you for all the fun projects, borrels, lab days and excursions over the years. Good luck to all of you with your projects and next steps in your careers!

Ook buiten Celbiologie en Biofysica zijn er een hoop mensen die bij hebben gedragen aan dit proefschrift, waarvan ik er een aantal specifiek wil bedanken. **Carlos** and **Geert**, thank you for the fun kinetochore collaboration! It was nice to see how we could fit microscopy into a new research question, and that it produced such nice results in the end. **Elly**, een groot deel van de FIB-SEM afbeeldingen in dit proefschrift zijn mogelijk geweest dankzij jouw kennis en geduld van samplevoorbereiding. Ik heb veel geleerd van jouw methodische aanpak. **Chris** en **Hans**, dank jullie wel voor jullie hulp en ondersteuning bij het gebruik van de microscopen die de UU rijk is. **Matthijs**, het was erg fijn om een 'FIB-SEM-veteraan' te hebben om mee te kunnen sparren. Dank voor alle tips en trucs voor dataverwerking en acquisitie! **Marco**, het was altijd gezellig om met jou in het lab te werken of te kijken wat we nu weer in de microscoop zagen. Ik ken weinig mensen die zo veel lol hebben in microscopie! **Niels** en **Annette**, dank jullie wel voor al jullie begeleiding tijdens mijn laatste masterstage. Dankzij jullie heb ik uiteindelijk de knoop durven doorhakken

om aan een promotie te beginnen, en ben enorm dankbaar voor alle lessen die ik de laatste paar jaar heb toe kunnen passen.

There are also quite a couple of people that I've worked with, but have graduated, retired, or left the lab before I finished: **Caspar, Ana, Romain, Jan, Nicola, Maureen, Romain, Eline, Huiying, Francesca, Mario, Luca, Janneke, Wienand, Daphne, Dave, Andri, Muriel, Rita, Jorg, Enric, Stephin, Emily, Desiré**. I'm very happy that I've had the opportunity to work with all of you over the years, and thanks for all the help and input.

Natuurlijk is er meer in het leven dan werk, daarom wil ik alle familie en vrienden bedanken voor alle hulp, adviezen, vermaak en steun. Lieve **Wouter, Alice, Jasmijn**, zonder jullie had ik hier niet gestaan. Als familie hebben jullie een bijzonder plekje in mijn hart. Ik heb me altijd enorm gesteund gevoeld in de beslissingen die ik maakte, en jullie stonden altijd voor me klaar, op zowel de makkelijke als de moeilijke momenten. Dank jullie wel!

**Job Fermie**

## About the Author

### Curriculum Vitae

Job Fermie was born on the 18th of August 1990, in Naarden, The Netherlands. Job finished his secondary education at the Sint Vituscollege Bussum in 2008, with the course profile of Nature & Health. Afterwards, he studied Biomedical Sciences at Utrecht University, receiving a Bachelor's degree in 2011 and a Master's degree in 2013, after internships in the labs of Prof. Dr. Jos van Putten and Dr. Niels Bovenschen. Job started a PhD track in 2014, under supervision of Prof. dr. Judith Klumperman and Prof. Dr. Hans Gerritsen, with daily supervision from dr. Nalan Liv and dr. Wally Müller. During his research he developed strong interests for 3D light and electron imaging in biology, and the development and validation of imaging equipment. The results of his PhD research are presented in this thesis. As of March 2019, Job is working at DELMIC B.V.

### Publications

#### Presented in this thesis:

- Fermie J, Liv N, ten Brink C, van Donselaar EG, Müller WH, Schieber NL, Schwab Y, Gerritsen HC, Klumperman J. Single organelle dynamics linked to 3D structure by correlative live-cell imaging and 3D electron microscopy. *Traffic*. 2018 May;19(5):354-69.
- Fokkema J, Fermie J, Liv N, van den Heuvel DJ, Konings TO, Blab GA, Meijerink A, Klumperman J, Gerritsen HC. Fluorescently Labelled Silica Coated Gold Nanoparticles as Fiducial Markers for Correlative Light and Electron Microscopy. *Scientific reports*. 2018 Sep 11;8(1):13625.

#### Other publications:

- Sacristan C, Ahmad MU, Keller J, Fermie J, Groenewold V, Tromer E, Fish A, Melero R, Carazo JM, Klumperman J, Musacchio A. Dynamic kinetochore size regulation promotes microtubule capture and chromosome biorientation in mitosis. *Nature Cell Biology*. 2018 Jul;20(7):800.
- Jonker CT, de Heus C, Faber L, ten Brink C, Potze L, Fermie J, Liv N, Klumperman J. An adapted protocol to overcome endosomal damage caused by polyethylenimine (PEI) mediated transfections. *Matters*. 2017 Dec 18;3(12):e201711000012.
- Wensink AC, Kok HM, Meeldijk J, Fermie J, Froelich CJ, Hack CE, Bovenschen N. Granzymes A and K differentially potentiate LPS-induced cytokine response. *Cell Death Discovery*. 2016 Dec 2;2.
- Wensink AC, Kemp V, Fermie J, Laorden MI, van der Poll T, Hack CE, Bovenschen N. Granzyme K synergistically potentiates LPS-induced cytokine responses in human monocytes. *Proceedings of the National Academy of Sciences*. 2014 Apr 22;111(16):5974-9.

